

**Search for Quantum Black Holes and ADD Extra Dimensions in
the opposite sign dimuon channel in proton-proton collisions with
the ATLAS detector at $\sqrt{s} = 8$ TeV**

Marc Cano Bret
Queen Mary University of London

Ph.D. Supervisor:
Dr. Eram Rizvi

Submitted to QMUL in fulfilment of the requirements for the award of **Doctor of
Philosophy**

March 13, 2015

Declaration

I, Marc Cano Bret, confirm that the research included within this thesis is my own work or that when it has been carried out in collaboration with, or supported by others, that this is duly acknowledged below and my contribution indicated. Previously published materials are also acknowledged.

I attest that I have exercised reasonable care to ensure that the work is original, and does not to the best of my knowledge break any UK law, infringe any third party's copyright or other Intellectual Property Right, or contain any confidential material.

I accept that the College has the right to use plagiarism detection software to check the electronic version of the thesis.

I confirm that this thesis has not been previously submitted for the award of a degree by this or any other university.

The copyright of this thesis rests with the author and no quotation from it or information derived from it may be published without the prior written consent of the author.

Signature:

London March 13, 2015

Abstract

A search for Beyond the Standard Model physics is performed with the ATLAS detector in the opposite sign dimuon channel using the 20 fb^{-1} of data collected in 2012 at $\sqrt{s} = 8 \text{ TeV}$. No excess is found above the Standard Model expectation. Using a Bayesian statistical analysis, model dependent 95% Credibility Level Bayesian exclusion limits are extracted for two models of gravitationally-related beyond the Standard Model phenomena. For the ADD and RS quantum black hole models, limits of 3.32 and 1.95 TeV are set on the extradimensional Planck Scale, and for ADD Large Extra dimensions, limits ranging from 2.8-4.4 TeV are set on the string scale for the GRW, HLZ and Hewett formalisms. In addition, a study is performed to estimate the effect of increasing noise cuts in the ATLAS Level-1 Calorimeter Trigger on the physics efficiency of $W \rightarrow e\nu$ and $t\bar{t}$ and on the Level-1 missing transverse energy trigger rate. Results suggest that higher noise cuts could reduce the Level-1 missing transverse energy trigger rate with a minimal loss of physics efficiency.

Acknowledgements

I would like to use my first words to thank my supervisor, Eram Rizvi, for his patience throughout endless conversations and email discussions in odd hours, for his support and, specially, for his never-ending supply of positive attitude and optimism. I count myself very lucky for having had him as my supervisor.

I am very grateful to the people in the ATLAS Exotics Lepton+X Working Group. Special thanks to Daniel Hayden, without his help and patience in explaining all the details I dare to say that my knowledge of the analyses presented here would be about ten times poorer. I want to thank as well Tulin Varol and Graham Savage, working with you has been a joy . Thanks to Rozmin Daya, Stephane Willocq and Douglas Gingrich, their help has been invaluable through important moments in my PhD.

Thank you to all the people in the Physics department of Queen Mary University. Special thanks to John Morris for his help throughout my service task and the solutions he provided for frustrating computing issues I could not find my way around, and to Adrian Bevan for his help in the statistical analysis of the results. His insights and inquisitive questioning have proved very valuable and helped deepen my knowledge. Thank you to Rob, Greg, Ruth, Linda and Cristiano for their friendship and the good moments together.

Thank you to all the people in the Pays de Gex basketball team and my friends at CERN: Damien, Steve, Clement, Jordan, Fred, Jo, Eric, Borja F, Borja M, Miguel and Pablo. Their help and encouragement allowed me to not lose focus, overcome a difficult injury and carry on playing the game we all love.

Thank you Ben for being the best friend one can have.

Thank you to my mum for always being there to support me. She managed to raise me in a difficult situation and deserves all the praise in the world. Perhaps immodestly, I would say she could not have done a better job. Thank you Agusti for showing me how to be a man.

And, finally, I would like to thank my wife, Natasha, for her support. I guess having an absent-minded partner can be hard to deal with, but her love and support has helped me become a better person.

“Of course it is happening inside your head, Harry, but why on earth should that mean that it is not real?”

Albus Dumbledore in Harry Potter and the Deathly Hallows, J.K. Rowling

“It is not true that people stop pursuing dreams because they grow old, they grow old because they stop pursuing dreams”

Gabriel García Márquez

Contents

1	Introduction	1
2	Theory	3
2.1	The road to Quantum Field Theory	3
2.2	The Standard Model	6
2.2.1	Quantum Electrodynamics	6
2.2.2	Quantum Chromodynamics	8
2.2.3	Weak Interactions	10
2.2.4	Electro-Weak Symmetry Breaking and unification	12
2.2.5	Summary	16
2.3	The Planck Scale and Extra Dimensions	16
2.3.1	ADD Large Extra dimensions	18
2.3.2	The Randall-Sundrum Model	20
2.4	Black Hole Production at the LHC	22
2.4.1	Semiclassical Black Holes	22
2.4.2	Quantum Black Holes	24
2.5	Summary	26
3	The ATLAS detector	28
3.1	Experimental Setup and detector overview	28
3.2	Momentum measurement of a charged particle	32
3.3	Inner Detector	34
3.3.1	The Pixel Detectors	34
3.3.2	The Semi-Conductor Tracker	36
3.3.3	The Transition Radiation Tracker	36
3.4	Calorimetry	36

3.4.1	The Electromagnetic Calorimeter	37
3.4.2	The Hadronic Calorimeter	38
3.5	The muon system	39
3.5.1	The Muon Spectrometer	40
3.5.2	Muon Precision Chambers	40
3.5.3	Muon Trigger chambers	44
3.5.4	Muon Reconstruction	47
3.6	Trigger and Data acquisition	49
3.6.1	Level-1 Trigger	49
3.6.2	Level-2 Trigger	50
3.6.3	Event Filter and data processing	50
3.7	Performance	51
4	Study of the ATLAS Level-1 Calorimeter Missing Transverse Energy Trigger at High Pile-up using 2012 data	56
4.1	The ATLAS Level-1 Calorimeter trigger	57
4.2	Performance of the ATLAS Level-1 Calorimeter E_T^{Miss} triggers	60
4.3	Bunch Crossing ID dependent noise cuts	64
4.4	Fractional Occupancy vs noise cuts	67
4.5	$W \rightarrow e\nu$ and $t\bar{t}$ selection	70
4.6	Rate and efficiency definition	73
4.7	Method	77
4.8	Results	80
4.9	Conclusion	82
5	Black Hole Event Generators	84
5.1	BlackMax	84
5.2	QBH	86

6	Data and Monte Carlo samples	88
6.1	Data	89
6.2	Signal samples	89
6.2.1	ADD Large Extra Dimensions	89
6.2.2	Quantum Black Hole	91
6.3	Background samples	93
6.3.1	Drell-Yan	93
6.3.2	Diboson	96
6.3.3	Top Quark	98
6.3.4	Photon-Induced corrections	98
6.4	Pile-up Reweighting	103
7	Dimuon event selection and corrections applied	104
7.1	Background Estimation	104
7.2	Event Selection	105
7.3	Corrections applied	115
7.3.1	Trigger Efficiency	116
7.3.2	Reconstruction Efficiency	118
7.3.3	Muon Momentum Scale and Resolution Corrections	119
7.4	Systematic Uncertainties	123
7.4.1	Theoretical systematic uncertainties	124
7.4.2	Experimental systematic uncertainties	131
7.4.3	Summary	137
7.5	Data-Monte Carlo comparison	137
8	Statistical Analysis	144
8.1	Bayesian Statistical Interpretation and limit setting	144
8.2	ADD Large Extra Dimensions	146

8.3	QBH	150
8.4	Channel Combination	152
8.5	Discovery statistics	153
9	Results of the search	155
9.1	Search for ADD Large Extra Dimensions	156
9.1.1	ADD Optimal Mass Cut	156
9.1.2	Results	158
9.2	Search for Quantum Black Holes	167
10	Conclusion	173
	Appendix	174
A	Dilepton p_T reweight	174
B	ADD Large extra dimensions limits with a uniform prior on the cross section	178
C	QBH Limits with the Frequentist CL_S method	180
D	Additional Plots	183
E	QBH Sensitivity studies	188
F	BlackMax parameter choice	193
G	QBH samples parameter choice	198
	References	200
	List of Figures	209
	List of Tables	223

1 Introduction

The Large Hadron Collider (LHC) is the crown jewel of particle accelerators at the present time, reaching centre-of-mass energies that eclipse its predecessors. Operations began in September 2008 by successfully accelerating proton beams in opposite directions. Unfortunately, this success proved to be short-lived: just a few days later a faulty connection between magnets caused an explosion that damaged other magnets in the area [1]. While safety measures ensured the incident had no human cost, operations were stopped while repairs took place. In November 2009, the LHC resumed operations and quickly broke the record for the highest energy particle collisions in an accelerator, held at the time by the Tevatron in Fermilab, near Chicago [2]. For the ensuing three years the LHC carried on producing proton-proton collisions that reached a maximum centre-of-mass energy of 8 TeV without major incidents. The particle accelerator was shut down in early 2013 in preparation for its restart in 2015, when it is expected to resume operations and produce proton-proton collisions reaching a centre-of-mass energy of 13 TeV, and eventually reaching the design value of 14 TeV.

The first few years of LHC operations have been a resounding success: the high energy reach of the LHC has allowed for tests of the Standard Model of Particle Physics in kinematic regions never probed before. The data collected by the four particle detectors¹ placed at different points in the LHC ring is still being analysed to this day by physicists from 562 institutions. For the general public, the most well known achievement during this period is the confirmation of the existence of a particle consistent with the long-ago predicted Standard Model Higgs boson [3] by both the ATLAS and CMS detectors [4, 5]. It should be noted that the data collected has also been used to test the Standard Model in precision measurements and constrain parameters from models predicting beyond the Standard Model phenomena, such as the mass of new particles predicted by Super-Symmetry or the size of extra dimensions at short distance scales.

The finding of the Higgs boson is a further confirmation of the success of the Standard Model of Particle Physics. Its predictions have been confirmed at various particle accelerators such as the LHC and its predecessors, the Stanford Linear Collider (SLC), the Hadron-Electron Ring Accelerator (HERA), the Large Electron-Positron (LEP) collider and the Tevatron. Despite its success, the Standard Model has shortcomings. Perhaps the most important one but by no means the only one is the fact that a description of the gravitational force at quantum level is yet to be found. This thesis is focused on that topic: chapter 2 contains a summary of the current state of the Standard Model together with the description of two models

¹The four particle detectors are ATLAS (A Toroidal LHC Apparatus), CMS (Compact Muon Solenoid), LHCb (LHC beauty) and ALICE (A Large Ion Collider Experiment). ATLAS and CMS are general purpose detectors designed to test the Standard Model and search for beyond the Standard Model phenomena, ALICE is used to detect heavy ion collisions whereas LHCb aims to analyse the properties of bottom quarks.

predicting gravitationally-related beyond the Standard Model phenomena. Data from LHC proton-proton collisions recorded by the ATLAS detector in 2012 is used to perform a search for such phenomena. Chapters 3 and 4 contain a description of the ATLAS detector and a study to optimise its performance. Chapters 5, 6, 7 and 8 describe the search strategy followed, and chapter 9 presents the results found. Plots and tables that are not the work of the author are appropriately referenced.

2 Theory

This section outlines the theoretical foundations on which this thesis is based. A short review of Quantum Mechanics and the Standard Model (SM) of Particle Physics can be found in sections 2.1 and 2.2. The Standard Model shortcomings and the models for Beyond the Standard Model (BSM) physics tested in this thesis are described in section 2.3 onwards.

2.1 The road to Quantum Field Theory

This section is largely based on the lecture notes written by Andreas Brandhuber for the course “Relativistic Waves and Quantum Fields”, which can be found in [6], and the lectures from the course “Introduction to Quantum Field Theory” taught at the RAL High Energy Physics Summer School [7].

The principles of Quantum Mechanics (QM) were developed in the beginning of the 20th century to address shortcomings of Classical physics, such as its failure to explain phenomena like the ultraviolet catastrophe in black body radiation². These principles can be summarized in a few key statements:

- The state of the system is represented by a wave function $|\Psi\rangle$, a vector in a Hilbert space. The wave function depends on the coordinates of an individual particle q_i and its quantum numbers. While the wave function by itself does not have any physical meaning, the quantity $|\Psi|^2 = \langle\Psi|\Psi\rangle$ is interpreted as the probability density function of the system.
- Observables such as the momentum of a particle or its energy are represented by Hermitian operators. The hermiticity requirement $\hat{H}=\hat{H}^\dagger$ ensures that the observables (or eigenvalues of the operators) are real.
- The result of any measurement is one of the eigenvalues of the operator. The expectation value of an operator \hat{H} is defined as an average over many measurements and is defined as:

$$\langle H \rangle = \langle \Psi | \hat{H} | \Psi \rangle = \int_{-\infty}^{\infty} d^3x \Psi^* \hat{H} \Psi \quad (2.1)$$

²In the context of classical physics, the 1905 Rayleigh-Jeans law predicts that a black body will radiate according to λ^{-4} . Therefore, at short wavelengths, black body emissions would tend to infinity. Earlier, in 1900, Max Planck had proposed an alternative description of black-body radiation which did not have that anomaly at short wavelengths. This alternative description was based on the assumption that electromagnetic radiation is emitted in packets (quanta as defined by Max Planck himself). Later on, Einstein would identify these packets as real particle now known as photons.

- The Schrodinger equation describes the time evolution of the system:

$$i\hbar \frac{d\Psi}{dt} = \hat{H}\Psi \quad (2.2)$$

Where \hat{H} is the Hamiltonian, the total energy of the system. Classically, the Hamiltonian is defined as $H = \frac{p^2}{2m} + V(x)$. In QM, the momentum is replaced by its corresponding QM operator $\hat{p} = i\hbar \vec{\nabla}$ and $\hat{H} = i\hbar \frac{\partial}{\partial t}$.

- The time evolution of a QM operator \hat{A} is summarized in the following equation:

$$i\hbar \frac{d\langle A \rangle}{dt} = \langle \Psi | [\hat{A}, \hat{H}] | \Psi \rangle \quad (2.3)$$

where $[\hat{A}, \hat{H}]$ is the commutator of operator \hat{A} with the operator \hat{H} . Therefore, if the operator \hat{A} commutes (e.g $[\hat{A}, \hat{H}]=0$) with the Hamiltonian operator it is then called a conserved quantity.

This version of QM however does not take into account the requirements of Einstein's Special Relativity (SR). The expression of the Hamiltonian operator used in non-relativistic QM is analogous to that used in Classical non-relativistic physics. Therefore, to obtain relativistic QM, the classical non-relativistic Hamiltonian is replaced by its SR equivalent:

$$H = \sqrt{p^2 c^2 + m^2 c^4} \quad (2.4)$$

Substituting this expression into the Schrodinger equation (2.2):

$$i\hbar \frac{d\Psi}{dt} = \sqrt{\hat{p}^2 c^2 + m^2 c^4} \Psi \quad (2.5)$$

From equation 2.5, the Klein-Gordon (KG) equation can be obtained:

$$\left(\frac{1}{c^2} \frac{\partial^2}{\partial t^2} - \nabla^2 + \frac{m^2 c^2}{\hbar^2} \right) \Psi = 0 \quad (2.6)$$

$$\left(\square + \frac{m^2 c^2}{\hbar^2} \right) \Psi = 0 \quad \text{where} \quad \square = \frac{1}{c^2} \frac{\partial^2}{\partial t^2} - \nabla^2 \quad (2.7)$$

From the point of view of non-relativistic QM, this equation has two major problems:

1. The probability density $|\Psi|^2$ is not positive definite.
2. There are negative energy solutions.

This equation was already written by Schrodinger but discarded for the reasons outlined. Coming back to equation 2.5, a different starting point is to require that the equation is linear in both time and space derivatives to avoid taking squares that lead to negative energy solutions. The resulting equation obtained is famously known as the Dirac equation. Using 4-vector index notation the free Dirac equation can be written as:

$$\left(i\hbar\gamma^\mu\partial_\mu - mc\right)\Psi = 0 \quad (2.8)$$

Where $\gamma^\mu = (\gamma^0, \vec{\gamma})$ are the Dirac Gamma matrices and $\partial_\mu = (\partial/\partial t, \vec{\nabla})$. The Dirac equation, unlike the KG equation, has a positive definite probability density. It however shares the presence of negative energy solutions. The interpretation of these negative energy solutions was explained by Dirac's hole theory: the vacuum is a state where all the negative energy states are filled and all the positive ones are empty. Given Pauli's exclusion principle, which excludes two fermions from occupying the same state, an electron cannot then emit photons and reach a negative energy state because those are already filled. Hole theory also led to the introduction of antiparticles, confirmed by the discovery of the positron in 1933. As a result, British physicist Paul Dirac was awarded the Nobel prize in that same year. The multi-particle nature of the new theory implies that the number of particles in a system is not necessarily conserved, as opposed to non-relativistic QM, where the wave function represented a single particle. Therefore, the joint requirements of SR and QM leads to the abandonment of the single particle interpretation of the wave function. This realisation led to the development of Quantum Field Theory (QFT). In the context of QFT the wave function describes the field generated by a given particle type. The solutions to the Dirac equation then describe the field generated by spin $\frac{1}{2}$ particles (known as fermions) while the solutions to the KG equation describe scalar fields for particles with spin 0.

Before going further, some tools from classical mechanics and classical field theory will be introduced. The Lagrangian formalism is an alternate definition of classical mechanics from which the equation of motion of a system can be derived. For that purpose, the Lagrangian is introduced as the difference between the kinetic and potential energy of a system. For a classical non-relativistic particle:

$$L(x, \dot{x}) = T - V = \frac{1}{2}m\dot{x}^2 - V(x) \quad (2.9)$$

The action (S) describes the path of the system:

$$S = \int_{t_0}^{t_1} L(x, \dot{x})dt \quad (2.10)$$

By requiring the principle of least action ($\delta S=0$), the Euler-Lagrange equation is obtained:

$$\frac{d}{dt} \frac{\partial L}{\partial \dot{x}} = \frac{\partial L}{\partial x} \quad (2.11)$$

Substituting equation 2.9 into equation 2.11:

$$-\frac{dV(X)}{dx} = F(x) = m\ddot{x} \quad (2.12)$$

As expected, Newton's second law is obtained. Moving to classical field theory, the particle position x is substituted by the field coordinates $\phi(x, t)$. A generalised version of the Euler-Lagrange equation can be obtained for the relativistic field case by requiring the Lorentz invariance of the action:

$$S = \int_{t_0}^{t_1} L(\phi, \dot{\phi}) dt = \int_{t_0}^{t_1} \mathcal{L}(\phi, \partial^\mu \phi) d^4x \quad \text{where} \quad L(\phi, \dot{\phi}) = \int \mathcal{L}(\phi, \partial^\mu \phi) d^3x \quad (2.13)$$

where \mathcal{L} is the Lagrangian density, commonly referred to as the Lagrangian in the context of Field theory. By requiring the principle of least action the Euler-Lagrange equations for a relativistic field are obtained:

$$\partial_\mu \frac{\partial \mathcal{L}}{\partial(\partial_\mu \phi)} = \frac{\partial \mathcal{L}}{\partial \phi} \quad (2.14)$$

The original aim of QFT was to quantize the electromagnetic field. That resulted in a very successful theory known as Quantum Electrodynamics (QED) and, later on, the development of the SM of Particle Physics. The Lagrangian contains all the information about a system. The aim is then to find the Lagrangian for the field generated by each of the elementary particles of the SM. Once the Lagrangian is obtained, cross sections or decay rates for a given process can be calculated and, more generally, make predictions that can be tested in experiments.

2.2 The Standard Model

The SM is a QFT which describes elementary particles and their interactions through the Electromagnetic and Weak and Strong nuclear forces. Originally, the techniques of QFT were used to quantise the electromagnetic field, which led to the successful development of QED during the 1930-40s. The theory for strong force interactions, Quantum Chromodynamics (QCD), and for weak interactions, were developed in the 1960-70s and, together with QED, formed what is now known as the SM of Particle Physics. This section aims to give a brief review of the different components of the SM of Particle Physics.

2.2.1 Quantum Electrodynamics

The starting point for QED is the Lagrangian density for a free Dirac field:

$$\mathcal{L} = \bar{\Psi}(i\gamma^\mu \partial_\mu - mc)\Psi \quad (2.15)$$

Where $\bar{\Psi}$ is the conjugate free Dirac field. It can be shown that using equation 2.14 for the fermion field Ψ the Dirac equation (2.8) is recovered. One of the requirements is that the Lagrangian density is invariant under local and global phase transformations, also known as gauge invariance. A global transformation such as $\Psi \rightarrow e^{i\theta}\Psi$, where θ is a real number, leaves the Lagrangian density of equation 2.15 invariant since $\bar{\Psi} \rightarrow e^{-i\theta}\bar{\Psi}$. However, a local transformation dependent on the coordinates of the form $\Psi \rightarrow e^{i\theta(x)}\Psi$ does not leave the Lagrangian invariant due to the presence of the derivative ∂_μ :

$$\partial_\mu \left(e^{i\theta(x)}\Psi \right) = e^{i\theta(x)}\partial_\mu\Psi + i\left(\partial_\mu\theta(x)\right)e^{i\theta(x)}\Psi \quad (2.16)$$

The second term in the right hand side (RHS) of equation 2.16 implies that the Lagrangian density for a free Dirac field is not gauge invariant under local transformations. In order to preserve local gauge invariance, a new vector field A_μ must be introduced that transforms such as $A_\mu \rightarrow A_\mu + \partial_\mu\theta(x)$. As shown in chapter 10.3 of [8], this new field must be massless in order to preserve gauge invariance³. Therefore, the introduction of this new massless vector field is a natural consequence from the local gauge invariance of the Lagrangian density. In the context of electromagnetism, A_μ can be identified as the photon field. As a result, the presence of the photon field is embedded in relativistic quantum mechanics. The full QED Lagrangian density then takes the form:

$$\mathcal{L} = -\frac{1}{4}F_{\mu\nu}F^{\mu\nu} + \bar{\Psi}(i\gamma^\mu\partial_\mu + iq\gamma^\mu A_\mu - mc)\Psi \quad (2.17)$$

where $F_{\mu\nu} = \partial_\mu A_\nu - \partial_\nu A_\mu$ represents the electromagnetic field strength tensor, and $F_{\mu\nu}F^{\mu\nu}$ is the kinetic term for the propagation of the photon field A_μ and q is the electric charge of the fermion field. A derivation of the Feynman rules of the theory can be found in chapter 7 of [8]. The photon field can then be thought of as the mediator of electromagnetic interactions. As shown in the Lagrangian density of equation 2.17, the photon field only couples to charged particles.

Figure 2.1 shows Feynman diagrams, where time is shown in the x -axis and position in the y -axis, for benchmark quantum electromagnetic processes such as electron-positron pair annihilation (left) and scattering (right). Since the photon only couples to charged particles, processes with the photon field interacting with itself are not allowed. Through Noether's theorem⁴, the requirement of gauge invariance also leads to the conservation of electric charge. In mathematical terms, local gauge transformations are described by the U(1) symmetry group⁵, formed by all 1 x 1 unitary matrices (satisfying $U^\dagger = U^{-1}$ and $\det[U] = 1$).

³If the field was not massless, the Lagrangian should include terms proportional to $A^\mu A_\mu$ to account for the massive nature of the field. This extra term would however violate gauge invariance for local transformations

⁴Noether theorem states that for every symmetry of the Lagrangian there is a conserved quantity. A symmetry is a transformation which leaves the Lagrangian invariant

⁵A group G is formed if a set of elements and operations fulfill the following conditions: $\forall a \exists G$, there should be $a \times I = a$ and $a \times a^{-1} = I$. Also, an operation between two elements of the group must result in another element of the set.

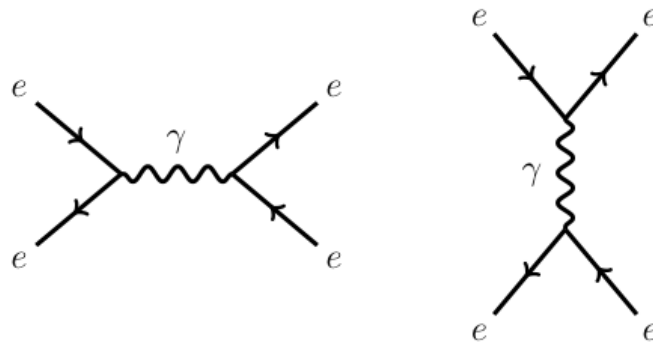


Figure 2.1: Feynman diagrams for electron-positron annihilation (left) and electron scattering (right) [9].

The theory of QED is one of the great achievements in the field of Particle Physics during the 20th century. Richard Feynman went as far as calling it “The jewel of physics” due to its accurate predictions⁶. However, as it was initially formulated, QED only allowed calculations to first order in perturbation theory, such as the diagram shown in figure 2.1. Higher order diagrams calculations, as shown in figure 2.2, require higher orders of perturbation theory to be calculated which, as QED was originally formulated, yielded divergent integrals. That held up the development of QED for almost two decades [8]. The solution was the process known as renormalization, which introduced suitable cutoffs in divergent integrals and running (energy-dependent) masses and coupling constants. Renormalization is described in [8] as artificial and “sweeping the infinities under the rug”, while Paul Dirac hinted that its use points to a fundamentally wrong understanding of interactions at subatomic level. However, renormalization has been and still is in use at the present time and all the theories describing the SM forces are required to be renormalizable.

2.2.2 Quantum Chromodynamics

The strong nuclear force is responsible for the stability of baryons like the proton. The theory for strong interactions shares a similar formalism to that shown for QED in section 2.2.1 with some modifications. Local gauge invariance in QED was described by the symmetry group $U(1)$. In QCD, the symmetry is generated by the $SU(3)$ symmetry group, the group of 3×3 unitary matrices with determinant $+1$. It has eight generators, known as the Gell-Mann matrices. Gauge invariance on local transformations leads to the introduction of 8 massless gluons, which act as mediators of the strong force and, through Noether’s theorem, to the

⁶The anomalous magnetic moment of the electron is the most accurate verification of a theoretical prediction in the history of physics.

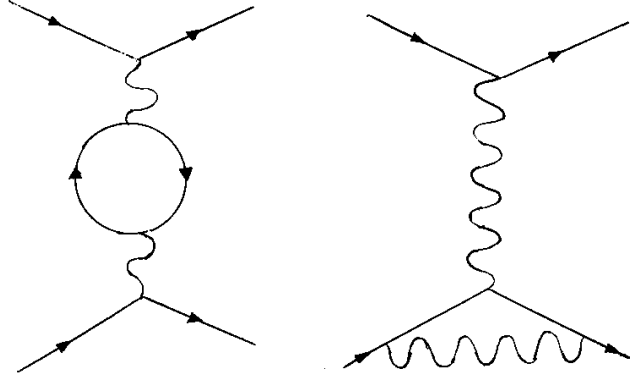


Figure 2.2: Feynman diagrams for higher order QED processes [9].

conservation of colour charge. Colour charge in QCD plays an analogous role to the electric charge in QED, but comes in three types, each with its own anti-charge: red, blue and green. As shown on the right hand side of figure 2.3 the gluon carries two types of colour charge which transfers to the quarks on a gluon-quark vertex interaction. A blue-coloured quark emitting a gluon might transform to a red quark. Therefore, given colour charge conservation, the gluon will carry both blue and anti-red coloured charges [8]. Given that the strong force mediator carries color charge, gluons can self-interact as shown in the three (left) and four gluon (middle) vertex interaction of figure 2.3. It should be noted that the gluon only couples to itself and to quarks. Leptons do not carry colour and hence do not “feel” the strong force. The Lagrangian for QCD is then:

$$\mathcal{L} = -\frac{1}{4}G_{\mu\nu}G^{\mu\nu} + \bar{\Psi}(i\gamma^\mu\partial_\mu + ig\lambda A_\mu - mc)\Psi \quad (2.18)$$

where $G_{\mu\nu} = \partial_\mu A_\nu^\alpha - \partial_\nu A_\mu^\alpha + gf_{abc}A_\mu^b A_\nu^c$ is the gluon field strength tensor, g is a dimensionless constant which summarizes the strength of the interaction with the gluon field and λ represents the Gell-man matrices. Note that there are now eight gauge fields represented in A_μ . The Lagrangian is similar to that of QED but the extra term in $G_{\mu\nu}$ accounts for the possibility of gluon self-interaction.

The strength of the strong nuclear force interaction is summarized in the coupling constant of QCD, α_s , which exhibits what is known as asymptotic freedom. This behaviour can be thought as similar to a spring coil: as the distance between quarks (or gluons) decreases, the strength of the gluon field also decreases. However, as the distance increases, the gluon field strength also increases and, beyond the size of a hadron, reaches a constant value. Given that the field strength increases proportionally with the distance between partons, even when separating a quark from a bound state the energy of the gluon field will create other quark

pairs. That results in the property called confinement: quarks will always form bound states of mesons or hadrons, and hence cannot be observed directly.

Thanks to asymptotic freedom, perturbative QCD calculations at high energy are possible as in this regime the coupling constant is small. However, and as a consequence of that, perturbation theory cannot be used for QCD calculations at low energy. Other solutions, such as a Lattice QCD, has been proposed in recent years to perform these calculations without the use of perturbation theory.



Figure 2.3: Feynman diagrams for a three gluon vertex interaction (left), four gluon vertex (middle) and interaction with quarks (right) [9].

2.2.3 Weak Interactions

The Weak nuclear interaction is responsible for radioactive decays such as the beta decay of a neutron to a proton. Its place in the SM was not fully confirmed until the recent discovery of the Higgs boson due to a singular characteristic: the mediators of the Weak interactions are not massless. The discussion of how to preserve local gauge invariance for mediators that are not massless can be found in section 2.2.4. The symmetry group associated with local gauge invariance transformations for the Weak interaction is $SU(2)$, leading to the conservation of the quantum number weak isospin (I_3) and to the introduction of 3 bosons acting as Weak force mediators: the W^+ , W^- and the Z^0 .

Another of the singular features of the Weak interaction is that quark flavour is not a conserved quantity of the interaction. In the Feynman diagram shown in figure 2.4, an Up quark transforms into a Down quark through the emission of a W^+ boson. These interactions are called Flavour Changing Charged Current (FCCC). The coupling between quarks in the Weak interaction is contained in the Cabibbo–Kobayashi–Maskawa (CKM) matrix [10], shown in equation 2.19. The values shown in the CKM matrix are not predicted by the SM but instead are obtained from experiment. As an example, the process shown in figure 2.4 contains a vertex with an Up quark coupling to a Down quark. The cross section of this process is then

proportional to $|V_{ud}|^2$ and, therefore, the value of the parameter can be inferred by observing such a process in an experiment.

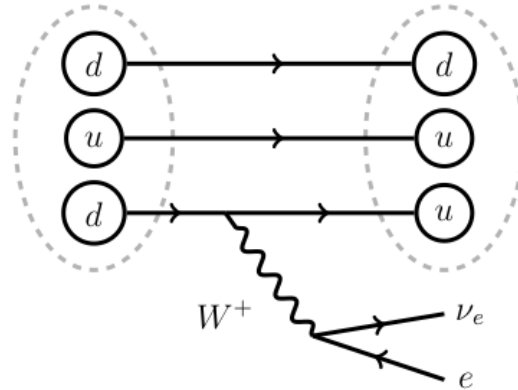


Figure 2.4: A neutron decays into a proton via the Weak interaction by the transformation of a Down quark into an Up quark [11].

$$V_{CKM} \equiv \begin{pmatrix} V_{ud} & V_{us} & V_{ub} \\ V_{cd} & V_{cs} & V_{cb} \\ V_{td} & V_{ts} & V_{tb} \end{pmatrix} = \begin{pmatrix} 0.97 & 0.22 & 0.03 \\ 0.22 & 0.97 & 0.04 \\ 0.01 & 0.04 & 0.99 \end{pmatrix} \quad (2.19)$$

The Weak interaction couples to all SM particles except gluons. As shown in the Feynman diagrams of figures 2.5 and 2.6 both the W^\pm and the Z^0 bosons can decay to quarks and leptons while conserving electric charge and lepton number. It should be noted that interactions mediated with the Z^0 boson do not lead to quark flavour changes or, at the very least, those have not yet been observed. Similarly to the gluon from QCD, the mediators of the Weak interaction can self-interact, as shown in figure 2.7. Due to the massive nature of the mediators, the range of the Weak interaction is the shortest among the forces described in the SM: 10^{-18} meters, about 0.1% of the proton diameter. At larger distances, the Weak interaction becomes irrelevant when compared to electromagnetism and the Strong nuclear force.

Neutrinos are fermions that only interact with other SM matter through the Weak interaction. As such, nucleon-neutrino interactions are quite rare even though the flux from solar neutrinos in Earth is of the order of $10^6 \text{ cm}^{-2}\text{s}^{-1}$. One of the most puzzling properties of neutrinos is the fact that they can change flavour. Such a property is known as neutrino oscillations. Predicted as early as 1957 by Bruno Pontecorvo [12], its effects were apparent when the expected flux from solar electron-neutrinos was found to be lower than expected. In 2001, the Sudbury Neutrino Observatory confirmed the existence of neutrino oscillations. In the same spirit as the CKM matrix, a neutrino mixing matrix named Pontecorvo–Maki–Nakagawa–Sakata

(PMNS) matrix is expected to describe the mixing between different quantum states. However, it should be noted that, unlike the case for quarks, neutrinos propagate as a mass eigenstate, while experiments detect the flavour eigenstate. As such, the PMNS matrix describes the mixing between the flavour and mass eigenstates. At present time, neutrino experiments are still in the process of determining some of the components of the mixing matrix.

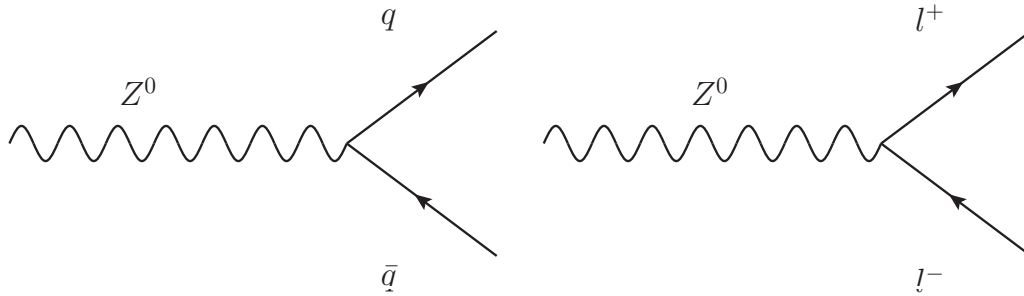


Figure 2.5: Z^0 boson decaying to a quark-antiquark pair (left) and to lepton-antilepton pair (right).

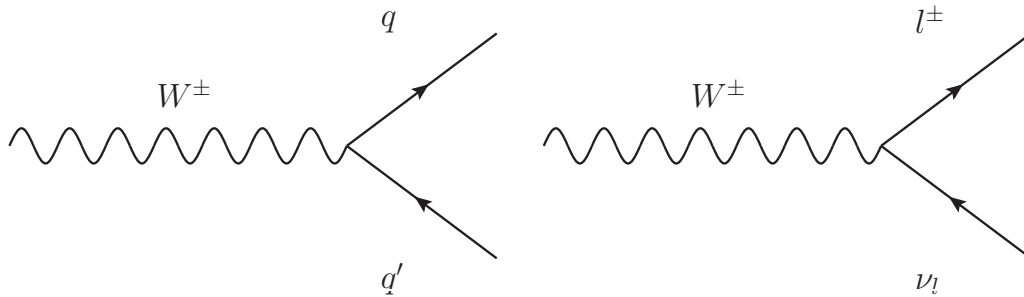


Figure 2.6: W^\pm boson decaying to a quarks (left) and to a lepton-neutrino pair (right).

2.2.4 Electro-Weak Symmetry Breaking and unification

The mass of the mediators of the weak interaction, the W^\pm and Z^0 bosons, is measured to be 80.4 and 91.2 GeV respectively [13]. As explained for the electromagnetic interaction, the massless nature of the photon field is essential to preserve gauge invariance on local transformations. In order to account for the mass of the bosons associated to the Weak interaction, one of the options is to introduce a term in the Lagrangian such as $m^2 A_\mu A^\mu$, where A_μ is the vector field generated by the Weak interaction mediators. That would however break local gauge invariance and, more worryingly, make the theory non-renormalizable [14]. Such an outcome is not desirable as it compromises the predictive powers of the theory. There-

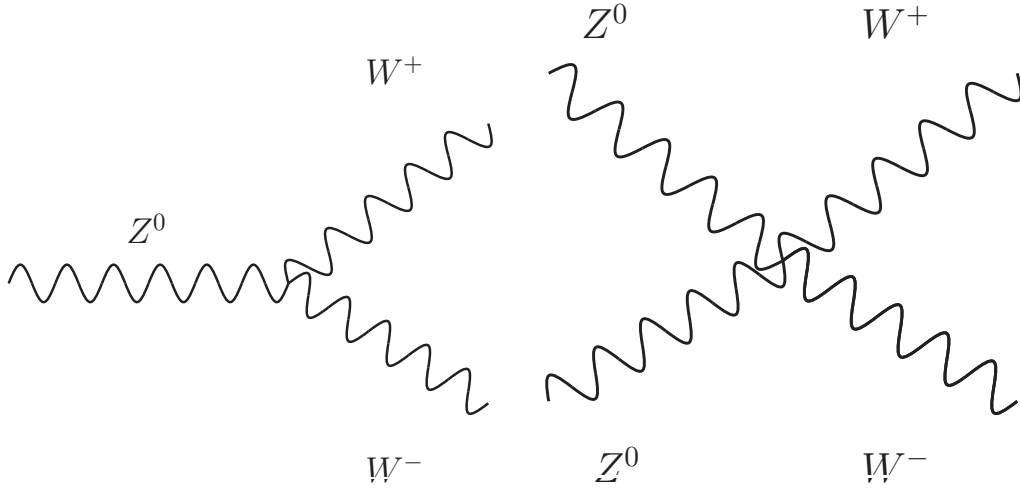


Figure 2.7: 3-vertex (left) and 4-vertex (right) self-interaction for the Weak force mediators.

fore, another mechanism is proposed in order to break the symmetry: spontaneous symmetry breaking (SSB).

SSB can be understood as a meta stable symmetry present in the Lagrangian of the system which is broken when the system reaches its true ground state. A common example of SSB is the Sombrero (Mexican Hat) potential for a scalar field, which can be written as:

$$V(\phi) = \mu^2 |\phi|^2 + |\phi|^4 \quad (2.20)$$

if μ is a real number, then $\mu^2 > 0$ and the minimum potential is found at $\phi = 0$. However, if we take μ to be complex then $\mu^2 < 0$ the potential looks like that shown in figure 2.8. In this case, the point at $\phi = 0$ is a local maximum instead of a global one. This potential is symmetric under rotations. However, in order for the system to roll to the ground state it has to choose a direction and, from the ground state perspective, the potential is no longer symmetric. Therefore, the Lagrangian of the system is invariant under rotation transformations whereas the ground state is not.

SSB is not a concept exclusive to Particle Physics as it is also used in the theory of phase transitions in the context of Statistical Mechanics. In the context of QFT, it is understood as a field which has a non-zero expectation value for the vacuum state. As shown in sections 10.8 and 10.9 of [8], the introduction of a scalar field solves the problem of the mass of the mediators of the Weak interaction while preserving local gauge invariance. This scalar field is commonly called the Higgs field in the honour of Peter Higgs, who proposed the introduction of the field in 1964 [3] and received the physics Nobel prize in 2013 alongside François Englert as a result of the confirmation of its existence. The mechanism by which

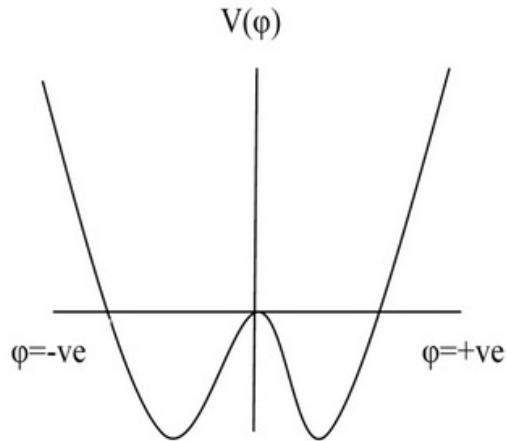


Figure 2.8: Graphical representation of the potential shown in equation 2.20.

the mediators of the Weak interaction become massive is commonly called Electro-Weak Symmetry Breaking (EWSB) or the Higgs Mechanism.

The existence of the Higgs also solves the problem of WW scattering. Similarly to the 4-vertex $WWZZ$ interaction shown in figure 2.7, a 4-vertex $WWWW$ interaction is also allowed. However, without the presence of the Higgs boson, the theory is compromised as the cross section for such a process would increase proportionally with the centre-of-mass energy squared and, eventually, violate unitarity.

Another of the yet open questions that the Higgs boson can answer concerns the stability of the universe. Depending on the mass of the Higgs and of the Top quark, the Electroweak vacuum state of the universe can be a stable, unstable or a metastable state. As shown in figure 2.9, the observed mass of the Higgs at the LHC suggests that the universe is in a metastable state, albeit a long-lived one. In such a situation, the universe could, at any time, reach its true ground state and the current universe would cease to exist [15]. More precise measurements of the Higgs and Top quark mass are required to make a firm statement on the fate of the universe.

One of the biggest success stories of the SM is the unification of the Weak and electromagnetic interactions. Above the Electro-Weak unification energy (of the order of a 100 GeV) the two forces can be described by a single theory called Glashow-Weinberg-Salam model, in honour of Abdus Salam, Sheldon Glashow and Steven Weinberg. They all received the 1979 Nobel prize as a result of their work on the topic. The symmetry group describing the unified force is a combination of the symmetry groups describing each of the individual forces below the unification energy: $SU(2) \times U(1)$. As a result of local gauge invariance, the theory

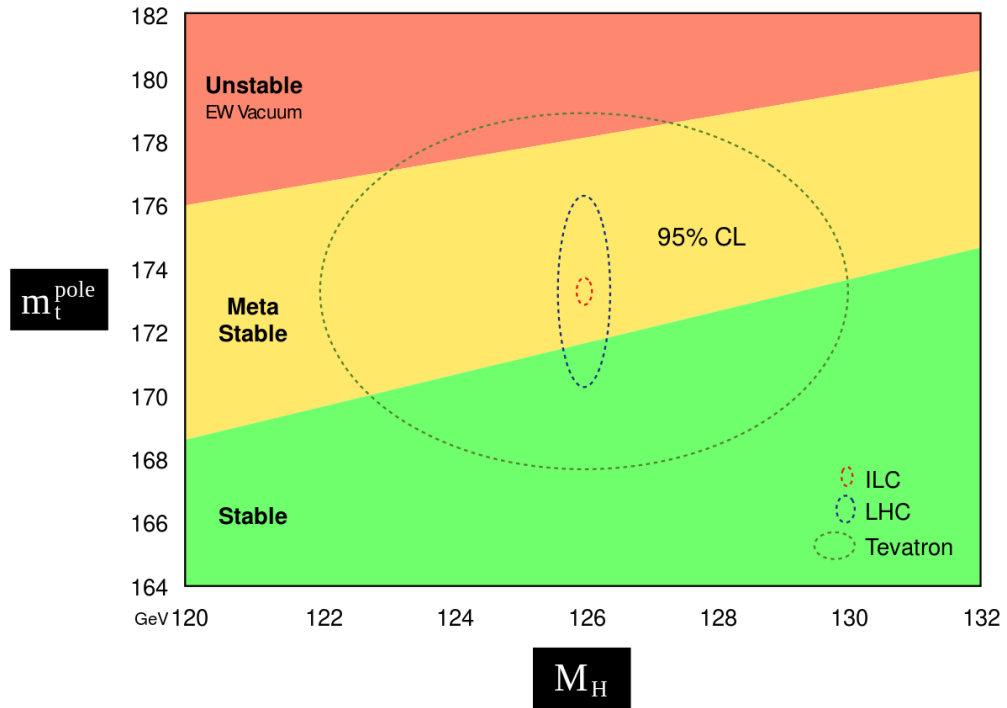


Figure 2.9: 2-D plane of the Top quark mass against the Higgs mass showing the different scenarios for the Electroweak vacuum state. The results obtained at the Tevatron and the LHC are shown at 95% confidence level, together with the expected results in the International Linear Collider [15].

gives rise to four mediators which should be massless. However, as already explained, three of them are not. It is postulated that the separation of the electromagnetic and Weak forces occurs due to the Electro-Weak Symmetry Breaking.

2.2.5 Summary

The SM is a very successful theory whose predictions have been verified in various experiments. The recent discovery of the Higgs boson [4, 5] is a further confirmation of the success of the theory. There are however issues with the SM that prevent it from being a “Theory of Everything”. The elementary particles from the SM comprise only 5% of the matter of the universe. The quantisation procedures that worked so well for the electromagnetic field do not apply to the gravitational field. The unification of the Weak and electromagnetic interactions leads to the possibility of unifying all the SM forces in one model, perhaps by the addition of a symmetry breaking mechanism similar to the Higgs, but attempts in that direction have so far been unsuccessful. Potential answers to such questions are provided in BSM or Grand unified theories. The predictions made by those theories can be tested in the LHC with the aim to find new physics or deviations from SM predictions. However, the first results coming from pp collisions at the LHC at centre-of-mass energies of 7 and 8 TeV point to the SM being correct at this energy scale.

Figure 2.10 is a summary of the elementary particles of the SM and their mass, spin and charge, together with forces each of the particles interacts with. Similarly to the values of the CKM matrix, the mass of the SM particles is not predicted but instead found from experiment. This raises questions such as the reason for the mass hierarchy, with the Top quark being 40 times more massive than any other fermion, and the reason behind the number of generations. As of now, these questions still do not have an answer.

2.3 The Planck Scale and Extra Dimensions

As explained above, the SM is very successful in describing the inner workings of three of the four known forces. A quantum theory of gravity is however still as elusive as it has been for the past century. Gravity is much weaker than the other three forces. Therefore, gravitational interactions between elementary particles would only be noticeable if those particles were accelerated to energies far beyond the reach of the LHC. The scale for Quantum Gravity is set by the Planck Mass (M_P):

$$M_P = \sqrt{\frac{\hbar c}{G_N}} \quad (2.21)$$

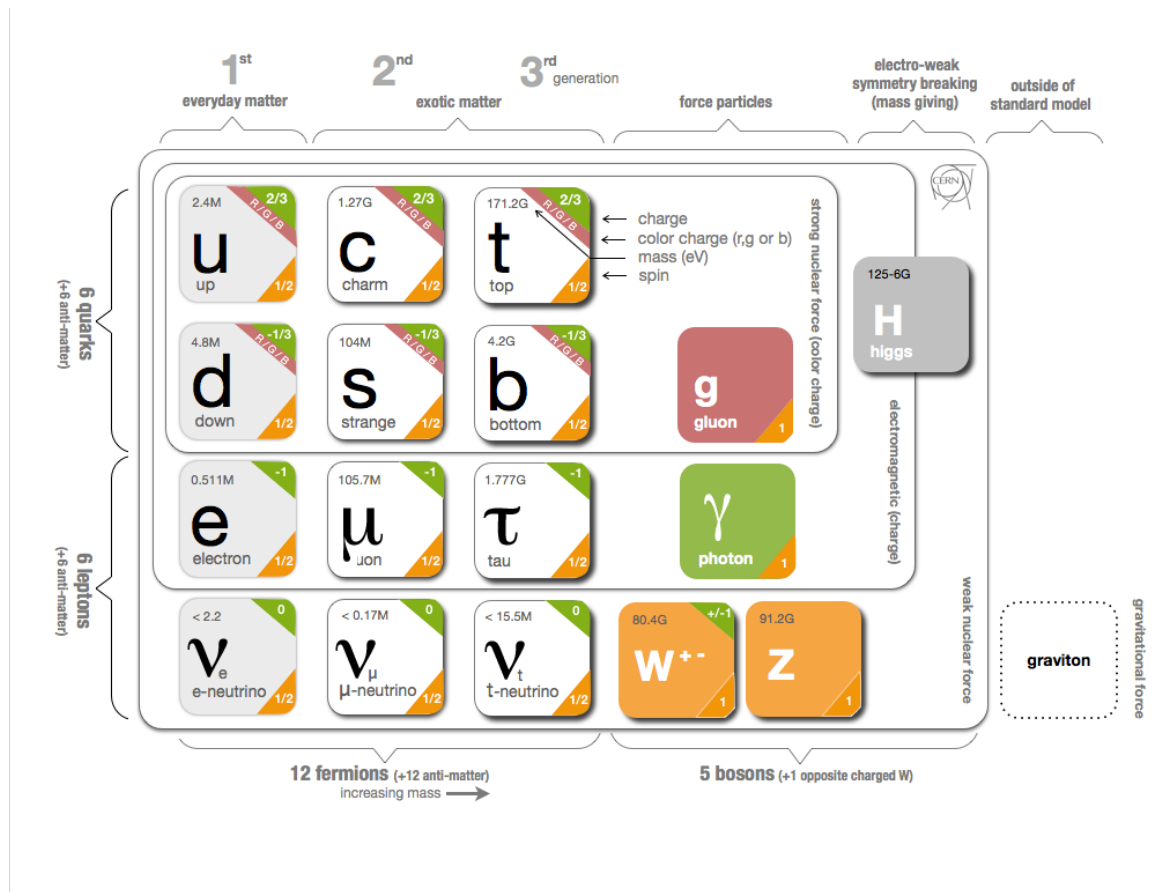


Figure 2.10: The elementary particles of the Standard Model of Particle Physics, together with their mass, charge, spin and the forces each of the particles interact with [16].

using the known values for the physical constants, the scale of Quantum Gravity is set to a currently unreachable 10^{16} TeV. A particle with such an energy would cause space-time to curve in lengths comparable to its wavelength and its behaviour would be described by a theory of Quantum Gravity [17]. This large energy scale immediately brings about the hierarchy problem: why is the Planck Scale so much higher than the Electro-Weak unification scale?

2.3.1 ADD Large Extra dimensions

One of the proposed answers is that the observed weakness of gravity is a by-product of living in a four-dimensional space. The existence of large extra dimensions could reduce the Planck Scale to energies within the reach of the LHC. The assumption is that while gravity can propagate through those extra dimensions, the Standard Model forces cannot. The strength of gravity in a four-dimensional space is diluted and only a fraction of its true strength is perceived. One such model is that proposed in [18] by Arkani-Hamed, Dvali and Dimopoulos (ADD). Its main feature is the addition of n extra spatial dimensions compactified to a radius R . In order to account for this difference, Newton's gravitational law is modified for distances shorter than R such as:

$$F = G_N \frac{m_1 m_2}{r^{2+n}} \quad (2.22)$$

hence, the value of Newton's constant changes depending on the radius of the extra dimensions R :

$$G_D = \frac{G_N}{R^n} \quad (2.23)$$

where G_D is the extradimensional Newton constant. Therefore, the extra-dimensional Planck Mass (M_D) can be written as:

$$M_D^{2+n} = \frac{\hbar c}{G_D} = \frac{M_P^2}{R^n} \quad (2.24)$$

for an $M_D \sim 1.0$ TeV and $n = 1$ the extra dimension would have a size of $\sim 10^{11}$ m. Such a case has been excluded as large scale General Relativity experiments would have observed deviations from theory expectations. For $n = 2$ the extra dimensions would have a radius of about $100 \mu\text{m}$. Tests of gravity at short distances have excluded extra dimensions with a radius larger than $130 \mu\text{m}$ [19]. Therefore, $n = 2$ is close to being ruled out. In extra

dimensions models, the Standard Model forces are confined to our 3 + 1 dimensions (referred to as “the brane”) while gravity can propagate through the extra dimensions (“the bulk”). The gravitational potential for the region $r \gg R$ can then be written as [18]:

$$V(r) \sim \frac{m_1 m_2}{M_D R^n} \frac{1}{r} \quad (r \gg R) \quad (2.25)$$

for the case $r \gg R$ the Newtonian potential is recovered.

The existence of extra dimensions as proposed by Arkani-Hamed et al could be a solution to the hierarchy problem. As shown in equation 2.24, extra dimensions with a sufficiently large radius could reduce the extradimensional Planck Scale to a similar order as the Electro-Weak scale. Standard Model particles are confined to the brane and the only particle that can propagate in the bulk is the Graviton. As a consequence, a collection of scalar fields for each of the extra dimensions (generally referred to as Kaluza-Klein (KK) towers) appear in the brane as excited states of the Graviton. The separation between each one of those states is proportional to $1/R$. Given that R is taken to be large to reduce the extradimensional Planck Scale to a value similar to the electro-weak scale, that would result in a continuous spectrum of KK Graviton modes. For the search presented in this paper, this effect is regulated by a cutoff taken to be the string scale (M_S), related to the extradimensional Planck Scale by the following equation [20]:

$$M_S = 2 \sqrt{\pi} [\Gamma(n/2)]^{1/(n+2)} M_D \quad (2.26)$$

where $\Gamma(t) = \int_0^\infty x^{t-1} e^{-x} dx$. The string scale is taken to be the onset of Quantum Gravity in the context of String Theory, where a full theory of Quantum Gravity requires the existence of extra spatial dimensions. Therefore, the ADD model is an effective model with a clearly defined cutoff.

Figure 2.11 shows a Feynman diagram for Graviton production at the LHC decaying into an opposite sign dilepton final state, the signal searched for in this paper. The total cross section for opposite sign dilepton production would then be the sum of the SM processes with an opposite sign dilepton final state and the contributions from Graviton decays. Therefore, the total differential cross section as a function of dilepton invariant mass can be written as [22]:

$$\frac{d\sigma}{dm_{\ell\ell}} = \frac{d\sigma_{SM}}{dm_{\ell\ell}} + \mathcal{F} \frac{F_I}{M_S^4} + \mathcal{F}^2 \frac{F_G}{M_S^8} \quad (2.27)$$

where $d\sigma_{SM}/dm_{\ell\ell}$ is the SM-predicted differential cross section for opposite sign dilepton production as a function of the dilepton invariant mass, F_I and F_G are the Drell-Yan-ADD interference (virtual Graviton exchange) terms and pure new physics term respectively, and \mathcal{F} represents the strength of Gravity in the extra dimensions. \mathcal{F}/M_S^4 characterizes the strength of the interaction and is obtained by using the Feynman rules of the effective model, as shown

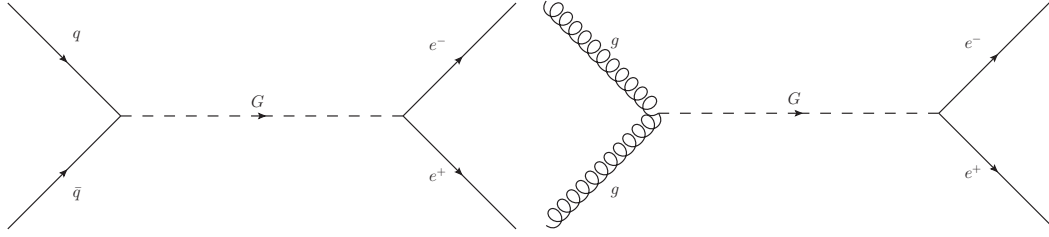


Figure 2.11: Leading-order production mechanisms for virtual Graviton production at the LHC, and decay to the dielectron final state. Similar diagrams apply to the muon and photon decay channel [22].

in [23]. The term \mathcal{F} is proportional to the strength of the interaction and different choices for its value are presented in [21] for the Han-Lykken-Zhang formalism, [23] for the Hewett formalism and [24] for the Giudice-Ratazzi-Wells (GRW) formalism. These different choices are presented here [22]:

$$\begin{aligned}
 \mathcal{F} &= 1, \quad (\text{GRW}) \\
 \mathcal{F} &= \begin{cases} \log\left(\frac{M_S^2}{m_{\ell\ell}^2}\right), & n = 2 \\ \frac{2}{n-2}, & n > 2 \end{cases}, \quad (\text{HLZ}) \\
 \mathcal{F} &= \frac{2\lambda}{\pi} = \frac{\pm 2}{\pi}, \quad (\text{Hewett})
 \end{aligned} \tag{2.28}$$

it should be noted that the the GRW and Hewett formalisms do not depend on the number of extra dimensions considered. The Hewett formalism has the particularity of considering the possibility of destructive interference with the Drell-Yan process. If there was to be destructive interference, the observed cross section for opposite sign dileptons could be lower than that predicted only from SM processes.

2.3.2 The Randall-Sundrum Model

Another possibility is the model published in [25] which, as opposed to compactified extra dimensions, proposes the existence of one curved global extra dimension to form a 5-dimensional Anti de Sitter space. Figure 2.12 shows the setup for the Randall-Sundrum (RS) model, with two 3-branes representing a four dimensional space enclosing a five dimensional bulk. One of the 3-branes is the four dimensional space where the SM forces are confined.

The metric of this model can then be expressed as [26]:

$$ds^2 = e^{\pm 2ky} \eta_{\mu\nu} dx^\mu dx^\nu + dy^2 \quad (2.29)$$

where $\eta_{\mu\nu}$ is the usual four dimensional Minkowskian spacetime and $e^{\pm 2ky}$ is an exponential warp factor depending on the position in the extra dimension (y), where k is the curvature of the extra dimension. Gravity originates from the other 3-brane in the figure and, due to the curvature of the extra dimension, the strength of gravity is suppressed. Similarly to the ADD model, this leads to a KK tower of excited states of the graviton that could be observed in particle collisions. The extradimensional Planck Scale in the RS model (\tilde{M}) can then be expressed as [27]:

$$\tilde{M} = \frac{M_{G^*}}{x_1 (k/\bar{M}_{Pl})^{2/3}} \quad (2.30)$$

where k is the curvature of the extra dimension, x_1 is the first zero of the Bessel function in the wavefunction of the RS graviton, and M_{G^*} is the mass of the first of the RS graviton excited states and \bar{M}_{Pl} is the reduced Planck Mass, defined as $M_{Pl}/8\pi$.

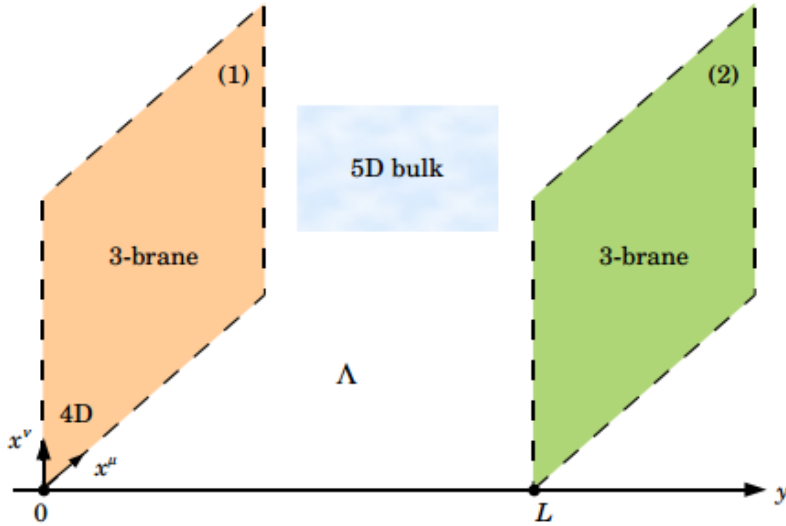


Figure 2.12: Setup for the five dimensional Randall-Sundrum model [26].

It can be argued that the ADD model does not solve the hierarchy problem but merely changes its formulation: why is the size of the compactified extra dimension so much smaller than that of the other dimensions? The RS model, with its exponential warping depending on the position in a five dimensional plane, can be argued to solve the hierarchy problem without introducing a similar problem.

2.4 Black Hole Production at the LHC

One of the most striking experimental consequences of the lowering of the Planck Scale through the addition of extra dimensions is the possibility of producing black holes in particle collider. As shown in figure 2.13, two sufficiently energetic particles crossing each other at a close enough distance will form a black hole. Since a theory of Quantum Gravity is yet unknown, the treatment applied to Standard Model processes to calculate production cross sections is not valid. There are no Feynman rules to apply to diagrams and it is not known how to treat a black hole state. However, there are predictions for black hole production in the literature, such as [28], which argue that a semi-classical treatment of the black hole is valid as long as $M_{BH} \gg 3 - 5 M_D$. In such a region, black holes would be produced with characteristics analogous to stellar size black holes. Below the threshold for semiclassical black hole production the semiclassical approximation is no longer valid as the regime of Quantum Gravity is reached. Models such as [27] and [29] are based in these region $M_D < M_{BH} < 3 - 5 M_D$, which would see the production of so-called quantum black holes or, perhaps more accurately, non-thermal black holes. Such models expect that some of the classical features of gravity are reproduced in the quantum regime and use such a hypothesis to build an effective theory. Throughout this section, semiclassical and quantum black holes and their respective decay processes will be discussed.

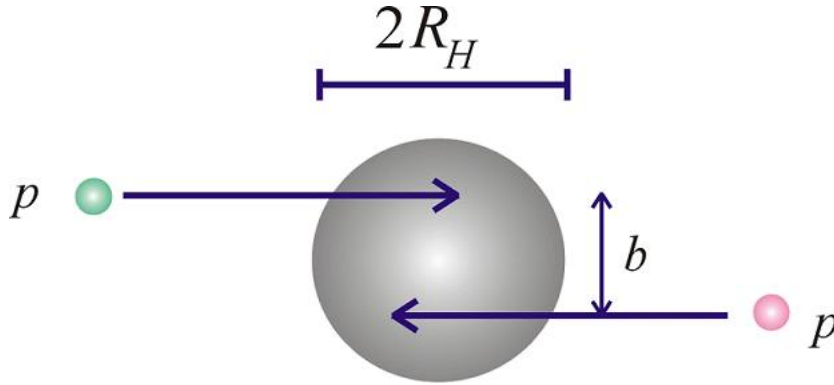


Figure 2.13: Two particles with an impact parameter b smaller than the Schwarzschild radius (R_H) can form a black hole [17]

2.4.1 Semiclassical Black Holes

In a $4 + n$ -dimensional spacetime, the Schwarzschild metric takes the form [17, 30]:

$$ds^2 = -\gamma(r)dt^2 + \frac{1}{\gamma(r)}dr^2 + r^2d\Omega_{(n+2)}^2 \quad (2.31)$$

$$\gamma(r) = 1 - \left(\frac{R_S}{R}\right)^{n+1} \quad (2.32)$$

where $d\Omega_{(n+2)}^2$ is the surface element of a $n + 3$ dimensional sphere and the assumption is that the Schwarzschild radius (R_S) is smaller than the size of the extra dimensions⁷. From [30] the expression for the extradimensional Schwarzschild radius takes the form:

$$R_S = k(n) \frac{1}{M_D} \left(\frac{M}{M_D}\right)^{\frac{1}{n+1}} \quad (2.33)$$

where $k(n)$ depends on the convention chosen to relate the extradimensional Planck scale to the extradimensional Newton constant G_N . There are different definitions such as the PDG [24], the Dimopoulos-Landsberg [28] or the Giddings and Thomas [31].

The partonic production cross section ($\hat{\sigma}$) for semiclassical black holes is then expressed through geometrical arguments as [29]:

$$\hat{\sigma} = \pi R_S^2 = \pi k^2(n) \frac{1}{M_D^2} \left[\frac{M_{BH}}{M_D}\right]^{\frac{2}{n+1}} \quad (2.34)$$

where M_{BH} is the mass of the produced black hole. For pp collisions the internal structure of the proton needs to be taken into account. Therefore, in order to obtain the hadronic cross section Eq. (2.34) is convoluted with the parton density function (PDF) [32][33]:

$$\sigma = \int dx_a dx_b f_A^a(x_a) f_B^b(x_b) \hat{\sigma} \quad (2.35)$$

Where x is the momentum fraction and f is the PDF which accounts for the internal structure of the proton, while a is a parton from hadron A and b is a parton from hadron B . That treatment leads to very large cross sections. According to [28] and [31], for a Planck Scale of the order of 1.0 TeV and the LHC working at $\sqrt{s} = 14$ TeV, a black hole would be produced every second at design instantaneous luminosity. That is of course a huge rate and would have serious consequences for Standard Model measurements [31].

Understanding the decay of these objects is crucial: black holes are expected to be short-lived and therefore cannot be detected directly but rather through their decay products. Classically, a black hole is the ultimate prison and a decay process is not allowed. However, quantum effects in a curved spacetime yield a surprising consequence. Following the prediction made by Stephen Hawking in his famous 1975 paper [34], black holes are expected to decay through a process known as Hawking radiation. Hawking radiation can be understood as particles using the tunnelling effect to escape the event horizon of a black hole. Pair production near

⁷If R_S is larger than the size of the extra dimensions then the metric becomes the usual four dimensional Schwarzschild metric.

the event horizon can lead to one of the particles of the pair tunneling out while the other stays inside the horizon. To an external observer, the particle that escapes has positive energy and, as a consequence, the mass of the black hole will be reduced. Therefore, a black hole is expected to have a finite lifetime and a non-zero temperature. The temperature of a black hole is referred to as the Hawking temperature and has the following form:

$$T_H = \frac{\hbar c^3}{8\pi G M K_b} \quad (2.36)$$

Given that a black hole temperature is inversely proportional to its mass, stellar mass black holes have temperatures close to the absolute zero. The amount of radiation is expected to be very small and therefore lifetime for stellar mass black holes is expected to be very large ($\sim 10^{75}$ s). For semiclassical black holes expected to be formed at the LHC, with masses of the order of a few TeV, the temperature is expected to be large and their lifetime is expected to be very short ($\sim 10^{-25}$ s). A semiclassical black hole with a mass of a few TeV is expected to decay to a large number of particles with a large transverse momentum. Such a signature is used for searches such as [35]. The decay process of a semiclassical black hole can be summarized in a few steps, as shown in figure 2.14:

1. During the balding state the black hole settles in a state that can be described with three properties: its mass, angular momentum and electrical charge.
2. Particle emission through Hawking Radiation. The black hole loses its charge and angular momentum and becomes a Schwarzschild black hole.
3. The black hole loses enough mass to enter the Quantum Gravity regime. The assumption is that either the black hole decays completely in a “final burst” or it forms a stable remnant.

2.4.2 Quantum Black Holes

While the production of semiclassical black holes at the LHC would produce a clear experimental signature, the region immediately above the Planck Scale is also worth investigating. Models such as [27], [29] and [36] argue that this region is physically more interesting as pure Quantum Gravity events would be observed and, potentially, information about quantum gravitational interactions such as the conserved quantum numbers or symmetries could be extracted.

The production of quantum black holes would occur similarly to that explained for semiclassical black holes, as shown in figure 2.13. Since the production cross section is not known,

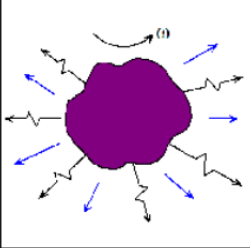
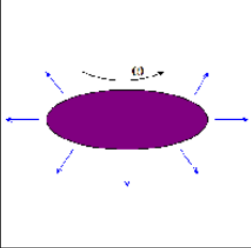
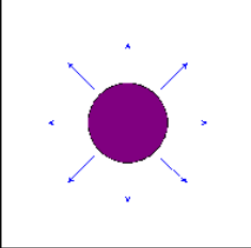
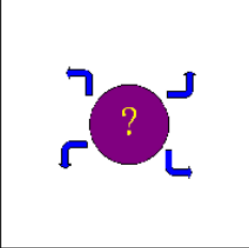
"Balding" stage	"Spin-down" stage	"Schwarzschild" stage	"Quantum gravity" stage
			

Figure 2.14: Stages of semi-classical black hole evaporation [37]

the geometrical cross section approach for semiclassical black holes is commonly also used for quantum black hole production. The mass of such objects would be confined to the quantum gravity region ($M_D < M_{BH} < 3 \cdot M_D$). However, a quantum black hole is expected to be a quantum state with yet unknown properties and possible decays. In order to bridge that problem, quantum black hole models commonly feature a democratic decay to Standard Model particles assuming that gravity couples equally to all particles, as is done in [27] and [29]. Models are constructed which conserve SM symmetries or which violate global symmetries such as baryon number (B), lepton number (L) or B-L.

In the LHC, quantum black holes could be formed by the collision of two partons. Assuming only two-particle decays, in [29] branching ratios (BR) for all possible quantum black holes decays are calculated depending on the initial state particles. Table 2.1 is a reproduction of the BRs published in [29], both for the case in which quantum gravitational interactions conserve and violate all of the SM global symmetries. Given that gravity is assumed to emit all SM particles with equal strength, the largest BR are for partonic decays. Leptonic decays are also allowed, albeit with a lower BR. Searches such as [38] have used a final state with a lepton and a quark for the search, albeit lepton number conservation must be violated for such a decay to be allowed. In the search presented in this paper, an opposite sign dilepton final state is used. Only initial states of quark-antiquark or gluon-gluon collisions forming the quantum black hole can lead to such a final state. As shown in table 2.1, the BR to a dilepton final state is 0.5% and 0.2% for a $q\bar{q}$ and gg initial state respectively. A two-particle decay is experimentally convenient given that reconstructing the mass of the quantum black hole from a two-particle decay is experimentally easier than the multi-particle decay of semiclassical black holes. As such, the decay of quantum black holes is expected to provide a clear experimental signature.

Table 2.1: Table extracted from [29] showing the branching ratios for the different allowed decays of a quantum black hole, depending on the electric charge (shown in the superindex in the column for State) and the initial state particles forming the QBH (shown in the lower index in the column for State). The branching ratios are calculated for both the case in which global symmetries are violated (V) and conserved (C).

State	Decay	BR (%)		State	Decay	BR (%)	
		C	V			C	V
$\text{QBH}_{q\bar{q}}^0 \rightarrow$	$u\bar{u}$	41.5	36.5	$\text{QBH}_{gg}^0 \rightarrow$	$u\bar{u}$	27.8	27.1
	$d\bar{d}$	41.5	36.5		$d\bar{d}$	27.8	27.1
	gZ	4.1	3.6		gg	27.8	27.1
	gg	4.1	3.6		gZ	7.0	6.8
	$g\gamma$	4.1	3.6		$g\gamma$	7.0	6.8
	$\ell^+\ell^-$	1.5	4.1		$\ell^+\ell^-$	0.5	1.6
	$\nu\nu$	1.2	2.7		$\nu\nu$	0.3	1.1
	W^+W^-	0.5	0.5		W^+W^-	0.4	0.4
	$\gamma\gamma$	0.5	0.5		$\gamma\gamma$	0.4	0.4
	ZZ	0.5	0.5		ZZ	0.4	0.4
	γZ	0.5	0.5		γZ	0.4	0.4
	gH		2.7		ZH		0.1
	γH		0.3		HH		0.1
	ZH		0.5		HG		0.2
	HH		0.1		GG		0.4
	gG		2.7				
	γG		0.3				
ZG		0.3					
GG		0.5					

2.5 Summary

The possible discovery of a signal involving extra dimensions or semiclassical or quantum black hole formation and decay has the potential to revolutionize our understanding of Physics and, in the case of the latter, confirm the existence of Hawking Radiation. The development of a theory of Quantum Gravity would receive a huge boost by the possibility of testing it directly at the LHC. That would however open the door to questions about the fundamental nature of the universe: why three of the spatial dimensions are large while the rest are warped, as proposed in the ADD model? Why is their size so different from the expected Planck length? A mechanism analogous to ESB could be responsible for that hierarchy. Or,

in the case of a signal from an RS model, raise questions about the structure of a five dimensional universe. The discovery potential of the LHC, highlighted by the recent finding of the Higgs boson, is expected to provide insight into all those questions.

3 The ATLAS detector

The ATLAS experiment is a general purpose particle detector built during the period 2003-2008 to provide information on the high-energy frontier set by the Large Hadron Collider. The ATLAS collaboration, created in 1992 and funded by the CERN member (and some non-member) countries, is responsible for building and operating the detector. Searches for BSM Physics yielding exclusion contours and the discovery of a particle consistent with the Standard Model Higgs Boson have been possible thanks to the high energy reach of the LHC and the performance of the ATLAS detector. After Run-1 (2010-2012) finished, the LHC entered the period known as Long Shutdown 1 (LS1). During LS1 the ATLAS detector is being readied for Run-2 (2015-2018), when proton-proton collisions are expected to reach a centre-of-mass energy of 14 TeV. Working at its design performance, the LHC will collide bunches of 10^{11} protons 40 million times per second at an instantaneous luminosity of $10^{34} \text{ cm}^{-2} \text{ s}^{-1}$ [39]. The instantaneous luminosity (\mathcal{L}) in the LHC is defined as:

$$\mathcal{L} = \frac{f n_b n_p^2}{A} \quad (3.1)$$

where A is the collision area, n_b is the number of bunches in a beam, n_p the number of protons in each bunch and f the frequency of the beam rotation. Maximising the instantaneous luminosity is a common aim in particle accelerators. The instantaneous luminosity conditions are an important factor in the design choices made during the construction of a particle detector.

This chapter provides a summary of the subdetectors that form ATLAS, as well as the trigger system in place to select interesting physics events among the large soft QCD background. Emphasis is placed on the muon detection process given the signal searched for in this paper.

3.1 Experimental Setup and detector overview

The LHC is a synchrotron type accelerator located near Geneva (Switzerland) in a circular tunnel 100 meters underground with a perimeter of 27 km. The tunnel was previously in use by the Large Electron Positron (LEP) collider, the LHC predecessor. However, extensive excavation works were required to build the caverns where the four experiments are placed. Figure 3.1 shows a schematic of the experimental setup, with various particle accelerators used previously at CERN taking part in the proton acceleration process. Initially, protons are extracted from hydrogen gas. They then go through an extensive pre-acceleration stage before entering the LHC ring. In the linear accelerator (LINAC-2) protons reach energies close to 50 MeV before being transferred to the Proton booster (Pb), where the energy reached

is 1.4 GeV. The following stage is the Proton Synchrotron (PS), the oldest accelerator in the chain, built in 1959. In the PS, protons reach energies up to 26 GeV and are then transferred to the Super Proton Synchrotron (SPS). In the SPS protons reach energies of 450 GeV and are finally transferred to the LHC ring in bunches that enter the main accelerator every 25 ns. It should however be noted that the LHC has operated at 50 ns bunch spacing throughout Run-1 but is expected to start working at its design value shortly after Run-2 begins⁸. Large superconducting magnets are then used to steer the proton beams around the LHC ring, while evenly spaced radio-frequency cavities further accelerate the proton beams, reaching TeV scale energies before colliding the beams head-on. During Run-1, the LHC has worked for most of the 2010-2012 period at beam energies of 3.5 and 4.0 TeV, giving a total centre-of-mass energy of 7 and 8 TeV respectively. In order to generate the 8.33 Tesla magnetic field required to steer proton bunches around the LHC ring to such high energies, the superconducting dipole magnets are kept at a temperature of 1.9 K. Collisions between bunches of protons moving in opposite directions occur only in the interaction points where the detectors are placed.

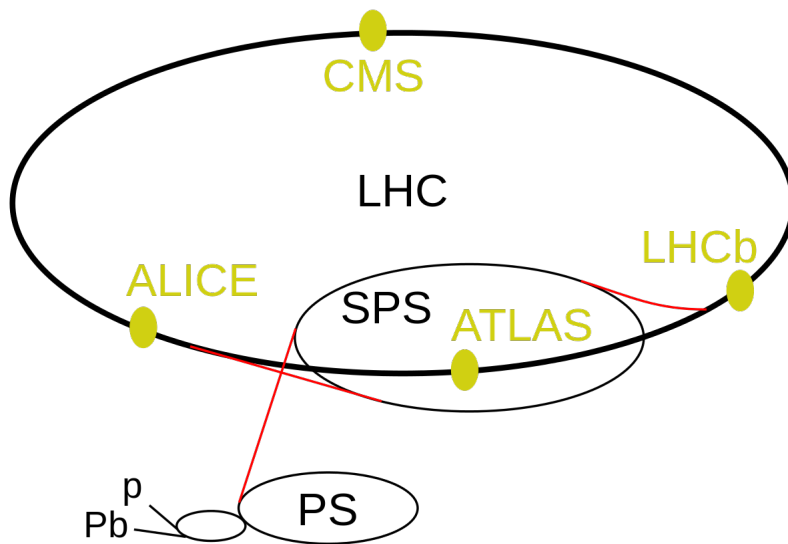


Figure 3.1: Schematic of the LHC ring with the location of each of the experiments: CMS, ATLAS, LHCb and ALICE. The Proton booster (Pb), Proton Synchrotron (PS) and Super Proton Synchrotron (SPS) accelerate the protons [40].

The ATLAS experiment is the one of the largest particle detectors ever built, standing at 25 meters high and 44 meters in length. Its weight is of 7000 tonnes, close to that of the Eiffel Tower in Paris. It is situated 92 meters underground in a large cavern called Interaction Point

⁸It is expected that the first month of data-taking in 2015 will use 50 ns bunch spacing

1. The control room of the detector is above ground near the French-Swiss border and directly in front of the CERN Meyrin site. The design of the ATLAS detector is part of a conscious effort to build a machine suitable for both Standard Model precision measurements and search for BSM phenomena. From a physics point of view, the ATLAS detector is required to provide the following features [39]:

- Lepton identification and momentum resolution at scales ranging from a few GeV to TeV scale as possible new bosons such as the W' and the Z' , with masses of the order of a few TeV, could decay to dilepton final states.
- Good hadronic jet momentum resolution to calculate the total energy of an event and estimate the dominant soft QCD background for Standard Model precision measurements.
- Flavour tagging to identify Higgs boson decays.
- Quantify the missing transverse energy of a final state. Some stable supersymmetric particles such as the neutralino, as well as the already known SM neutrinos, are not expected to interact with the ATLAS detector components and could only be noticed by the presence of missing energy.
- A trigger system to reduce the large soft QCD jet production background and avoid signals from different events overlapping.
- Particle charge identification.

With those ideas in mind, the ATLAS detector, shown in a computer generated image in figure 3.2, is composed of four main concentric components each responsible for identifying and reconstructing different types of particles:

- The inner detector measures the momentum of charged particles and provides primary and secondary vertex identification.
- The electromagnetic and hadronic calorimeters measure the energy of electrons, jets, hadrons and missing transverse energy.
- The Muon Spectrometer tracks the trajectories of muons and measures their charge and momentum.
- Two magnet systems: a solenoid magnetic field in the inner detector region, and a toroidal magnetic field for the Muon Spectrometer, which bend the trajectory of outgoing charged particles and allow for charge and momentum measurements.

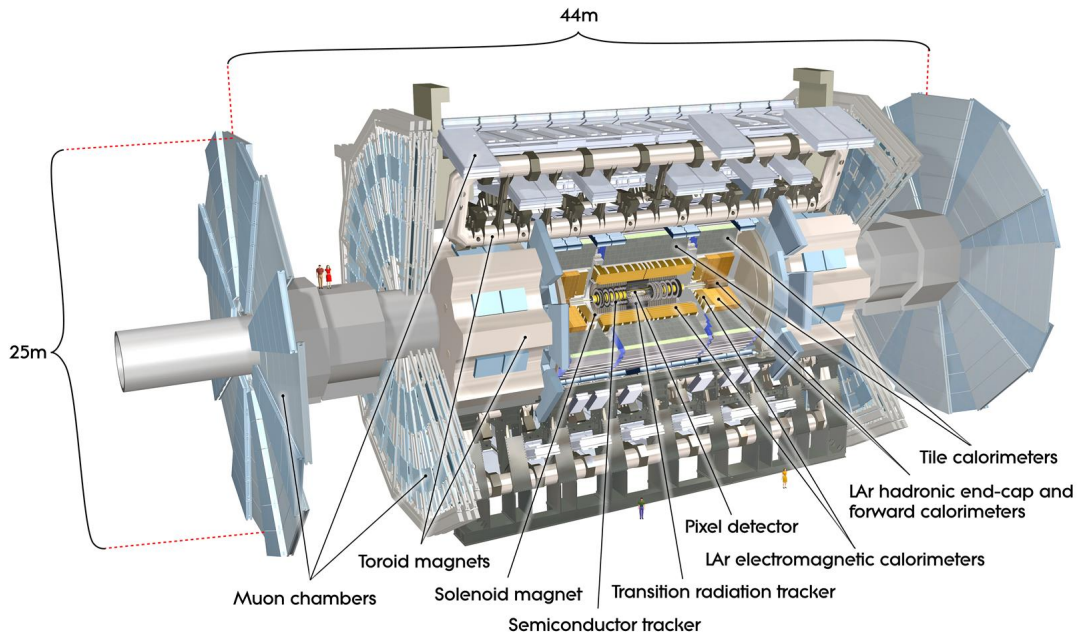


Figure 3.2: The ATLAS detector and its internal structure [39]

ATLAS uses a right-handed coordinate system that takes the interaction point as the origin. The beam pipe defines the z -axis, with the x -axis pointing towards the center of the LHC ring and the y -axis pointing towards the surface. The plane formed by the x - y axis is referred to as the transverse plane, shown in figure 3.3, used to measure quantities such as the transverse momentum (p_T). Given that incoming bunches of protons travel along the beam axis and have no initial momentum in the transverse plane, the use of transverse quantities is common. Cylindrical coordinates (r, θ, ϕ) are in use: the azimuthal angle ϕ is defined as the angle around the beam pipe in the transverse plane, whereas θ is the polar angle from the positive z -axis (the beam axis), and r is defined as the distance to the interaction point.

The pseudo-rapidity (η) is a useful quantity commonly used instead of the polar angle, describing the angle of the particle with respect to the beam axis. In the massless limit the pseudo-rapidity is defined as:

$$\eta = -\ln \left[\tan \left(\frac{\theta}{2} \right) \right] \quad (3.2)$$

hence, for $\eta = 0$ the particle is orthogonal to the beam pipe, and for $\eta = \pm\infty$ particles travel horizontally in the direction of the positive z -axis. For massive objects, the equivalent quan-

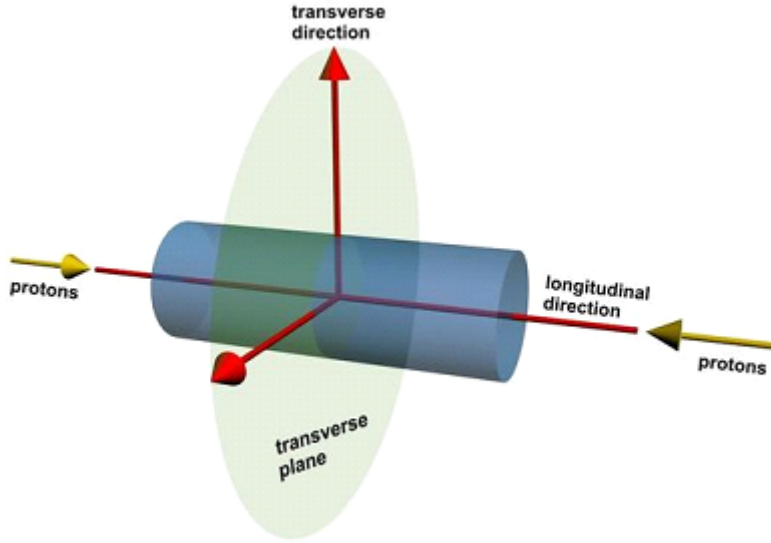


Figure 3.3: Schematic of the ATLAS coordinate system [41]

tity is the rapidity (Y), defined as:

$$Y = \frac{1}{2} \ln \left[\frac{E + p_z}{E - p_z} \right] \quad (3.3)$$

another useful quantity is the distance in η - ϕ space represented by ΔR :

$$\Delta R = \sqrt{\Delta\eta^2 + \Delta\phi^2} \quad (3.4)$$

3.2 Momentum measurement of a charged particle

The ATLAS detector contains a solenoidal magnetic field surrounding the inner detector and a toroidal one in the muon spectrometer region. Charged particles in a magnetic field feel a force perpendicular to its direction of motion. The force is proportional to the charge of the particle and the magnitude of the magnetic field, and allows a measurement of the momentum of charged particles. This can be summarized in the following equation:

$$\vec{F} = q \cdot (\vec{v} \times \vec{B}) \quad (3.5)$$

where \vec{v} is the velocity of the particle. The magnetic field will bend the trajectory of a charged particle, which would describe a circle of radius r , commonly referred to as the radius of curvature. The momentum measurement is based on the measurement of the sagitta⁹(s) of a

⁹The sagitta is the distance of the centre of the arc described by the trajectory of the particle to its base

charged particle in the magnetic field. As shown in figure 3.4, the sagitta of a particle can be related to the radius of curvature using the following expression:

$$s = r \left(1 - \cos\left(\frac{\theta}{2}\right) \right) \quad (3.6)$$

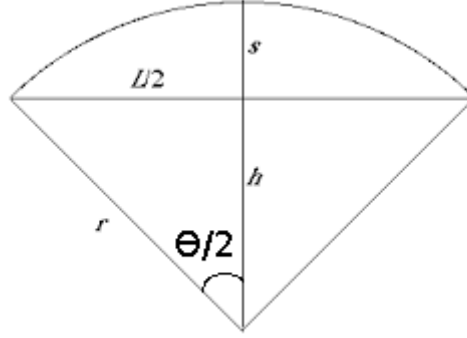


Figure 3.4: Sagitta (s) of a particle in a magnetic field, where r is the radius of curvature and L is the length traversed by the particle.

for the case in which the direction of motion is orthogonal to the magnetic field, the momentum is then related to the radius of curvature as:

$$F = \frac{\gamma m v^2}{r} = qvB \quad \rightarrow \quad p[\text{GeV}/c] = 0.3 \cdot B[\text{T}] \cdot r[\text{m}] \quad (3.7)$$

the momentum can then be related to the sagitta of a charged particle:

$$s = \frac{0.3BL^2}{8p} \quad (3.8)$$

the capacity to provide a precise measurement of the sagitta is then the factor that determines the momentum resolution ($\Delta p/p$) of a detector. As inferred from equation 3.8, increasing momentum yields straighter tracks. Or, in other words, for higher momentum tracks the bending of their trajectory due to the surrounding magnetic field will be smaller, and, as a result, the difficulty of providing a precise momentum measurement increases. The momentum resolution can then be written as:

$$\frac{\Delta p}{p} = \frac{\Delta s}{s} = \frac{\Delta s \cdot 8p}{0.3BL^2} \quad (3.9)$$

the momentum resolution then worsens linearly with p .

3.3 Inner Detector

The Inner Detector (ID) is the component of the ATLAS detector closest to the interaction point. Immersed in a 2.0 Tesla magnetic field generated by the surrounding solenoid magnet, the ID reconstructs the trajectories of charged particles in the region $|\eta| < 2.5$ and identifies primary and secondary vertices. Figure 3.5 shows a schematic the ATLAS inner detector, highlighting the barrel and endcap components of the subsystems making up the ID. These subsystems, ordered from closest to furthest from the interaction point, are the pixel detector, used to determine primary and secondary vertices, the semi-conductor Tracker, responsible for particle momentum measurement and the transition radiation tracker, which complements the tracking provided by the pixel detectors. Figure 3.6 shows the internal structure of the ID and the layout of the subsystems, together with the distance of each of them to the interaction point.

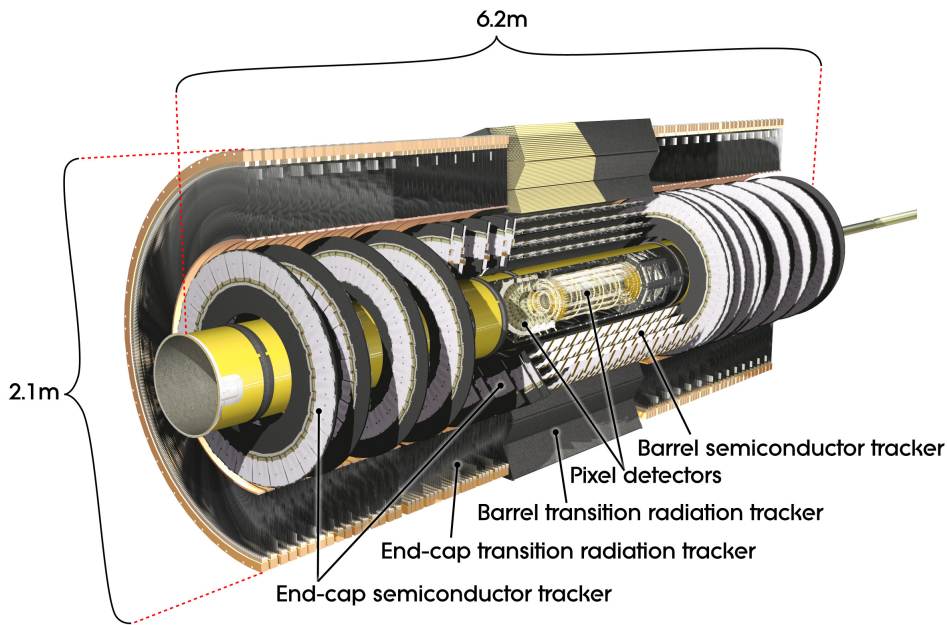


Figure 3.5: The ATLAS inner detector [39]

3.3.1 The Pixel Detectors

A pixel detector (PD) consists of a total of 1744 sensors. Each sensor is made up of silicon and contains 47232 pixels. A charged particle traversing through a pixel releases electrons from the silicon. Due to the surrounding electric field, these electrons and resulting holes

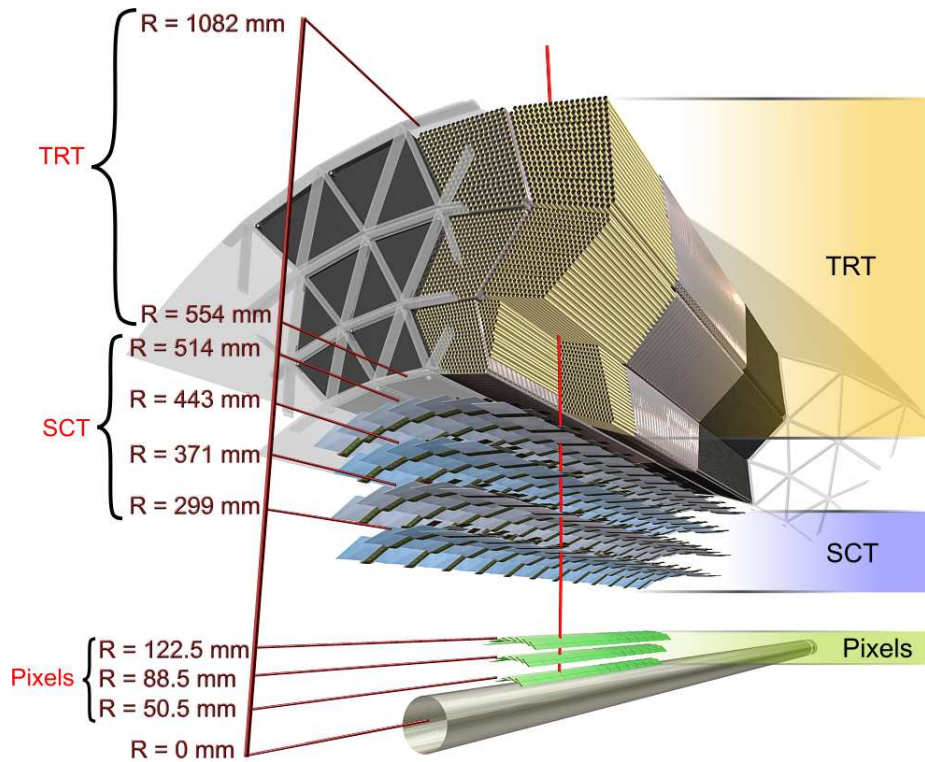


Figure 3.6: The ATLAS inner detector internal structure is shown together with the distance to the interaction point. The subsystems shown are the following ones: the pixel detector, the semi-conductor trackers and the transition radiation trackers [39]

are pulled in opposite directions, generating a current which acts as signal that a charged particle has traversed a given pixel. The PD operates at a temperature of -5°C to -10°C in order to reduce the contribution of noise after radiation damage, as the lower temperature reduces thermal excitations of electrons holes into the conduction band, which can produce some leakage current.

The pixel detector (PD) consists of three layers in the barrel region ($|\eta| < 1.05$) and two layers in the endcap ($1.05 < |\eta| < 2.5$). As shown in figure 3.6, the pixel detector PDs are the closest component of the ATLAS detector to the interaction point. The large particle flux and therefore large amounts of radiation that the PDs receive means that they are expected to be replaced approximately every three years to ensure good tracking performance [39]. The granularity provided is the finest among all of the subsystems: 80 million pixels, each acting as a read-out channel with a size of $50\ \mu\text{m} \times 400\ \mu\text{m}$ (about 10% of them are slightly larger: $50\ \mu\text{m} \times 600\ \mu\text{m}$). For every charged particle three measurements are taken in the PD (one in each layer), providing a resolution of $10\ \mu\text{m}$ in r - ϕ space.

3.3.2 The Semi-Conductor Tracker

The sensor technology used for the semi-conductor tracker (SCT) is similar to that used for the PD: silicon sensors kept at temperatures of -5°C to -10°C . The SCTs consist of 15912 sensors arranged in strips of $80\ \mu\text{m} \times 12\ \text{cm}$ around the pixel detectors, with about 6 million read-out channels. The granularity is then lower than in the PD and hence the resolution is a bit worse: $17\ \mu\text{m}$ in r - ϕ space.

The strips are arranged in four concentric circles in the barrel region and in six in the endcap region and provide tracking up to $|\eta| < 2.5$. A track particle can deposit energy in several strips in one layer, and can then be reconstructed into a space-point. A charged particle will typically leave from four to nine hits in the SCTs. The SCT is used in conjunction with the PD hits to determine the momentum of charged particles and the position of primary and secondary vertices.

3.3.3 The Transition Radiation Tracker

The transition radiation tracker (TRT) is formed of a total of about 300,000 straw drift tubes, each with a diameter of $4\ \text{mm}$ and containing a gas mixture of Xe , CO_2 and O_2 . A uniform electric field is provided by the anode of the TRT. As charged particles traverse the tubes the gas is ionised, such that free electrons and holes drift towards the wire at the centre of the tube at a constant velocity due to the surrounding electric field. The wire acts as a read-out channel to record the position of the particle.

The TRT is the largest part of the ID, covering a radial distance from 554 to 1082 mm from the interaction point, as shown in figure 3.6, and providing tracking up to $|\eta| = 2.0$. Given its large size, the number of hits is expected to be around 35, with a resolution of $130\ \mu\text{m}$ in r - ϕ space. Unlike the SCT and the PD, the TRT operates at room temperature as materials are not expected to degrade as quickly due to the radiation damage being reduced in the outer circle of the ID.

3.4 Calorimetry

As shown in figure 3.7 with all its different components, the calorimetry system in ATLAS is built around the ID. With a coverage up to $|\eta| < 4.9$, the aim of the calorimeter is to trigger and measure the energy of jets, electrons and photons, as well as quantifying the missing transverse energy of an event due to neutrino production or some yet unknown BSM physics process. The energy of particles is measured by the particle showers created when traversing

the detector.

There are two main types of calorimeter in ATLAS: the electromagnetic calorimeter (ECal) and the hadronic calorimeter (HCal). The ECal identifies photons and electrons and measures their energy, while the HCal absorbs and measures highly energetic hadrons that traverse the ECal and prevents them from reaching the outer parts of the ATLAS detector where the muon system is in place.

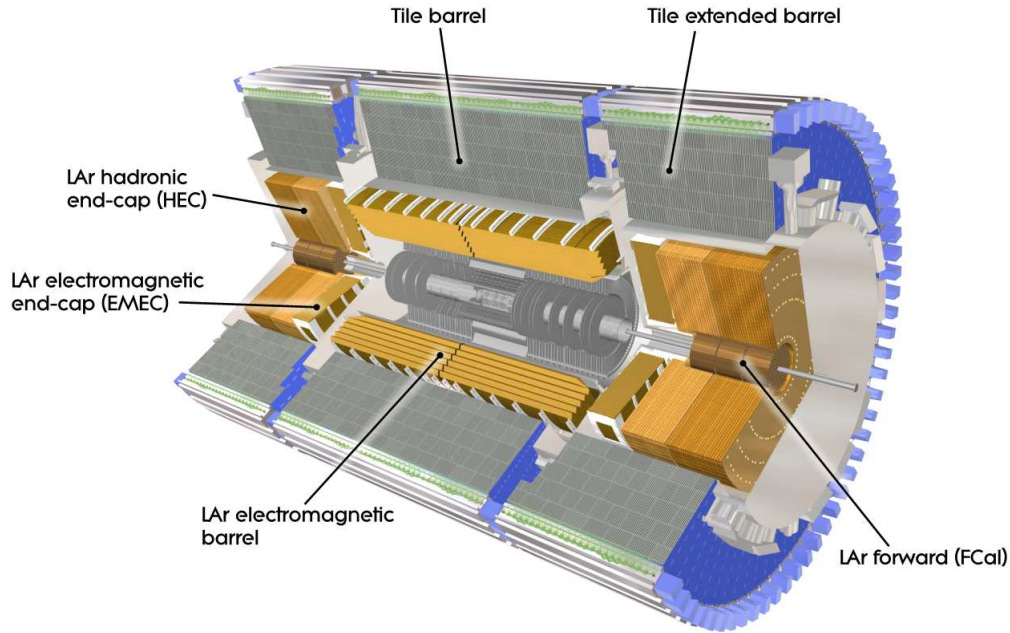


Figure 3.7: Computer generated image of the ATLAS calorimeter system, showing each of the barrel and endcap components [39].

3.4.1 The Electromagnetic Calorimeter

The ECal is composed of a barrel and endcap components with a coverage of $|\eta| < 1.37$ and $1.52 < |\eta| < 3.2$ respectively, together with a forward component providing coverage very close to the beam (up to $|\eta| < 4.9$). The region $1.37 < |\eta| < 1.52$ is normally called the crack region, where the cooling systems for the ID are placed. The region also contains a subsystem known as the PreSampler (PS), in place for $|\eta| < 1.8$ and used to estimate the energy loss by particles before reaching the ECal.

A structure of lead and steel layers together with the use of Liquid Argon (LAr) is in place to

identify and measure the energy of photons and electrons. An incident particle on steel and lead layers loses some of its energy and a particle shower is produced as a result. The particle shower ionizes the LAr producing free electrons and ions. The charge is collected thanks to the presence of an electric field and read out, allowing for an energy measurement¹⁰.

Photons and electrons traverse several layers depending on their energy before being absorbed. The ECal needs to be thick enough such that particles like electrons and photons deposit all their energy in the calorimeter region¹¹. The radiation length (X_0) of a material is defined as the length travelled before electrons lose $1/e$ of its original energy. The barrel and endcap components have radiation lengths of 22 and 24 X_0 respectively. Figure 3.8 is a schematic of a section of the LAr ECal, showing the different layers each with its corresponding radiation length. The strip cells, each with a thickness of 4.69 mm, have the finest granularity and are used for particle identification. Square cells provide energy measurements and are larger than the strip cells. The third layer has the lowest granularity and adds extra depth to the calorimeter. Trigger towers are formed by a combination of calorimeter cells and are used in the Level-1 trigger. More details on the Level-1 trigger and the role of trigger towers can be found in sections 3.6 and 4.1.

3.4.2 The Hadronic Calorimeter

The HCal is designed to detect and measure the energy of hadrons and their decay products, and to prevent leaks to the muon system in the outer layer of the ATLAS detector. Hadrons traverse the ECal region and deposit most of their energy in the HCal. The HCal is composed of three different components with a large $|\eta|$ coverage: the tile calorimeter covering the region $|\eta| < 1.7$, the hadronic LAr endcap ($1.7 < |\eta| < 3.2$) and the LAr forward calorimeter (FCal) with coverage $3.2 < |\eta| < 4.9$. The LAr endcap and FCal use the same technology used in the ECal to absorb and measure the energy of particles, however, due to the expected higher activity in the region, the absorbing material used is copper and tungsten.

The tile calorimeter, unlike the LAr one, uses steel as a material to absorb the incoming particles, and scintillating plastics to detect the particle showers created as a result of traversing particles. As jets and hadrons traverse the steel layers, the particle shower generated interacts with the scintillating plastic producing photons, which interact with the photomultiplier tubes. The number of photons generated is a measure of the energy of the incoming particle.

The depth of the hadronic calorimeter is an important design choice to ensure that incoming particles from pp collisions are absorbed. It is measured in interaction lengths (λ). An

¹⁰The amount of charge deposited is proportional to the energy of the incident particle

¹¹Muons are expected to traverse the ECal and therefore a system is in place to measure muons after they exit the calorimeter

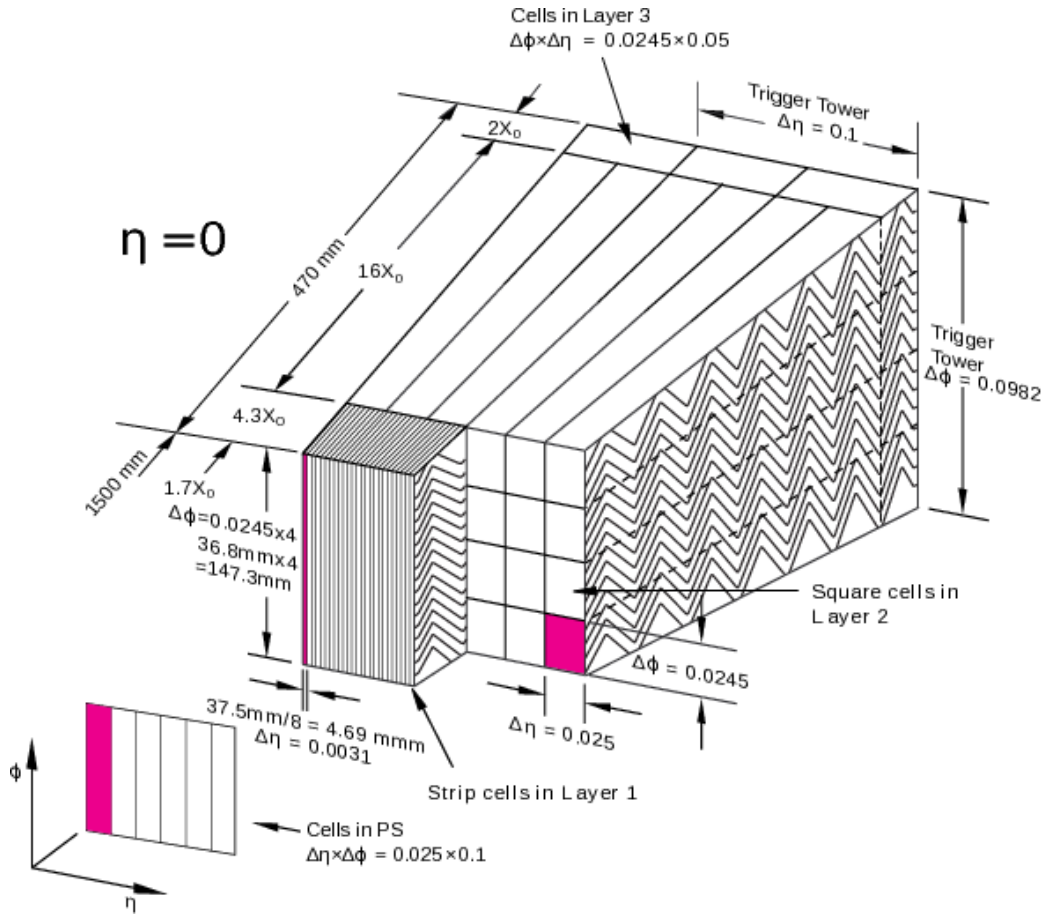


Figure 3.8: Schematic of a section of the LAr ECal showing the radiation lengths of each of the layers and the length in $\Delta\eta \times \Delta\phi$ of the trigger towers used for the Level-1 trigger of online event selection [39].

interaction length is defined as the average distance a particle travels in a material before interaction. The depth in interaction lengths is equivalent to 9.7λ in the barrel region and 11λ in the endcap, sufficient for energy measurements and to prevent leaks to the muon system.

3.5 The muon system

Muons with a momentum above ~ 4 GeV are expected to traverse the calorimeter system without being absorbed. As such, they have a dedicated component in the ATLAS detector: the muon spectrometer. Given the signal searched for in this thesis, this section aims to give

an extensive summary of the system used in ATLAS to identify and reconstruct muons. The muon spectrometer and all its subcomponents are described, as well as the algorithms and techniques used for muon reconstruction.

3.5.1 The Muon Spectrometer

The muon spectrometer (MS), shown in figure 3.9 with all of its components, identifies and reconstructs the trajectories of muons and measures their momentum. Built around the calorimeter system, the MS is the ATLAS subdetector furthest from the interaction point. Coverage is provided up to $|\eta| < 2.7$, with the barrel and endcap components covering the region $|\eta| < 1.0$ and $1.0 < |\eta| < 2.7$ respectively. The MS consists of three layers of precision chambers to accurately measure the momentum of muons, covering a range from a few GeV to a few TeV. It should be noted that the ID also provides a measurement of the muon momentum, albeit with a worse resolution. Figure 3.10 shows an early 2010 performance plot showing the muon momentum resolution provided by the ID and the MS against increasing muon p_T . The simulation assumes a perfectly aligned ATLAS detector, while the smeared simulation reproduces the resolution found in data in $Z \rightarrow \mu\mu$ decays. The resolution provided by the MS is better for muons with a transverse momentum larger than 100 GeV. For muons with a p_T of the order of 1.0 TeV the resolution is expected to be $\sim 10\%$ [39]. Muons with low momentum (eg. a few GeV) are not expected to traverse the three muon stations and, therefore, the resolution provided by the MS for those muons is lower than the one provided by the ID.

Muon momentum in the MS is measured through the deflection of the muon in a magnetic field by two large superconducting air-core toroid magnets in the Barrel and Endcap regions. In the range $|\eta| < 1.4$ the magnetic field is provided by the Barrel toroid magnet. From this point on until $|\eta| = 1.6$ the magnetic field is provided by a combination of the Barrel and the Endcap, and hence this region is known as the magnetic transition region. From $|\eta| > 1.6$ until $|\eta| < 2.7$ the magnetic field is provided by the Endcap toroid magnet. The magnetic field is mostly orthogonal to the muon trajectory [39].

3.5.2 Muon Precision Chambers

The precision chambers used to track the trajectories of muons are arranged in concentric circles, as shown in figure 3.11 for the barrel region. The barrel and endcap regions consist of three layers of precision chambers located between the barrel toroid magnet and in front and behind of the endcap toroid magnet, as shown in figure 3.12. Each of these layers is located at a radii of 5, 7.5 and 10 m from the interaction point, and is composed of sixteen components,

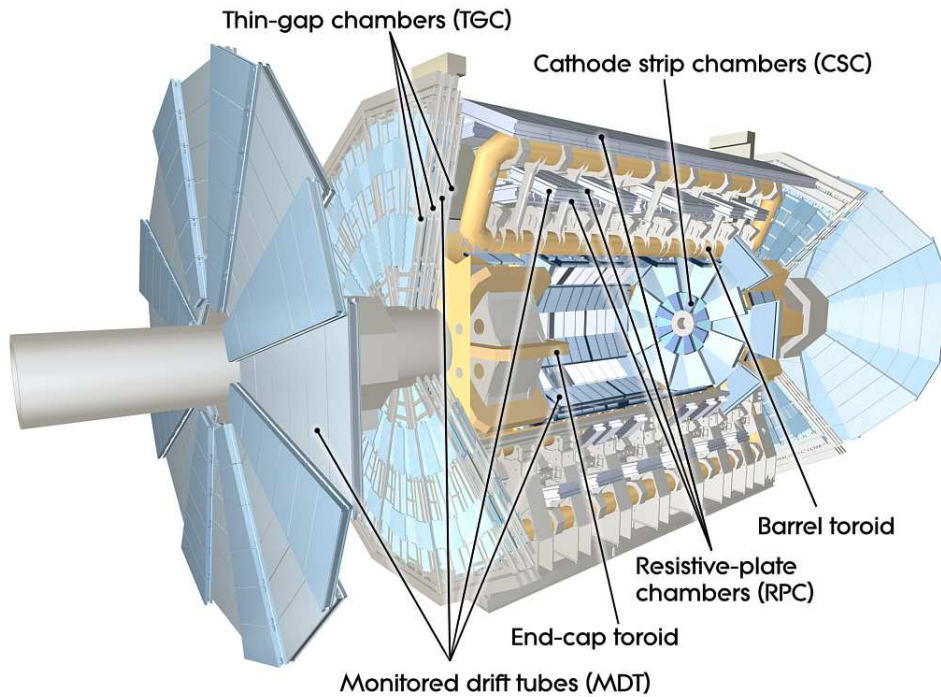


Figure 3.9: Computer generated image of the ATLAS muon system, showing each of the components of the muon spectrometer [39].

known as sectors, to cover the whole ϕ range. Sectors are divided into small chambers, aligned with the magnet coils, and large chambers, located between the magnet coils. Small and large sectors have a small overlap in their coverage to ensure that there are no gaps in the ϕ coverage and, by measuring tracks that pass through both kinds of sector, to provide a measurement of the alignment between chambers. In order to provide a reliable momentum measurement, precision chambers need to be properly aligned. An optical alignment system is in place to accurately control the alignment chamber by chamber and to monitor changes in its position.

The naming convention shown in figure 3.11 to refer to a particular chamber is the following:

- Barrel and endcap chambers are referred to with B and E respectively
- The three layers are referred as inner (I), middle (M) and outer (O), with the inner chambers being the closest to the interaction point
- Each chamber can be of a different sector type: small (S) and large (L)

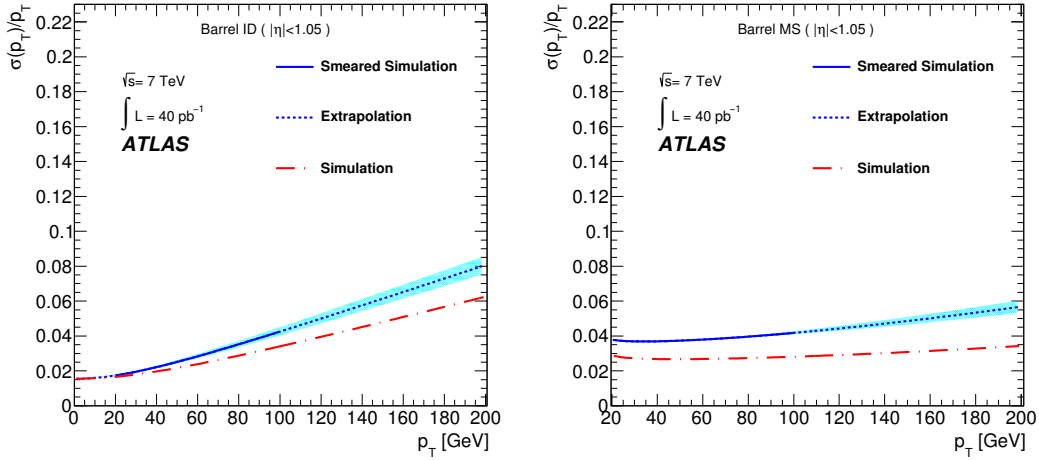


Figure 3.10: The resolution of the muon transverse momentum measurement is shown in the barrel region of the ID (left) and MS (right). The red line assumes a perfectly aligned ATLAS detector, while the solid blue line smears the simulated resolution to reproduce the one found in data. The shaded region shows the uncertainty on the extrapolation to high transverse momentum, coming from the uncertainties of the parameters used to smear the simulated resolution [42].

- The number refers to a particular ϕ sector

As an example, the chamber BIL 5 is a large chamber placed in sector 5 of the barrel inner layer. Other chamber types include those next to the rail system (referred to with a letter R) used to move the calorimeters to gain access to every part of the detector, and those near the detector support structure system (commonly known as feet). These latter chambers are referred to with a letter F. To accommodate the presence of rails and feet, chambers in those regions are smaller. As a result, the acceptance in those regions is expected to be reduced, as figure 3.13 shows for muons with $p_T = 100$ GeV in the ϕ regions between 240° and 300° [39]. For $|\eta| < 0.1$, no momentum measurement is possible due to services to for the solenoid magnet, the calorimeters and the inner detector being present [39]. The gap at $|\eta| = 1.3$ is due to the absence of muon stations in that region due to the presence of the ATLAS feet [39]. Finally, an extra chamber known as Barrel Endcap Extra (BEE) is used for tracks with barrel-endcap overlap.

Monitored drift tubes (MDTs) provide tracking and momentum measurement for all muons in the region $|\eta| < 2.7$, except for the inner endcap layer where their coverage extends only up to $|\eta| < 2.0$. Cathode Strip Chambers (CSCs) are used to cover the region $2.0 < |\eta| < 2.7$. MDTs are formed of two multilayers of drift tubes separated by 200 mm, with each multilayer made up of three or four layers of drift tubes. The drift tubes, as the name implies, are the

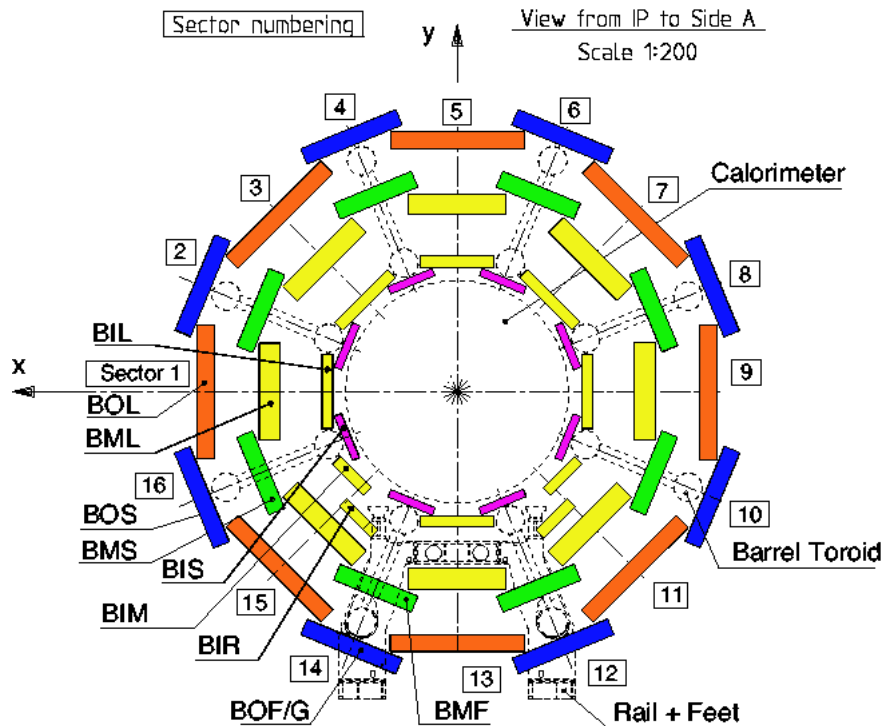


Figure 3.11: Layout of the muon tracking precision chambers in the barrel region in the transverse plane. The diameter of the outer circle is about 20 m [39].

basic component of the MDT, with a diameter close to 30 mm. Each drift tube contains a mix of Ar and CO₂ gas with a 93/7 proportion, with the readout channels in one end and the high voltage supply (3080 V) at the other end. As muons traverse the tube, the gas is ionised. Due to the high voltage, electrons drift and are collected by the tungsten-rhenium wire at the centre of the MDT [39]. Figure 3.14 shows the structure of an MDT chamber, with the length of the tubes varying from 1 to 6 m. The advantage of the design of the MDTs is that they are able to operate even if one of the individual tubes fails. The spatial resolution achieved in the position of an incoming muon is of 40 μm per chamber and 80 μm per tube layer.

CSCs have a finer granularity than the MDTs. The layout of the CSC endcap is similar to that explained earlier: eight small and eight large chambers to cover the whole ϕ range. The technology used for detection is also similar: the gap between cathode strips contains a gas mix of Ar/CO₂ (80/20). Freed electrons drift to wires placed between the strips to allow for a position measurement. Each CSC chamber consists of four layers of cathode strips and anode wires, positioned perpendicular to each other to provide a measurement in the transverse and bending planes. A schematic of the structure of a CSC is shown in figure 3.15. The spatial resolution achieved is of 60 μm in the bending plane, better than the 80 μm of each of the

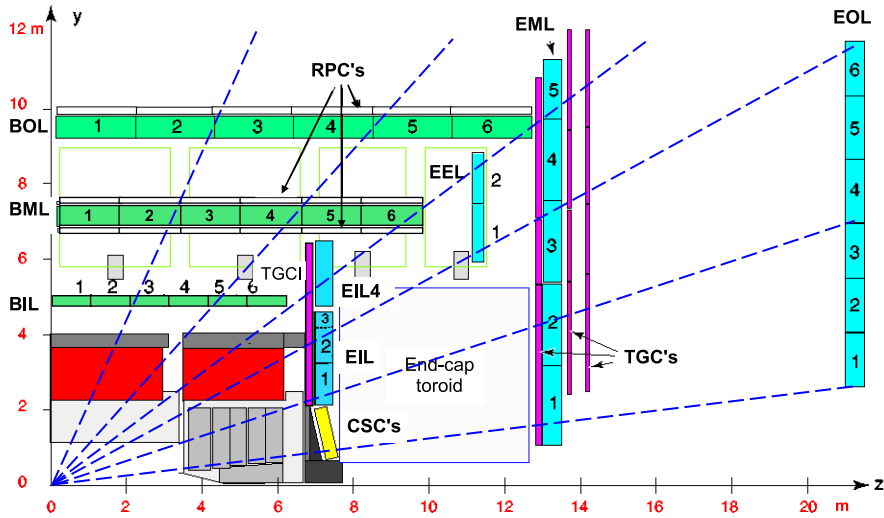


Figure 3.12: Layout of the muon system seen from the y - z plane as defined in the ATLAS coordinate system. The dashed lines show the trajectories of infinite momentum muons. Muons are expected to traverse the three precision layers of precision tracking chambers [39].

MDTs tubes. CSCs are only used for the region $2.0 < |\eta| < 2.7$ in the endcap instead of MDTs. The reason behind this choice is that the muon rate in that region is expected to exceed the limit for MDT safe operation.

3.5.3 Muon Trigger chambers

The precision chambers are not adequate for the trigger system given that their response time is too slow. As such, dedicated muon trigger chambers are incorporated in the MS. The trigger system covers a range of $|\eta| < 2.4$ through the use of Resistive Plate Chambers (RPCs) up to the region $|\eta| < 1.05$ and Thin Gap Chambers (TGCs) to cover the remaining region. The choice of different systems in the barrel and endcap are motivated by the different rates expected in each region. The aim of the muon trigger system is to provide fast information on muons traversing the detector to allow the Level-1 trigger (see section 3.6.1) to make a decision on whether to record an event and pass the information to the next trigger level [39]. In order to cover the full azimuthal angle range, RPCs and TGCs are divided in 16 sectors with three and four layers each respectively (also known as trigger stations), in a similar arrangement as the already mentioned muon precision chambers. Various p_T trigger thresholds are used at Level-1. To avoid unnecessary use of bandwidth, if a high p_T muon exceeds more than one of such thresholds only the highest p_T trigger is recorded. The requirements for a

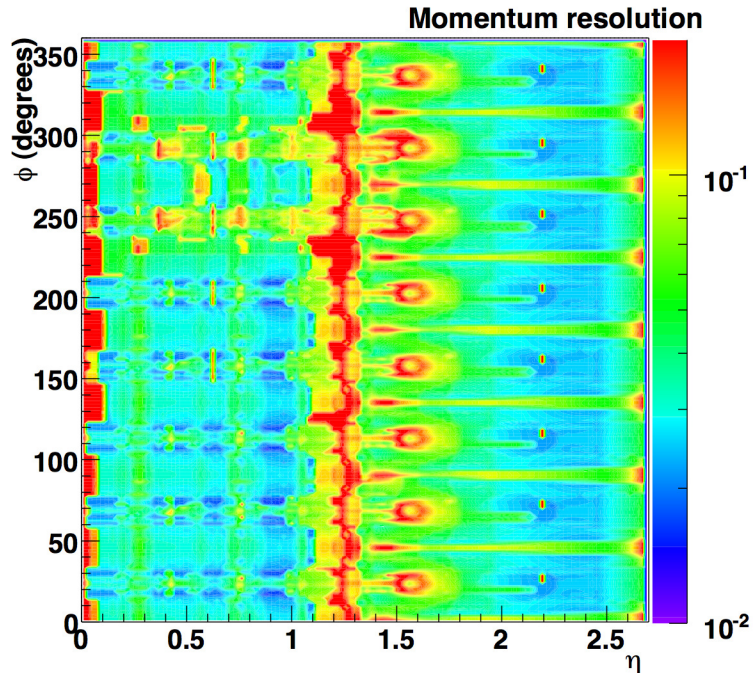


Figure 3.13: Expected muon momentum resolution provided by the standalone muon spectrometer measurement for muons with $p_T = 100$ GeV as a function of the η - ϕ position [39].

muon to pass the Level-1 stage of selection is to have hits in three trigger stations to accurately reconstruct the trajectory of the particle, minimise background from fake muons and ensure a good estimation of the non-uniform toroidal magnetic field (shown in figure 3.16 against increasing $|\eta|$) [39].

RPCs are made of two high voltage plates of bakelite, with a spacing of 2 mm where a gas mix of tetrafluorethane and isobutane in a 97/3 proportion is kept. The electric field in the gap is of 4900 V/mm, in order to transport electrons and ions resulting from gas ionisation to the strips placed outside the plate for readout purposes. The drift time of electrons in such a system is of 5 ns, low enough to work with the Level-1 trigger requirements. The barrel region ($|\eta| < 1.05$) is covered by RPCs due to their time resolution and rate capability [39]. The three layers of RPCs are attached respectively to the inside and outside barrel medium layer and the outside of the barrel outer layer, as shown in figure 3.17. Each of the trigger stations is made up of two independent layers.

TGCs are multiwire chambers consisting of two cathode plates and anode wires acting as readout channels. The gas used is a mix of n-pentane and CO_2 . The wire-to-wire and wire-

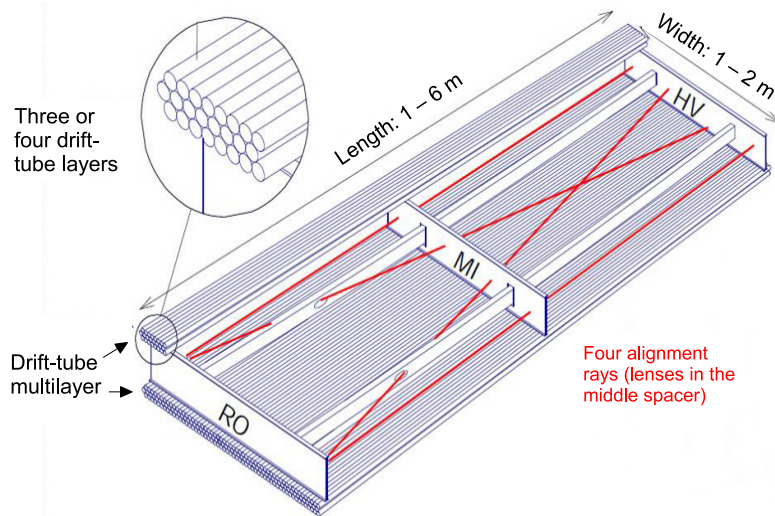


Figure 3.14: Mechanical structure of an MDT chamber, showing the position of the read out (RO) electronics and the high voltage (HV) supplies [39].

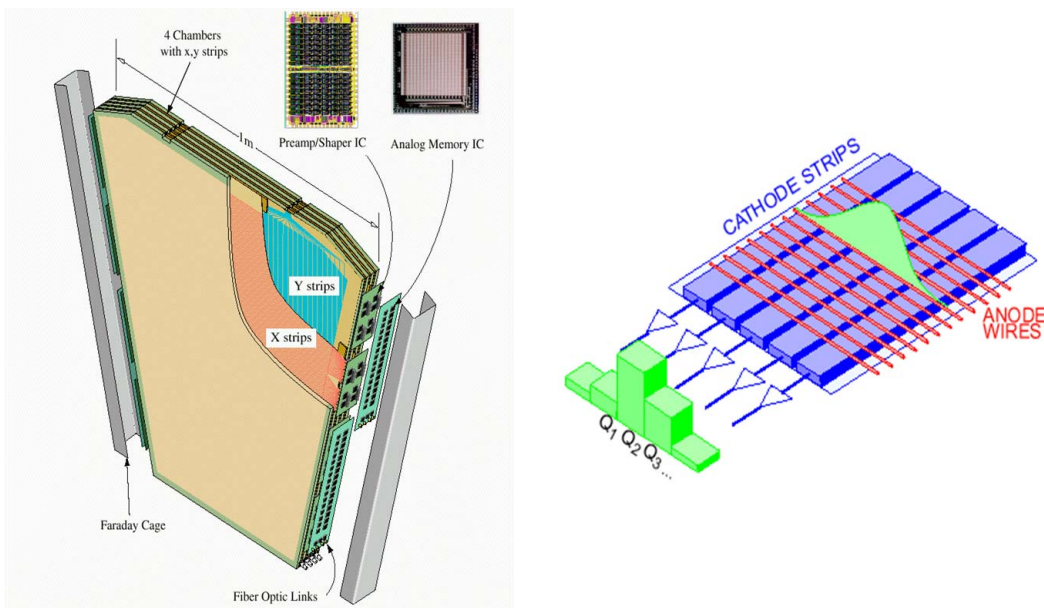


Figure 3.15: Structure of a CSC chamber (left), and one of its strips (right) [43].

to-cathode distances are 1.8 mm and 1.4 mm respectively, leading to the good time resolution required for the Level-1 trigger. As mentioned in the previous section, the particle flux in

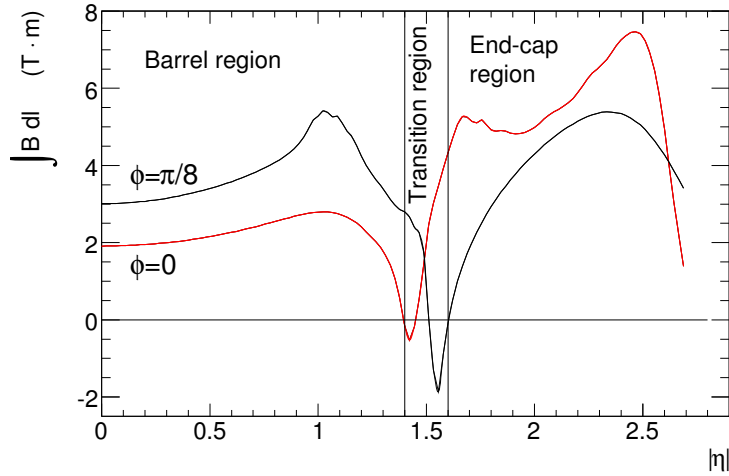


Figure 3.16: Expected magnetic field integral as a function of $|\eta|$ for two particles with an azimuthal angle of 0 and $\pi/8$ [39].

the endcap is expected to be larger. As such, TGCs are used to provide trigger coverage in the region $1.05 < |\eta| < 2.4$ due to their fine granularity and good time resolution. Also, they provide a second measurement of ϕ in the transverse plane, reaching up to $|\eta| < 2.7$. Figure 3.18 shows the layout of the muon trigger system, with one of the TGC stations mounted in front of the inner endcap layer of the muon precision chambers, and the other three in front and behind the middle endcap layer.

3.5.4 Muon Reconstruction

Muons passing the online trigger stage of event selection can be reconstructed in three different ways:

- Using only ID and calorimeter information
- Using only MS information
- Forming a combined track out of the two individual ID and MS measurements

The first option yields what is known as a segment-tagged muon, the second one is known as a standalone muon, while the latter one is known as combined muon. Combined muons are expected to provide the best momentum resolution, given that they combine the information

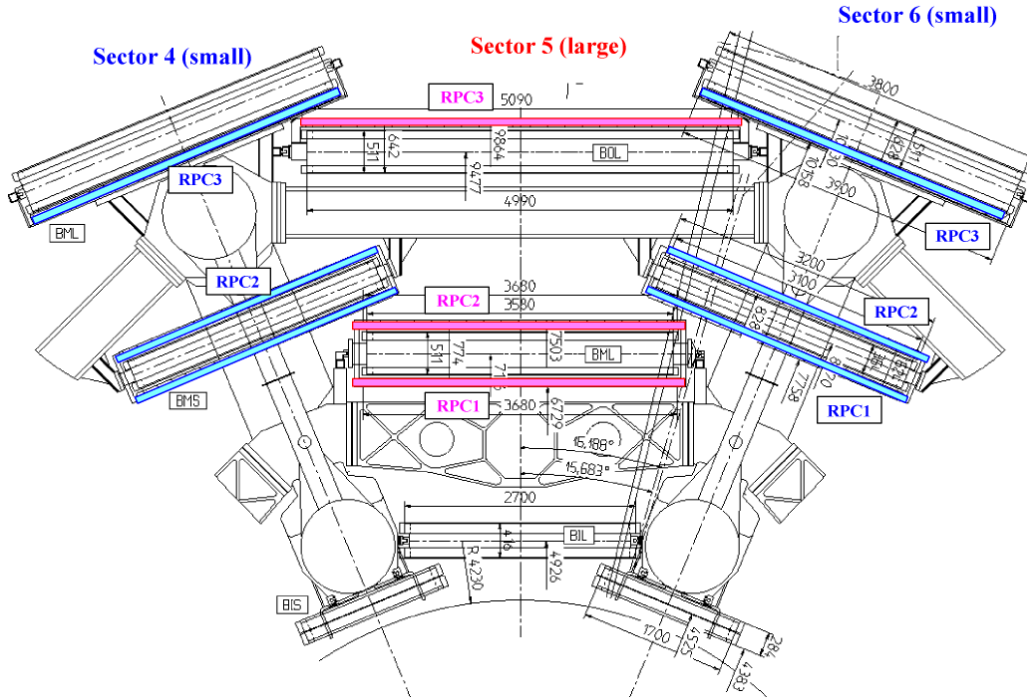


Figure 3.17: Structure of the muon trigger in the barrel region. The first two layers of RPCs are mounted above and below the middle layer of MDTs respectively. The third layer of RPCs is mounted in the outer layer of MDTs [39].

from the ID, which provides a better measurement of the impact parameter, and the information from the MS, that provides the best momentum resolution, as shown in figure 3.10.

In the MS, the hits in the MDT and CSC chambers are used to reconstruct the trajectory of a muon back to the interaction point and calculate its kinematic variables, while estimating the energy deposited in the calorimeters. Hits in the RPC and TGC trigger chambers are used to obtain the azimuthal coordinate. Low momentum muons ($p_T < 6$ GeV) are not expected to reach the middle and outer layers of the MS and hence the reconstruction can only be done using ID information. In the ID muons are reconstructed by using the hits in the SCTs and TRTs and the energy deposits in the calorimeter compatible with that of a minimum ionising particle to extrapolate back to the interaction point.

During Run-1, two algorithms were in place to perform muon reconstruction: STACO [44] and MuID [45]. The name of the algorithms comes from the procedure used to obtain a combined muon. In the case of STACO, a statistical combination of the two standalone measurements is used, whereas MuID uses a global refit of the full track. For Run-2 and with

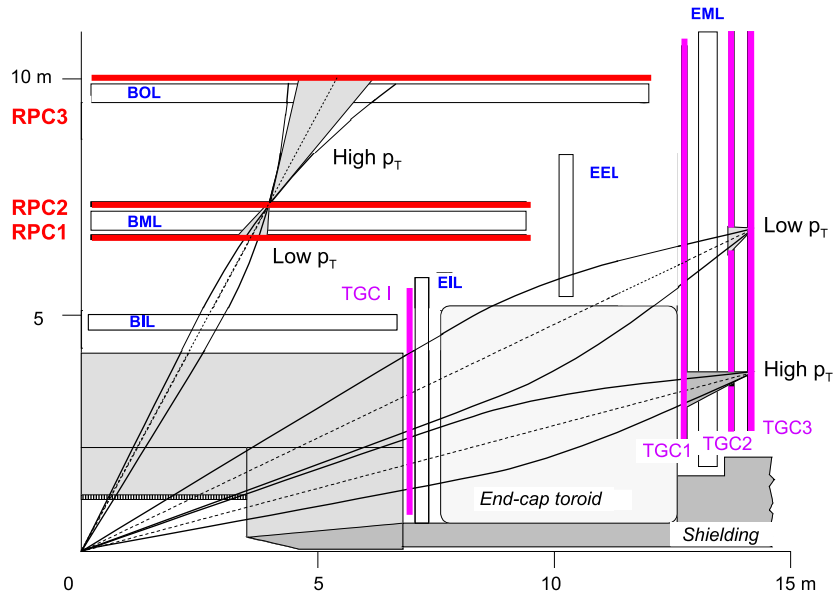


Figure 3.18: Structure of the muon trigger chambers in the transverse plane [39].

the aim to unify analysis involving muons, a new algorithm called Muons [46] combining the two existing ones will be in place.

3.6 Trigger and Data acquisition

The ATLAS trigger and data-acquisition (TDAQ) system is based on three levels of online event selection: the Level-1 trigger, the Level-2 trigger and the Event Filter. These last two form what is known as the High-Level Trigger (HLT). Given the high interaction rate of the LHC, it is necessary to choose carefully the events that are recorded. A poorly designed trigger system would either discard too many interesting physics events or record too many and overwhelm the storage capacity in ATLAS. The aim of the TDAQ is then to select interesting events for physics analysis among the large soft QCD background with a high efficiency.

3.6.1 Level-1 Trigger

The Level-1 Trigger (L1) is the first stage of online event selection. The rate of selected events must be reduced to 100 kHz starting from an interaction rate of 40 MHz without affecting the efficiency of selecting interesting physics processes. Trigger decisions have to be delivered

to the Central Trigger Processor (CTP) system in less than $2.5 \mu\text{s}$ after each bunch crossing. To fulfill this task, the L1 trigger uses a limited amount of detector information to search for muons, jets, electrons, photons, τ leptons, as well as selecting events with a high total and missing transverse energy. Regions of interest (RoI) are defined as the geographical coordinates of the detector where an interesting feature has been identified, such as a threshold for a L1 trigger¹² being satisfied. This information is passed to the second stage of the trigger system, the Level-2 trigger (L2), for further selection [47]. Figure 3.19 shows a diagram of the L1 trigger. The CTP uses the input from the two L1 subsystems, the Level-1 Calorimeter and the Muon trigger, to deliver decisions and decide whether to send the information to the HLT.

3.6.2 Level-2 Trigger

The Level-2 Trigger (L2) is the second stage of online event selection. Finer granularity and information from precision chambers is used at this stage to analyse the RoI passed by the L1 trigger. The rate of selected events is reduced to about 3.5 kHz. Given the finer granularity, the processing time for every event is larger than at L1. On average, an event takes 40 ms to get processed [39]. As shown in figure 3.20, a schematic of the ATLAS trigger system, while L2 decisions are made the event information is kept in the Read-out Buffers (ROBs). If an event fulfills any of the L2 trigger requirements it is passed to the Event Filter for final selection.

3.6.3 Event Filter and data processing

The final stage of online event is known as the Event Filter (EF). The rate of selected events is reduced to about 200 Hz. The EF uses offline reconstruction algorithms to accurately reconstruct events that pass the L2 trigger. As a result, the decision time on whether to record an event is increased to a few seconds. Events passing the EF are recorded at the Tier-0 centre at CERN, with events being classified depending on the EF triggers passed and sent to different offline data streams for fast processing.

The recorded data is then processed according to the ATLAS event data model (EDM). The aim of the ATLAS EDM is to have a common interface for all of the data analysis to ensure easy maintenance and maintain coherence between different physics analyses [48]. Figure 3.21 shows the layers of the EDM, where the size of an event is reduced at each step. The Event Summary Data (ESD) is produced directly from raw data and contains information

¹²Trigger requirements include a variety of cuts in different kinematic variables. The whole set of L1 triggers is referred as the L1 trigger menu.

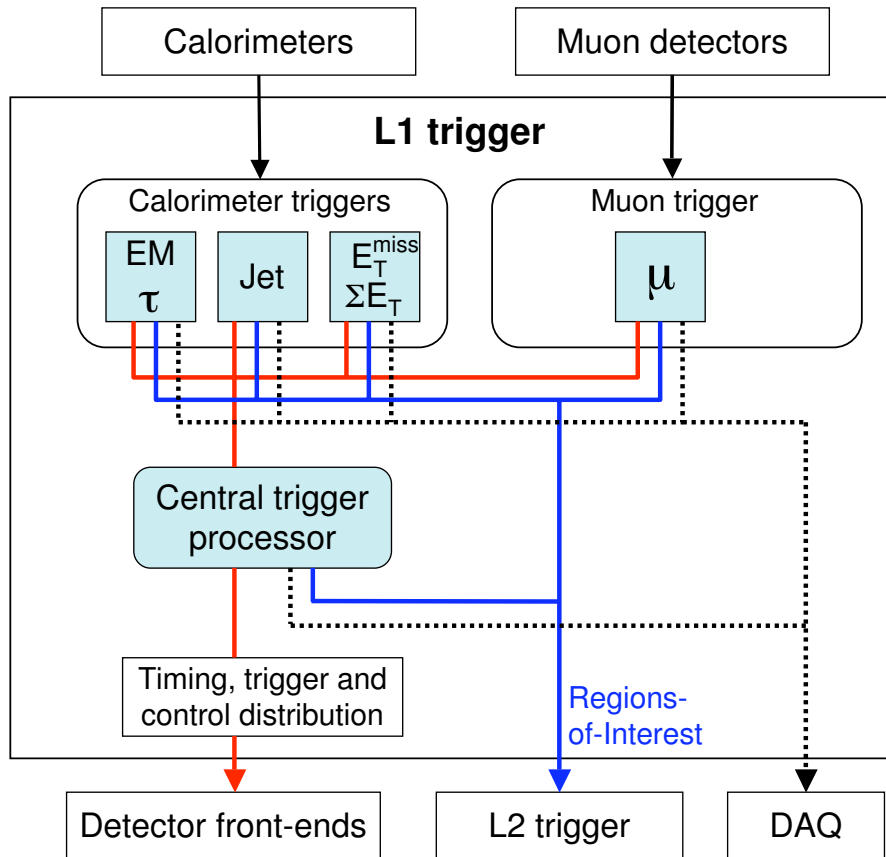


Figure 3.19: Diagram of the L1 Trigger, composed of the Level-1 Calorimeter and the Muon trigger. The Central Trigger Processor, using input from the L1 systems, makes the decision on whether to accept an event and pass it to the next stage of trigger selection. [39].

about the detector reconstruction. Performance analysis commonly use the ESD format. For physics analysis, data stored in the Analysis Object Data (AOD) format is sufficient given that it contains a summary of the reconstructed event. Given the widespread use of ROOT, a C++ based language, physics groups convert AODs into a format compatible with it known as Derived Physics Data (DPD).

3.7 Performance

The LHC began its activity (Run-1) in December 2009 and stopped in the end of 2012 for the Long Shutdown 1 (LS1). This section explains the evolution of the performance of the

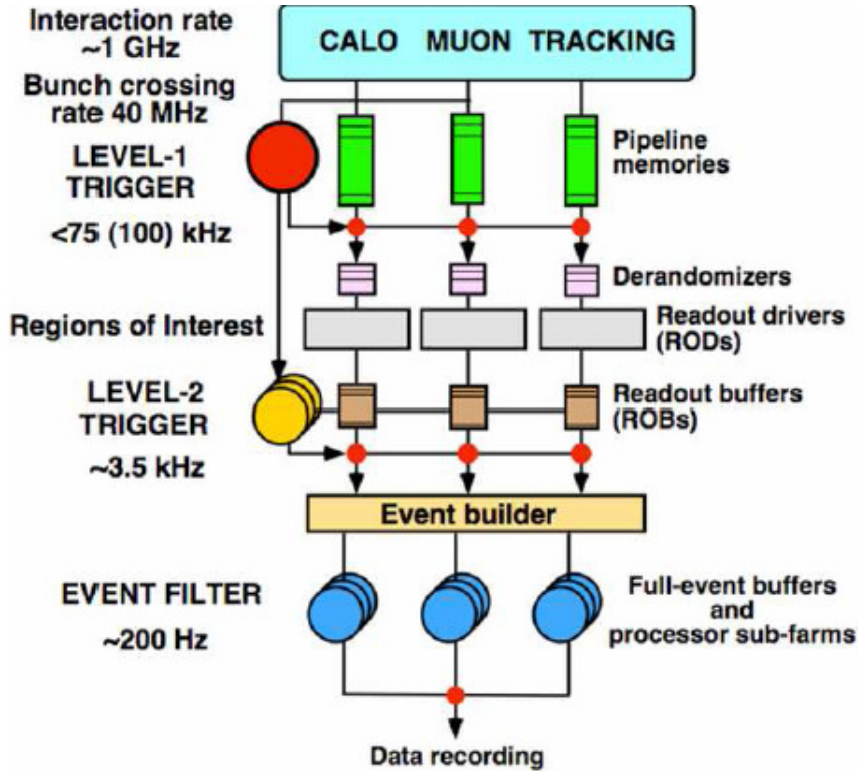


Figure 3.20: Diagram of the ATLAS Trigger system [39].

ATLAS detector during this active period.

The first proton-proton (pp) collisions in December 2009 recorded data for centre-of-mass energies of 0.9 TeV and 2.36 TeV, yielding a relatively small amount of integrated luminosity: $9.0 \mu\text{b}^{-1}$ and $0.7 \mu\text{b}^{-1}$ respectively [51]. In 2010, the centre-of-mass energy increased to 7 TeV and the number of bunches per beam increased to 368. The instantaneous luminosity increased accordingly, reaching $2.1 \cdot 10^{32} \text{ cm}^{-2} \text{ s}^{-1}$ and the total integrated luminosity collected was 45 pb^{-1} . The maximum number of interactions per bunch crossing, or pile-up, was 3. In 2011, the bunch spacing was decreased to 50 ns and the number of bunches per beam increased to 1380. The instantaneous luminosity and the peak pile-up increased as shown in figures 3.22 and 3.23. The centre-of-mass energy was increased to 8 TeV in 2012, the peak pile-up reached values close to 40, well above the expected value of 23 [49], due to the instantaneous luminosity reaching a value close to the design one: $7.7 \times 10^{33} \text{ cm}^{-2} \text{ s}^{-1}$. As can be seen in figure 3.24, the total integrated luminosity collected during Run-1 in those conditions is close to 30 fb^{-1} . In Run-2, with a 25 ns bunch spacing and a larger centre of mass energy, it is expected that the ATLAS detector can deliver close to 100 fb^{-1} of integrated luminosity.

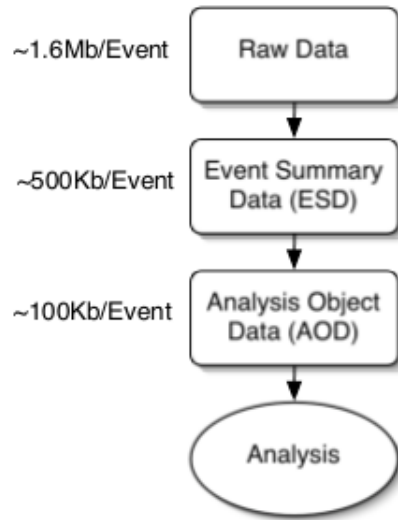


Figure 3.21: Layers of the ATLAS computing model [48].

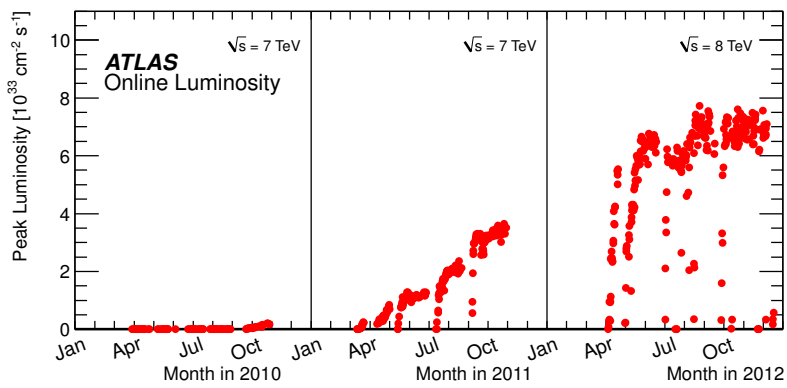


Figure 3.22: Peak instantaneous luminosity vs time [50].

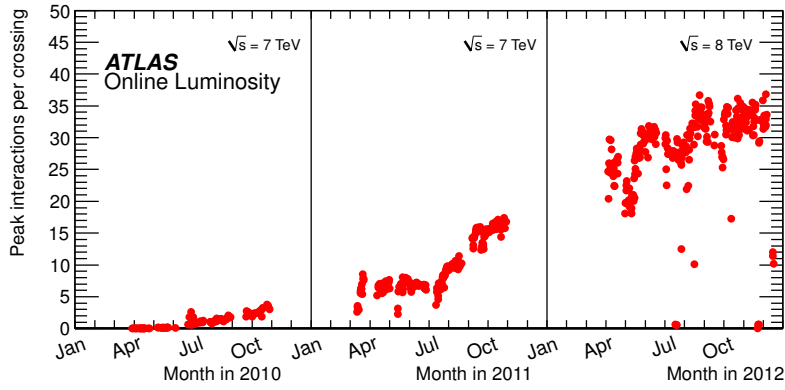


Figure 3.23: Peak pile-up vs time [50].

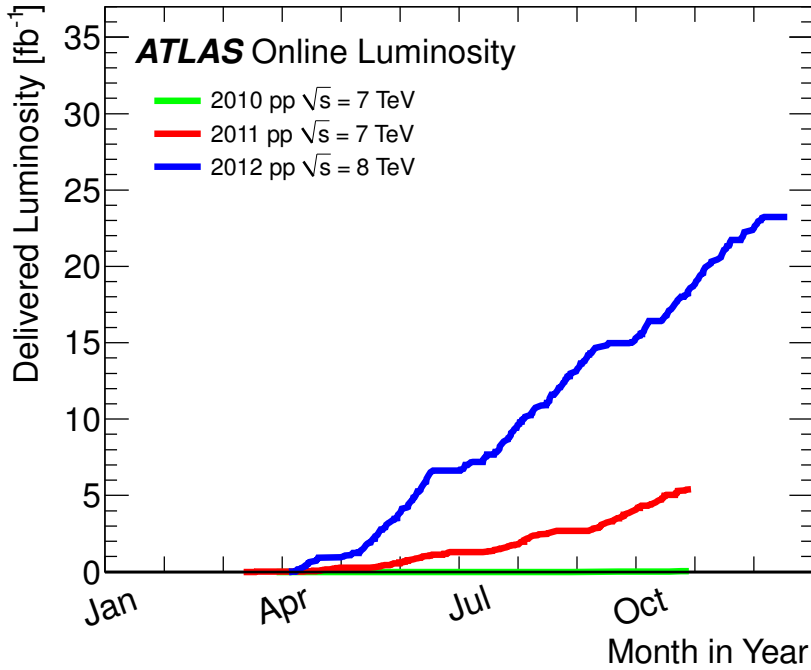


Figure 3.24: Integrated luminosity delivered vs time [50].

To ensure that only good quality data is used for physics analysis, a Good Runs List (GRL) is used to discard data recorded when the ATLAS detector or the LHC beam was not in proper working conditions. As such, the luminosity used for physics analysis is always slightly lower than the one delivered by the LHC and the one recorded by ATLAS. As shown in figure 3.25,

from the 22.8 fb^{-1} delivered by the LHC about 90% is used in ATLAS physics analysis.

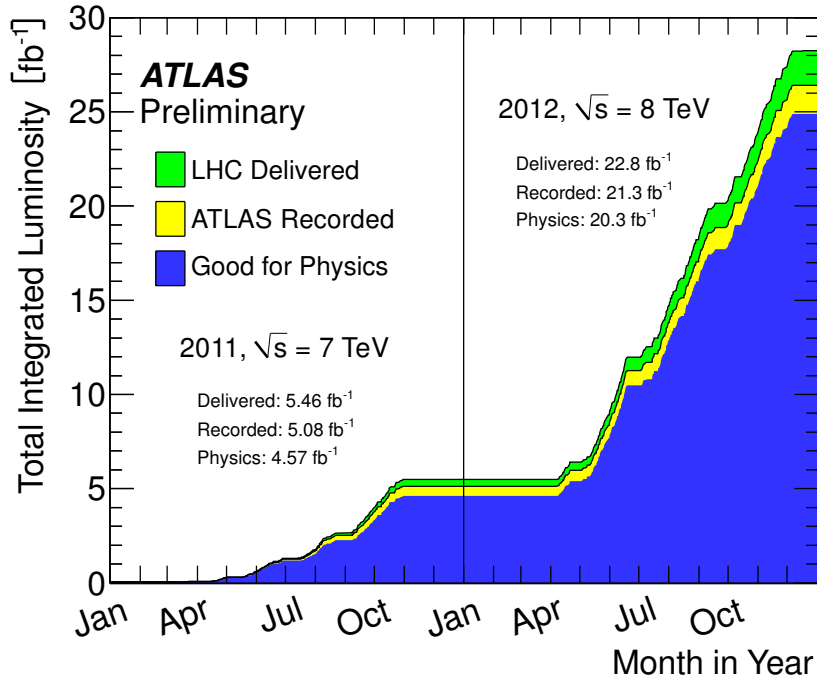


Figure 3.25: Integrated luminosity delivered by the LHC compared to the one recorded by ATLAS and used in physics analysis [50].

4 Study of the ATLAS Level-1 Calorimeter Missing Transverse Energy Trigger at High Pile-up using 2012 data

During Run-1 (2009-2012), the ATLAS detector collected close to 30 fb^{-1} of integrated luminosity in pp collisions at $\sqrt{s} = 7$ and 8 TeV. In Run-2 (2015-2018), the amount of data collected is expected to be close to 100 fb^{-1} . The increase in instantaneous luminosity, together with the increase in centre-of-mass energy to 13 TeV, will bring an increase in the average number of collisions per bunch crossing (pile-up), and therefore the number of jets and the activity in the forward regions of the detector will increase too. That brings technical challenges that must be overcome to ensure the optimal performance of the ATLAS detector. One of these challenges is controlling the rate at which the ATLAS Level-1 Calorimeter trigger (L1Calo), a major component of the L1 trigger, provides decisions to record data. In particular, missing transverse energy (E_T^{Miss} or MET) triggers at L1 are problematic since E_T^{Miss} is sensitive to energy observed in the entire L1Calo system and is therefore susceptible to fluctuations in hadronic activity which can produce fake E_T^{Miss} .

Triggering on E_T^{Miss} is important to record benchmark physics processes such as $W \rightarrow l\nu$ ¹³ and for new physics searches such as graviton production or Supersymmetry. Other processes, such as a hadronic decay to jets, can also contain missing energy if one of the jets goes into the forward regions where it cannot be detected. The former processes contain (or are expected to contain) real E_T^{Miss} coming from a known or expected physics processes. The second process contains what is called fake E_T^{Miss} , as the presence of missing energy is not inherent to the physics process but instead due to the characteristics of the detector. It is desirable to suppress the fake E_T^{Miss} contribution to the L1 E_T^{Miss} trigger rate. However, that should not reduce the efficiency of recording events with real E_T^{Miss} .

The E_T^{Miss} of a candidate event is calculated using the vector sum of transverse energies [51]. The calculation of the total transverse energy at L1 is performed, as explained in section 4.1, using the sum of analogue signals from the trigger towers. This calculation can be affected by noise originating from two sources: the electronics and pile-up. The electronics can produce small signals due to the high granularity of trigger towers, which appears as Gaussian fluctuations in energy. Pile-up noise (or real noise) is proportional to the activity in the detector. There are two kinds of pile-up noise: in-time and out-of-time. In-time pile-up originates from collisions from the same bunch. Out-of-time pile-up originates from collisions from different bunches overlapping due to the larger response times of a detector subsystem. Figure 3.23 shows that the average number of interactions per bunch crossing increased throughout Run-1. Therefore, this type of noise due to pile-up is also expected to increase during that Run-2, specially when the bunch spacing is reduced to 25 ns. In order to reduce sensitivity

¹³Neutrinos cannot be detected by ATLAS and their presence can only be inferred by the presence of E_T^{Miss}

to noise, trigger towers with very small signals in E_T are set to zero and are not used for the total transverse energy calculation. This prevents summing over too many towers and reduces the sensitivity to electronic and pile-up noise. η -dependent energy thresholds are set for each of the trigger towers used at L1 to prevent summing over too many towers and artificially increasing the E_T^{Miss} . These energy thresholds are set to reduce noise contributions and, throughout this chapter, will be referred to as noise cuts. As will be shown, optimising the noise cuts is a useful tool to control the L1 E_T^{Miss} trigger rate.

Following an overview of the L1Calo system and the methods used to control the L1 trigger rates during Run-1, this chapter describes a more detailed and extended study performed to optimise the performance of the L1 E_T^{Miss} triggers while taking into account the expected pile-up conditions during Run-2. The study uses data collected in 2012 by the ATLAS detector at $\sqrt{s} = 8$ TeV.

Throughout this chapter different E_T^{Miss} quantities are used. For clarity, all these different quantities are defined here:

- The online or L1 E_T^{Miss} is the E_T^{Miss} measured by the entire L1Calo system and is used to make L1 trigger decisions. The smallest piece of information used to obtain the L1Calo E_T^{Miss} is the trigger tower.
- The offline E_T^{Miss} is evaluated using all the information from the calorimeter cells and final object calibrations, giving a more accurate value than the online one. Throughout this chapter, two different definitions of offline E_T^{Miss} are used:
 - The offline topological E_T^{Miss} is the offline E_T^{Miss} calculated using only calorimeter information (no tracks or muons are used) to mirror the L1 E_T^{Miss} calculation [52].
 - MET_Ref_Final is the final offline E_T^{Miss} calculation for all of the ATLAS detector using all subdetector information [52].

Section 4.1 and 4.2 contain an overview of the L1Calo system and its performance during Run-1. Sections 4.3 and 4.4 are a summary of the techniques used in Run-1 to control the L1 E_T^{Miss} trigger rate and the Run-2 proposal to keep that same rate within its allocated bandwidth. Chapter 4.5 onwards presents the work of the author: investigating one of the proposals to control the L1 E_T^{Miss} trigger rate during Run-2.

4.1 The ATLAS Level-1 Calorimeter trigger

The Level-1 Calorimeter (L1Calo) is a major component of the L1 trigger situated in USA 15, a large electronics cavern located off the detector area. L1Calo uses information from

all of the ATLAS calorimeters to measure high energy electrons, photons, τ leptons, jets and the E_T^{Miss} . Decisions on whether to pass events to the next stage of the online selection are delivered in $2.1 \mu\text{s}$, within the maximum allowed decision time by the L1 CTP [53].

The input data is provided by around 250,000 calorimeter cells which are combined in groups of 3 to 60 cells, depending on the η range, to form 7168 trigger towers. The trigger tower, as defined in [47], is the smallest element of calorimeter information used in L1Calo. It has dimensions of approximately 0.1×0.1 in $\Delta\eta$ - $\Delta\phi$. Trigger tower analogue signals are summed in the detector over the full depth of the calorimeter region concerned and sent to USA 15 for digitisation. The granularity of trigger towers in the ATLAS detector depends on the η region and is shown in table 4.1. For $|\eta| < 2.5$ the granularity is constant in $\Delta\eta \times \Delta\phi$. For the forward regions ($|\eta| > 2.5$) the granularity is reduced.

Table 4.1: Trigger tower granularity of L1Calo for different $|\eta|$ regions.

Detector Region	Granularity
$ \eta < 2.5$	0.1×0.1
$2.5 < \eta < 3.1$	0.2×0.2
$3.2 < \eta < 4.9$	0.4×0.4

The L1Calo system identifies different trigger objects and measures their transverse energy, E_T . This process is handled by the three main subsystems that form L1Calo [53]:

- The PreProcessor (PPr) consists of 124 PreProcessor Modules (PPMs) which contain Analogue to Digital Converters (ADC) to digitize the analogue signals coming from the trigger towers, perform bunch crossing identification (BCID) by assigning each pulse to a given bunch crossing and extract the E_T for the hit towers [47, 54]. A look-up table (LUT) is used as a conversion table to transform the digitised trigger tower signals into values of energy used to make trigger decisions.
- The Cluster Processor (CPM) identifies candidate electrons, photons and τ leptons with high transverse energy and calculates the activity around them (also known as isolation), required to identify benchmark physics processes such as $Z \rightarrow \mu\mu$ or for new physics searches.
- The Jet/Energy-sum (JEM) finds jets and calculates the total transverse energy ($\sum E_T$) as well as the E_T^{Miss} of the event. These values are sent to the Central Trigger Processor (CTP), which combines the information from the different parts of L1 to make trigger decisions.

The architecture of L1Calo is shown in figure 4.1.

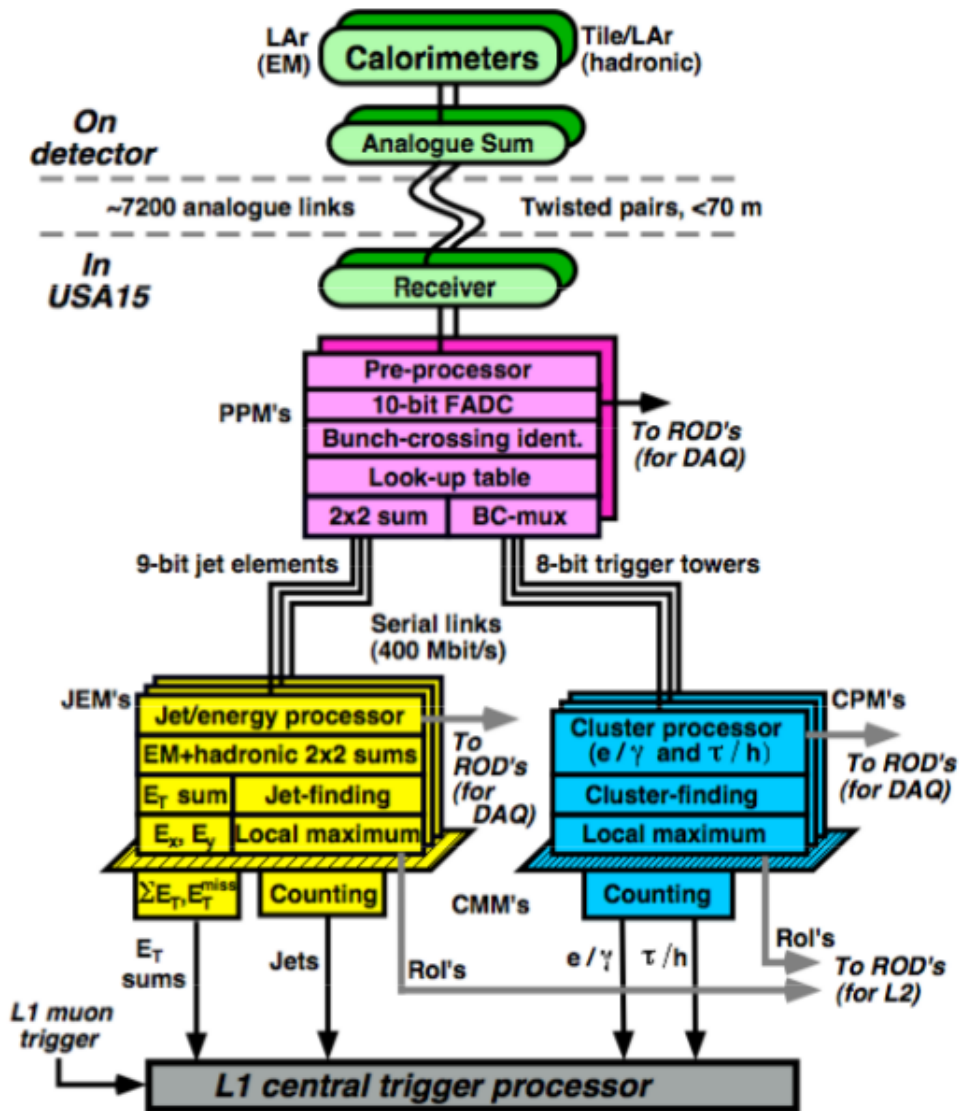


Figure 4.1: Architecture of the L1Calo trigger [53].

4.2 Performance of the ATLAS Level-1 Calorimeter E_T^{Miss} triggers

The changing conditions of the LHC beam throughout Run-1 required an optimization of the L1 trigger. L1 should reduce the rate of selected events to a maximum of 100 kHz. The increase in instantaneous luminosity and pile-up present a challenge, as the L1 trigger rates increase and can exceed their original allocation. Some triggers increase linearly with instantaneous luminosity. Others, however, increase much faster than linearly and present a more serious challenge [49]. There are different strategies to control the trigger rates:

- Introduce a prescale factor. Triggers with a prescale will reject a fraction of the events they would normally accept. As an example, a trigger with a prescale of 5 will record only 20% of the triggered events. This is a simple way of reducing the rate but it has the obvious drawback of reducing the integrated luminosity collected.
- Increase a trigger threshold. Increasing the lowest transverse energy required for triggering will also reduce the trigger rate. However, this can also reduce the efficiency of selecting physics processes.
- Increase the trigger tower noise cuts. Summing over too many calorimeter cells due to pile-up or electronic noise can have a large effect on triggers that select events with a large $\sum E_T$. Increasing the noise cuts will reduce the rates, but very large thresholds can distort the energy calculation by eliminating too many trigger towers from the final calculation.

The implementation of any of the strategies described above has to be done through careful studies to ensure the efficiency of selecting interesting physics processes does not deteriorate. As an example, the lowest transverse energy trigger for electrons and photons was increased from 16 to 18 GeV during the 2012 data taking to compensate for the increased rate due to increased instantaneous luminosity. The threshold increase however was η -dependent and only applied in regions where the L1 efficiency is high enough to ensure no major loss of physics efficiency [49].

Figure 4.2 shows the rate of several L1 triggers against increasing luminosity. Single object triggers such as muon, electron, photon or jet triggers scale linearly with luminosity. The E_T^{Miss} trigger depends on the transverse energy vector sum, obtained by summing trigger towers over the entire calorimeter. Notice that at high instantaneous luminosities the E_T^{Miss} trigger scales faster than linearly.

In order to control the E_T^{Miss} trigger rate at L1, the trigger tower noise cuts were optimised using 2011 and early 2012 data. Figure 4.3 shows the L1 E_T^{Miss} trigger rate against the L1 E_T^{Miss} trigger threshold for different sets of noise cuts. Introducing higher noise cuts in the forward

calorimeter regions reduces the rate significantly. However, a further noise cut increase or the removal of the forward calorimeter from the missing energy calculation does not reduce the rate significantly. Figure 4.4 shows the efficiency of selecting $W \rightarrow e\nu$ processes, which contain real missing energy, against the offline topological E_T^{Miss} for different noise cut settings. The thresholds are optimized in each case to reduce the rate while having the smallest impact possible on the efficiency of selecting such physics events. The FCAL settings for an average number of interactions per bunch crossing ($\langle\mu\rangle$) of 15 and 20 only raise the thresholds in that region, whereas the FCAL/EMEC-IW also increases the noise cuts in the EndCap Inner Wheel (EMEC-IW) [56]. The noise cut increase in the forward regions does not reduce the efficiency of selecting $W \rightarrow e\nu$ events.

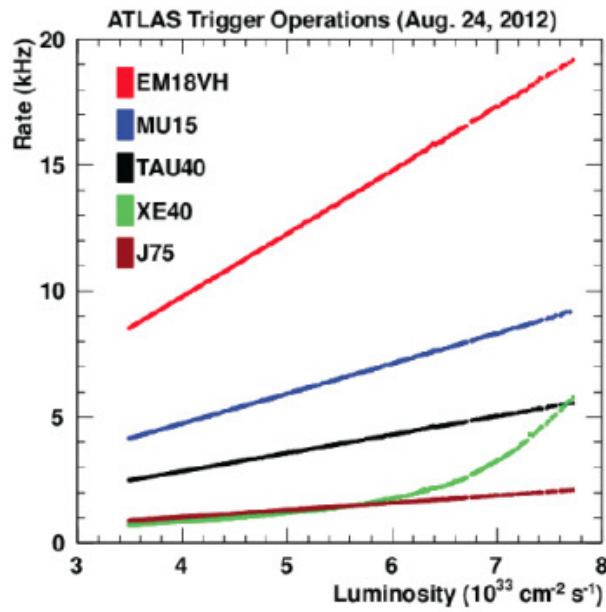


Figure 4.2: The rate for different LI triggers is shown against increasing instantaneous luminosity. The triggers EM18VH, MU15, TAU40, J75 and XE40 look for electrons, photons, muons, τ leptons, jets and E_T^{Miss} respectively. The number indicates the transverse energy threshold in GeV for the trigger to activate [55].

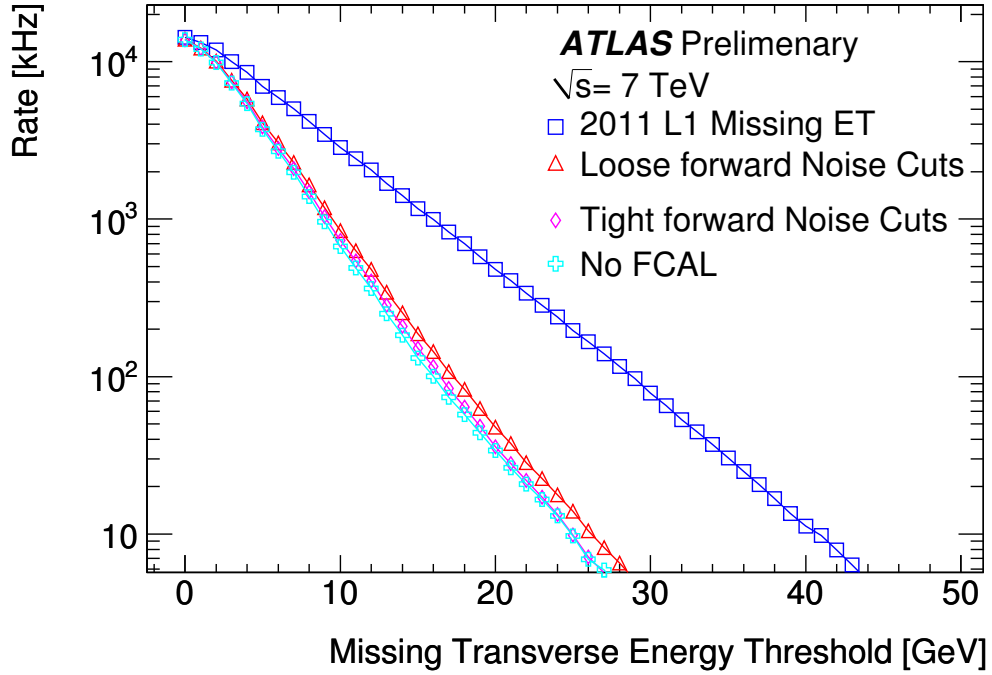


Figure 4.3: Figure showing the overall E_T^{Miss} rate at L1 for different noise cut settings. The 2011 configuration corresponds to a 1 GeV threshold for all trigger towers. The “Loose Forward” configuration increases the noise cuts in the forward calorimeter (FCAL) regions ($|\eta| > 3.5$): 6.5, 5.5 and 2.5 GeV in the first layer of the FCAL and 4.5 GeV in the second layer. The “Tight Forward” configuration further increases the noise cuts in the FCAL by 1 GeV and also increases the thresholds beyond $|\eta| = 2.5$ by 0.5 GeV. Finally, the “No FCAL” removes the forward calorimeter from the missing energy calculation. The data used to estimate the rate was taken in run 191426 during 2011 and corresponds to a pile-up of 15 and an instantaneous luminosity of $3.2 \cdot 10^{33} \text{ cm}^{-2} \text{ s}^{-1}$ [56].

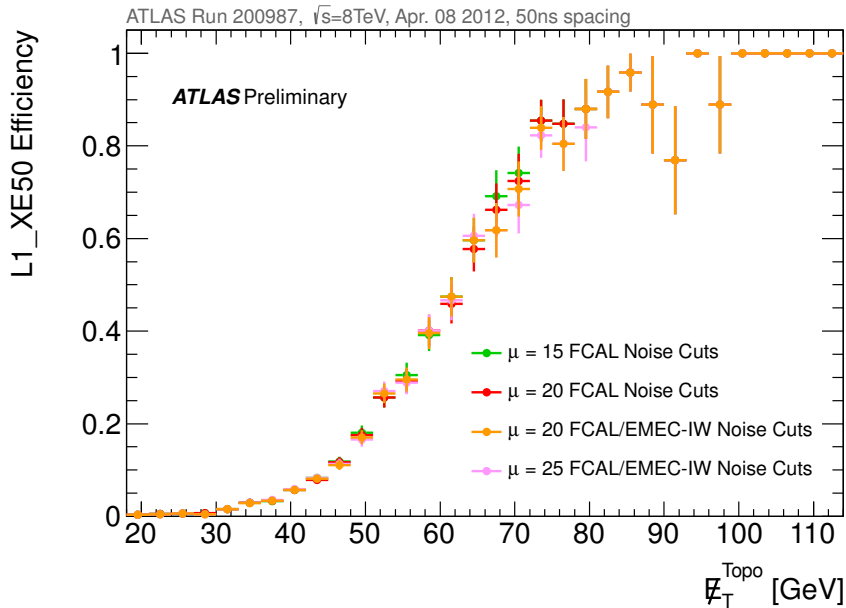


Figure 4.4: The L1_XE50 efficiency of selecting $W \rightarrow ev$ processes is evaluated as a function of the offline topological E_T^{Miss} . The trigger L1_XE50 selects events with an E_T^{Miss} larger than 50 GeV. Four different cases are simulated offline depending on the different settings for the trigger tower thresholds and the average number of interactions per crossing ($\langle\mu\rangle$ in the plot) [56].

Figure 4.5 shows the rate of several L1Calo triggers normalised to the instantaneous luminosity of each run against increasing pile-up. The rate of single object triggers (except L1_FJ75) increased between 2011 and 2012 due to the increased centre-of-mass energy. The decreased rate for L1_FJ75, L1_XE50 and L1_XE50_BGRP7 is due to the increased noise cuts in the forward calorimeter region. However, at a $\langle\mu\rangle$ of 23 the E_T^{Miss} rate already exceeded that of 2011 and kept increasing. When Run-2 starts in mid-2015, the bunch spacing will be reduced to 25 ns and the centre-of-mass energy will be increased to 13 TeV. The increase in instantaneous luminosity and $\langle\mu\rangle$ is expected to bring a large increase in the E_T^{Miss} trigger rate in L1. Figure 4.3 shows that further increasing the noise cuts has a marginal effect on the L1 E_T^{Miss} trigger rate. In order to ensure the optimal functioning of the L1 trigger the E_T^{Miss} trigger rate cannot exceed its allocated bandwidth. The next section describes a strategy proposed to achieve that aim.

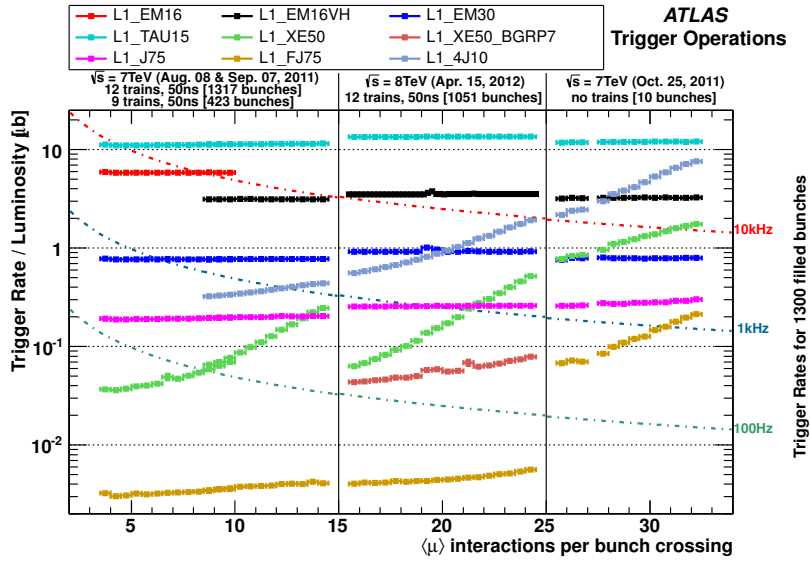


Figure 4.5: The plot shows the $\langle\mu\rangle$ -dependence of the rate of several L1Calo triggers through different runs with a 50 ns spacing between bunches, normalised to the instantaneous luminosity of each run. The left side corresponds to data taken during two runs in 2011 at $\sqrt{s} = 7\text{ TeV}$. The middle figure shows data from a 2012 run at $\sqrt{s} = 8\text{ TeV}$ and 50 ns spacing. The right side shows the results for a special high luminosity run in 2011. L1_EM, L1_TAU and L1_J triggers look for electrons/photons, τ leptons and central jets ($|\eta| < 3.2$) respectively. L1_XE50 and L1_XE50_BGRP7 are E_T^{Miss} triggers. L1_XE50_BGRP7 has a veto on the first three bunches of a train. L1_4J10 activates when an event contains more than 4 jets each with $E_T > 10\text{ GeV}$ and L1_FJ75 looks for forward jets ($|\eta| > 3.2$) with $E_T > 75\text{ GeV}$. The dashed lines correspond to fixed-rate lines [56].

4.3 Bunch Crossing ID dependent noise cuts

As established in the previous section, new strategies need to be found to control the L1 E_T^{Miss} in Run-2. As seen in figure 4.3 the approach followed in Run-1 has reached maximum effectiveness: further increasing the noise cuts in the forward regions of the detector does not yield a significant trigger rate reduction.

The strategy proposed is the introduction of bunch crossing ID dependent noise cuts. The aim is to take advantage of the shape of the LAr pulse, shown in figure 4.6, and the bunch train structure of the LHC. Every bunch train is made up of 36 bunch crossings and, after every bunch train, there is a gap of four bunch crossings. As explained in section 4.1 of [57], at the start of the bunch train the L1 E_T^{Miss} trigger rate is increased, as shown in figure 4.7, due to unbalanced overlaying of the bipolar calorimeter pulse shapes used as input in L1Calo. Pulse shapes constructively overlay each other at the start of the bunch train resulting in fake L1

E_T^{Miss} measurements. After the first few bunches, the negative contributions from the bipolar pulse shape of the initial bunches balance the contributions of the nearest bunches and the fake L1 E_T^{Miss} is reduced.

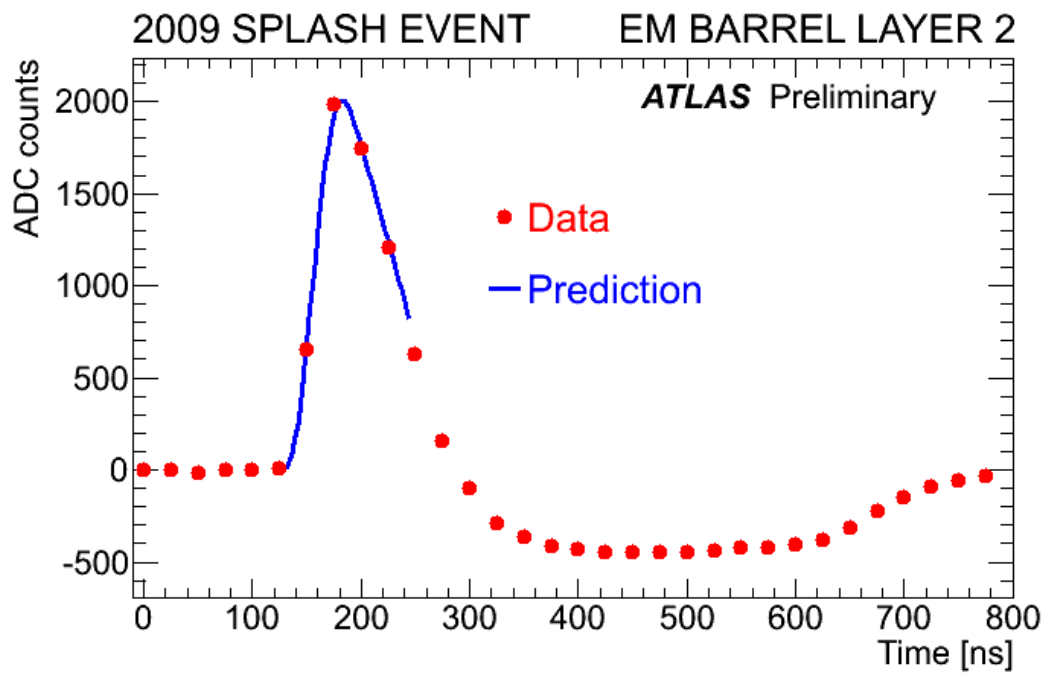


Figure 4.6: The shape of the liquid Argon pulse in ADC counts is shown against time [58].

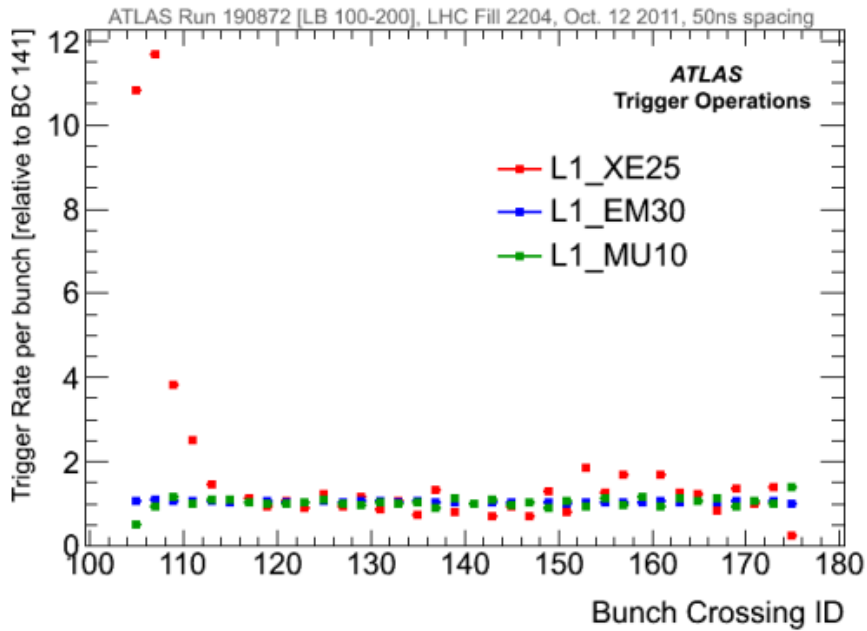


Figure 4.7: Trigger rates for three L1 objects per bunch crossing. The rates are relative to that of bunch crossing 141, in the middle of the bunch train. The E_T^{Miss} trigger is L1_XE25 [58].

Figure 4.8 shows the number of events activating an L1 E_T^{Miss} trigger for a whole bunch train. The strategy investigated by the author is to introduce two sets of noise cuts as shown in the same figure: one set for the first four bunches (“the start”) and another set for the rest of the bunch train (“the bulk”). The first four bunches have a higher L1 E_T^{Miss} trigger rate than the rest of the bunch train and should be treated separately. Given the increased activity at the start of the bunch train, the noise cuts can be set to higher values at the start and lowered afterwards.

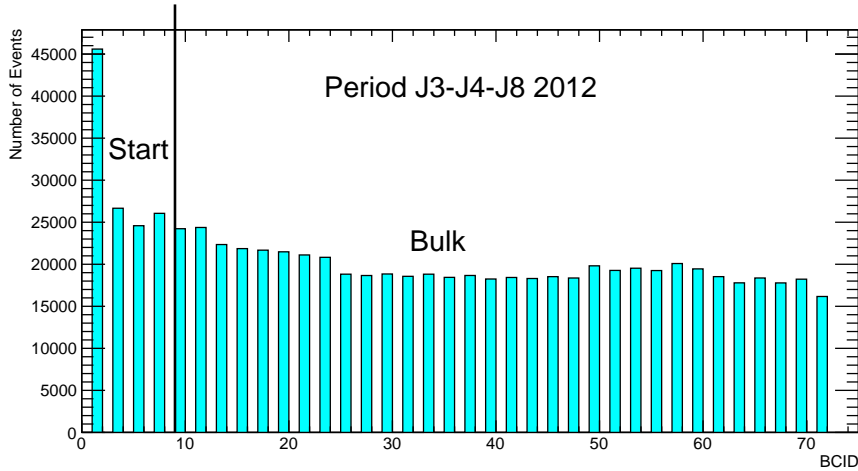


Figure 4.8: Number of events activating the E_T^{Miss} trigger L1_XE25 per bunch crossing for a whole bunch train. The figure proposes the separation of the bunch train in two parts: the “Start” and the “Bulk”.

4.4 Fractional Occupancy vs noise cuts

During the 2011 data-taking, the noise cuts were set to 1.0 GeV for all η regions. In 2012 they were increased in the FCAL/EMEC-IW region to control the E_T^{Miss} rate. For Run-2, new configurations will be needed to accurately control the L1 E_T^{Miss} trigger rate. A noise cut configuration is the set of values used as noise cuts for each of the η regions in L1Calo. Noise cuts are set for trigger towers in the three L1Calo η regions: the barrel, the endcap and the forward detectors, corresponding to the design of the calorimeter system. For this study, the proposal is to derive noise cuts configurations based on a target value of fractional occupancy. A fractional occupancy value is chosen and a noise cut configuration that leads to that target value is generated. The fractional occupancy is defined as the ratio between the number of trigger towers that pass a threshold in E_T over the total number of trigger towers in a given η region, calculated as an average over runs. Each value of fractional occupancy leads to a different noise cut configuration, with lower values of occupancies leading to higher noise cuts.

The tool used to derive the new configurations is named TriggerTowerAnalysis [59]. The tool was developed during LS1 in order to perform dedicated studies to optimise the noise cuts such as the one presented in this paper. One of the features of the tool is to derive different noise cut configurations for each of the η regions considered depending on the expected pile-up and the fractional occupancy required. Monte Carlo simulation is used to derive noise cut

configurations for values of $\langle\mu\rangle$ larger than those reached in 2012. The gradual increase of $\langle\mu\rangle$ during Run-1, shown in figure 3.23, is expected to be repeated during Run-2 given that the instantaneous luminosity will increase. Therefore, values higher than those reached in 2012 are considered in this study.

The aim of this study is to check the effect of these fractional occupancy based noise cut configurations on the efficiency of selecting benchmark physics processes and the L1 E_T^{Miss} trigger rates using data taken in 2012. The decision to use data rather than simulation is taken in order not to rely on the quality of the Monte Carlo simulation of L1Calo. That decision, however, has the consequence that only configurations which increase the thresholds from 2012 settings can be used. Assessing the effect of lower noise cuts on data already taken is not possible. The noise cut configurations evaluated were provided by Dr. Ivana Hristova.

In order to estimate the effect of the new configurations a tool is used to recalculate the L1 E_T^{Miss} for each recorded event: the L1CaloD3PDMaker [60]. The tool recalculates the L1 E_T^{Miss} with each of the occupancy-based noise configurations. Using larger noise cuts, trigger towers with signals smaller than the new noise cuts will not be used in the calculation. The L1 E_T^{Miss} can then drop below the threshold for triggering in some cases. For such an event, the L1 E_T^{Miss} trigger would not have been fired. For this study, the trigger used is L1_XE25. Choosing this trigger is motivated by the fact that it has the lowest threshold in L1 E_T^{Miss} (25 GeV) and is therefore expected to be the largest contribution to the overall L1 E_T^{Miss} trigger rate.

Figures 4.9, 4.10 and 4.11 show the derived configurations for the start of the bunch train for three different values of $\langle\mu\rangle$ (23, 54 and 81) and values of occupancy ranging from 0.01% to 1%. These noise cuts are derived for fixed occupancies for all $\langle\mu\rangle$ values considered. Choosing three different values of $\langle\mu\rangle$ is considered a conservative choice given the yet unknown conditions in Run-2. A $\langle\mu\rangle$ of 23 is expected to reproduce conditions similar to Run-1, whereas $\langle\mu\rangle$ values such as 54 and 81 are expected to be reached during Run-2. As a benchmark, a choice of occupancy of 1% yields approximately the same noise cuts used in the 2012 data taking.

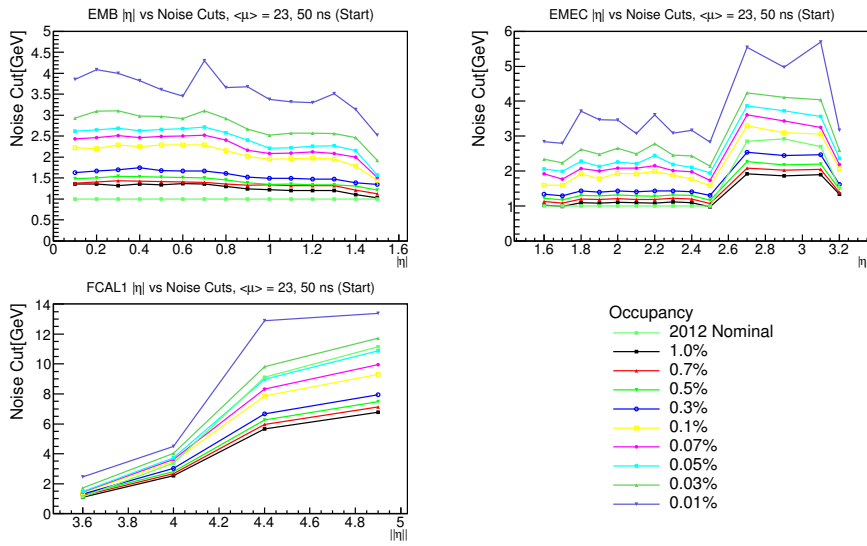


Figure 4.9: Noise cuts optimized for the start of the bunch train for $\langle\mu\rangle=23$ for different values of occupancy vs $|\eta|$ in 3 regions of the electromagnetic calorimeter.

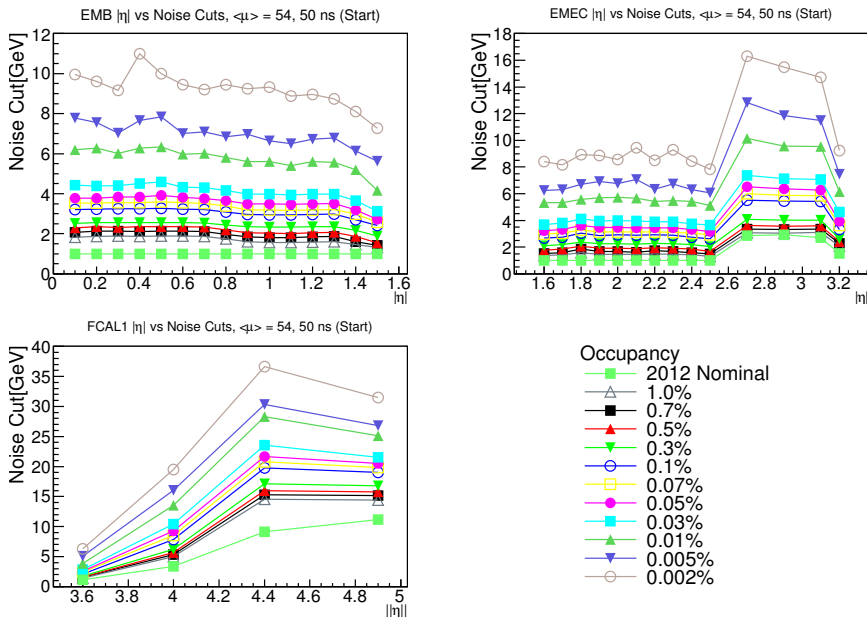


Figure 4.10: Noise cuts optimized for the start of the bunch train for $\langle\mu\rangle=54$ for different values of occupancy vs $|\eta|$ in 3 regions of the electromagnetic calorimeter.

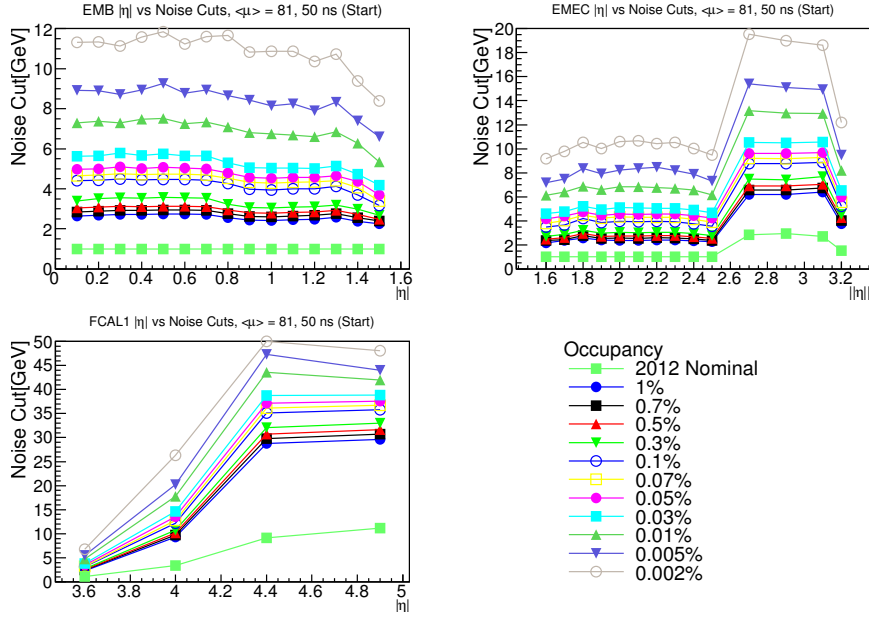


Figure 4.11: Noise cuts optimized for the start of the bunch train for $\langle\mu\rangle=81$ for different values of occupancy vs $|\eta|$ in 3 regions of the electromagnetic calorimeter.

4.5 $W \rightarrow e\nu$ and $t\bar{t}$ selection

The effect of the new occupancy-based noise cuts are tested for well known benchmark physics processes. This section outlines the event selection used to select $W \rightarrow e\nu$ and $t\bar{t}$ processes.

To select $W \rightarrow e\nu$ events the following selection cuts are applied, based on the guidelines set by the ATLAS Standard Model Working Group [61]:

Event Selection

- Single electron trigger EF_e24vhi_medium1 or EF_e60_medium1, which require the presence of an electron with high E_T and fulfilling medium quality requirements.
- GRL
- MET_Ref_Final_Et > 25 GeV to ensure the presence of real E_T^{Miss} in the final state
- Transverse Mass > 40 GeV

Electron Selection

- $E_T > 25$ GeV
- Author 1 or 3
- Tight++Iso
- $|\eta| < 2.47$ excluding $1.37 < |\eta| < 1.52$

The author requirement indicates which algorithm is responsible for reconstructing the electron candidate. An electron fulfilling the “Tight++Iso” requirement makes use of all the particle identification tools currently available in order to avoid jets faking electrons. More information on the requirements outlined can be found in [62], [63] and [64].

The transverse mass (M_T) is defined as:

$$M_T = \sqrt{2 \cdot E_T \cdot E_T^{Miss} \cdot (1 - \cos(\phi - E_T^{Miss\phi}))} \quad (4.1)$$

where $E_T^{Miss\phi}$ is the azimuthal angle of the missing energy, E_T is the electron transverse energy and ϕ is the azimuthal angle of the electron. Events with more than one good electron are vetoed to have a pure sample of $W \rightarrow e\nu$ events. Events with less than 25 GeV in MET_Ref_Final are also vetoed to ensure the presence of real missing energy in the final state. The data used corresponds to Period J3-J4 and J8 of the 2012 data taking with a total integrated luminosity of 1.05 fb^{-1} . The dataset used is “data12_8TeV.periodJ.physics_Egamma.PhysCont.DESD_SGLEL.t0pro14_v01”. Figures 4.12 and 4.13 show the distributions for kinematic variables and the offline topological and final E_T^{Miss} distributions for selected events. For $t\bar{t}$, a sample with a high purity of such events is used. The dataset used is “user.morrisj.data12_8TeV.Allyear.DESDM_EGAMMA.TTBARSkim” and only contains events from the 2012 dataset that fulfill the following criteria:

Event Selection

- At least 4 jets with $p_T > 20$ GeV and $|\eta| < 2.5$
- At least 1 b-jet from any of the ≥ 4 jets above
- Veto events with muons
- MET_Ref_Final_Et after final calibrations > 30 GeV
- $M_T > 30$ GeV

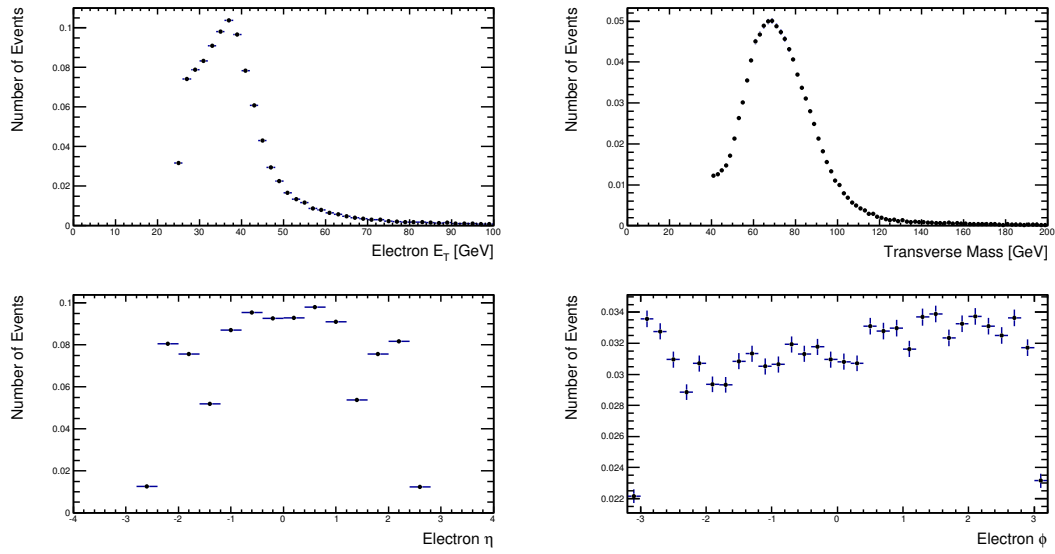


Figure 4.12: Control plots for $W \rightarrow e\nu$ selection. The kinematic variables shown are the electron E_T (top left), transverse mass (top right), η (bottom left) and ϕ (bottom right). All plots are normalised to unity.

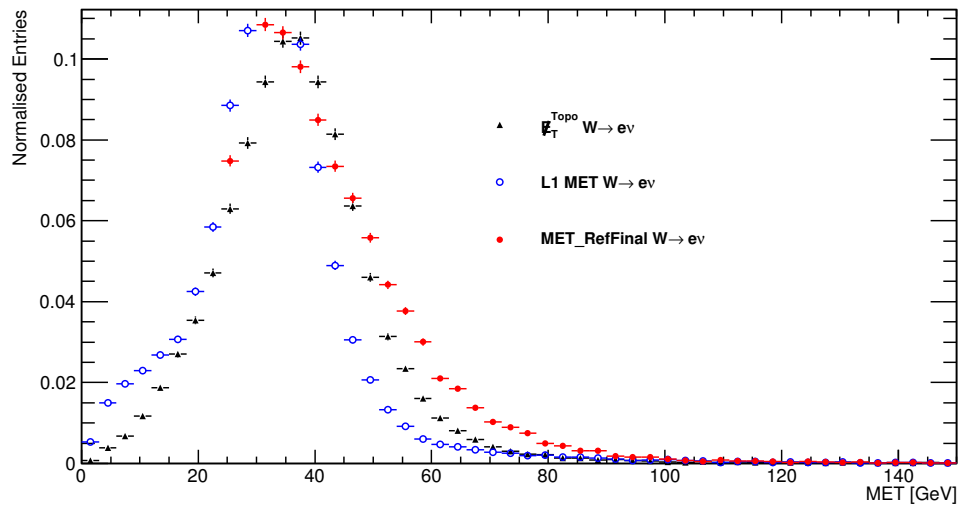


Figure 4.13: $L1 E_T^{\text{Miss}}$, $MET_Reffinal_Et$ and E_T^{Topo} for the $W \rightarrow e\nu$ selection. All plots are normalised to unity.

Electron Selection

- $E_T > 25$ GeV

The E_T^{Miss} calculation for $t\bar{t}$ events uses the MET_Ref_Final as a basis to calculate the final E_T^{Miss} used for selection. The package “TopD3PDCorrections” [65] contains tools to recalculate the MET based on final calibrated objects specially used for $t\bar{t}$ events. Figures 4.14 and 4.15 show the kinematic variables and the offline topological and final E_T^{Miss} distributions for events fulfilling the criteria outlined. The MET_Ref_Final_Et distribution is shown before all final calibrations are applied.

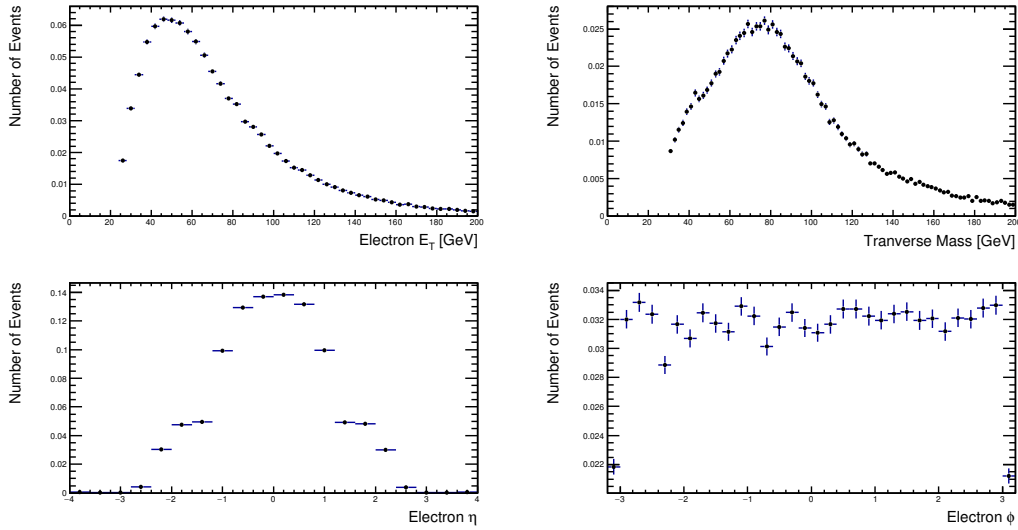


Figure 4.14: Control plots for $t\bar{t}$ selection. The kinematic variables shown are the electron E_T (top left), transverse mass (top right), η (bottom left) and ϕ (bottom right). All plots are normalised to unity.

4.6 Rate and efficiency definition

For this study, the L1 E_T^{Miss} trigger rate is defined as the number of events by which the lowest L1 E_T^{Miss} trigger threshold (25 GeV) is exceeded over a given period of time. A calculation of the total rate is not important for this study. The focus is placed on the relative change between different configurations. Since this study uses the full 2012 dataset the relative rate is then the ratio between the number of events that exceed the lowest L1 E_T^{Miss} trigger for a given configuration and that obtained with the 2012 settings. Zero Bias data is used to estimate the L1_XE25 rate for each configuration. Zero Bias triggers are activated one revolution of

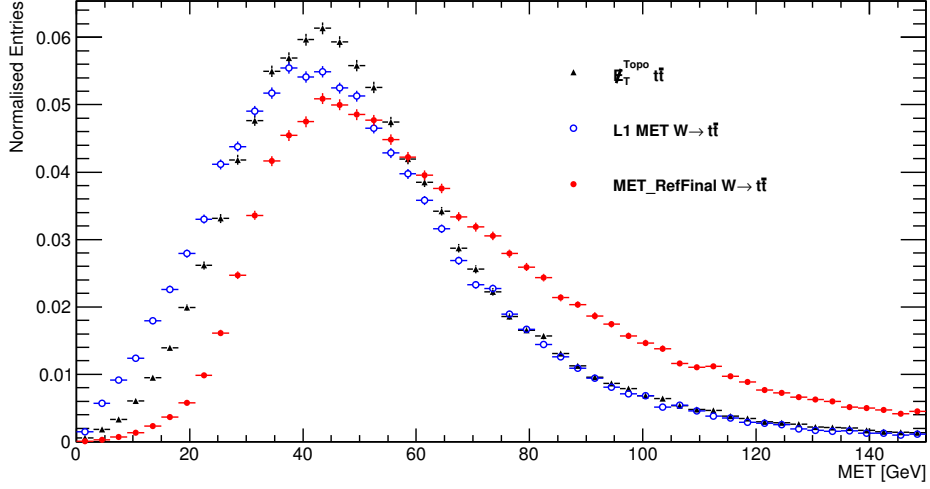


Figure 4.15: L1 E_T^{Miss} , MET_RefFinal_Et and E_T^{Topo} for the $t\bar{t}$ selection. All plots are normalised to unity.

the LHC beam after any physics trigger has been activated. The result is data free of any bias towards any physics process. The dataset used is named “data12.8TeV.AllYear.physics ZeroBias.merge.ESD.r4065_p1278” and contains all of the 2012 Zero Bias data recorded by the ATLAS detector. Figure 4.16 shows the L1 E_T^{Miss} distribution for Zero Bias data. As expected, only a small fraction of events have L1 $E_T^{\text{Miss}} > 25$ GeV. Figure 4.17 shows the number of L1_XE25 against counts against decreasing values of fractional occupancy. As expected, the rate of the L1 E_T^{Miss} trigger is reduced as the fractional occupancy decreases, as lower values of fractional occupancy lead to higher noise cuts.

The E_T^{Miss} trigger efficiency is defined as a linear fit to the ratio between the distribution of the offline topological E_T^{Miss} for selected events exceeding the 25 GeV threshold in L1 E_T^{Miss} (e.g. events that trigger L1_XE25) and the overall topological E_T^{Miss} distribution for selected events (without requirements on the L1 E_T^{Miss}). Figure 4.18 shows the L1_XE25 efficiency against the offline topological E_T^{Miss} . The non-zero values of efficiency at low E_T^{Miss} is evidence of poor detector resolution. The metric chosen to evaluate changes in L1_XE25 efficiency is the average value of the L1_XE25 efficiency for offline topological $E_T^{\text{Miss}} > 40$ GeV. This definition is chosen because of its advantages:

- Not susceptible to statistical fluctuations
- Valid for a wide range of noise cuts

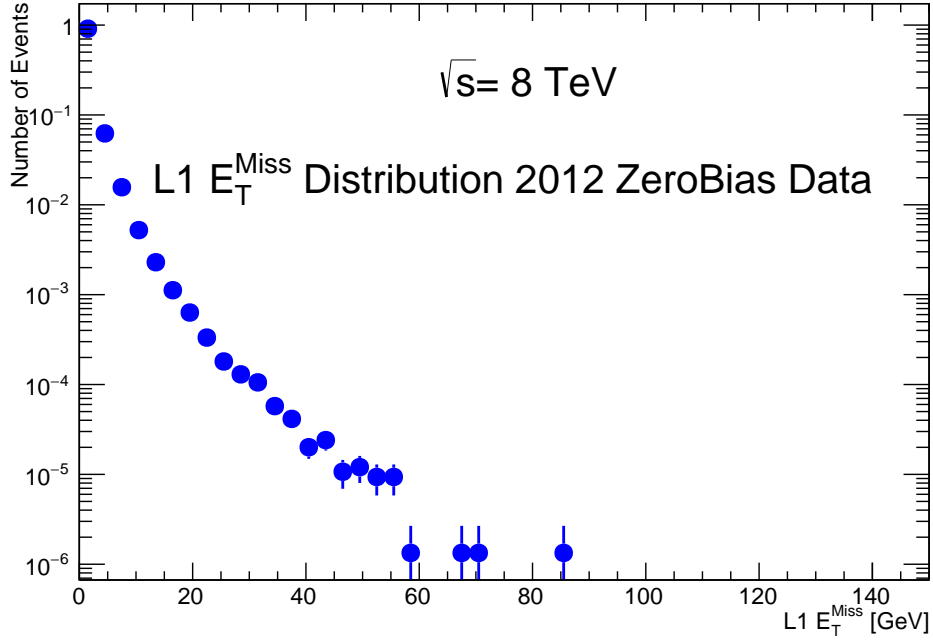


Figure 4.16: L1 E_T^{Miss} distribution for Zero Bias data from the 2012 data-taking. The plot is normalised to unity.

- Robust and easy to implement
- Easy to assess changes between different configurations

In order to validate the use of higher noise cuts during the 2012 data taking the effect of the new noise configurations on the efficiency of selecting $W \rightarrow e\nu$ processes was checked, as shown in figure 4.4. However, different physics processes can be affected differently by increasing noise cuts. For this study, in an effort to be more comprehensive, the efficiency of two benchmark physics processes is evaluated: $W \rightarrow e\nu$ and $t\bar{t}$, as outlined in the previous section. The choice of these two processes is motivated by the presence of real missing energy, high cross sections and their different topologies: $W \rightarrow e\nu$ contains E_T^{Miss} in the form of a neutrino, whereas a $t\bar{t}$ event, with the top quark subsequent semileptonic and hadronic decays, contains a large quantity of jets as well as neutrinos in the final state.

Figures 4.19 and 4.20 show the L1_XE25 efficiency against the offline topological E_T^{Miss} for the $W \rightarrow e\nu$ and $t\bar{t}$ selections respectively for a few benchmark values of occupancy and expected $\langle\mu\rangle$. Due to the different event topologies the two figures look different at low

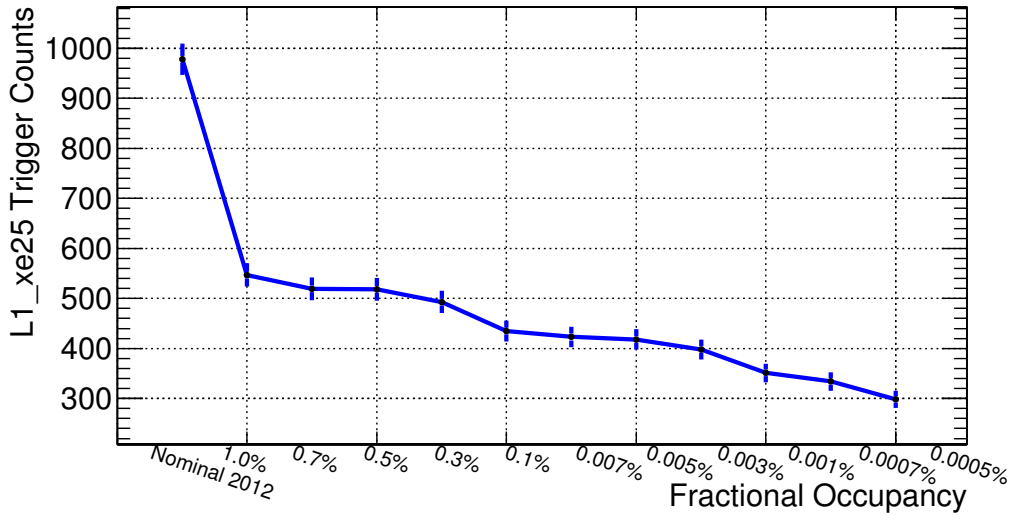


Figure 4.17: Number of L1_XE25 counts against fractional occupancy using Zero Bias data from the 2012 data-taking.

missing energy. As shown in the previous section, a $t\bar{t}$ event is required to have at least 4 jets with $p_T > 25$ GeV after all final calibrations. The corresponding L1 objects do not include calibrations and hence their L1 p_T is quite different. As shown in figure 4.21, the transverse momentum measured at L1 consistently undershoots that measured after all final calibrations are applied. Figure 4.22 shows the E_T^{Miss} resolution by comparing the offline topological E_T^{Miss} and the L1 E_T^{Miss} . As expected, the missing energy resolution of the $t\bar{t}$ selection is worse due to the presence of jets. The same effect can be observed in figure 4.23, which shows that the missing energy resolution of $W \rightarrow e\nu$ events gets worse as the jet multiplicity increases. This low resolution is however not expected to affect the study since the metric chosen is the average efficiency for $E_T^{\text{Miss}} > 40$ GeV.

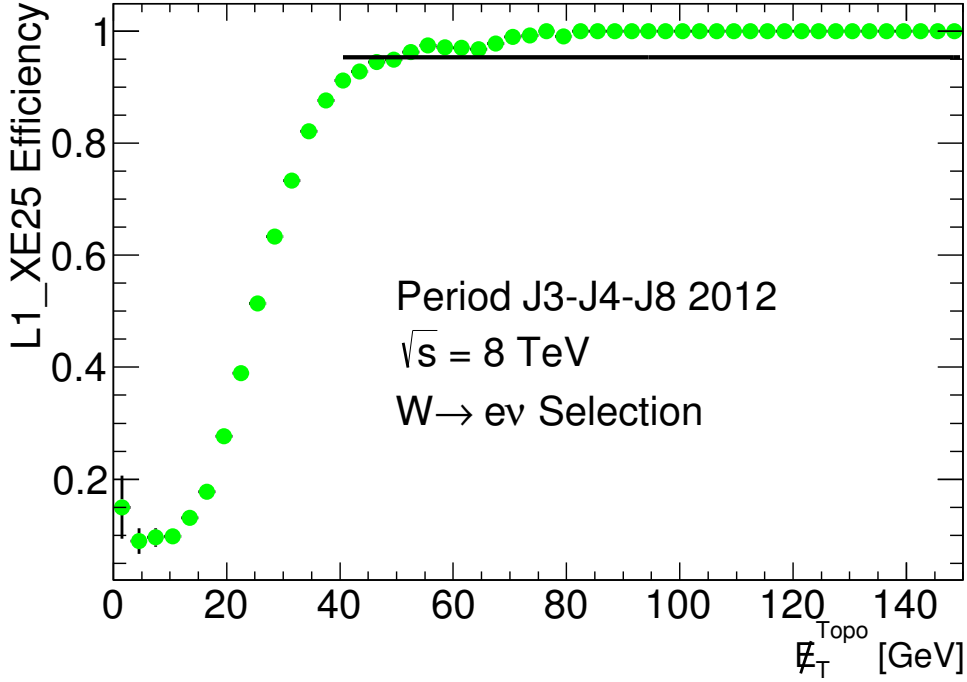


Figure 4.18: The efficiency of the L1 E_T^{Miss} trigger L1_XE25 efficiency for a $W \rightarrow e\nu$ selection is shown against the offline topological E_T^{Miss} . The average efficiency for $E_T^{\text{Miss}} > 40$ GeV is marked in black.

4.7 Method

The method followed is summarized in a few steps:

- New configurations are derived using the tool TriggerTowerAnalysis based on fractional occupancy and expected $\langle\mu\rangle$.
- The effect of the new noise cut configurations on the L1 E_T^{Miss} is calculated using the package L1CaloD3PDMaker.
- The effect of the new noise cut configurations on the efficiency of selecting benchmark physics processes is evaluated relative to that of the 2012 settings.
- The rate of the lowest L1 E_T^{Miss} trigger, L1_XE25, is evaluated relative to 2012 settings for each noise cut configuration using Zero Bias data.
- The choice of a particular set of thresholds will be determined by the interplay between the L1 E_T^{Miss} trigger rate and the efficiency of selecting the benchmark physics

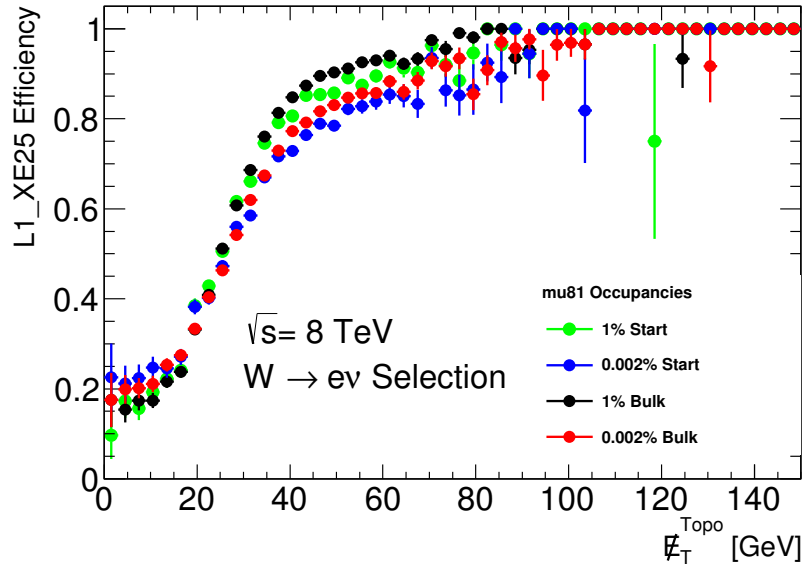


Figure 4.19: L1_XE25 efficiency for the lowest and highest values of occupancy used for the $W \rightarrow e\nu$ selection against the offline topological E_T^{Miss} .

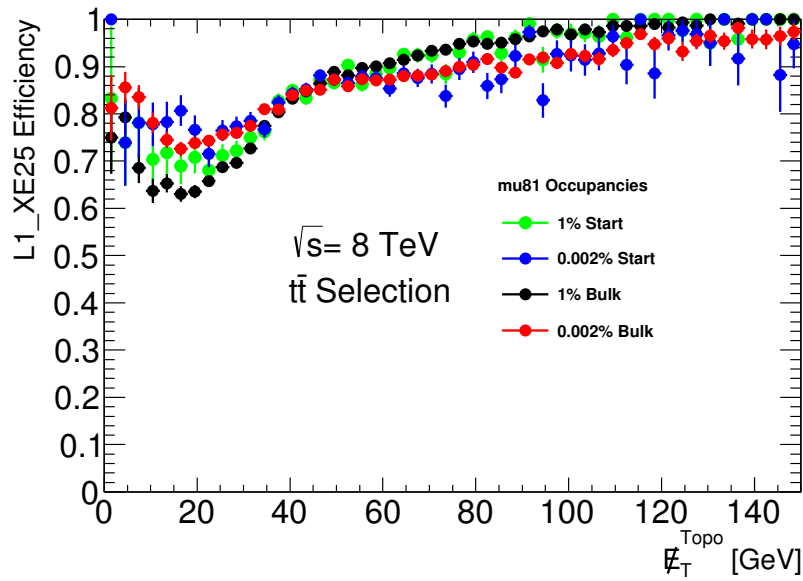


Figure 4.20: L1_XE25 efficiency for the lowest and highest values of occupancy used for the $t\bar{t}$ selection against the offline topological E_T^{Miss} .

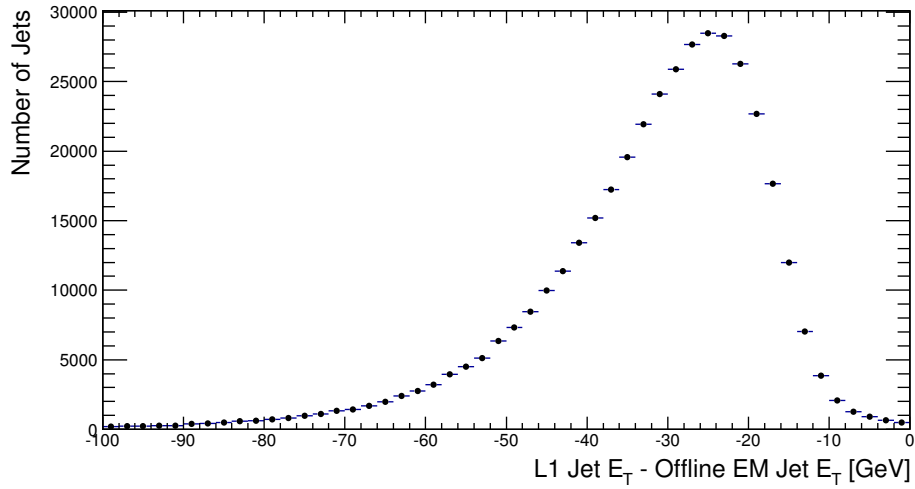


Figure 4.21: The E_T resolution of offline calibrated jets against the L1 jets is shown. The L1 jets consistently undershoot the E_T of the final calibrated jets.

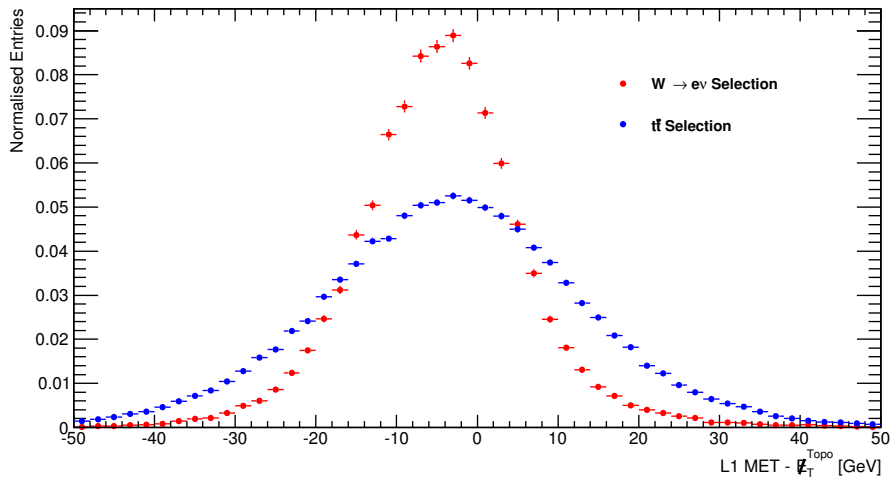


Figure 4.22: The MET resolution is shown by subtracting the offline topological E_T^{Miss} from the L1 E_T^{Miss} for both the $W \rightarrow e\nu$ and $t\bar{t}$ selection.

processes considered. An ideal scenario would involve a value of occupancy which reduces the L1 E_T^{Miss} trigger rate without losing physics efficiency.

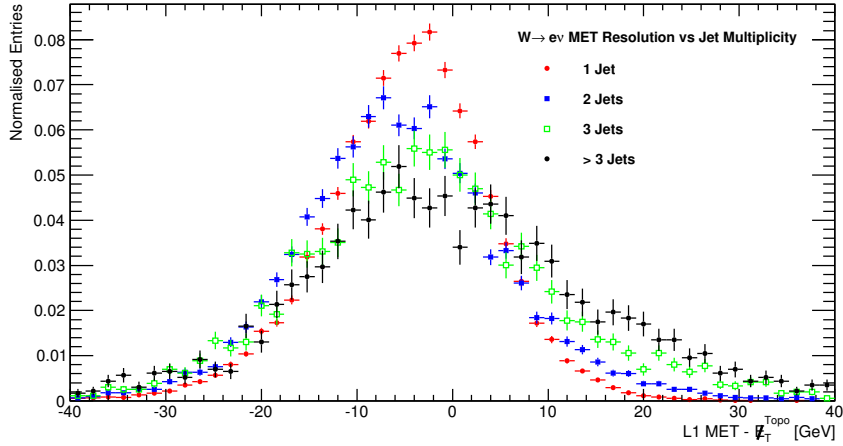


Figure 4.23: The E_T^{Miss} resolution is shown for the $W \rightarrow e\nu$ selection for different jet multiplicities.

4.8 Results

The results are presented in terms of the efficiency and rate relative to the nominal 2012 thresholds for the two different cases as proposed in figure 4.8: start and bulk of the bunch train, for the two physics processes investigated: $W \rightarrow e\nu$ and $t\bar{t}$ production.

Figures 4.24 and 4.25 show the results for the start of the bunch train for the $W \rightarrow e\nu$ and $t\bar{t}$ processes respectively. Given the increased activity in the start of the bunch train due to the shape of the LAr pulse, the noise cuts at the start of the bunch train are larger than for the bulk for the same occupancy values. The efficiency is then expected to have a steeper fall for the start configurations. Increasing the value of $\langle\mu\rangle$ also requires increasing the noise cuts to maintain the same values of occupancy. For the $\langle\mu\rangle = 23$ and 54 cases, the results suggest that it is possible to increase the noise cuts and reduce the L1_XE25 trigger rate to about 50% of its 2012 value, while losing less than 3% in physics efficiency. However, the higher values of $\langle\mu\rangle$ also provide a warning: increasing the noise cuts beyond a fractional occupancy of about 0.07% yields a quick drop in efficiency without reducing the L1_XE25 rate, hence showing that there are limits to this strategy. For the most extreme case, $\langle\mu\rangle = 81$, larger values of occupancy could be considered to find a better working point. However, that was not possible for the scope of this study, as further increasing the occupancy would reduce the noise cuts in some regions below the 2012 noise cuts. It should be noted that for the case $\langle\mu\rangle = 23$ less fractional occupancies were evaluated given that, for higher values of fractional occupancy, the noise cuts in some regions dropped below that of the 2012 settings. No significant differences are observed in the behaviour of the two physics processes considered.

Figures 4.26 and 4.27 show the results for the bulk of the bunch train for the $W \rightarrow e\nu$ and $t\bar{t}$ processes respectively. The results for the two physics processes considered follow the same pattern: the results obtained do not show a $\langle\mu\rangle$ dependence. Given the decreased activity with respect to the start of the bunch train, the difference between the thresholds used for the three pile-up scenarios considered for the same values of occupancy is not as large as for the start, and hence the efficiency decrease is not as steep for the bulk case.

The difference in behaviour between the two cases considered (start and bulk) suggest that they should be optimised separately.

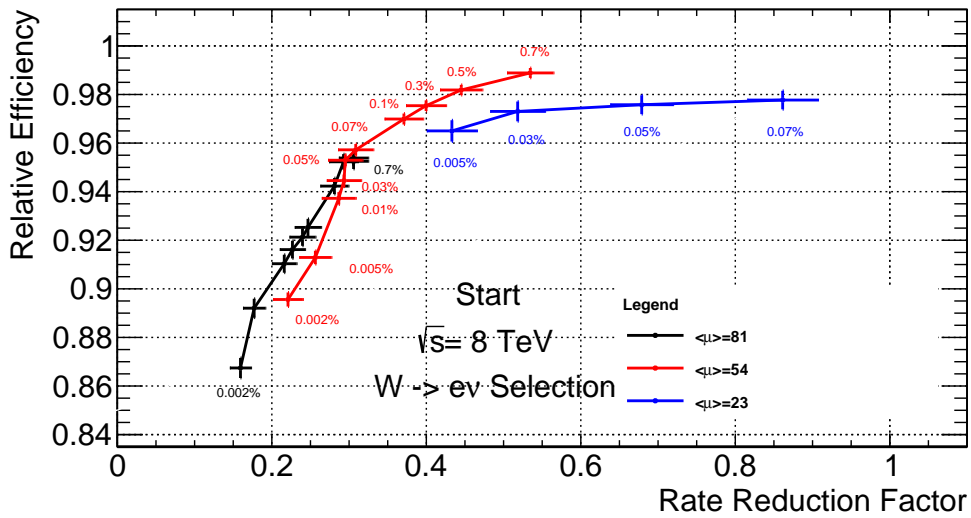


Figure 4.24: Relative efficiency of selecting $W \rightarrow e\nu$ vs Rate reduction factor with respect to the 2012 settings for the start of the bunch train. The occupancy values are next to each point.

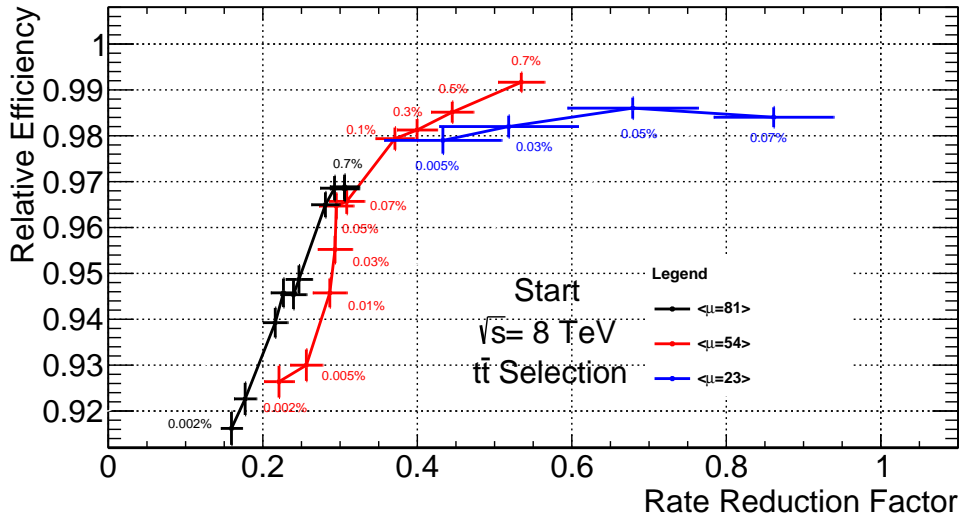


Figure 4.25: Relative efficiency of selecting $t\bar{t}$ vs Rate reduction factor with respect to the 2012 settings for the start of the bunch train. The occupancy values are next to each point.

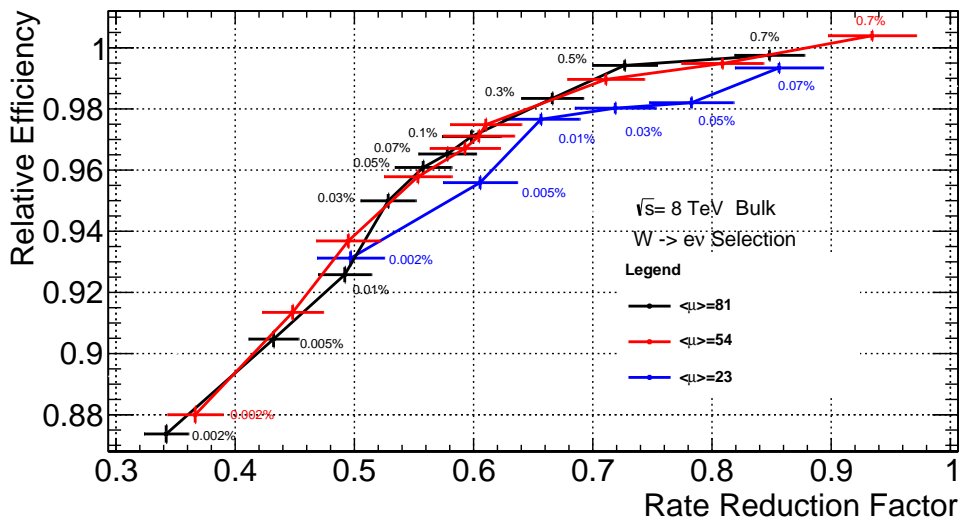


Figure 4.26: Relative efficiency of selecting $W \rightarrow e\nu$ vs Rate reduction factor with respect to the 2012 settings for the bulk of the bunch train. The occupancy values are next to each point.

4.9 Conclusion

The different behaviours for the start and the bulk of the bunch train suggest that setting BCID dependent noise cuts is a valid approach to control the L1 E_T^{Miss} trigger rate. That is

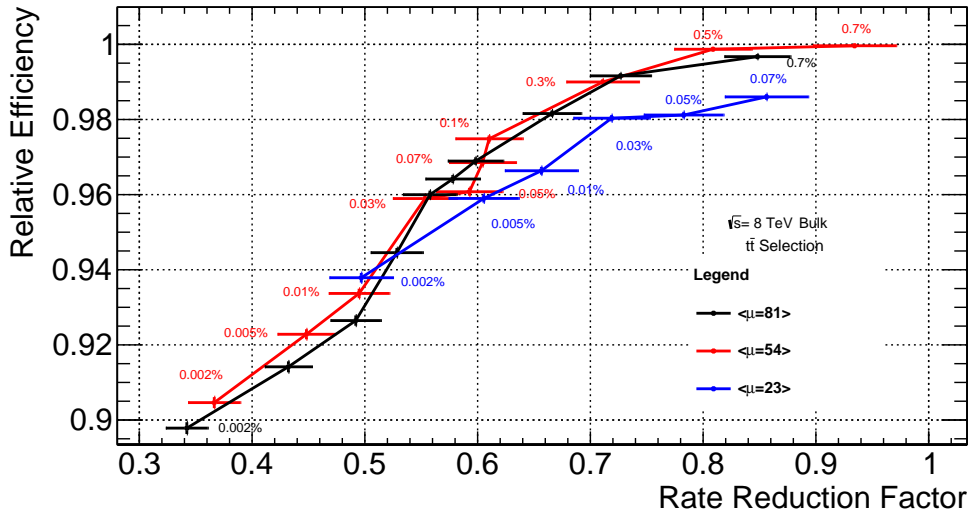


Figure 4.27: Relative efficiency of selecting $t\bar{t}$ vs Rate reduction factor with respect to the 2012 settings for the bulk of the bunch train. The occupancy values are next to each point.

specially relevant for Run-2, where the increase in centre-of-mass energy and the decrease in bunch crossing spacing will increase the instantaneous luminosity and the average number of interactions per bunch crossing. In such conditions, the L1 E_T^{Miss} trigger rate at the start of the bunch train can become quite problematic due to the increased activity with respect to the rest of the bunch train. Careful optimization will be required and treating the start and the bulk (as defined in this chapter) of the bunch train separately is shown to be a sensible choice.

The results obtained suggest that it is still possible to increase the thresholds to reduce the L1 E_T^{Miss} trigger rate without major losses in physics efficiency. However, and similarly to what was observed in Run-1 with noise cut increase in the forward regions, this approach has limitations: for the lowest values of fractional occupancy the L1 E_T^{Miss} trigger rate is only marginally reduced while the physics efficiency rapidly decreases. This shows that without careful optimisation the choice of noise cuts can damage the physics efficiency while not significantly decreasing the rate of L1 E_T^{Miss} triggers. The choice of an optimal working point should take these factors into account.

Since Run-2 conditions are still unknown, another strategy to reduce the L1 E_T^{Miss} trigger rate would be to increase the minimum value of E_T^{Miss} that L1Calo triggers on. However, this could reduce the efficiency of selecting physics processes such as the ones considered in this study. Investigating the possibility of increasing the trigger thresholds would be a good complement to the study presented here and would help decide the best strategy to control the L1 E_T^{Miss} trigger rate during Run-2.

5 Black Hole Event Generators

Black hole event generators were available as early as 2001. The first example is TRUENOIR, developed by Greg Landsberg and based on the model for semiclassical black hole models presented in [28]. The model was relatively simple: it did not take into account black hole angular momentum or charge and relied on the democratic nature of black hole decays. CHARYBDIS [66] and CATFISH [67] were developed in 2003 and 2006 respectively to simulate the production of semiclassical black holes including gray-body factors¹⁴ and, exclusive to CATFISH at the time, the possibility of gravitational energy loss during the formation of the black hole. More recently, BlackMax [68] included all of the already presented features including four different models for black hole production: Schwarzschild and rotating semiclassical black holes, Schwarzschild black holes including brane tension and a model for quantum black hole two particle decay based on [27]. QBH [69] is an event generator exclusively dedicated to the quantum regime: the generator simulates quantum black hole production and decay to two particle final states, including conservation (or violation) of symmetries such as SU(3) and U(1). All of these generators interact with Pythia [70] or Herwig [71] in order to simulate the underlying event, the simulation of all the particles involved in the high energy collision in full detail (also known as the parton shower). The author has worked with both BlackMax and QBH and a short description of both simulators is provided in this section.

5.1 BlackMax

BlackMax is a black hole event generator which simulates the experimental signature of semi-classical and quantum black hole production, evolution and decay at particle colliders¹⁵. The source code can be found in [72] and a comprehensive manual can be found in [73]. The generator offers the user freedom in terms of choosing the parameter space, such as the number of extra dimensions, the value of the extra-dimensional Planck Mass or the minimum and maximum mass of the black hole. Physical choices such as conservation of baryon or lepton number can be switched on or off. The decay of black holes is also carefully considered. Gray-body factors are included in the calculations. Those factors depend on the properties of the particle the black hole decays to as well as the parameter choice: number of extra dimensions, input parton distribution function, extradimensional Planck Mass and symmetries conserved among others. A full list of the parameter choice offered by BlackMax can be found in appendix F.

BlackMax includes four different models for black hole production and decay. However,

¹⁴Gray body factors account for the probability of a particular decay mode.

¹⁵BlackMax can be configured to simulate Proton-Proton, electron-positron and proton-antiproton collisions.

the author has mainly worked with two of these models: the rotating black hole and the two particle model. The rotating black hole considers the formation of semi-classical black holes with non-zero angular momentum. At the LHC protons collide with a non-zero impact parameter, it is hence likely that the resulting black hole from a collision between partons will have a non-zero angular momentum. The main difference between a rotating black hole and its Schwarzschild counterpart is that the former forms a region of spacetime called the ergosphere, shown in figure 5.1. The ergosphere is a region formed between the limit of stationarity¹⁶ and the event horizon which rotates at very high angular speeds. For more information on the classical treatment of a rotating black hole, see [74]. The two particle model considers the production of quantum black holes decaying to two particle final states, as proposed in [27]. Due to the lack of knowledge on the topic of Quantum Gravity, the emission spectrum of the quantum black holes is taken to be the emission spectrum of the semiclassical Schwarzschild black hole.

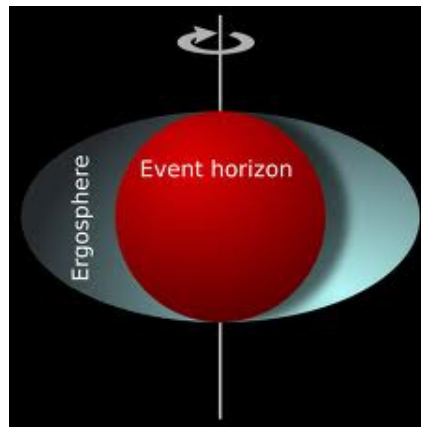


Figure 5.1: A rotating black hole and its ergosphere [75]

Figure 5.2 shows a comparison between the output produced by BlackMax for each of the models mentioned for a number of variables such as the number of particles produced, the black hole mass per event and the PDGID of the particles produced. A centre-of-mass energy of 14 TeV and an extradimensional Planck Scale of 4.0 TeV is chosen. As expected, the main difference between the models is the number of particles produced in the final state. The two particle model produces five particles per event in the final state, including three gravitons: two of them are emitted in the extra dimensions while the third one is introduced by hand to ensure momentum conservation momentum in all dimensions. The decay of the semiclassical rotating black hole produces close to eleven final state particles per event. Due to this difference, the average momentum carried by each particle is larger in the two particle model.

¹⁶An object reaching the limit of stationarity would be forced to rotate with the black hole.

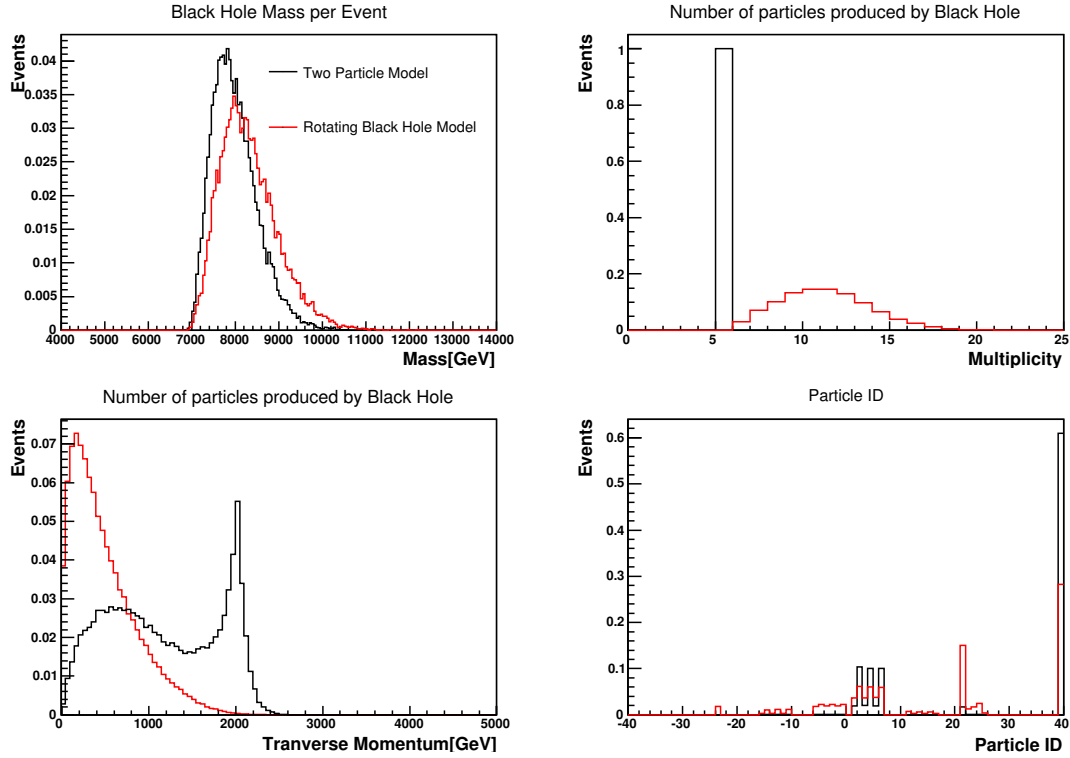


Figure 5.2: Comparison of the output of the BlackMax rotating black hole model and the two particle model for a number of variables: black hole mass (top left), total number of particles produced by the black hole decay (top right), particle transverse momentum (bottom left) and PDGID of the particles produced (bottom right). All histograms are normalised to unity.

The BlackMax source code is written in C++ and interfaces with Pythia according to the Les Houches Accord [76]. The version of the code used to produce the figures shown in this section is 2.0.2.

5.2 QBH

QBH is a black hole event generator with a similar structure to BlackMax, written in C++ and interacting with Pythia8 for initial and final state radiation, parton shower and hadronisation using the Les Houches Accord [69]. The source code can be found in [77]. The main difference with the two particle model BlackMax is that the generator is based on the model proposed in [29]. Therefore, the decay of a quantum black hole is assumed to be a democratic decay to SM particles. The main advantage of QBH is that it allows the user to generate

quantum black holes according to a particular choice of initial state particles and their spin configuration, giving rise to a quantum black hole with a particular charge and spin. This is particularly useful in the context of the search presented in this paper, as quantum black holes can only decay to an opposite sign dilepton final state if the quantum black hole has zero charge and spin, as shown in table 2.1.

6 Data and Monte Carlo samples

This thesis presents searches for both quantum black holes (QBH) and ADD large extra dimensions (ADD LED) in the opposite charge dimuon channel. These two searches were part of separate analyses: the quantum black hole search is published in [78], a search for resonant phenomena in both the opposite sign dielectron and dimuon channels, whereas the search for large ADD extra dimensions is published in [79], a search for non-resonant phenomena in the same channels. The two analyses have a large degree of overlap and, unless specified, the content presented in this chapter and the following one applies to both searches. Throughout this chapter and the ones that follow the term generator (or Born) level will be used to refer to the value of the relevant variable before any Final State Radiation, as generated by the Monte Carlo simulator in use. Variables at reconstructed level refer to the value of variables after undergoing reconstruction by the ATLAS detector.

All signal and background processes are estimated using simulated Monte Carlo samples generated in the ATLAS offline software framework called ATHENA [80], based on the GEANT4 particle simulation [81] given that the ATLAS detector geometry is constructed in that format. The aim is to accurately simulate the interaction of particles with the ATLAS detector. The simulation is divided in three steps [80]:

- Event generation and decays.
- Interaction with the ATLAS detector.
- Digitization of signals from particles into outputs in identical format to the ATLAS readout.

The samples used in this paper are generated with ATHENA release 17. The specific generators used to simulate each individual process are outlined in this chapter. The Monte Carlo samples are used in DPD format, the same as data. Given that the SM background processes are well understood electroweak processes, no data-driven estimates are used as Monte Carlo simulation is expected to correctly model the background processes considered.

The luminosity of all Monte Carlo samples is normalized to the ratio between data and the sum of all SM background Monte Carlo after applying selection cuts (outlined in section 7.2) in the Z-peak region, defined as $80 < m_{\mu\mu} < 120$ GeV. The luminosity of each Monte Carlo sample can be calculated using the following equation:

$$\mathcal{L} = \frac{N_{evt}}{\sigma \cdot BR \cdot \epsilon_f} \quad (6.1)$$

where N_{evt} is the number of generated events, $\sigma \cdot BR$ is the cross section times branching ratio of the relevant process and ϵ_f is the filter efficiency, defined as the ratio of generated events which pass the filter applied over the total number of generated events. A filter can be requirements in generator level invariant mass, lepton transverse momentum or η . Such requirements are meant to discard events that would not pass the event selection cuts used in this search. After normalizing the event yields to known luminosity from data, an extra normalisation is applied to account for differences in the Z -peak region between data and Monte Carlo. Normalising to the Z -peak region has the advantage of making the analysis insensitive to mass-independent systematic uncertainties. All Monte Carlo samples are normalised to the highest order theoretical cross section prediction available in QCD and Electro-Weak related processes.

6.1 Data

Only data present in the Good Runs List (GRL) is used for analysis. The data analysed was collected by the ATLAS detector during 2012 at a centre of mass energy of 8 TeV. After using the following GRL from the Muon Combined Performance (MCP) Working Group [82]: data12_8TeV.periodAllYear_DetStatus-v61-pro14-02_DQDefects-00-01-00_PHYS_Combined_Perf_Muon_Muon.xml.

The total integrated luminosity is of 20.5 fb^{-1} for the trigger EF_mu24i_tight¹⁷.

6.2 Signal samples

This section presents the Monte Carlo samples used to estimate the ADD LED and quantum black hole signal processes.

6.2.1 ADD Large Extra Dimensions

The ADD LED signal samples are generated with Sherpa [84] at NLO with the CT10 [85] PDF set. The parton shower and hadronisation is also simulated by Sherpa. Samples are generated for both the GRW and HLZ $n = 2$ formalisms for a number of benchmark M_S (eq. 2.26) values¹⁸. Both signal ADD LED and Drell-Yan processes are included in the

¹⁷As calculated by the ATLAS luminosity calculator [83]

¹⁸The GRW samples can be reweighted to other formalisms such as Hewett and HLZ $n = 3 - 7$. However, for HLZ $n = 2$, as shown in equation 2.28, the conversion depends directly on the dilepton invariant mass and hence the conversion cannot be performed. Therefore, dedicated samples are produced for that case.

samples. As explained in chapter 2, there is interference between the Drell-Yan and BSM physics processes. In order to estimate the pure signal contribution, a sample with $M_S = 50$ TeV was produced. For the dimuon invariant mass range this search focuses on (0.08-4.5 TeV), such a high value of M_S is equivalent to a pure Drell-Yan sample generated with Sherpa. The pure ADD signal event yield is then obtained by subtracting the contribution of the $M_S = 50$ TeV sample from the lower M_S samples outlined in table 6.1.

Table 6.1: Sherpa NLO cross-sections ($\sigma \cdot BR(G^* \rightarrow \mu\mu)$) for benchmark M_S values used in the ADD model search for the GRW formalism. Values are given for the true $m_{\mu\mu}$ range of each generated MC sample. For each mass range considered 10000 events were generated [22].

GRW Formalism	$\sigma \cdot BR$ [fb]		Signature
	True $m_{\mu\mu}$ sample range [TeV]		
M_S [TeV]	0.6 – 1.2	> 1.2	
3.00	16.1	2.7	$G^*/\gamma^*/Z \rightarrow \mu\mu$
3.25	16.1	1.8	$G^*/\gamma^*/Z \rightarrow \mu\mu$
3.50	16.0	1.3	$G^*/\gamma^*/Z \rightarrow \mu\mu$
3.75	15.5	0.9	$G^*/\gamma^*/Z \rightarrow \mu\mu$
4.00	15.6	0.8	$G^*/\gamma^*/Z \rightarrow \mu\mu$
4.75	15.7	0.6	$G^*/\gamma^*/Z \rightarrow \mu\mu$
50.0	20.6	0.5	$G^*/\gamma^*/Z \rightarrow \mu\mu$

New phenomenon produced by the existence of ADD LED is expected to appear as broad deviations from SM expectation in the dilepton invariant mass spectrum. The model cut-off is at $m_{\mu\mu}=M_S$, since the model is no longer valid for dimuon invariant masses larger than the string scale. While the cutoff at M_S is unphysical it should be noted that, for dimuon invariant masses exceeding the string scale, the onset of Quantum Gravity would take place and some new physics could be observed. The nature of this new physics is yet unknown. One of the proposals for the region beyond the string scale is that explained in section 2.4, proposing that black holes of a semiclassical or quantum nature could be formed. Figure 6.1 shows the dimuon invariant mass spectrum for a few benchmark values of M_S ranging from 3.0 to 4.75 TeV, with the $M_S = 50$ TeV sample shown for comparison. As already noted, for an M_S of 50 TeV no excess from SM expectation is expected for the mass range considered and it is hence shown for comparison. The ADD LED samples are produced only for dimuon masses larger than 120 GeV as no new physics is expected in the Z-peak region.

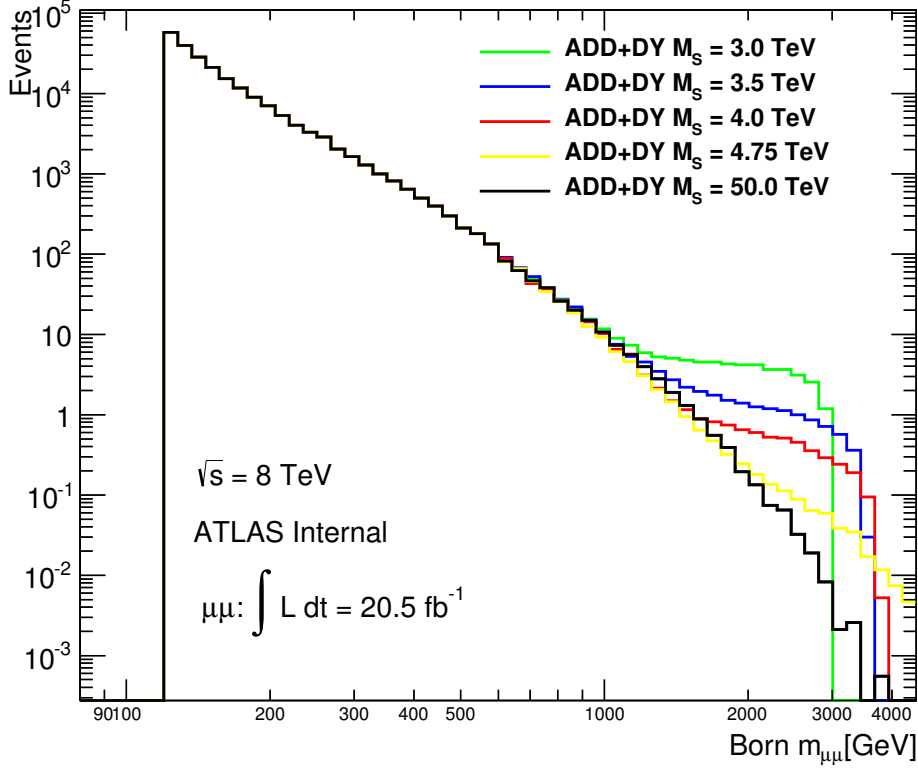


Figure 6.1: Born Drell-Yan(DY)+ADD dimuon mass distribution for the ADD model in the GRW formalism normalised to 20.5 fb^{-1} . The cut-off at M_S is included since the model is no longer valid for dimuon invariant masses larger than the string scale.

6.2.2 Quantum Black Hole

A quantum black hole with zero electric charge and spin could decay to an opposite charge dimuon final state, as explained in section 2.4.2. That would produce an excess of dimuon final state events over SM expectations if the threshold for forming quantum black holes (M_{th}) is reached. For the specific model considered for this search, it is expected that a continuous spectrum would be formed with quantum black holes masses ranging from M_{th} to $3 - 5 \cdot M_{th}$, when it is expected that thermal black holes start being formed. For the samples produced a conservative $3 \cdot M_{th}$ is chosen as a mass limit for a quantum black hole. Figure 6.2 shows a comparison of the generator-level Drell-Yan distributions with the expected distribution for ADD QBH signal processes for various benchmark M_{th} values. These signal processes are

expected to show deviations from SM expectations for dimuon masses larger than M_{th} .

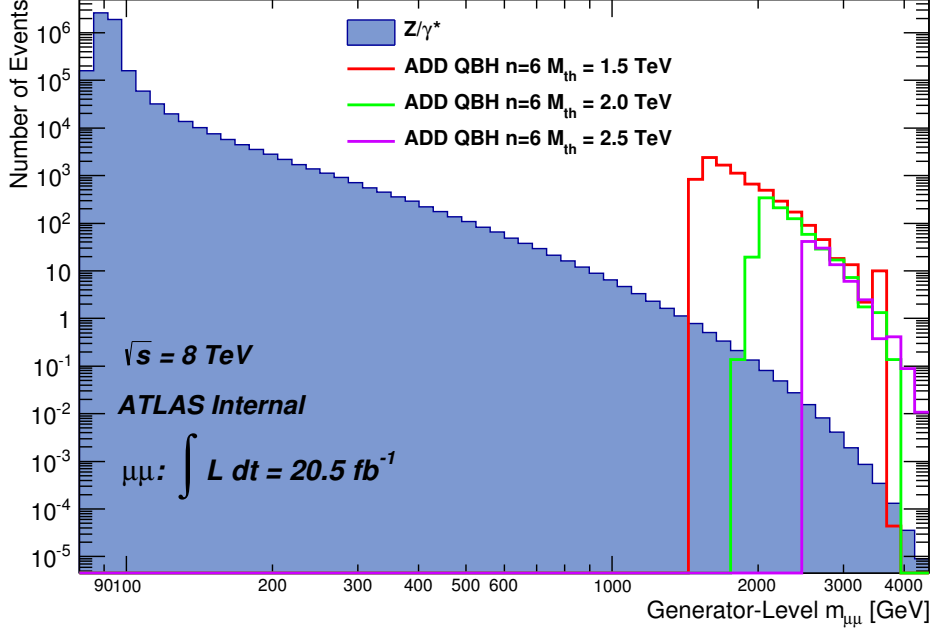


Figure 6.2: A comparison between generator-level Drell-Yan and generator-level QBH processes for various M_{th} values is shown.

The quantum black hole signal samples are simulated with the black hole event generator QBH [69] using the MSTW2008LO PDF [86], while Pythia8 [70] provides simulation for the parton shower and hadronisation. QBH allows the user to choose the value of parameters such as the minimum mass of the quantum black hole or the number of extra dimensions and its model (ADD or Randall-Sundrum). Symmetry restrictions can also be chosen in order to simulate different Quantum Gravity scenarios. Each sample is generated with a fixed value for the extra-dimensional Planck Mass. Samples were generated separately for the case of ADD and Randall-Sundrum extra dimensions with the extra-dimensional Planck mass ranging from 0.5 TeV to 4.0 TeV. The samples used and their $\sigma \cdot BR(QBH \rightarrow \mu^+ \mu^-)$ are outlined in table 6.2. A full list of the choice of parameters used to generate the samples can be found in appendix G.

Table 6.2: QBH samples for the ADD $n=6$ extra-dimension formalism used in the dimuon channel for the analysis presented in [78]. The first column shows the value of M_{th} , the second column the internal ATLAS run number and the third the QBH generator cross section times branching ratio to a dimuon final state. For each M_{th} value 10000 events were generated [87].

$M_{th}[\text{TeV}]$	Dataset ID	$\sigma Br[\text{pb}]$	Signature
0.5	158485	$4.12 \cdot 10^2$	QBH $\rightarrow \mu\mu$
1.0	158486	$1.13 \cdot 10^1$	QBH $\rightarrow \mu\mu$
1.5	158487	$8.70 \cdot 10^{-1}$	QBH $\rightarrow \mu\mu$
2.0	158488	$9.83 \cdot 10^{-2}$	QBH $\rightarrow \mu\mu$
2.5	158489	$1.27 \cdot 10^{-3}$	QBH $\rightarrow \mu\mu$
3.0	158490	$1.83 \cdot 10^{-4}$	QBH $\rightarrow \mu\mu$
3.5	158491	$2.55 \cdot 10^{-5}$	QBH $\rightarrow \mu\mu$
4.0	158492	$3.22 \cdot 10^{-6}$	QBH $\rightarrow \mu\mu$

6.3 Background samples

SM background processes include irreducible backgrounds such as Drell-Yan and photon-induced dilepton production and reducible backgrounds such as top quark processes and diboson production. These backgrounds are estimated through the use of Monte Carlo simulated samples.

Other background contributions such as QCD multijet production and W+Jets are considered negligible. One of the aims of selection cuts outlined in section 7.2 is to reduce the contribution from muons coming from heavy flavour decays: $b\bar{b}$ and $c\bar{c}$ production and its subsequent semi-leptonic decay. This background was estimated in earlier versions of the searches presented here: [88], section 4 of [89] and section 4.4 of [90]. Given the stringent isolation requirement on all muons, the contribution from the QCD multijet background to the overall SM background was found to be negligible. Similarly, the background due to the W boson semi-leptonic decay and associated jet production was also found to be negligible from Monte Carlo simulation. Therefore, they will not be considered in this search.

6.3.1 Drell-Yan

The main irreducible SM background for an opposite charge dilepton final state is the Drell-Yan process: $q\bar{q} \rightarrow Z/\gamma^* \rightarrow \ell^+\ell^-$, as shown in figures 6.3 and 6.4 for a leading order (LO) process and a next-to-leading-order (NLO) process respectively. Monte Carlo samples

simulating the Drell-Yan process are generated with Powheg [91], an NLO generator, using the CT10 PDF set [85]. Pythia8 [70] is used to simulate the parton shower. In order to have statistical precision across all dimuon invariant mass ranges, samples binned in dimuon invariant mass were produced from 250 to 3000 GeV in 250 GeV steps. For the Z-peak region a high statistics sample was produced for Born masses above 60 GeV and is used to estimate the region $60 < m_{\mu\mu} < 250$ GeV. To estimate the Drell-Yan background up to the highest invariant mass used in this analysis, 4.5 TeV, a sample for invariant masses above 3.0 TeV was also produced. A full list of the samples used and their respective $\sigma \cdot BR(\mu^+\mu^-)$ can be found in table 6.3.

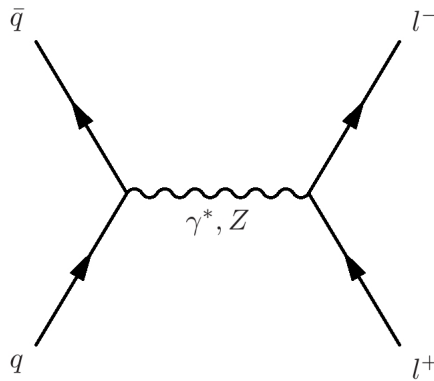


Figure 6.3: The Drell-Yan Process.

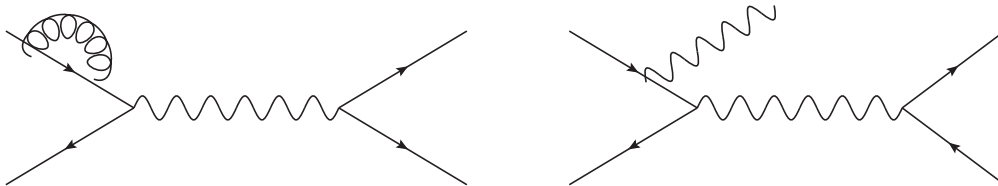


Figure 6.4: Example of higher order corrections to the Drell-Yan Process with a gluon emission-absorption (left) and initial state radiation (right).

While the generator used to produce the Drell-Yan Monte Carlo samples is an NLO generator, the differential cross section times branching ratio of the process can be underestimated due to contributions from higher order QCD at Next-to-Next-to-leading-order (NNLO) or EWK corrections at NLO unaccounted for in the Monte Carlo generator used. These higher order corrections to simulated processes are dependent on dilepton mass and are calculated for this analysis using FEWZ [92] and PHOTOS [93]. PHOTOS models the higher order EWK corrections, from which the dominant part is Final State Radiation (FSR) due to photon emission,

Table 6.3: Drell-Yan Monte Carlo samples used in the dimuon channel for this analysis. The first column shows the internal ATLAS run number, then the generator level cross section times branching ratio and the mass range it corresponds to. In the last two columns, the number of events generated and the process it corresponds to are shown [87].

Dataset ID	$\sigma\text{BR}[\text{pb}]$ Powheg	$m_{\mu\mu}$ Range[GeV]	$N_{\text{evt}}[\text{k}]$	Signature
147807	1109.8	> 60	10000	$\gamma^*/Z \rightarrow \mu\mu$
129524	9.8460	120-180	3300	$\gamma^*/Z \rightarrow \mu\mu$
129525	1.571	180-250	100	$\gamma^*/Z \rightarrow \mu\mu$
129526	0.5492	250-400	100	$\gamma^*/Z \rightarrow \mu\mu$
129527	$8.966 \cdot 10^{-2}$	400-600	100	$\gamma^*/Z \rightarrow \mu\mu$
129528	$1.51 \cdot 10^{-2}$	600-800	100	$\gamma^*/Z \rightarrow \mu\mu$
129529	$3.75 \cdot 10^{-3}$	800-1000	100	$\gamma^*/Z \rightarrow \mu\mu$
129530	$1.293 \cdot 10^{-3}$	1000-1250	100	$\gamma^*/Z \rightarrow \mu\mu$
129531	$3.577 \cdot 10^{-4}$	1250-1500	100	$\gamma^*/Z \rightarrow \mu\mu$
129532	$1.123 \cdot 10^{-4}$	1500-1750	100	$\gamma^*/Z \rightarrow \mu\mu$
129533	$3.838 \cdot 10^{-5}$	1750-2000	100	$\gamma^*/Z \rightarrow \mu\mu$
129534	$1.389 \cdot 10^{-5}$	2000-2250	100	$\gamma^*/Z \rightarrow \mu\mu$
129535	$5.226 \cdot 10^{-6}$	2250-2500	100	$\gamma^*/Z \rightarrow \mu\mu$
129536	$2.017 \cdot 10^{-6}$	2500-2750	100	$\gamma^*/Z \rightarrow \mu\mu$
129537	$7.891 \cdot 10^{-7}$	2750-3000	100	$\gamma^*/Z \rightarrow \mu\mu$
129538	$5.039 \cdot 10^{-7}$	> 3000	100	$\gamma^*/Z \rightarrow \mu\mu$

and is already included in the Drell-Yan Monte Carlo samples outlined in table 6.3. FEWZ is used to calculate both NNLO QCD corrections and missing NLO EW corrections such as initial state photon radiation (ISR) and loop corrections. For consistency, the input PDF to FEWZ is CT10, the same one used to generate the Powheg Drell-Yan samples. The corrections applied to the Drell-Yan spectrum are then derived as a ratio of the NNLO differential cross section calculated by FEWZ and the Powheg NLO cross section as a function of generator level dilepton invariant mass. These corrections are commonly named K -factors and are defined for the Drell-Yan process as:

$$K_{NNLO} = \frac{\sigma_{NNLO}^{FEWZ}(m_{\ell\ell})}{\sigma_{NLO}^{Powheg}(m_{\ell\ell})} \quad (6.2)$$

where K_{NNLO} is the K -factor applied and $m_{\ell\ell}$ is the generated dilepton invariant mass before any Final State Radiation (FSR). These corrections are applied on an event-by-event basis. The K -factor used as a function of the Born dilepton invariant mass is shown in figure 6.5. Further details on the higher order corrections used and their calculation can be found in appendix E of [87].

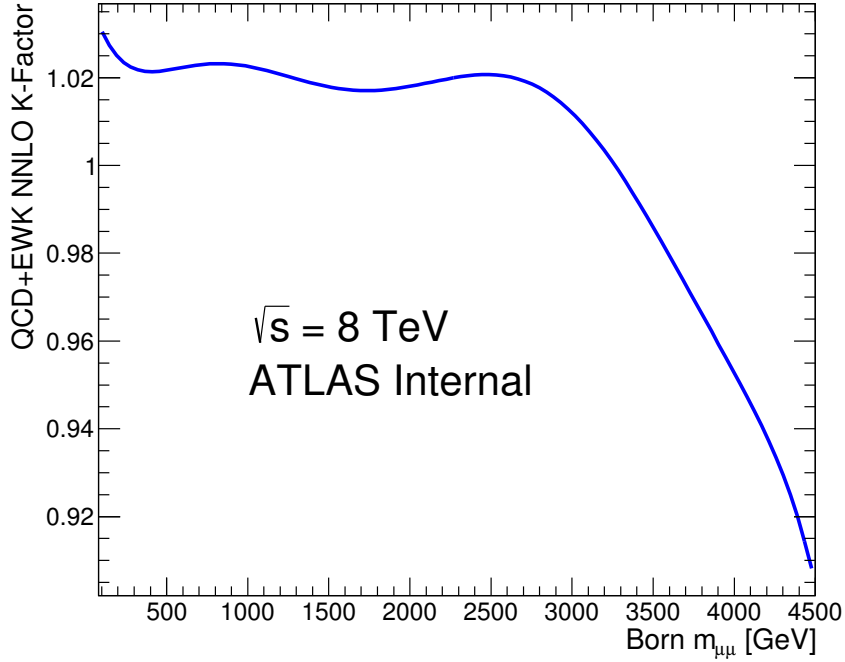


Figure 6.5: EW+QCD K -factor as a function of Born dilepton mass.

6.3.2 Diboson

Diboson production includes WW , WZ and ZZ processes, and is a non-negligible reducible source of SM background. As shown in figure 6.6, the decay of vector bosons can produce opposite sign muon pairs in the final state. Monte Carlo samples are generated with HERWIG, a LO generator, with CTEQ6L1 [94] used as the PDF set. While the generator used only calculates LO matrix elements, the highest order cross section known for these processes is at NLO. A list of the samples used to estimate the diboson background can be found in table 6.4, together with the generator level and NLO cross sections times branching ratio available. The samples are filtered to contain at least two leptons with Born level $p_T > 10$ GeV and $|\eta| < 2.8$. The filter efficiency is also quoted in table 6.4. Specific Monte Carlo samples binned in the diboson pair invariant mass (m_{Dib}) were generated between 400 and 1000 GeV and 1000 GeV onwards to ensure good statistical precision.

Similarly to Drell-Yan, the K -factor is the ratio of the NLO differential cross section with that of the LO Herwig generated samples used. A single mass independent K -factor is used to scale the diboson production cross section times branching ratio to NLO accuracy. According

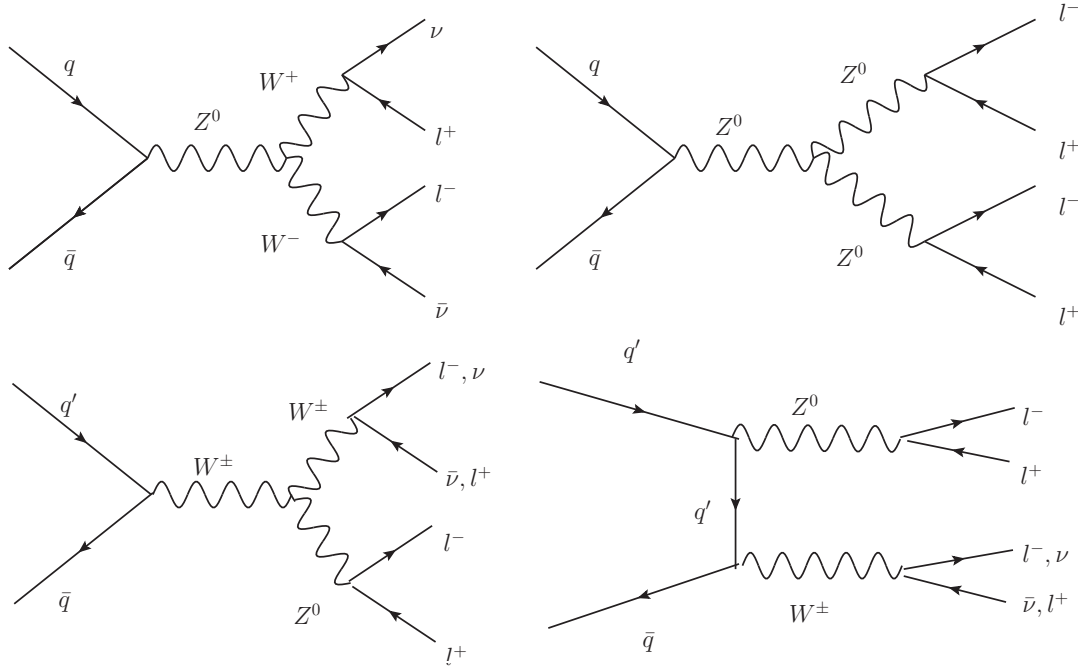


Figure 6.6: Diboson production at the LHC with leptons in the final state: WW production (top left), ZZ (top right) and WZ (bottom left and right).

Table 6.4: Summary of Diboson Monte Carlo samples used for this search. The Born level diboson invariant mass range of each sample is given in the second column. Both the generator level cross section used to generate the sample and the NLO cross section of each process are given in the third and fourth columns. The fifth columns shows the filter efficiency [87].

Dataset ID	$m_{Dib}[\text{GeV}]$	$\sigma_{BR}[\text{pb}]$ Herwig	NLO $\sigma_{BR}[\text{pb}]$	$\epsilon_F[\%]$	$N_{evt}[\text{k}]$	Signature
105985	N/A	32.501	56.829	38.21	2500	WW $\rightarrow lX$
105986	N/A	4.6914	7.3586	21.17	250	ZZ $\rightarrow X$
105987	N/A	12.009	21.478	100	1000	WZ $\rightarrow X$
180457	400-1000	0.37894	0.66255	0.75	10	WW $\rightarrow \mu\nu\mu\nu$
180458	> 1000	0.37896	0.66261	0.01	10	WW $\rightarrow \mu\nu\mu\nu$
180459	400-1000	0.46442	0.83038	0.003	10	WZ $\rightarrow \mu\mu$
180460	> 1000	0.46442	0.83038	0.0001	10	WZ $\rightarrow \mu\mu$
180461	400-1000	0.34574	0.54229	0.001	10	ZZ $\rightarrow \mu\mu$
180462	> 1000	0.34574	0.54229	0.00003	10	ZZ $\rightarrow \mu\mu$

to [95], that is a valid approach as long as one of the bosons is on-shell. Given that the search for new phenomena presented here is focused on the TeV range, it is expected that this

condition is fulfilled. Therefore, the use of a mass independent K -factor is validated [87].

6.3.3 Top Quark

Top quark related processes are a non-negligible reducible source of SM background. The top quark, via its decay through the weak interaction, can produce final states with opposite sign muon pairs. Feynman diagrams of processes involving the top quark are shown in figure 6.7: top pair production (left) and single top production associated with a W boson (right), where the bottom quark also decays via the weak interaction and can produce a muon. The single top production process can occur via both the s and t channels, but the cross section for the s channel process is about 10 times smaller and therefore considered negligible for this analysis. Monte Carlo samples are generated using MC@NLO [96], a NLO generator, while the parton shower is simulated by HERWIG [71]. The PDF used is CT10. A list of the samples used can be found in table 6.5.

A NNLO production cross section of 252.89 pb and 22.37 pb is used to scale events from the $t\bar{t}$ and single top processes, following the latest recommendations from the ATLAS Top Quark Working Group [97] at $\sqrt{s} = 8$ TeV using top++2.0 [98]. As described for diboson processes, the K -factor is the ratio of the NNLO cross sections quoted and the the MC@NLO generator level cross sections, both shown in table 6.5.

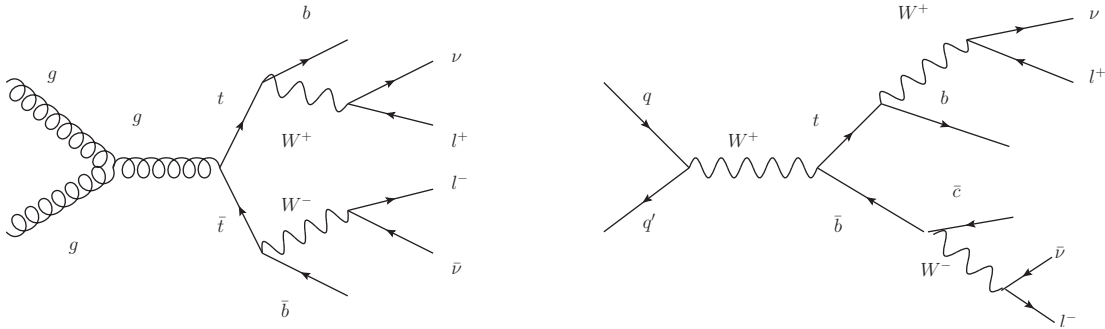


Figure 6.7: Feynman diagram for $t\bar{t}$ (left) and single top (right) production. The top and bottom quark decays through the weak interaction can produce opposite sign dimuon final states.

6.3.4 Photon-Induced corrections

The Photon-Induced (PI) process is a non-negligible irreducible source of SM background, arising from a $\gamma\gamma$, γq or $\gamma\bar{q}$ initial state. The latter two involve photon absorption and Z/γ^*

Table 6.5: Top quark Monte Carlo samples used for this analysis. Both the MC@NLO cross section and the NNLO cross section are given in the second and third columns. The fourth column shows the filter efficiency [87].

Dataset ID	$\sigma_{\text{BR MC@NLO}}[\text{pb}]$	NNLO $\sigma_{\text{BR}} [\text{pb}]$	$\epsilon_F[\%]$	$N_{\text{evt}}[\text{k}]$	Signature
105200	208.13	252.89	54.26	15000	$t\bar{t} \rightarrow lX$
108346	20.67	22.37	100.0	2000	$Wt \rightarrow X$

emission with a subsequent dilepton decay. Both the t (as shown in figure 6.8) and u channel processes are allowed. The PI process is calculated at Leading-Order (LO) with the MRST2004QED PDF [99]. For the QBH search presented in [78], the PI process is calculated using FEWZ [92] and implemented as a K -factor to the Drell-Yan dimuon invariant mass spectrum. For the ADD LED search presented in [79], a full kinematic description of the event was required and therefore dedicated Monte Carlo samples were generated with Pythia8. The samples produced and their generator level cross sections are listed in table 6.6.

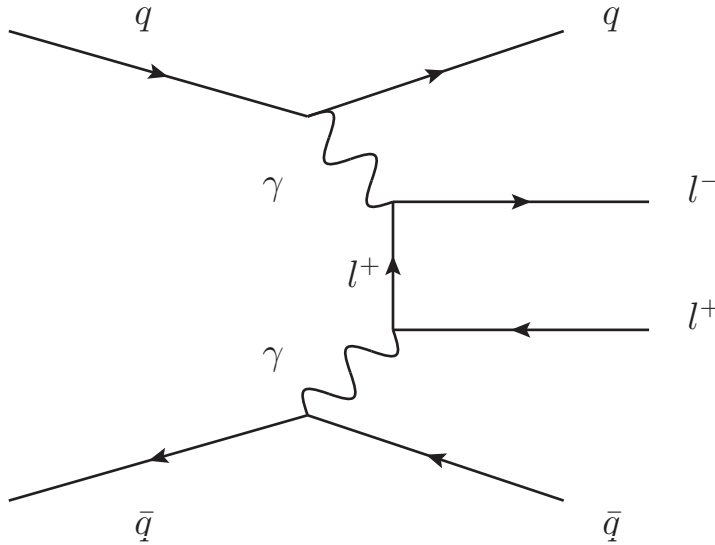


Figure 6.8: Feynman diagram of a Photon-Induced process at the LHC with a dilepton final state.

The difference between the results obtained with the two approaches is summarized in figure 6.9, which shows a comparison between these two estimations. The nominal PI estimation

Table 6.6: Summary of Photon-Induced Monte Carlo samples used for this search. The invariant mass range of each sample is given in the second column. The generator level cross section times branching ratio is shown in the third column [22].

Dataset ID	$m_{\mu\mu}$ [GeV]	σBr [pb] Pythia	N_{evt} [k]	Signature
129662	60-200	2.69	500	$\gamma\gamma \rightarrow \mu\mu$
129663	200-600	0.10	20	$\gamma\gamma \rightarrow \mu\mu$
129664	600-1500	$2.66 \cdot 10^{-3}$	10	$\gamma\gamma \rightarrow \mu\mu$
129665	1500-2500	$3.55 \cdot 10^{-5}$	10	$\gamma\gamma \rightarrow \mu\mu$
129666	> 2500	$9.78 \cdot 10^{-7}$	10	$\gamma\gamma \rightarrow \mu\mu$

used in [78] (“PI Correction nominal”) is shown in blue against the Born-level dimuon invariant mass, together with the upwards and downwards systematic shifts on that estimation. The fraction of PI corrections from the overall Drell-Yan spectrum (“PI/DY + 1”) is calculated at generator level using the dedicated PI Monte Carlo samples, as done in [79].

The two approaches yield different results but are in agreement within uncertainties. The reason behind the difference is that the PI K -factor used for the QBH search in [78] is calculated as an average of two calculations assuming either current or constituent quark masses¹⁹. Given the large uncertainties on the quark masses the uncertainty on the PI calculation is large. As an example, the differential cross section for each of the two quark masses assumptions as a function of generator level dilepton mass can be found in figure 6.10. The dedicated Monte Carlo samples used for the ADD LED search [79] were generated assuming current quark masses and hence correspond to an upper estimate for this background.

¹⁹As explained in section 4.3 of [8], the constituent quark mass comprises the current quark mass and the energy of the gluon field that surrounds the quark when it is confined in a hadron. The current quark mass is then the “naked” mass of the quark without the cover of the gluon field.

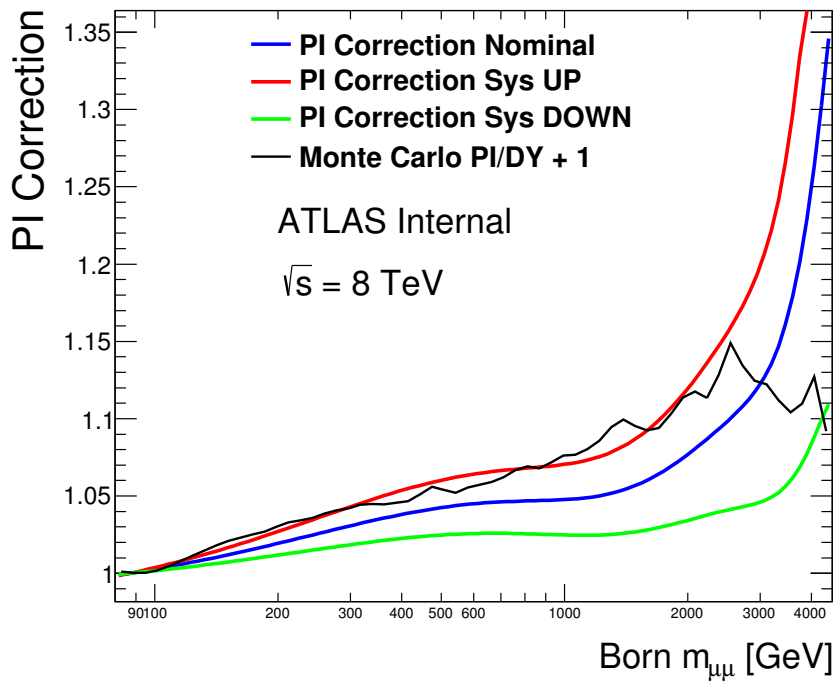


Figure 6.9: PI correction to the Drell-Yan spectrum as a function of generator level dimuon mass for the analysis presented in [87] (“PI Correction”), with PI process estimated as K-factor, and [22] (“MC PI/DY + 1”), estimated directly from Monte Carlo samples.

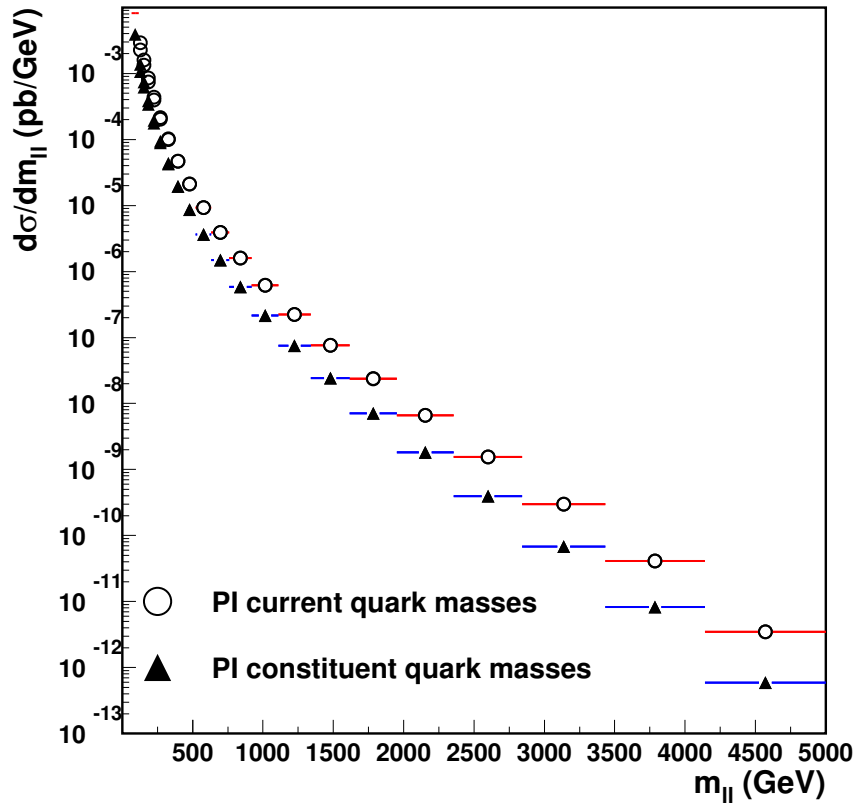


Figure 6.10: LO parton-level cross section for photon-induced dilepton production as a function of dilepton invariant mass. Calculations are done using FEWZ and MRST2004qed PDF assuming either current quark or constituent quark mass [87].

6.4 Pile-up Reweighting

The Monte Carlo samples used to simulate signal and background processes include a pile-up model that covers a range of possible $\langle\mu\rangle$ values observed in data. The samples were however produced before actual data-taking began. As explained in chapter 4, the average number of interactions per bunch crossing increased throughout Run-1 and exceeded the design value of the ATLAS detector. As a result, the $\langle\mu\rangle$ distribution in the Monte Carlo simulated samples is not well modelled, as can be seen on the left side of figure 6.11. The analysis presented is sensitive to the amount of detector activity. As shown in section 7.2, one of the selection cuts requires that the muon is isolated in a cone in $\Delta R = \sqrt{\Delta\phi^2 + \Delta\eta^2}$. Therefore, increased activity can lead to different values of the isolation variable. The official Pile-up Reweighting (PURW) tool [100] is used to obtain the $\langle\mu\rangle$ distribution in Monte Carlo found in data and correct for pile-up effects as a function of $\langle\mu\rangle$. The tool calculates a weight on an event-by-event basis. As shown in figure 6.11 on the right, the agreement between data and Monte Carlo is recovered after this weight is applied. The version of the tool used for the searches presented in this paper is PileUpReweightingTool-00-02-12.

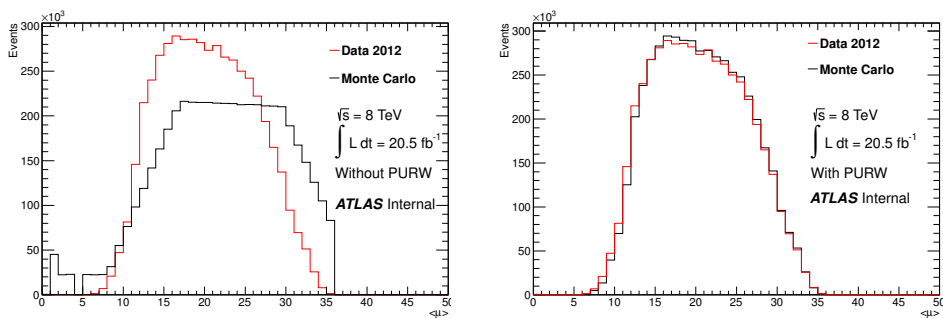


Figure 6.11: The $\langle\mu\rangle$ distribution for data and Monte Carlo is shown on the left before and after applying the corrections from the PileUpReweightingTool to the simulated processes.

7 Dimuon event selection and corrections applied

The selection cuts applied to search for new phenomena in the opposite sign dimuon channel with the 2012 data collected by the ATLAS detector are outlined. The corrections applied to simulated processes are described and a comparison is made between the observed and expected event yields in the dimuon invariant mass spectrum. The systematic uncertainties associated to the estimation of signal and background processes are presented.

7.1 Background Estimation

As explained in chapter 6, the SM background is estimated through the use of Monte Carlo simulated samples. However, for the top quark background, the statistical precision of the samples is not sufficient to estimate the contribution of this background beyond 1.0 TeV in dimuon invariant mass. Therefore, an extrapolated fit is used to estimate the high mass region. Two functional forms are investigated:

$$\text{Dijet function : } a \cdot x^b \cdot x^{c \ln(x)} \quad (7.1)$$

$$\text{Monomial function : } \frac{a}{(x + b)^c} \quad (7.2)$$

As explained in section 4.4 of [87], these two functions are chosen for their stability when varying the fit range and for the quality of the fit. Using a second function allows to evaluate the systematic uncertainty associated with this estimation. Figure 7.1 shows the expected number of Top background events after event selection (outlined in section 7.2) against the reconstructed dimuon invariant mass. The Top quark related background estimation obtained using each of the two functional forms is shown. The fit region is chosen to be between 191 and 734 GeV in reconstructed dimuon invariant mass (motivated by the binning used in dimuon invariant mass plots). In that region, the statistical precision of the Monte Carlo samples is still high and the range is large enough to correctly capture the behaviour of the Top quark background. It should be noted that the fit is not expected to work below the threshold region in dimuon invariant mass since the functions are chosen to describe the high mass region. The “stitching” point between the Monte Carlo prediction and the fit is selected to be at 560 GeV, where the statistical error of the background estimation by the Monte Carlo samples starts to increase. The dijet function is chosen as the central value of the Top quark related background as it provides a slightly more conservative background estimation.

The choice of a “stitching” point does not affect the results of the estimation. As shown in table 7.1, varying the choice of “stitching” point by 70-80 GeV both upwards and downwards changes produces a maximum change of 1.5% on the top background estimation found using

the central value. This variation is much smaller than the statistical error of the Monte Carlo estimation. The statistical error associated to the Monte Carlo at 700 GeV is close to 20%.

Table 7.1: The total number of top quark background events for $m_{\mu\mu} > 400$ GeV is shown for different “stitching” point choices. The error quoted comes from the uncertainty on the fit parameters.

Stitching Point [GeV]	top quark background events for $m_{\mu\mu} > 400$ GeV
490.5	146.7 \pm 2.1
524.6	149.2 \pm 2.2
561.0	148.2 \pm 2.1
600.0	148.1 \pm 2.1
641.7	150.3 \pm 2.2

The estimation obtained with the fit is shown in figure 7.2. The resulting histogram is obtained by combining the Monte Carlo samples estimation up to the “stitching” point, while the region beyond that point is estimated using the dijet fit. The shaded brown region in the top and bottom plots is the systematic uncertainty associated with the Top background Monte Carlo estimate. The systematic errors are a result of the combination in quadrature of two sources of systematic uncertainty:

- The variation of the fitting range of the dijet function. 25 different fit ranges are used, the systematic error is then the difference between the maximum error from the shifted fits and the central one.
- The difference between the results obtained using the monomial and the dijet function for the central fitting range.

7.2 Event Selection

The selection cuts used for the searches presented in this paper are based on those used in earlier ATLAS BSM searches in the opposite sign dimuon channel with the full 2011 dataset [101]. In 2012, given the increased centre of mass energy (from 7 to 8 TeV) and subsequent changes to the trigger menu, the selection cuts were slightly modified. The aim of the selection cuts however remained the same: select muons with the best possible momentum resolution to accurately reconstruct the invariant mass of the dimuon pair, and to minimize possible sources of reducible background. Given that this search expects a signal at the TeV scale in dimuon invariant mass, it is important to ensure that events are well reconstructed

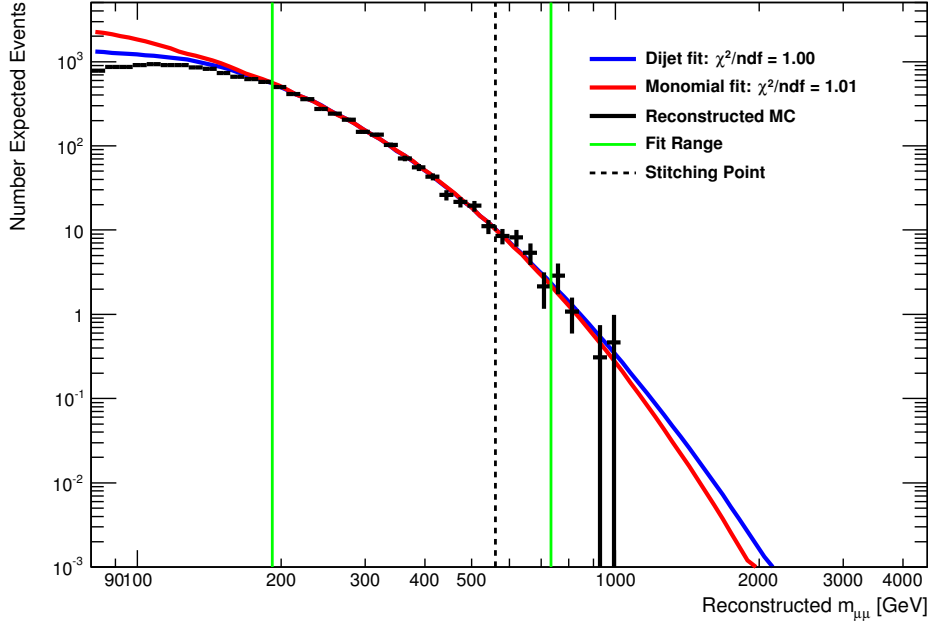


Figure 7.1: The reconstructed dilepton invariant mass is shown against the number of expected top quark background events and two fit functions are overlaid: dijet (blue) and Monomial (red). The “stitching” point of the top background at high mass is shown in black. The fit range is shown by the green lines. The black points show the the top quark background estimation from the Monte Carlo samples together with statistical errors.

with the best possible mass resolution. Low resolution could lead to low mass events migrating to higher masses, producing what could be a fake signal. For this purpose, only Combined (CB) muons are used. CB muons combine the track reconstruction information from the individual inner detector (ID) and muon spectrometer (MS) measurements to form a combined track [102]. To ensure the best possible resolution each of the selected muons is required to have a minimum number of hits in each of the ID components and MS stations. Muons fulfilling this criteria are expected to have a transverse momentum resolution ranging from 19 to 32% for a p_T of 1.0 TeV [87].

The full selection applied follows, starting with a preselection to quickly discard events that are not of interest for the search. The hits requirement in both the ID and the MS are detailed below [103].

Preselection

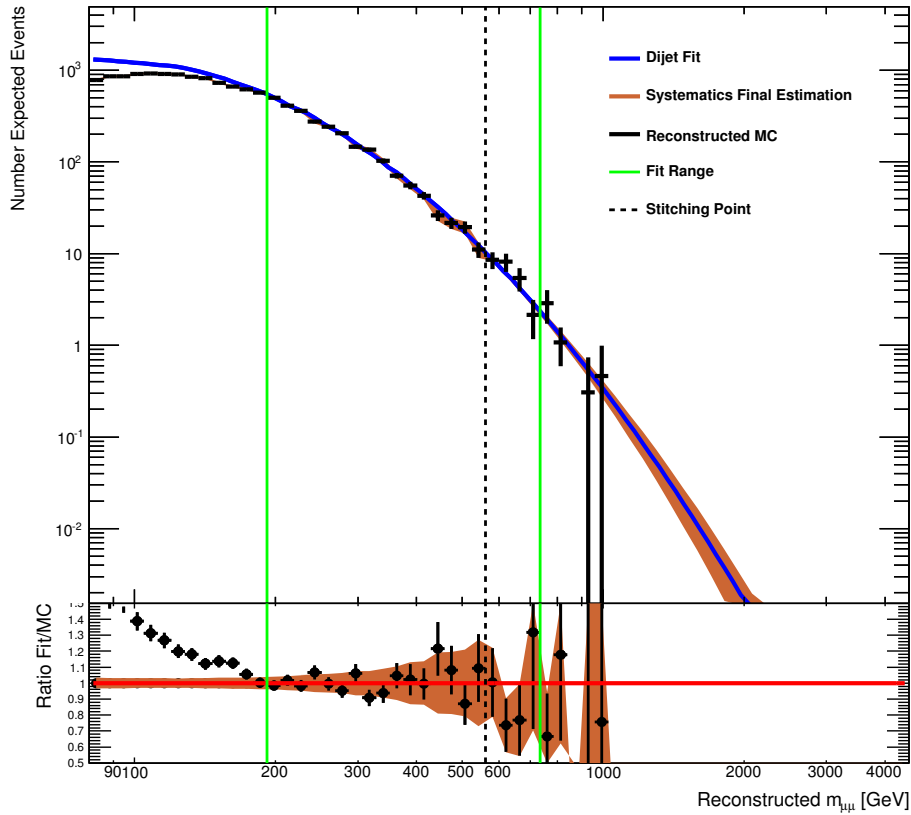


Figure 7.2: The reconstructed dilepton invariant mass is shown against the number of expected top quark background events. The Monte Carlo estimation is shown in black and the dijet fit is shown in blue. The shaded brown region shows the systematic uncertainties associated with the estimation method. The fit range is shown by the green lines. The ratio between the dijet fit and the Monte Carlo estimate is shown in the bottom, with the shaded region showing the error associated with the ratio between the final estimation and Monte Carlo.

- Passes the Good Run List to ensure good data quality
- Trigger EF_mu24i_tight or EF_mu36_tight must be fired. The trigger requirement ensures the presence of at least one muon with $p_T > 24$ GeV at L1. The use of an additional higher threshold trigger is motivated by small inefficiencies with the isolation requirement in EF_mu24i_tight. Trigger matching to an offline reconstructed muon is not required.
- At least one primary vertex with more than two tracks above the minimum threshold for

reconstruction of 400 MeV [104]. The primary vertex distance from the centre of the detector along the z -axis ($|z_{PV}|$) is required to be less than 200 mm to suppress background from cosmic ray muons and ensure the event is the result of a hard process²⁰.

- At least two combined MuID muons with $p_T > 10$ GeV in the event to ensure a dimuon pair can be formed.

If an event does not fulfill these criterion it is rejected without further selection. If the event selection is passed, at least two muons are required to pass further criterion outlined below:

Muon Selection

- Muon $p_T > 25$ GeV.
- Each muon must pass the ID track quality cuts outlined by the ATLAS Muon Combined Performance Working Group [105].
- The transverse and longitudinal impact parameters of muons with respect to the primary vertex must not exceed 1.0 and 0.2 mm respectively to suppress background from cosmic ray muons and soft QCD processes.
- In a cone of $\Delta R = \sqrt{\Delta\phi^2 + \Delta\eta^2} = 0.3$, the isolation requirement (I_μ), defined as the ratio of the p_T of all tracks to the muon p_T in the region defined:

$$I_\mu = \frac{\sum_i^{n_{tracks}} p_{T_i}}{p_T^\mu} \quad (7.3)$$

must not exceed 0.05 to suppress background from heavy-flavoured jets (top, bottom or charm quarks) decays.

- Each muon must fulfill the Muon Station Hits Requirements to ensure the muons are reconstructed in the MS with the best possible momentum resolution.

The ID track quality requirement ensures that the standalone ID track is of the best quality. Similarly, the muon station hits requirements ensures the best possible quality of the MS track. Together, they ensure that high p_T CB muons are well reconstructed and have the best possible momentum resolution [105]. No explicit cut on the muon η is required. However, the muon station hits indirectly introduces a requirement on the trajectories muons can follow in

²⁰In QCD, soft processes are collisions with a low momentum transfer. In the pp collisions at the LHC, the dominant cross section comes from soft processes. Given that this search focuses on the high mass range it is important to suppress background from soft processes to probe the shortest distance scales.

the detector, as a number of hits is required in each of the stations of the MS. The requirements on ID and MS tracks are outlined in more detail below.

MCP Inner Detector Hits requirements

- At least one B-Layer hit if the muon passes through the B-Layer region
- At least 1 Pixel hit, including Pixel dead sensors crossed
- At least 5 SCT hits, including SCT dead sensors crossed
- At most 2 Pixel or SCT holes
- If $0.1 < |\eta| < 1.9$: at least 6 TRT hits, including TRT outliers, with the TRT outlier fraction < 0.9
- If $|\eta| \leq 0.1$ or $|\eta| \geq 1.9$: only if at least 6 TRT hits, including TRT outliers, are observed, require the outlier fraction to be < 0.9

Muon Station Hits requirement

Muons reconstructed with a minimum number of hits in each of the three MS stations are called three station muons. They must fulfill the following criteria [87]:

- At least 3 hits in all 3 layers of Barrel or Endcap Inner, Middle and Outer MDT/CSC precision layers. No Barrel-Endcap overlap is allowed, such that muons with hits in both Barrel and Endcap are discarded.
- At least one hit in the non-bending plane (ϕ hit) in two separate RPC/TGC/CSC chambers to ensure a good magnetic field estimation.
- Muons with hits in known misaligned chambers (BEE and BIS7/8) are rejected.
- The difference between the standalone momentum measurements from the ID and the MS must not exceed 5 times the sum in quadrature of the standalone uncertainties for each muon:

$$|p_T^{MS} - p_T^{ID}| \leq 5 \cdot \sqrt{\sigma_{p_T^{MS}}^2 + \sigma_{p_T^{ID}}^2} \quad (7.4)$$

While the three station requirement on muons ensures the best possible momentum resolution, its stringent requirements have a large effect on the efficiency of the selection applied. Throughout this analysis a quantity referred to as acceptance times efficiency ($A\epsilon$) will be

used. The acceptance refers to the region (both in direction and energy) where particles can be detected and is dependent on the design of the particle detector. The efficiency is the ratio between the number of events with particles falling in the detector acceptance region fulfilling the selection criteria and the total number of events with particles falling in that region. Therefore, the $A\epsilon$ of a given selection is the ratio between the number of events that pass all the selection requirements over the total number of events. As shown in figure 7.3 on the left, the $A\epsilon$ for the muon selection with the three station requirement is 42% for a theoretical new boson, the Z' , with a mass of 2.5 TeV. The $A\epsilon$ for the electron channel selection criteria for the same phenomena is around 70%, as no stringent requirements to improve the resolution are needed. In order to improve the $A\epsilon$, if a muon does not pass the three station requirement a secondary muon selection is used. Muons fulfilling the following criteria will be referred to as two station muons:

- $|\eta| < 1.05$
- At least 5 hits in both the Barrel Inner and Outer MDT precision layers
- At least one ϕ hit in one RPC layer
- No hits in the BIS7/8 or Endcap MDT chambers due to known misalignments
- No hits in MS chambers with known residual misalignments:
 - In sectors 4 or 6 with $|\eta| > 0.85$
 - In sector 9 with $0.20 < |\eta| < 0.35$
 - Or in sector 13 with $0.00 < |\eta| < 0.20$
- The difference between the standalone momentum measurements from the ID and MS must not exceed 3 times the sum in quadrature of the standalone uncertainties:

$$|p_T^{MS} - p_T^{ID}| \leq 3 \cdot \sqrt{\sigma_{p_T^{MS}}^2 + \sigma_{p_T^{ID}}^2} \quad (7.5)$$

Muons that pass all of the requirements outlined are ordered by decreasing p_T and used to form an opposite charge dimuon pair. The dimuon pair is required to have an invariant mass larger than 80 GeV and lower than 4500 GeV. The upper mass cut is used as no theoretical background estimation is available beyond that figure. For the case of an event containing more than two muons passing all criteria, the opposite charge pair with the highest muon p_T sum is chosen. It should be noted that only 0.1% of the selected events have more than two muons fulfilling all the criteria outlined. On first instance, pairs are formed using only three station muons (3+3 pair). If its not possible to form a 3+3 pair, the second option is to form a pair of a three station and a two station muon (3+2 pair). Pairs formed of only two station

muons are not used as their mass resolution is expected to be worse than three station dimuon pairs. Events containing a valid 3+3 pair are said to pass the “tight muon selection”. If no suitable 3+3 pairs are found, but a 3+2 pair fulfills all requirements, the event is said to pass the “loose muon selection”. The $A\epsilon$ of the “loose” dimuon selection is shown on the right of figure 7.3. Given that 3+2 pairs are only allowed if a 3+3 pair cannot be found, the $A\epsilon$ for the “loose” dimuon selection is much lower than for the “tight” selection. The addition of “loose” dimuon pairs increases the $A\epsilon$ of the overall dimuon selection to 46% for a Z' with a mass of 2.5 TeV.

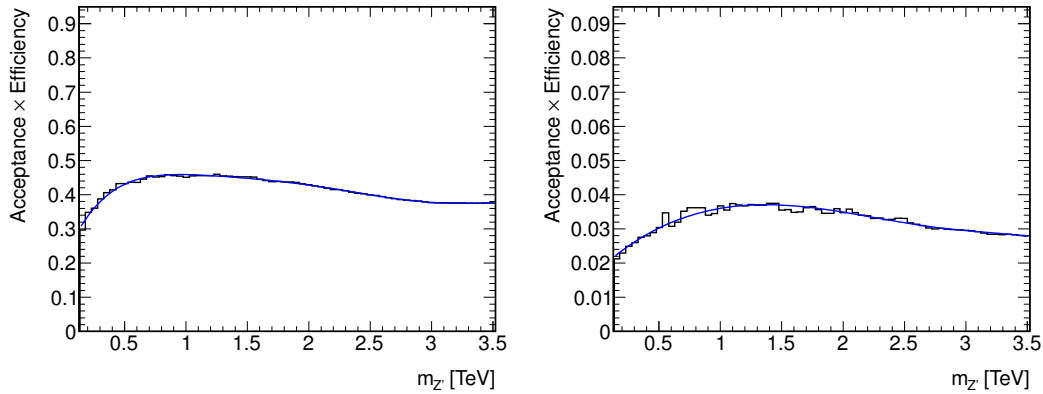


Figure 7.3: Total acceptance times efficiency for the tight dimuon selection (left) and the loose dimuon selection (right) as a function of the Z' pole mass. The blue line shows a 3rd order polynomial fit to the $A\epsilon$ [87].

Figure 7.4 shows the average fractional difference between the muon transverse momentum at generator (p_T^{MC}) and reconstructed (p_T^{RECO}) level as a function of generator level muon p_T for three station muons (left) and two station muons (right). The error bars represent the RMS of deviations from the mean value in a given bin and is taken as a measurement of the resolution. A bias in the range of 5 to 10% is observed in the muon momentum reconstruction for transverse momenta larger than 1.0 TeV and, as expected, the resolution becomes worse with increasing muon transverse momentum. Figure 7.5 shows the resolution as a function of generator level muon transverse momentum after FSR. The resolution is taken to be the RMS of the of the deviations from the mean value in figure 7.4. The resolution for two station muons is worse than for three station muons in the barrel region, and is comparable to three station muons outside the barrel. The resolution values found are in agreement within errors with those obtained in [87]. Due to the low resolution of two station muons, low mass events coming from 3+2 pairs could be misreconstructed due to the decreasing resolution and migrate to higher masses. This is particularly significant for a search such as the ADD LED, which looks for a broad deviation from SM expectation across a large dimuon invariant mass range: a few events migrating to higher mass could produce a fake signal-like fluctuation.

As a consequence, only three station muons are used for the ADD LED. More details on the statistical analysis of the results can be found in chapters 8 and 9.

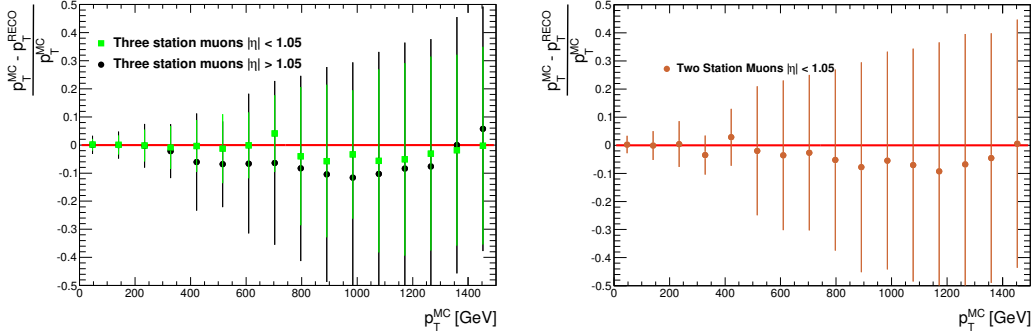


Figure 7.4: The average fractional difference between the muon transverse momentum at generator and reconstructed level is shown as a function of generator level muon p_T . 3 station muons (left) and 2 station muons (right) are shown. The RMS from the mean value in each bin is shown.

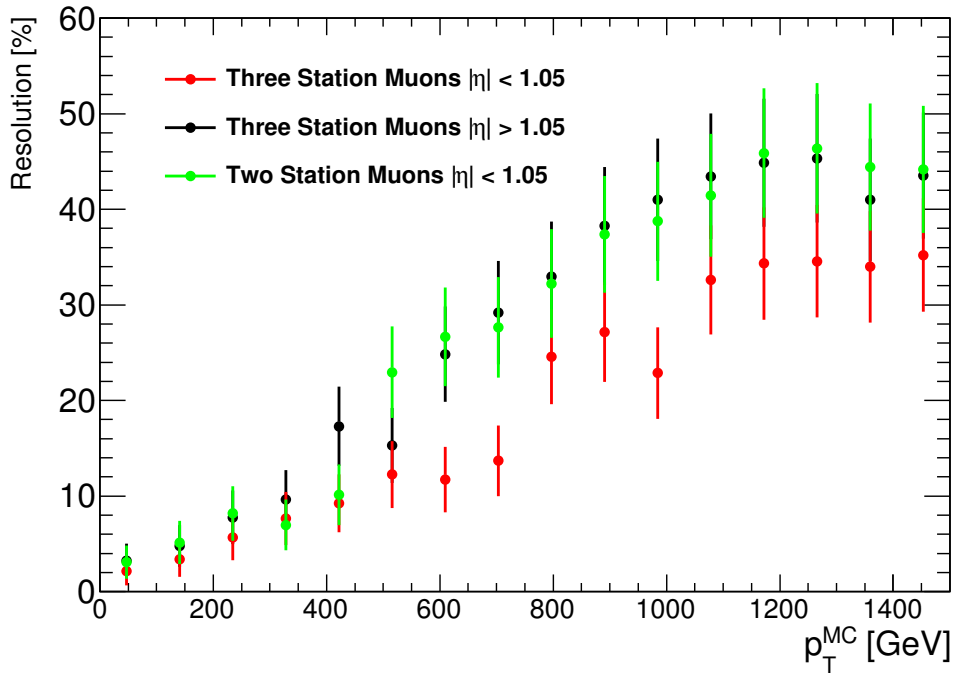


Figure 7.5: The resolution for 3 and 2 station muons is shown for increasing generator level muon p_T . The error bars represent the error on the RMS from figure 7.4.

Tables 7.2, 7.3 and 7.4 show a cut flow for two Drell-Yan Monte Carlo samples covering the

range of 1.0-1.25 TeV and 2.0-2.25 TeV in generator level dimuon invariant mass and for the expected signal QBH for four values of M_{th} : 1.0, 2.0, 3.0 and 4.0 TeV. The object quality requirements include the requirements on the ID track and the transverse and longitudinal impact parameters. The muon station hits is the most stringent requirement and reduces the total $A\epsilon$ by $\sim 30\%$. It can also be observed that the opposite charge requirement, that has almost no effect for 1.0 TeV dimuon masses, loses efficiency when reaching 2.0 TeV dimuon masses. Higher momentum muons results in muons being charge misidentified. The curvature of muons in the magnetic field decreases with increasing momentum and charge misidentification becomes more likely. An estimation of the charge misidentification rate can be found in section 7.4.2. For the tables detailing the cut flow of the QBH signal process, the upper requirement on dimuon mass becomes an important effect for values of M_{th} larger than 2.0 TeV. Given that quantum black holes are expected to be formed in the region $M_{th} < M_{QBH} < 3 \cdot M_{th}$, for M_{th} values exceeding values exceeding 2.0 TeV the upper dimuon invariant mass cut of 4500 GeV has a large effect, reducing the total $A\epsilon$ by as much as 17% for $M_{th} = 4.0$ TeV.

Table 7.2: Cutflow table presenting the relative and cumulative efficiencies for each important criterion for the tight (3 station muons) and tight+loose (3+2 station muons) muon selection. The efficiency values correspond to Monte Carlo samples for the dominant Drell-Yan background at dimuon masses in the range of 1.0-1.25 TeV and 2.0-2.25 TeV, each with 100000 generated events. Object quality includes the ID hits requirements together with the requirements on z_0 and d_0 [22].

Criterion	Relative Eff [%]		Cumulative Eff [%]	
	$m_{\mu\mu} = 1$ TeV	$m_{\mu\mu} = 2$ TeV	$m_{\mu\mu} = 1$ TeV	$m_{\mu\mu} = 2$ TeV
Trigger	89.8	89.2	89.8	89.2
2 Combined Muons	88.8	88.8	79.7	79.2
2 muons with $p_T > 25$ GeV	98.2	98.3	78.3	77.8
Object Quality	98.6	98.4	77.2	76.6
Isolation	97.5	97.8	75.2	74.9
3 (3+2) Station Muons	63.1 (67.9)	62.1 (66.6)	47.4(51.1)	46.5 (50.0)
Charge	99.5 (99.7)	96.4 (96.6)	47.4 (51.1)	45.0 (48.3)

The validity of the Monte Carlo description of the data after applying the selection cuts outlined is evaluated in the control region ($m_{\mu\mu} < 400$ GeV), where no new physics is expected, for a selection of muon and dimuon kinematic variables. Figure 7.6 shows a comparison between simulation and data for events with $m_{\mu\mu} < 400$ GeV for the muon kinematic variables η , ϕ and p_T , while figures 7.7 and 7.8 show the dimuon rapidity and transverse momentum. Monte Carlo simulation provides a good description of the data for the muon kinematic variables and dimuon rapidity. A 5-6% discrepancy is found for values of muon η and dimuon rapidity smaller than -2. This discrepancy is covered by the systematic uncertainties, given the 4% uncertainty due to the Z-peak normalisation and the PDF-related uncertainties, cov-

Table 7.3: Cutflow table presenting the relative and cumulative efficiencies for each important criterion for the tight (3 station muons) and tight+loose (3+2 station muons) muon selection. The efficiency values correspond to Monte Carlo samples for the signal QBH process for M_{th} values of 1.0 and 2.0 TeV, each with 10000 generated events. Object quality includes the ID hits requirements together with the requirements on z_0 and d_0 .

Criterion	Relative Eff [%]		Cumulative Eff [%]	
	$M_{th} = 1$ TeV	$M_{th} = 2$ TeV	$M_{th} = 1$ TeV	$M_{th} = 2$ TeV
Trigger	90.1	88.6	90.1	88.6
2 Combined Muons	89.4	88.3	80.6	78.3
2 muons with $p_T > 25$ GeV	98.0	97.7	80.0	76.5
Object Quality	99.3	99.2	78.5	75.9
Isolation	98.8	99.2	77.5	75.4
3 (3+2) Station Muons	65.1 (69.6)	63.7 (67.6)	50.5 (54.3)	48.0 (51.4)
Charge	99.5 (99.4)	94.7 (94.6)	50.3 (54.0)	45.5 (48.6)
$m_{\mu\mu} > 80$ GeV	100.0 (100.0)	100.0 (100.0)	50.3 (54.0)	45.5 (48.6)
$m_{\mu\mu} < 4500$ GeV	99.8 (99.8)	96.7 (96.6)	50.2 (53.8)	44.1 (47.0)

Table 7.4: Cutflow table presenting the relative and cumulative efficiencies for each important criterion for the tight (3 station muons) and tight+loose (3+2 station muons) muon selection. The efficiency values correspond to Monte Carlo samples for the signal QBH process for M_{th} values of 3.0 and 4.0 TeV, each with 10000 generated events. Object quality includes the ID hits requirements together with the requirements on z_0 and d_0 .

Criterion	Relative Eff [%]		Cumulative Eff [%]	
	$M_{th} = 3$ TeV	$M_{th} = 4$ TeV	$M_{th} = 3$ TeV	$M_{th} = 4$ TeV
Trigger	87.9	87.1	87.9	87.1
2 Combined Muons	87.9	87.2	77.3	76.1
2 muons with $p_T > 25$ GeV	97.5	96.9	75.4	73.7
Object Quality	99.1	99.2	74.8	73.1
Isolation	99.5	99.7	74.5	72.9
3 (3+2) Station Muons	62.0 (65.6)	62.6 (66.3)	46.2 (49.0)	45.6 (48.3)
Charge	87.2 (87.0)	83.2 (82.8)	40.3 (42.4)	38.0 (39.8)
$m_{\mu\mu} > 80$ GeV	100.0 (100.0)	100.0 (100.0)	40.3 (42.4)	38.0 (39.8)
$m_{\mu\mu} < 4500$ GeV	81.8 (81.3)	59.8 (59.0)	33.0 (34.9)	22.4 (23.9)

ered in the following section and detailed in table 7.5. The dimuon transverse momentum distribution is not well described and requires further treatment. The effect that such poor description can have on the invariant mass distribution is investigated in appendix A and found to be negligible. Figure 7.9 shows the dimuon invariant mass distribution up to 400 GeV. Good agreement is found between data and the sum of all SM background simulated processes.

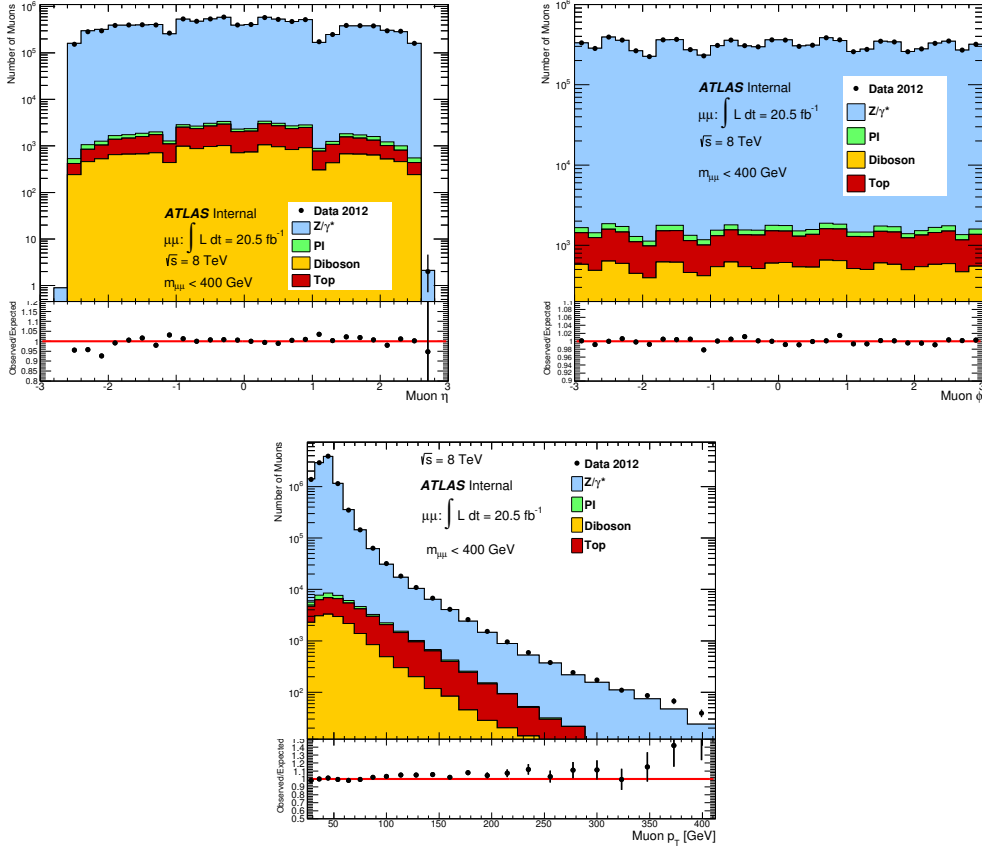


Figure 7.6: Reconstructed muon η (top left), ϕ (top right), and p_T (bottom) distributions for data and the SM background estimate using the Tight+Loose Muon selection for events with $m_{\mu\mu} < 400$ GeV.

7.3 Corrections applied

The ATHENA simulation of the ATLAS detector and the generation of Monte Carlo samples is done before data taking begins. It is therefore common that some aspects of the simulation are found to be different in real data taking conditions. Some relevant examples for this paper

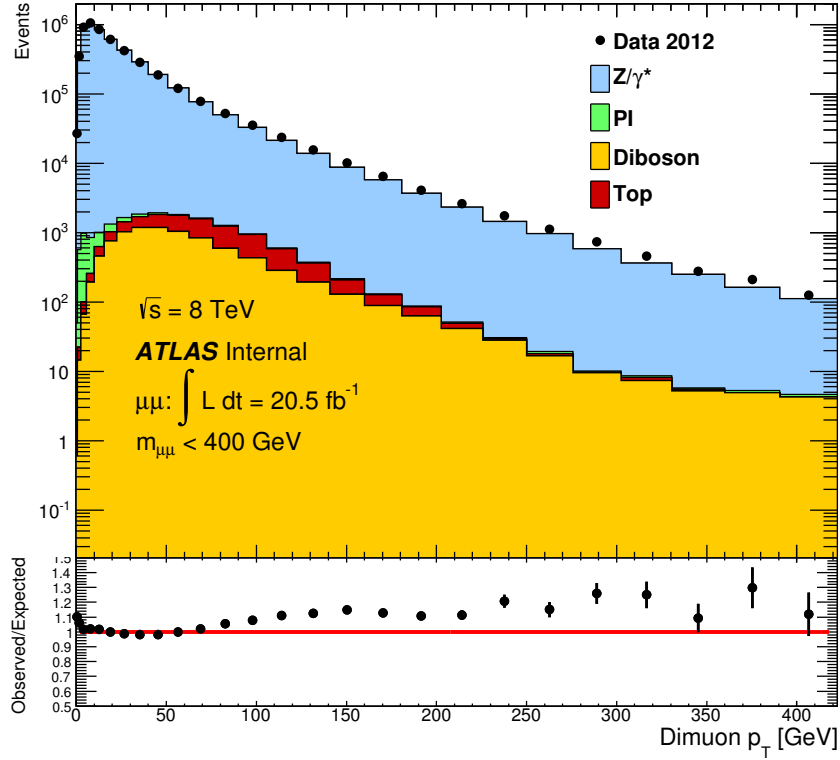


Figure 7.7: Comparison of the Dilepton p_T distribution in Data and Monte Carlo for events with $m_{\mu\mu} < 400$ GeV.

are the the muon momentum resolution and the muon reconstruction efficiency in different regions of the ATLAS detector. The performance groups within ATLAS develop software tools used to correct these differences in Monte Carlo simulated processes. These corrections are commonly called scale factors (SF). This section outlines the corrections applied to simulated processes in order to ensure a fair comparison between Monte Carlo and the 2012 data collected by the ATLAS detector.

7.3.1 Trigger Efficiency

The event selection described in section 7.2 requires that either the trigger `EF_mu24_i_tight` or `EF_mu36_tight` are fired to retain an event. The efficiency of such a trigger selection in data is found to be 99% [87]. The simulation of ATLAS can have discrepancies in the trigger efficiency found in data and that of the Monte Carlo simulated processes. A per event trigger

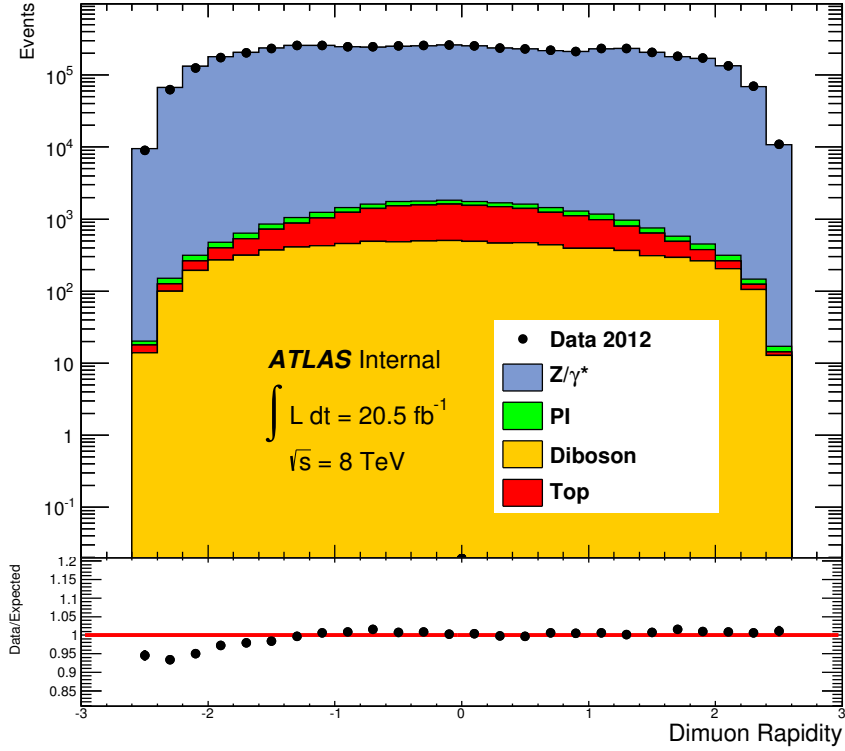


Figure 7.8: Comparison of the Dilepton Rapidity distribution in Data and Monte Carlo for events with $m_{\mu\mu} < 400$ GeV.

scale factor can then be obtained using the following equation [106]:

$$SF = \frac{1 - \prod_{n=1}^{N_l} (1 - \epsilon_{Data,l_n})}{1 - \prod_{n=1}^{N_l} (1 - \epsilon_{MC,l_n})} \quad (7.6)$$

where SF is the scale factor for a given trigger, ϵ_{Data,l_n} and ϵ_{MC,l_n} are the data and Monte Carlo efficiencies respectively, dependent on l_n , the number of muons in the event. Given that the analysis uses a relative normalisation to the Z-peak region, mass-independent corrections in Monte Carlo simulated processes are already taken into account. The corrections due to trigger efficiencies are expected to fall in this category. The validity of this statement is investigated using the official ATLAS tool to calculate the trigger scale factor: TrigMuon-Efficiency [107]. The version used is 00-02-48. The trigger SF as a function of the dimuon invariant mass for events passing the tight dimuon selection can be found in figure 7.10. Only Drell-Yan Monte Carlo is used to make the plot. The uncertainties shown in the plot are statistical uncertainties and are larger at the highest dimuon masses where statistical precision

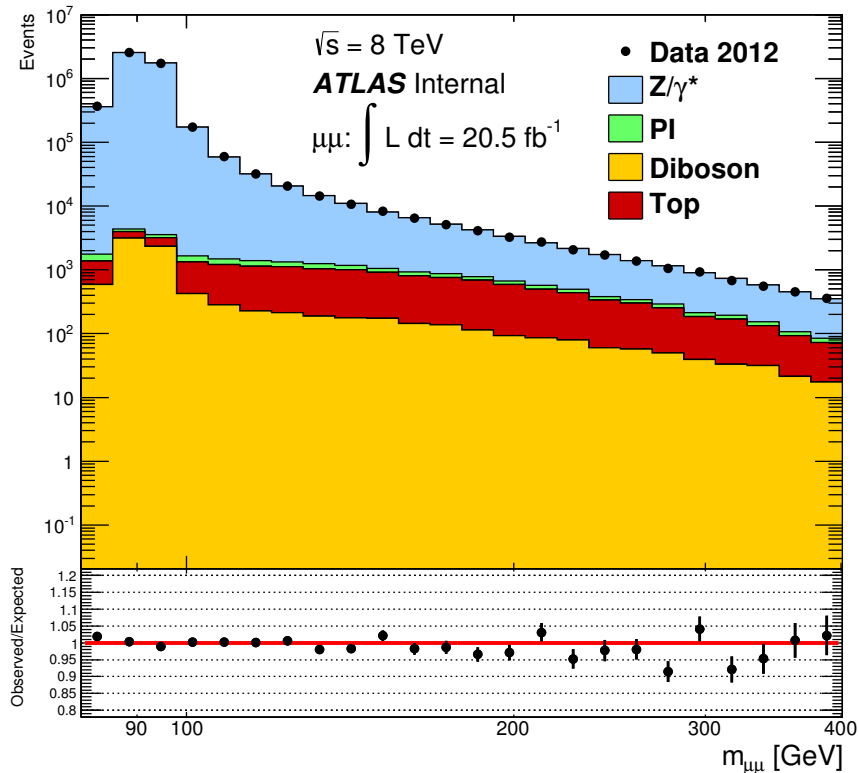


Figure 7.9: Comparison of the dimuon invariant mass distribution in Data and Monte Carlo for events with $m_{\mu\mu} < 400 \text{ GeV}$.

is poorer, beyond 3.0 TeV. As expected, the trigger SF does not have a strong dependence on the dimuon invariant mass and is therefore not used in this analysis.

7.3.2 Reconstruction Efficiency

The muon reconstruction efficiency is measured in data and simulation using a tag-and-probe method²¹ in $Z \rightarrow \mu^+\mu^-$ events. A full description of the method can be found in [108]. The discrepancies between data and simulation are taken into account using the ATLAS software MuonEfficiencyCorrections-02-00-15 [109]. The latest results show that the muon reconstruction efficiency is well described in simulation and that there is no significant p_T depen-

²¹The tag-and-probe uses a combined muon coming from a Z boson decay as the tag. The probe is a muon reconstructed in the inner detector, forming a dimuon pair with the tag close to the Z boson mass. The fraction of reconstructed probes is taken as the muon reconstructed efficiency.

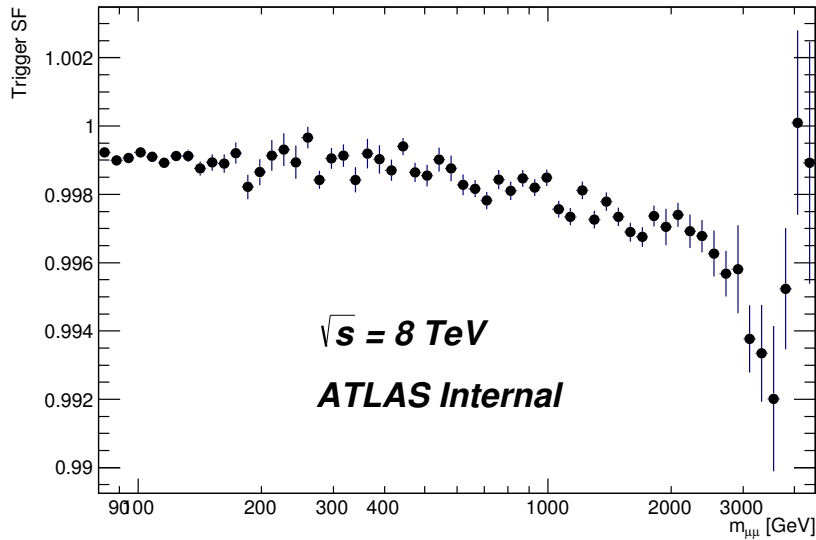


Figure 7.10: Average trigger scale factor as a function of the dimuon invariant mass.

dence [110]. The effect of the reconstruction scale factors is then expected to be taken into account by the Z -peak normalisation used in this analysis. The validity of this statement is checked using the official corrections included in the package `MuonEfficiencyCorrections`, which retrieves a SF depending on the muon p_T and η . Version 02-01-12 of the package was used. Figure 7.11 shows the efficiency SF against the dimuon invariant mass for simulated Drell-Yan events passing the tight dimuon selection. Only the Drell-Yan Monte Carlo is used to make the plot. Similarly to figure 7.10, the quoted errors are statistical. As expected, the efficiency SF does not depend significantly on the dimuon invariant mass as is therefore not used in this analysis.

7.3.3 Muon Momentum Scale and Resolution Corrections

The `MuonMomentumCorrections` is a software tool developed by the ATLAS MCP working group to account for differences in the muon momentum measurement between data and simulated processes. Misalignments in chambers in the ATLAS detector found during data taking are likely to not be included in Monte Carlo simulation. The scale of the momentum measured in data can also be different to that measured in Monte Carlo, leading to the momentum being underestimated or overestimated in simulation. Therefore, both resolution and scale corrections are required to ensure a fair comparison between data and simulated

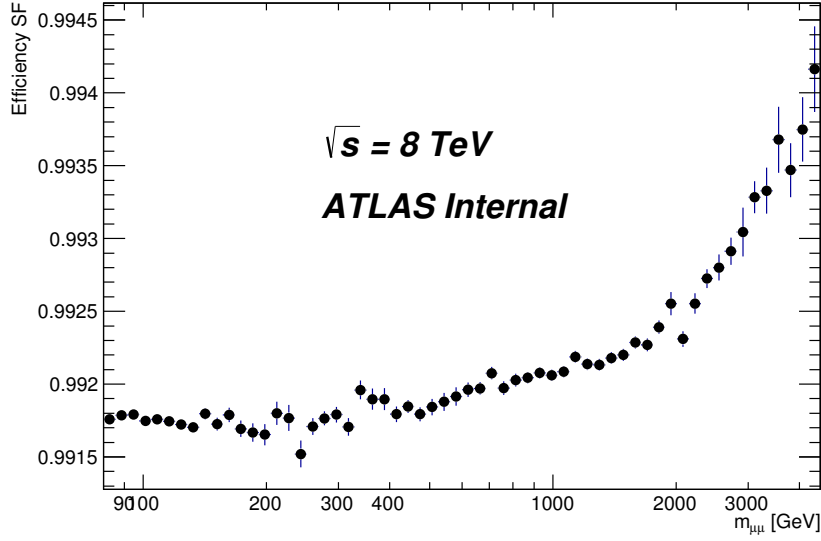


Figure 7.11: Average efficiency scale factor as a function of the dimuon invariant mass.

processes. The muon momentum resolution can be parametrized as:

$$\frac{\sigma_{p_T}}{p_T} = P_1 + P_2 \cdot p_T \quad (7.7)$$

Where P_1 and P_2 are resolution parameters related to the contributions from multiple scattering and intrinsic curvature resolution respectively [87, 111]. The first term is p_T -independent. As a result, the second term becomes dominant for $p_T \sim 100$ GeV. As the momentum of muons increases the intrinsic curvature due to the magnetic field in ATLAS is reduced, the tracks become straighter and the resolution of the momentum measurement is decreased. It should be noted that the resolution is also dependent on the region of the detector. Figure 7.12 shows the data and uncorrected Monte Carlo dimuon mass resolution for Combined muons from Z boson decays for different η regions of the detector. The muon momentum resolution for simulated processes does not accurately model that of the measured data. In all of the regions probed the resolution of the uncorrected simulation is better than that of the data. Corrections are then derived for the simulated muon transverse momentum as a function of η - ϕ in order to recover the resolution found in data. The corrected simulation ("Simulation with smearing") overcorrects in the region $|\eta| > 1.7$, although it should be noted that most of the muons fall in the region $|\eta| < 1.7$, where the corrected simulation is in good agreement with the data. Full details on the calculation of the corrections to the muon momentum can be found in [110] and [112].

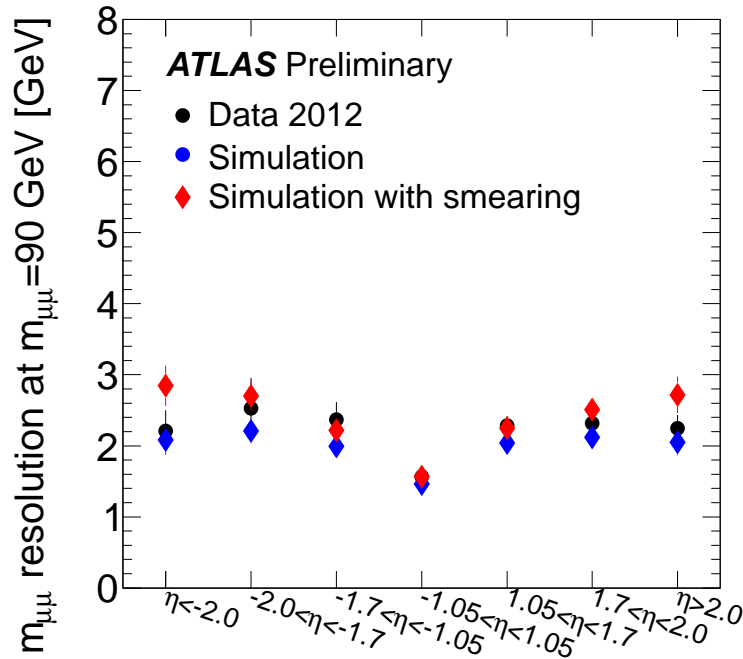


Figure 7.12: This plot shows the dimuon mass resolution for Combined muons coming from Z boson decays for data, simulated processes without corrections to the muon transverse momentum and simulated processes with the corrections applied. The resolution is the width of a Gaussian convoluted with the dimuon mass resolution at generator level [113].

Scale corrections are also applied to the muon transverse momentum. For 2012 data, these are however minor corrections and only reach 1% for the magnetic transition region ($1.4 < |\eta| < 1.7$) [110].

Figure 7.13 shows the average effect of the momentum corrections against the uncorrected muon p_T . Only simulated Drell-Yan events fulfilling all criteria outlined in section 7.2 are used for the plot. The corrections can be observed separately for muons inside and outside the barrel region. As can be observed, the corrections depend on the region in the detector where the muon is reconstructed. As expected from figure 7.12, the corrections for muons outside the barrel region of the ATLAS detector have a larger spread. Figure 7.14 on the left shows the effect on the invariant mass spectrum for selected Drell-Yan events and, on the right, the Z-peak region is shown for both corrected and uncorrected Monte Carlo and data. The corrections in the Z-peak improve agreement between simulation and data.

The version of the Muon Momentum Corrections tool used is *MuonMomentumCorrections-00-09-08*.

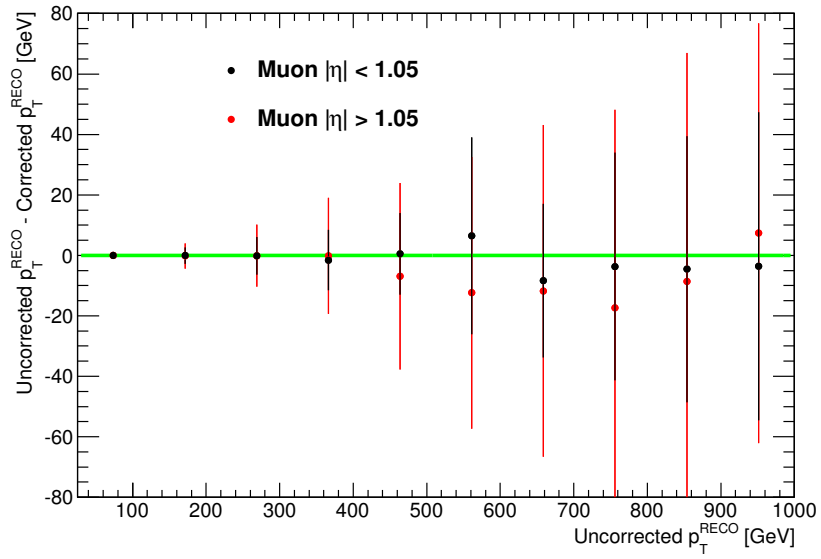


Figure 7.13: This plot shows the effect of the corrections on the muon transverse momentum with the RMS on the y-axis.

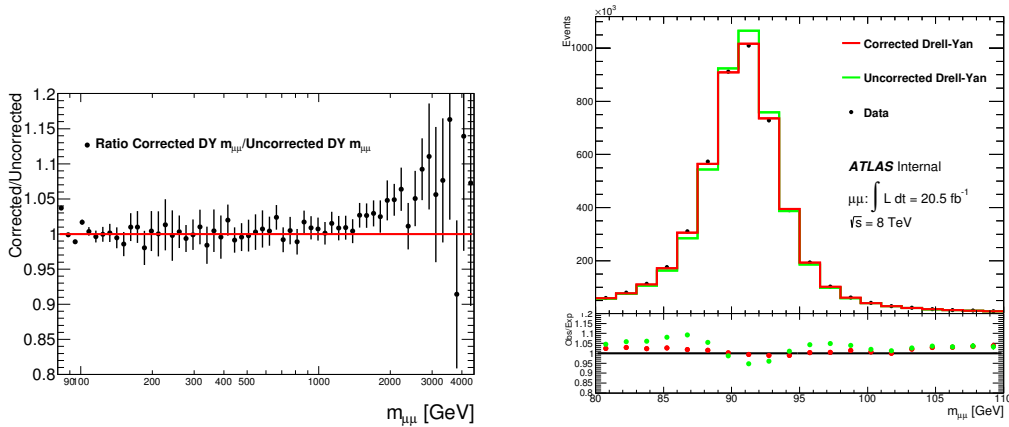


Figure 7.14: The ratio of the smeared and scaled and nominal reconstructed dimuon invariant mass distributions is shown on the left. The plot on the right zooms in the Z peak region to show the effect of the MuonMomentumCorrections.

7.4 Systematic Uncertainties

This section covers the systematic uncertainties associated with the SM background and signal processes estimation. Sources of systematic uncertainty are divided in two categories: theoretical and experimental. Uncertainties on the predicted cross section times branching ratio of the processes considered is regarded as a theoretical uncertainty, while uncertainties relating to detector limitations or simulation of the detector response are regarded as experimental uncertainties.

Both signal and Monte Carlo simulated processes are normalised to data in the region 80-120 GeV in dimuon invariant mass. As already mentioned, the advantage of such an approach is that the analysis is then insensitive to the uncertainty on the integrated luminosity and mass-independent uncertainties such as trigger or reconstruction efficiency scale factors. The analysis is however sensitive to the uncertainty on the $Z/\gamma^* \rightarrow \mu\mu$ production cross section in the normalisation region. Systematic uncertainties on the background estimation are calculated for the Drell-Yan process only as a function of the dimuon generator-level mass where relevant. The contributions from top and diboson backgrounds only comprise 5 and 8% respectively of the total SM background estimate at an invariant dimuon mass of 1.0 TeV. Therefore, the systematic uncertainties associated to the estimation of these processes is expected to have a negligible effect on the statistical analysis of the results. Theoretical uncertainties on signal processes are considered only if they affect the $A\epsilon$ of the process. That is part of the ATLAS Exotics Working Group recommendations to avoid bias due to the choice of theoretical uncertainties.

A list of the systematic uncertainties considered follows [22]:

Theoretical systematic uncertainties:

- $Z/\gamma^* \rightarrow \mu\mu$ production cross section
- PDF variation
- PDF choice
- PDF α_s scale
- EWK higher-order corrections
- Photon-Induced effect

Experimental systematic uncertainties:

- Muon charge mis-identification
- Muon momentum scale and resolution
- Muon Reconstruction Efficiency
- Beam energy scale
- Monte Carlo statistics

7.4.1 Theoretical systematic uncertainties

$Z/\gamma^* \rightarrow \mu\mu$ production cross section

A flat 4% uncertainty is assigned to both signal and background process cross sections to account for the uncertainty of the Z/γ^* production cross section in the normalisation region. The cross section calculation and its uncertainty due to PDF variation and α_s was computed using VRAP [114]. This uncertainty is larger than the luminosity uncertainty, estimated to be close to 3%, but as mentioned earlier using a normalisation to the Z -peak region has the advantage of making the analysis insensitive to mass independent systematic uncertainties.

PDF Variation

The method described in this paper to assess the uncertainty due to PDF variation is based on Appendices F and G of [87]. A summary of how systematic uncertainties on PDFs are determined can be found in section 3.3 of [33].

The variation of the set of independent parameters associated with each Parton Distribution Function (PDF), commonly referred to as the PDF eigenvectors, is used to obtain systematic uncertainties due to the PDF variation on the Drell-Yan process cross section. Each PDF set provides variations of these eigenvectors. Each eigenvector can be varied upwards or downwards. These parameter variations cause shifts on the predicted cross section times branching ratio of a given process. The asymmetric uncertainty on the cross section in each of the mass ranges considered can be calculated using the equations below:

$$\Delta\sigma^+ = \sqrt{\sum_{i=1}^n (\max(\sigma_i^+ - \sigma_0, \sigma_i^- - \sigma_0, 0))^2} \quad (7.8)$$

$$\Delta\sigma^- = \sqrt{\sum_{i=1}^n (\max(\sigma_0 - \sigma_i^+, \sigma_0 - \sigma_i^-, 0))^2} \quad (7.9)$$

where $\Delta\sigma^+$ and $\Delta\sigma^-$ are the asymmetric uncertainty on the cross section for a given mass range, σ_i^+ (σ_i^-) is the cross section for an upwards (downwards) shift of the i -th eigenvector of the PDF and σ_0 is the central cross section value calculated with the nominal PDF. Only the largest of the upwards or downwards variations of each eigenvector is used to estimate the systematic uncertainty on the cross section. The Drell-Yan cross section as a function of generator level $m_{\ell\ell}$ for each of the PDF eigenvector variations is computed using the program VRAP [114] with the MSTW2008nnlo PDF [86] and each of the 20 PDF eigenvector variations with the upwards and downwards variations at 90% Confidence Level (CL). The results are shown in figures 7.15 and 7.16.

Each of these eigenvector variations should be introduced in the statistical analysis as a separate systematic uncertainty. That would however increase the computing time required for the statistical analysis to prohibitive levels: running the full statistical analysis could potentially take more than a week. In order to improve computing time, PDF eigenvectors are grouped into four combinations with similar variations in dilepton mass ($m_{\ell\ell}$). The following list shows the eigenvectors in each combination. A minus sign means that the downwards eigenvector shift is exchanged with the upwards one so that each of the components shift the cross section in the same direction. A plus sign means that no such change is required [87].

- Group A consists of eigenvectors 2+, 13+, 14-, 17-, 18+ and 20+. It is dominant nowhere, but its contribution is not negligible.
- Group B consists of eigenvectors 3-, 4-, 9+ and 11+. It is dominant for $m_{\ell\ell} < 400$ GeV.
- Group C consists of eigenvectors 1+, 5+, 7+, and 8-. It is dominant in the range $400 \text{ GeV} < m_{\ell\ell} < 1500$ GeV.
- Group D consists of eigenvectors 10+, 12+, 15-, 16- and 19+. It is dominant for $m_{\ell\ell} > 1500$ GeV.

For each of these groups, the total asymmetric uncertainty on the Drell-Yan cross section at each mass point can be calculated using the following equations [87]:

$$\Delta\sigma_G^+ = \sqrt{\sum_{i=1}^{n_G} \text{sign}(\sigma_i^+ - \sigma_0)(\sigma_i^- - \sigma_0)} \quad (7.10)$$

$$\Delta\sigma_G^- = \sqrt{\sum_{i=1}^{n_G} \text{sign}(\sigma_0 - \sigma_i^+)(\sigma_0 - \sigma_i^-)} \quad (7.11)$$

where the summation is over the eigenvectors in a given group, sign is the sign of the term to ensure positivity and σ_i^+ (σ_i^-) is the cross section for the eigenvector upwards (downwards)

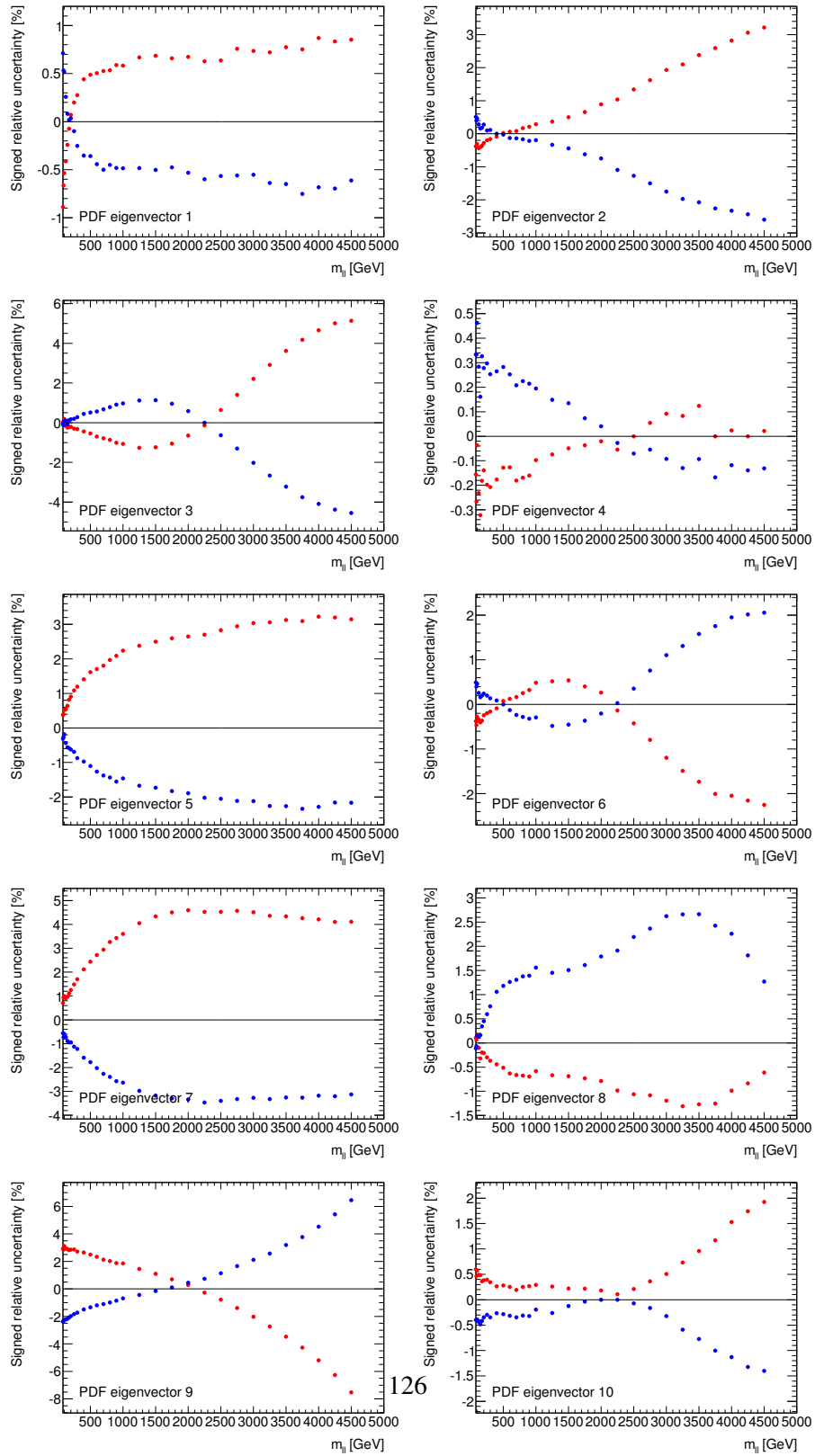


Figure 7.15: Asymmetric uncertainty on the Drell-Yan cross section as a function of generator level $m_{t\bar{t}}$ due to each PDF eigenvector taken separately. Here eigenvectors 1 to 10 are shown. The upwards and downwards PDF eigenvector variation are shown in red and blue respectively [87].

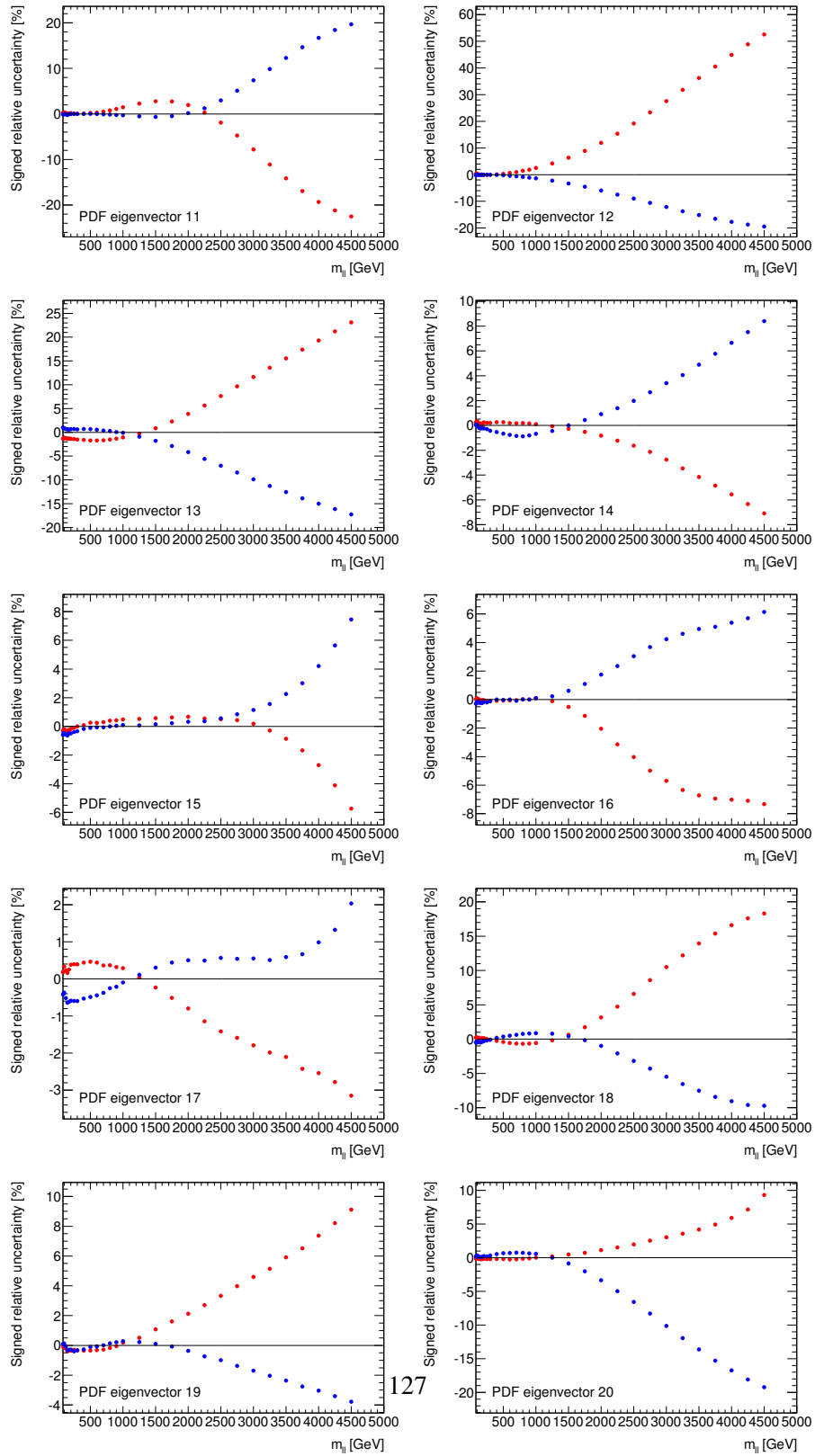


Figure 7.16: Asymmetric uncertainty on the Drell-Yan cross section as a function of generator level $m_{t\bar{t}}$ due to each PDF eigenvector taken separately. Here eigenvectors 11 to 20 are shown. The upwards and downwards PDF eigenvector variation are shown in red and blue respectively [87].

variation, or downwards (upwards) if the eigenvectors are exchanged to ensure a cross section shift in the same direction. Figure 7.17 shows the systematic uncertainty on the Drell-Yan cross section due to PDF variation against the generator-level invariant mass for each of the groups. The combination in quadrature of all the PDF uncertainties ("PDF All") is shown in black.

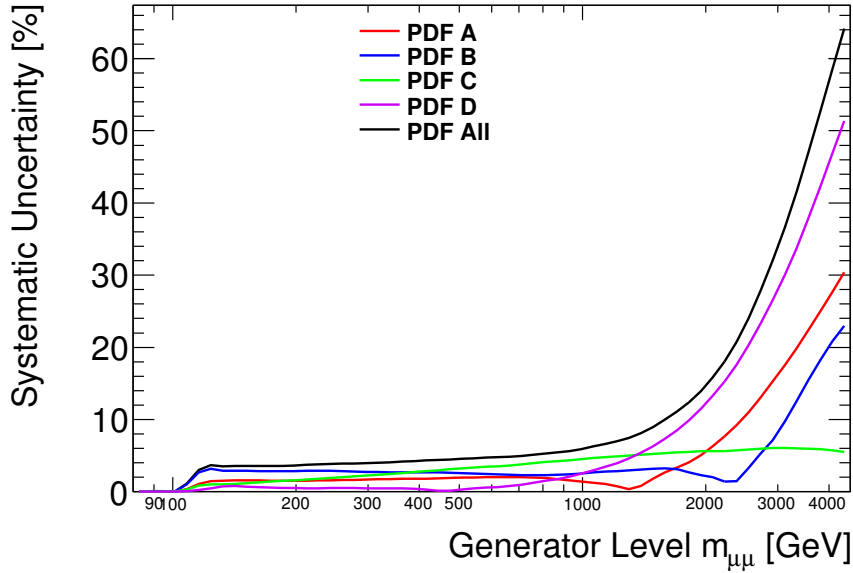


Figure 7.17: The systematic uncertainty due to PDF variation on the Drell-Yan cross section is shown for each of the PDF variation groups used as a function of generator level dimuon mass. The black line shows the addition in quadrature of all the PDF variation systematic uncertainties.

While the effect of PDF variation on the signal cross section is not considered as a systematic uncertainty for the statistical analysis, the effect on the signal acceptance was investigated for a Z' model in appendix F of [87]. Z' signal templates were produced for the 40 PDF error sets associated to each MSTW2008 and CT10. The signal acceptance was calculated for each of the variations with respect to the nominal acceptance and all variations were added in quadrature. The total uncertainty was found to be between 0.1% and 0.2% for the PDFs used. Given that the quantum black hole model uses the same search region and that the samples were generated with the same PDF (MSTW2008) this effect is then deemed negligible and not used for the statistical analysis of the results [87].

Given that the ADD LED search only makes use of the 1900-4500 GeV region in dimuon invariant mass, the PDF uncertainties on the calculation of the $A\epsilon$ no longer cancel in both numerator and denominator, as is the case for the QBH search. The effect of the PDF variation

on the A_ϵ is then found to be non-negligible, as can be seen in figure 7.18. Signal Monte Carlo at generator-level is reweighted using the sum in quadrature of the variations for each of the PDF combinations to recalculate the A_ϵ . A flat 3% uncertainty is obtained and used for the statistical analysis of the results.

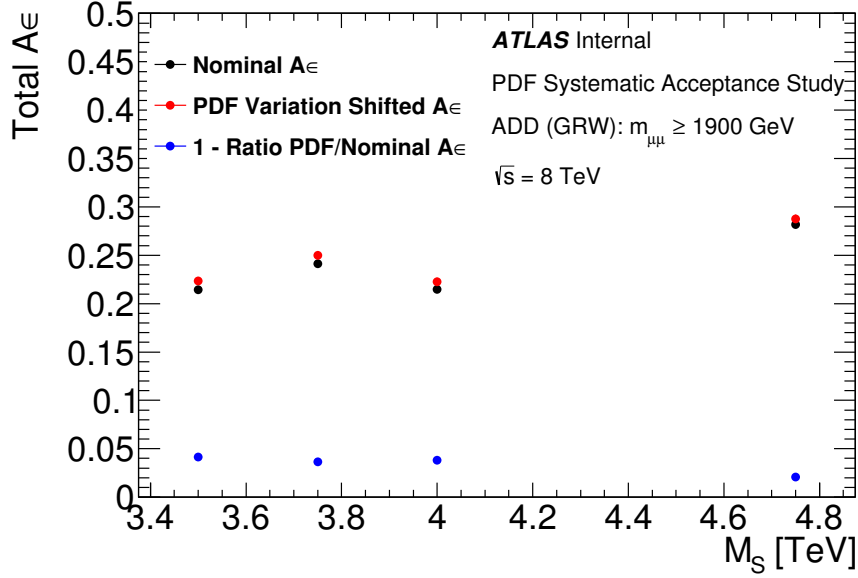


Figure 7.18: The A_ϵ for the ADD LED and its change due to PDF variation is shown for a few different benchmark values of M_S .

PDF Choice

To evaluate the systematic uncertainty due to the PDF choice, the Drell-Yan $\sigma \cdot \text{BR}$ values obtained from the central MSTW2008nnlo PDF set and its 90% C.L. error set are compared to the Drell-Yan $\sigma \cdot \text{BR}$ values obtained using the following PDFs sets at NNLO and $\alpha_s = 0.117$: CT10NNLO [85], NNPDF2.3 [115], ABM11 [116] and HERAPDF1.5 [117]. Except ABM11, the central values of the Drell-Yan $\sigma \cdot \text{BR}$ obtained from each of the PDF sets considered are compatible with the 90% C.L. error set of MSTW2008nnlo. An uncertainty is assigned to the Drell Yan cross section by taking the envelope of the PDF variation and the difference with ABM11 [87].

PDF α_s scale

The systematic uncertainty on the Drell Yan cross section due to the variation of the QCD coupling strength (α_s) is also evaluated. The Drell-Yan cross section as a function of $m_{\ell\ell}$

is evaluated for the 90% C.L. limits on α_s in the MSTW2008 PDF. The extremal variations of α_s correspond to values of 0.11365 and 0.12044. Figure 7.19 shows a summary of the PDF uncertainties on the Drell-Yan cross section. The largest contribution is from the PDF variation.

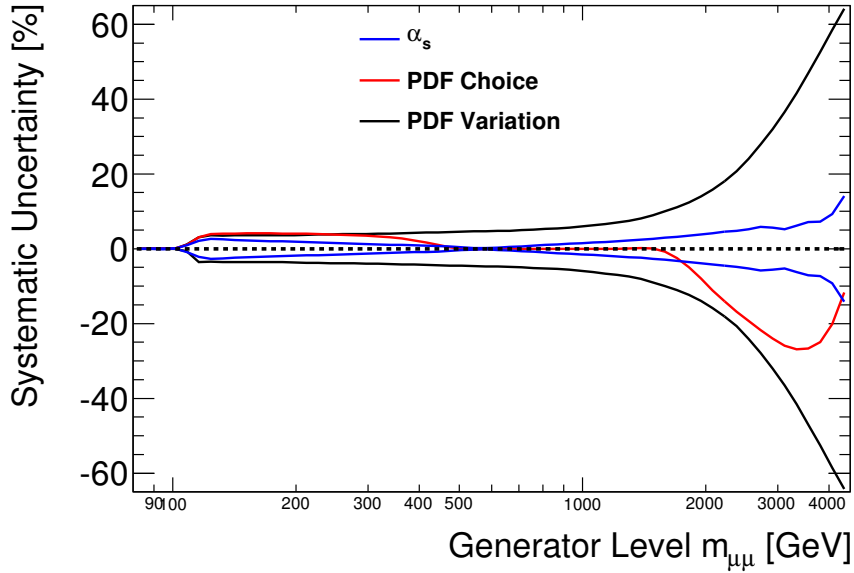


Figure 7.19: A summary of the PDF systematic uncertainties on the Drell-Yan cross section as a function of generator level dimuon mass.

EWK higher order corrections

Missing higher order electro-weak (EWK) corrections in the simulated Drell-Yan process can be obtained using two approaches: applying a constant factor for each QCD order (factored approach) or adding an additional cross section for each QCD order where this additional factor is dependent on the QCD order (additive approach). The version of FEWZ used to calculate the higher order EWK corrections is FEWZ 3.1.b2 and is based on the additive approach, which is argued to be the correct one from a theoretical point of view in [118] and taken to be the nominal one for the searches presented here. MC-SANC [119] is used to calculate the factors for both the additive and factor approaches as a function of dimuon invariant mass, with the former agreeing with the results from FEWZ within 0.2 and 0.3 %. A systematic uncertainty is assigned to account for the different results obtained using the factored and additive approaches. Figure 7.20 shows the systematic uncertainty due to this

difference as a function of generator level dilepton mass.

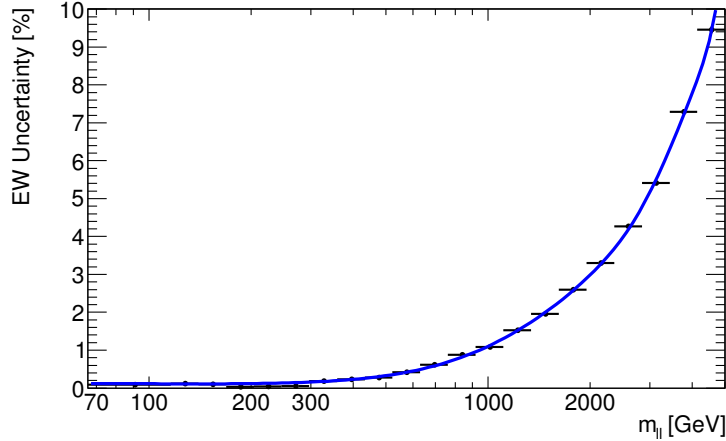


Figure 7.20: Systematic uncertainties due to different higher order EWK corrections calculations as a function of generator level dilepton mass. A quadratic fit to the points is shown in blue [87].

Photon-Induced effect

The systematic uncertainties due to the PI corrections are assessed differently for the ADD LED and the QBH searches due to the different approaches in estimating that background. For the QBH search, an average is taken from the upper and lower estimate of this background, as explained in section 6.3.4. The systematic uncertainty is then the difference between the average and the upper and lower limits of this background, obtained by calculating the PI corrections with current and constituent quark masses respectively. While the uncertainty on the PI K -factor is large (shown in figure 6.9), the PI background constitutes, for its upper estimate, 5% (10%) of the total Drell-Yan background at 1.0 (2.0) TeV in dimuon invariant mass. For the ADD LED search, where a full kinematic description of the event is required and dedicated Monte Carlo samples were generated, the upper estimate of the background using current quark masses is used as a central value. A systematic uncertainty is then obtained by studying the effect of not including the PI corrections in the Drell-Yan estimate (also shown in figure 6.9 as “Monte Carlo PI+DY + 1”). A conservative 100% uncertainty on the PI event yields is used for the statistical analysis.

7.4.2 Experimental systematic uncertainties

Muon charge misidentification

To study the effect of charge misidentification, reconstructed muons from simulated Drell-Yan events fulfilling all selection criteria are matched to generator level muons by requiring the ΔR between the reconstructed and generator level track to be less than 0.2. The reconstructed muon charge is then compared to the generator level charge. The possibility of charge misidentification for combined muons is expected to be small as the combined track uses information from both the ID and MS individual measurements. Given that the selection cuts require two opposite charge muons, a “good” event can be rejected if the charge of one of the muons is misidentified²². Figure 7.21 (top) shows the efficiency of the opposite charge requirement against the dimuon invariant mass using Drell-Yan Monte Carlo simulation. Up to 2.0 TeV in reconstructed dimuon invariant mass, the efficiency of the opposite charge requirement is close to 100%, at which point the efficiency of the opposite charge requirement starts to drop. As observed in table 7.2 for the Drell-Yan sample covering the range 2.0-2.25 TeV in generator level dimuon invariant mass, the opposite charge requirement has an efficiency of 96.5%, a decrease of 3% from the equivalent Drell-Yan sample in the 1.0-1.25 TeV range.

Charge identification is expected to be closely related to the muon transverse momentum: the straightness of the track increases with muon transverse momentum. Therefore, tracks with large transverse momentum are more likely to have its charge misidentified. Figure 7.21 (bottom) shows the charge misidentification rate as a function of the reconstructed muon transverse momentum. As expected, for muons below 1.0 TeV the charge misidentification rate is found to be negligible, albeit for muons with higher momentum the misidentification rate is found to be of about 3%. Given that at the time of writing no official ATLAS estimate of the muon charge misidentification rate exists, a conservative 20% systematic uncertainty is assigned to the measured misidentification rate. Such an approach is taken to account for the possibility that the measured charge misidentification rate in Monte Carlo simulation underestimates the misidentification rate found in data taking conditions. As shown in figure 7.22, adding an extra 20% to the measured misidentification rate yields a negligible change in the Drell-Yan dimuon mass spectrum (< 2% at 3.0 TeV). Therefore, the systematics associated to the estimation of the muon charge misidentification rate are not used in the statistical interpretation of the results.

Muon momentum scale and resolution

As explained in section 7.3.3, corrections are applied to Monte Carlo simulated processes to ensure that data and Monte Carlo have the same muon momentum resolution parameters. The systematic uncertainty associated to the use of these corrections is included in the official ATLAS MCP tool MuonMomentumCorrections, mentioned in section 7.3.3. The uncertainty on the smearing and scaling parameters applied to recover the resolution found in data is used

²²The probability of two muons in a pair having its charge misidentified is considered to be negligible. It should be noted that a “good” event would still be accepted if the charge of both muons was to be misidentified.

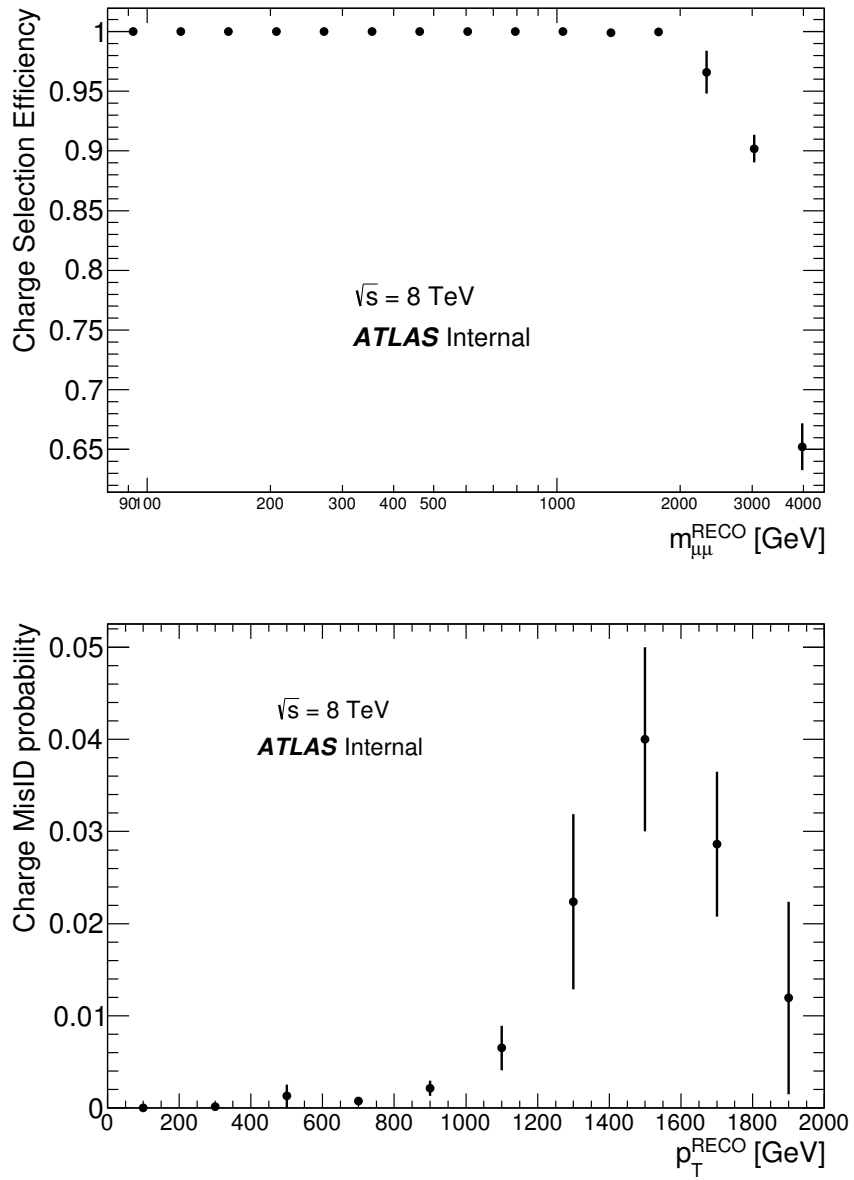


Figure 7.21: The charge selection efficiency (top) and the muon charge misidentification rate (bottom) is shown against the reconstructed invariant mass for the Monte Carlo simulated Drell-Yan process.

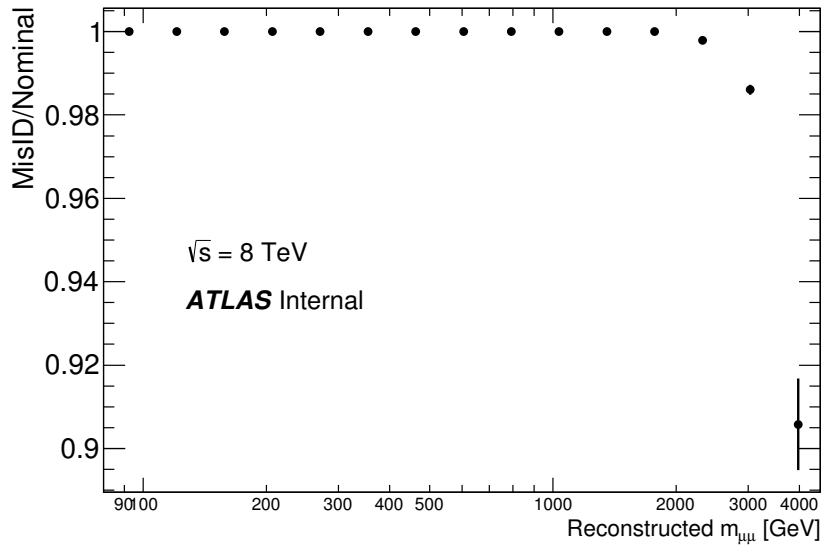


Figure 7.22: The plot shows the ratio between the Drell-Yan dimuon invariant mass spectrum obtained by increasing the rejection probability due to charge misidentification by 20% and the nominal Drell-Yan spectrum.

to estimate the possibility of oversmearing and overscaling by increasing these parameters by their respective uncertainty²³. The variations obtained by separately oversmearing and overscaling are combined in quadrature to obtain a total uncertainty. Figure 7.23 shows the total systematic uncertainty against the dimuon reconstructed mass, obtained by taking the ratio of the nominal Drell-Yan invariant mass spectrum and the oversmeared and overscaled one.

The effect of using the Muon Momentum Corrections on the mass spectrum is investigated, as shown in figure 7.14, as the smearing could cause a small non-resonant excess if low mass events migrate to higher masses. That uncertainty is only used in both signal and background processes for the ADD LED search.

Muon Reconstruction Efficiency

Reconstructed muons in both the ID and MS have to traverse the calorimeter region separating the two subdetectors. As a result of muons not being highly ionising, the expected energy

²³The systematic uncertainty associated to the possibility of undersmearing and underscaling is symmetric to the possibility of oversmearing and overscaling. Therefore, only the possibility of the latter is considered to obtain the systematic uncertainty.

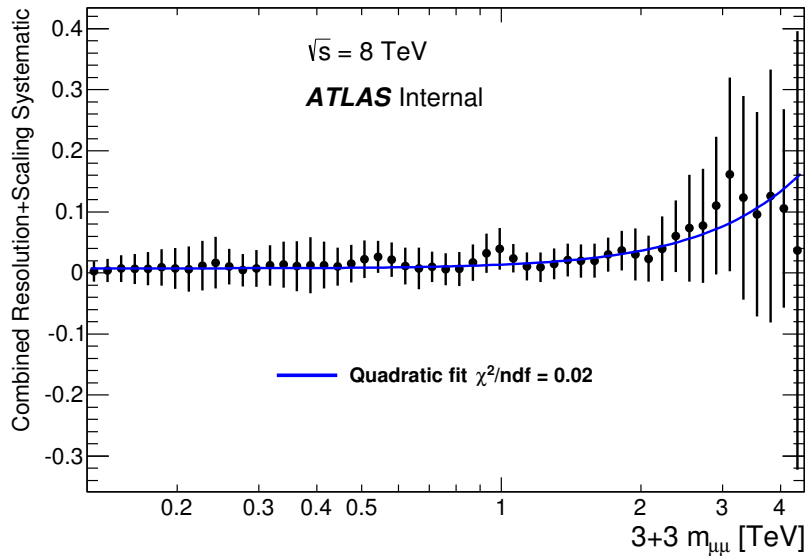


Figure 7.23: The total systematic uncertainty due the possibility of oversmearing and overscaling for Combined muons is shown against the reconstructed dimuon invariant mass. A quadratic polynomial fit is overlaid.

loss due to the Bremsstrahlung is expected to be of a few GeV for muons with a transverse momentum in the range 10-100 GeV. A correction is applied in the MS track to account for this loss based on the materials traversed by the relevant muon [87]. The muon reconstruction efficiency in Data and Monte Carlo were evaluated using a tag and probe method using a $Z \rightarrow \mu\mu$ decays, as described in appendix I.2 of [120]. However, the p_T range covered by this method is not expected to go beyond 100 GeV. Given the aim of the searches to probe the high mass region, the expectation is that muons can have p_T reaching the TeV scale. For such muons, the energy loss in the calorimeter via Bremsstrahlung is expected to be larger and could cause a reduction in the reconstruction efficiency. As such, Monte Carlo simulation was used to estimate the high p_T region, as explained in appendix K.1 of [120]. The reconstruction efficiency was found to drop by about 3.0%/TeV. Given the use of simulation to estimate the high p_T region, the inefficiency encountered in Monte Carlo was doubled artificially as a conservative measure. Assuming a 100% uncertainty in this estimate, the expected decrease in efficiency for invariant dimuon masses of 1.0 TeV was found to be of the order of 3.0%.

Beam energy

The uncertainty on the beam energy of the LHC during the 2012 data taking has been documented in [121] and found to be close to 30 GeV. Figure 7.24 shows the effect for various benchmark SM processes. The effect on the Drell-Yan cross section is negligible in the normalisation region but reaches 5% at a dilepton invariant mass of 3.0 TeV. For the ADD signal process, the uncertainty is the same as for the background process due to interference with Drell-Yan. For the QBH search, the effect is investigated by calculating the signal cross section with the upwards and downwards shift on the beam energy. This is found to have a negligible impact on the signal cross section (<1%). The effect on the other SM backgrounds is neglected due to their relatively small contributions.

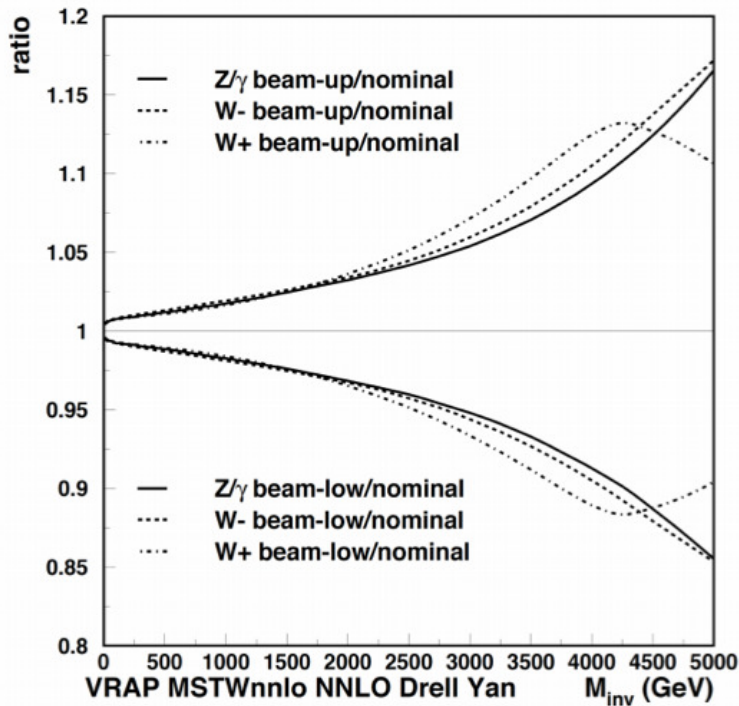


Figure 7.24: The ratio between the beam uncertainty shifted cross section and the nominal cross section for vector boson production at 8 TeV is shown for increasing invariant mass [121].

Monte Carlo statistics

The statistical uncertainties due to the statistical precision of the Monte Carlo simulated processes are combined with the uncertainty on the top background extrapolation. The statistical uncertainty on the Monte Carlo simulated Drell-Yan is found negligible due to the use of samples binned in generator level dimuon invariant mass. Therefore, this uncertainty is not

used in the background for the statistical interpretation. For signal processes, given the lower statistical precision, this uncertainty is used in the statistical interpretation.

7.4.3 Summary

A summary of the systematic uncertainties for the signal and background processes can be found in table 7.5.

For background processes, the systematic uncertainty is driven the PDF-related uncertainties. The PDF variation is the leading uncertainty, followed by the PDF Choice. The combined uncertainty from these two processes alone reaches 20% for dimuon masses of 3.0 TeV. The effect of uncertainty on the contribution from the PI corrections is the largest non-PDF related uncertainty given the decision to use a 100% uncertainty on this background contribution. The effect of experimental uncertainties such as the scale and resolution corrections, beam energy and statistical uncertainties are small compared to the theoretical PDF uncertainties.

For signal processes, given that PDF uncertainties are only considered if they affect the signal acceptance, the leading systematic effects are experimental ones and the overall uncertainty is lower than for background processes. Due to the decreasing muon momentum resolution with increasing dimuon mass, the uncertainty on the scale and resolution corrections becomes the leading systematic effect for dimuon masses of 3.0 TeV. Statistical uncertainties are larger than those for background processes due to lower statistical precision but still represent a small contribution to the overall systematic uncertainty. It should be noted that given the nature of the ADD LED search, with a search performed in a single mass bin, the uncertainties applied on that process are more conservative than those for the QBH search, giving a larger overall systematic uncertainty. As an example, the effect of the PDF variation on the signal acceptance for the QBH search is found to be negligible, while for the ADD LED search a 3.0% uncertainty is obtained.

7.5 Data-Monte Carlo comparison

After applying the event selection to both data and Monte Carlo simulated processes, using all the corrections described above and normalising to the 80-120 GeV region in reconstructed dimuon invariant mass, the SM expectation is compared to data. The Z-peak normalisation scale factor after normalising to known luminosity for the standalone tight muon selection used for the ADD LED search is 0.99, while for the combination of tight and loose muon selections for the QBH search is 0.98.

Figure 7.25 and 7.26 show the reconstructed dimuon invariant mass distribution for the region

Table 7.5: Quantative summary of the systematic uncertainties taken into account for the expected number of events in the non-resonant dilepton analysis. Values are provided at three relevant benchmark dilepton masses of 1 TeV (2 TeV) [3 TeV]. N/A indicates that the uncertainty is not applicable.

Source	Signal ADD LED	Signal QBH	Background
Normalization	4.0% (4.0%) [4.0%]	4.0% (4.0%) [4.0%]	4.0% (4.0%) [4.0%]
PDF Variation	3.0% (3.0%) [3.0%]	< 0.1% (< 0.1%) [< 0.1%]	5.0% (12.0%) [17.0%]
PDF Choice	N/A	N/A	1.0% (6.0%) [12.0%]
α_s	N/A	N/A	1.0% (3.0%) [4.0%]
EW Corrections	N/A	N/A	1.0% (3.0%) [3.0%]
Photon-Induced	N/A	N/A	6.5% (9.5%) [10.5%]
Momentum Corrections	3.0% (6.0%) [9.0%]	N/A	3.0% (6.0%) [9.0%]
Efficiency	3.0% (6.0%) [9.0%]	3.0% (6.0%) [9.0%]	N/A
Scale/Resolution	1.0% (4.0%) [10.0%]	1.0% (4.0%) [10.0%]	1.0% (4.0%) [10.0%]
Beam Energy	1.0% (3.0%) [5.0%]	< 1.0% (< 1.0%) [< 1.0%]	1.0% (3.0%) [5.0%]
Charge MisID	< 0.1% (< 0.5%) [< 2.0%]	< 0.1% (< 0.5%) [< 2.0%]	< 0.1% (< 0.5%) [< 2.0%]
Statistical	3.0% (3.0%) [3.0%]	3.0% (3.0%) [3.0%]	0.5% (0.5%) [0.5%]
Total	6.7% (11.5%) [17.3%]	5.8% (8.8%) [14.3%]	9.2% (18.7%) [27.8%]

80-4500 GeV after applying the full event selection outlined in section 7.2, for the QBH and ADD LED searches respectively. The expected signal shape for a selection of M_S and M_{th} values is overlaid to show how the data would differ from SM expectation if any of the models searched for were to be correct in the range considered. The band in the ratio represents the combination in quadrature of all the systematic uncertainties. The data point close to 2.0 TeV is above Standard Model expectation, but the significance of this excess is found to be a little below 2.0σ , as shown in figure 9.1. Tables 7.6 and 7.7 show the expected and observed event yields in different reconstructed invariant mass bins.

Table 7.6: The expected and observed number of events in the combined (tight + loose) dimuon channel for the QBH search. The region 80-120 GeV is used to normalize the total background to data. The errors quoted are the combination of statistical and systematic uncertainties, except for the total background expectation numbers where the statistical and systematic uncertainties are quoted separately and in that order [87].

Process	$m_{\mu\mu}$ [GeV]					
	120 – 200	200 – 400	400 – 800	800 – 1200	1200 – 3000	3000 – 4500
Drell-Yan	68000 ± 4000	11000 ± 700	1000 ± 60	49 ± 5	7.3 ± 1.1	0.034 ± 0.022
Top	5650 ± 350	2300 ± 140	160 ± 10	3.0 ± 1.7	0.17 ± 0.15	0 ± 0
Diboson	1220 ± 60	520 ± 30	65 ± 4	4.2 ± 0.4	0.69 ± 0.05	0.002 ± 0.001
Total	$74770 \pm 280 \pm 4000$	$13820 \pm 90 \pm 720$	$1180 \pm 10 \pm 70$	$56.2 \pm 0.4 \pm 5.8$	$8.16 \pm 0.04 \pm 1.03$	$0.036 \pm 0.001 \pm 0.009$
Data	73836	13479	1122	49	8	0

Figures 7.27 and 7.28 show the dimuon transverse momentum and rapidity in the region $m_{\mu\mu} > 400$ GeV. The Monte Carlo description of both distributions in data is reasonable,

Table 7.7: Expected and observed event yields in the dimuon channel for the tight dimuon channel in the ADD LED search. The region 80-120 GeV is used to normalize the total background to data. The quoted errors consist of both the statistical and systematic uncertainties added in quadrature, except for the total background expectation numbers where the statistical and systematic uncertainties are quoted separately and in that order [22]

Process	$m_{\mu\mu}$ [GeV]					
	120 – 200	200 – 400	400 – 800	800 – 1200	1200 – 3000	3000 – 4500
Drell-Yan	64000 ± 3830	10100 ± 700	887 ± 53	45 ± 5	6.5 ± 0.9	0.027 ± 0.008
Top	5400 ± 330	2170 ± 130.0	144.3 ± 10.1	1.66 ± 0.70	0.11 ± 0.05	< 0.002
Diboson	1170 ± 60	488 ± 27	62.9 ± 3.0	3.75 ± 0.26	0.62 ± 0.04	< 0.003
Photon-Induced	1100 ± 1100	400 ± 400	47 ± 47	3.3 ± 3.3	0.57 ± 0.57	< 0.006
Total SM	$71000 \pm 270 \pm 4000$	$13100 \pm 90 \pm 720$	$1140 \pm 10 \pm 70$	$53.6 \pm 0.3 \pm 6.0$	$7.85 \pm 0.04 \pm 1.05$	$0.032 \pm 0.001 \pm 0.009$
Data	70724	12912	1079	47	8	0

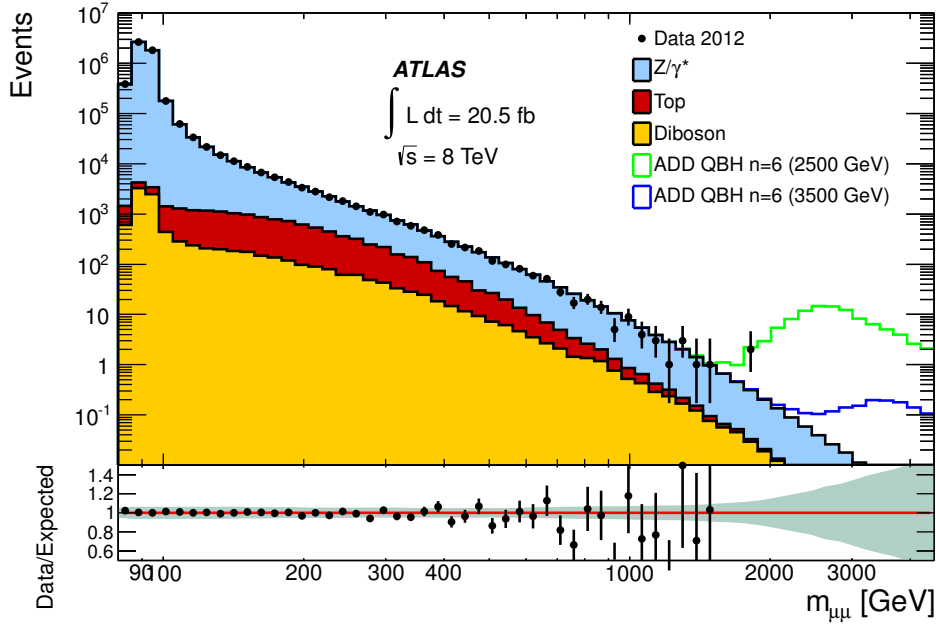


Figure 7.25: Comparison of the invariant mass distribution for data and Monte Carlo for the QBH search combining the tight (3-station) and loose (2-station) muon selection. The expected QBH signal dimuon invariant mass distribution for two benchmark M_{th} values is shown. The ratio plot shows the ratio between data and the SM background. The grey band shows the range covered by all systematic uncertainties added in quadrature.

with discrepancies covered by statistical errors and the expected systematics in the high mass region. Appendix A shows that the modelling of the dimuon p_T spectrum has a negligible impact on the dimuon invariant mass spectrum. The comparison between data and Monte Carlo is also shown for the muon kinematic variables η, ϕ and p_T in figure 7.29. Similarly,

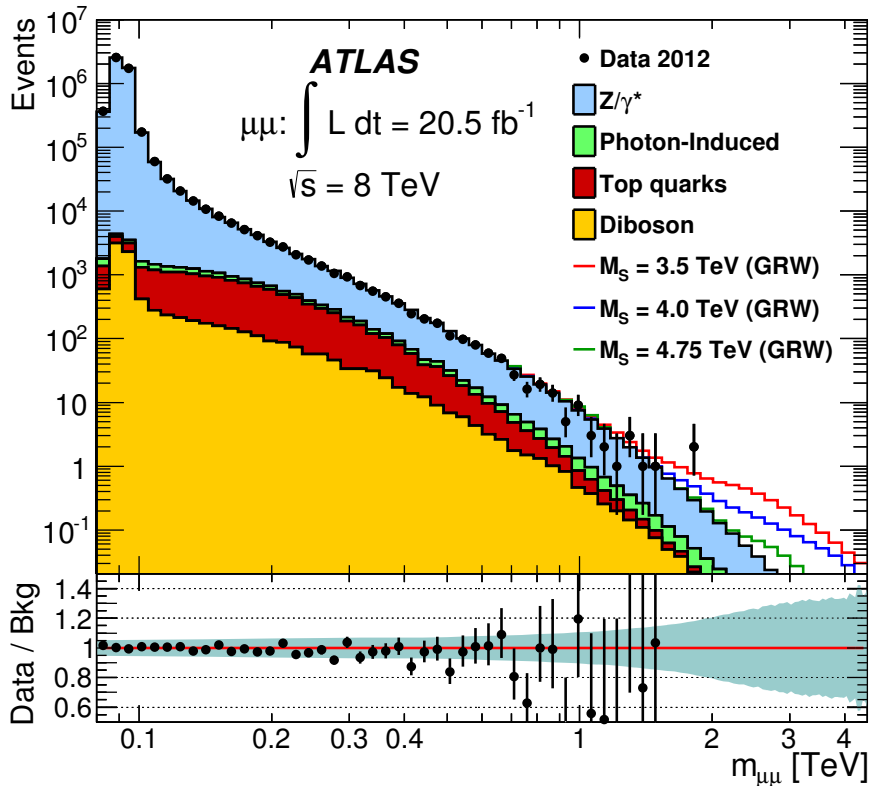


Figure 7.26: Comparison of the invariant mass distribution for Data and Monte Carlo for the ADD LED search. Only 3-station muons are used for this search. The expected signal ADD LED+Drell-Yan invariant mass distribution for three benchmark M_S values is shown. The ratio plot shows the ratio between data and the SM background. The grey band shows the range covered by all systematic uncertainties added in quadrature.

the Monte Carlo provides a reasonable description of the data. It should be noted that, as can be clearly observed in the muon ϕ distribution, the Monte Carlo overestimates the data by 7-8% in the region $m_{\mu\mu} > 400 \text{ GeV}$. Such a discrepancy is covered by the statistical uncertainty on data and the expected uncertainty on the background, as shown in tables 7.6 and 7.7.

There is no evidence for an excess in data from SM expectation. The following chapter outlines the statistical methods used to test the agreement between data and SM expectation.

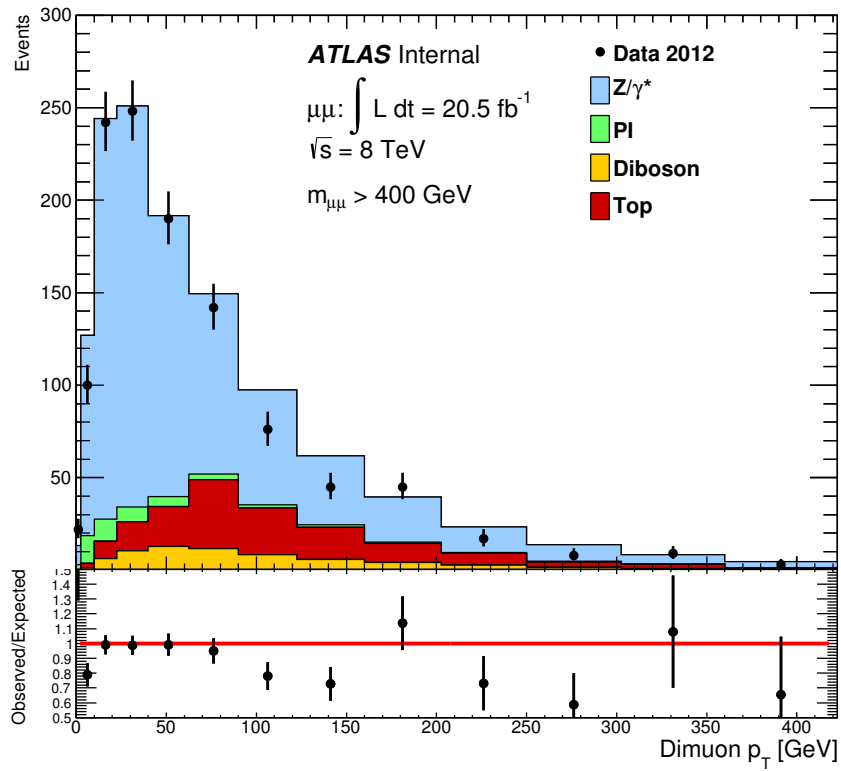


Figure 7.27: Comparison of the Dilepton p_T distribution in Data and Monte Carlo for $m_{\mu\mu} > 400$ GeV.

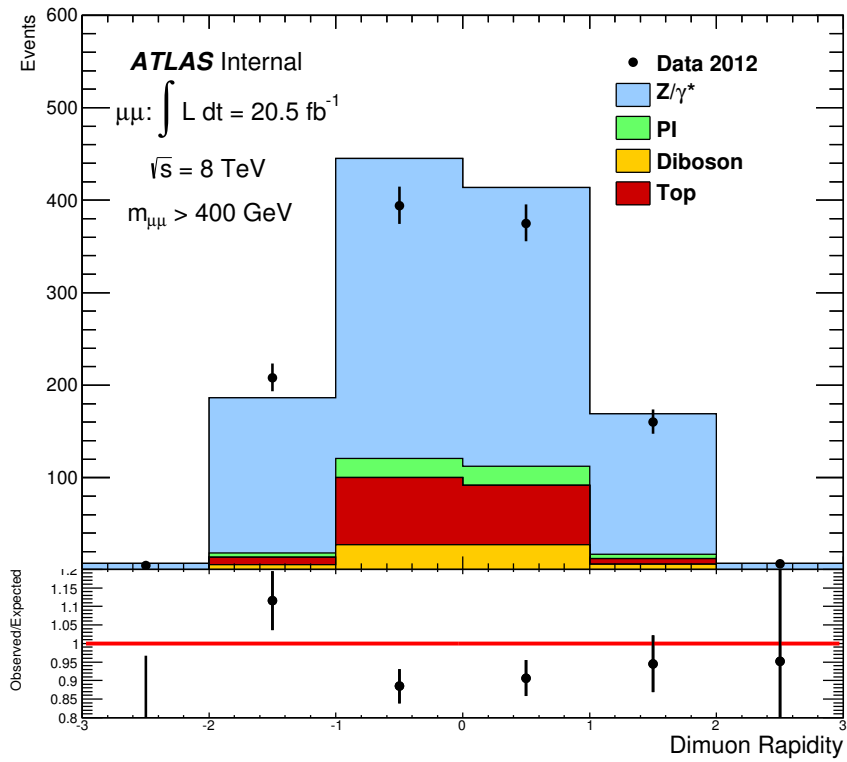


Figure 7.28: Comparison of the Dilepton Rapidity distribution in Data and Monte Carlo for $m_{\mu\mu} > 400 \text{ GeV}$.

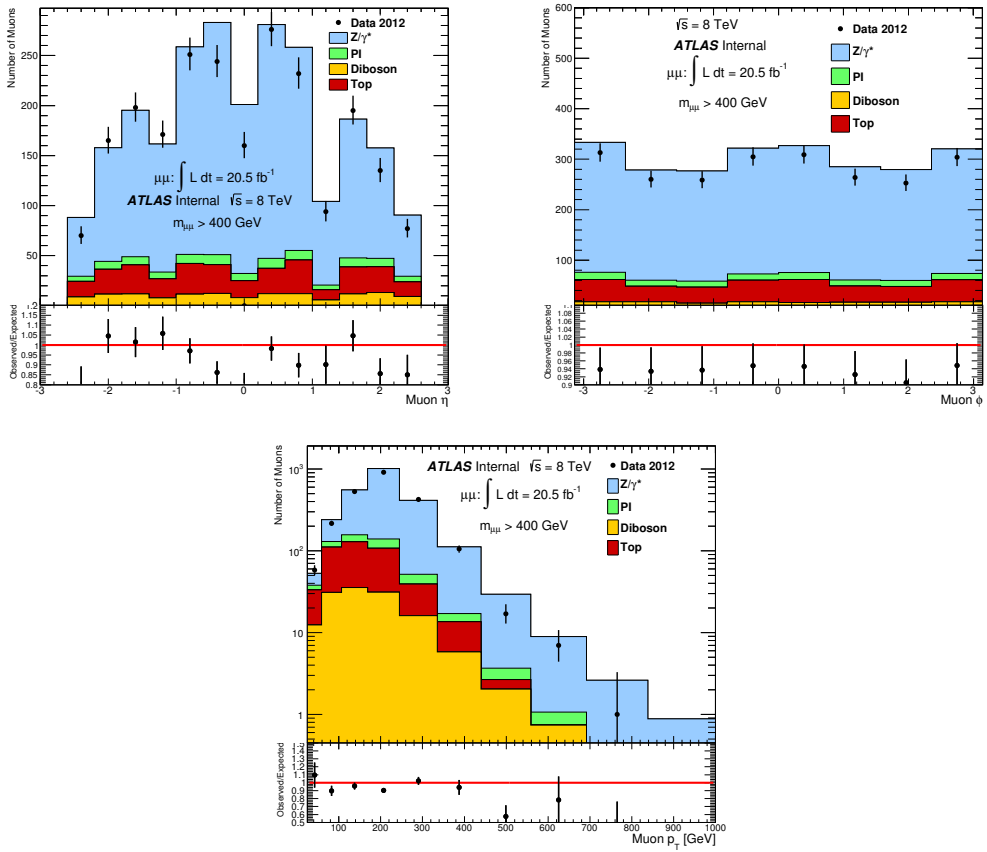


Figure 7.29: Reconstructed muon η (top left), ϕ (top right), and p_T (bottom) distributions for data and the SM background estimate using the Tight+Loose Muon selection for $m_{\mu\mu} > 400 \text{ GeV}$.

8 Statistical Analysis

The aim of the statistical analysis is to test the consistency of the data collected by the ATLAS detector against the SM background only and Signal+SM background hypotheses. If an excess is observed in data above SM expectation, the goal is to quantify its significance and to test the agreement with the Signal+SM background hypothesis. If no excess is found and the SM only hypothesis is found to be valid, exclusion limits are derived on the fundamental parameters of the signal BSM physics models under investigation.

A Bayesian treatment is used for the statistical analysis. A short review of Bayesian statistics is followed by the methods and techniques used in the ATLAS Exotics Working Group to quantify a potential excess and extract exclusion limits. The Bayesian statistical treatment is handled with the help of a software package called Bayesian Analysis Toolkit (BAT), presented in [122]. The statistical analysis used for the ADD LED and QBH searches is broadly similar but has some subtle differences which are discussed throughout this chapter. The term exclusion limit will be used to refer to the 95% Bayesian upper limit.

This chapter is largely based on chapters 1.1 and 1.2 of [123] and the ATLAS internal note [124].

8.1 Bayesian Statistical Interpretation and limit setting

In Bayesian statistics, the interpretation of probability is that of a subjective probability, which represents the degree of belief in a given hypothesis. The Bayesian probability interpretation is encapsulated in Bayes' theorem. For a given observed data sample A and a hypothesis B :

$$P(B|A) = \frac{P(A|B)}{P(A)}P(B), \quad (8.1)$$

where $P(A|B)$ is the probability of observing A assuming the hypothesis B is true, $P(B)$ is subjective part of this approach: the prior probability (the degree of belief in hypothesis B), $P(A)$ acts as a normalisation constant and $P(B|A)$ is the posterior probability of hypothesis B being true assuming the observation of A . Since $P(A)$ is a constant and non-zero, it is common to write an expression for the posterior probability in the following manner:

$$P(B|A) \propto P(A|B)P(B) \quad (8.2)$$

The posterior probability of hypothesis B given the observed data is then proportional to the subjective degree of belief on hypothesis B and the probability of observing the data under the assumption that such a hypothesis is true, normally referred to as the likelihood. In the context of a search for BSM physics, the hypothesis is that the observed data is a combination

of the existing SM and a new physics model, which is the signal being searched for. As such, it is common to write the likelihood (\mathcal{L}) as the Poissonian probability of observing n_{obs} events:

$$\mathcal{L}(n_{obs}|\mu) = \frac{\mu^{n_{obs}} e^{-\mu}}{n_{obs}!} \quad \text{where} \quad \mu = n_{signal} + n_{SM} \quad (8.3)$$

where n_{signal} and n_{SM} are the expected number of signal and SM background events respectively and n_{obs} is the number of observed events in data. The number of expected signal events is dependent on a parameter of interest (θ) associated with the signal model. Therefore, equation 8.3 can be rewritten in terms of the expected number of events as a function of θ .

Systematic uncertainties affecting the signal and background event yields are introduced in the likelihood as nuisance parameters. Nuisance parameters are defined as parameters other than the parameter of interest that affect the expected signal and background event yields of the model. Assuming a vector of nuisance parameters $\hat{\Omega}$ the likelihood takes the following form:

$$\mathcal{L}(n_{obs}|N(\theta), \hat{\Omega}) = \frac{\mu^{n_{obs}} e^{-\mu}}{n_{obs}!} \prod_{i=1}^{N_{Sys}} G(\Omega_i, 0, 1) \quad \text{where} \quad \mu = \sum_j N_j(\theta)(1 + \Omega_i \epsilon_{ij}) \quad (8.4)$$

where $N(\theta)$ is the total number of expected events as a function of the parameter of interest, ϵ_{ij} is the relative change in event yields for signal ($j=1$) and background ($j=2$) due to the systematic uncertainty i and $G(\Omega_i, 0, 1)$ is a unit Gaussian assumed to be the probability density function for the nuisance parameter Ω_i . All systematic errors are assumed to be Gaussian in nature.

The dependence of the likelihood on the vector of nuisance parameters is removed by the use of a Markov Chain Monte Carlo (MCMC) integration technique [125] included in the BAT. This integration is performed by the BAT assuming that systematic uncertainties are uncorrelated, but uncertainties affecting both signal and background processes are correlated. The marginalised likelihood \mathcal{L}' is the result of the integrating out the vector of nuisance parameters:

$$\mathcal{L}'(n_{obs}|N(\theta)) = \int \mathcal{L}(N(\theta), \Omega_1, \dots, \Omega_N) d\Omega_1, \dots, d\Omega_N \quad (8.5)$$

the likelihood is now only dependent on the parameter of interest chosen and the usefulness of Bayes theorem for BSM searches is highlighted. A posterior probability density function for the parameter of interest can now be constructed. A 95% Bayesian upper limit on θ can then be obtained by integrating the posterior probability distribution:

$$P(N(\theta)|n_{obs}) = \frac{1}{\mathcal{Z}} \mathcal{L}'(n_{obs}|N(\theta))P(\theta) \quad (8.6)$$

$$0.95 = \frac{\int_0^{\theta_{95}} \mathcal{L}'(n_{obs}|N(\theta))P(\theta)d\theta}{\int_0^{\infty} \mathcal{L}'(n_{obs}|N(\theta))P(\theta)d\theta} \quad (8.7)$$

where \mathcal{Z} is a normalisation constant and θ_{95} is the value of the parameter of interest for which the 95% Bayesian upper limit is obtained. These calculations are also performed using the BAT. The choice of prior probability and parameter of interest are dependent on the model being searched for and are discussed in the following sections. For both the ADD LED and QBH searches the discriminant variable for the search is the dilepton invariant mass spectrum. In order to obtain an expected limit for the SM only hypothesis, a 1000 pseudo-experiments (PE) are run for each formalism of each model. Due to the effect of systematic uncertainties and the random walk method used in MCMC integration techniques, each PE can yield different 95% Bayesian upper limits for the parameter of interest. The expected exclusion limit for the parameter of interest of each model is then the median of the expected limit PE distribution. The one and two standard deviation intervals on the expected limit are obtained from the spread of 95% Bayesian upper limits obtained for the 1000 PE run with the BAT.

8.2 ADD Large Extra Dimensions

For the ADD LED search, a single bin counting experiment above a minimum dilepton invariant mass threshold is used to search for new physics. The expected and observed event yields in a single dilepton invariant mass bin are used to form the likelihood function, shown in equation 8.3. The single bin approach is appropriate given that ADD LED predicts a broad non-resonant excess, as shown in figure 7.26. Given that the signal turn-on is sharp, by optimizing the lower mass threshold of the single bin the signal to background ratio can be maximised. Also, since the cutoff at M_S can be argued to be unphysical, by using a single bin approach the focus is on the number of expected signal events in the search bin, rather than on the shape of the excess, which could be poorly described by the Monte Carlo simulation. The magnitude of the excess from SM expectations depends on the value of M_S . For an M_S of 3.0 TeV the excess could start to be observed at dimuon invariant masses around 900-1000 GeV, as shown in figure 8.1. If the value of M_S is higher than 5.0 TeV, the excess would be visible at higher masses and is it likely that, with the data collected at $\sqrt{s} = 8$ TeV in 2012, it would not be possible to claim a discovery.

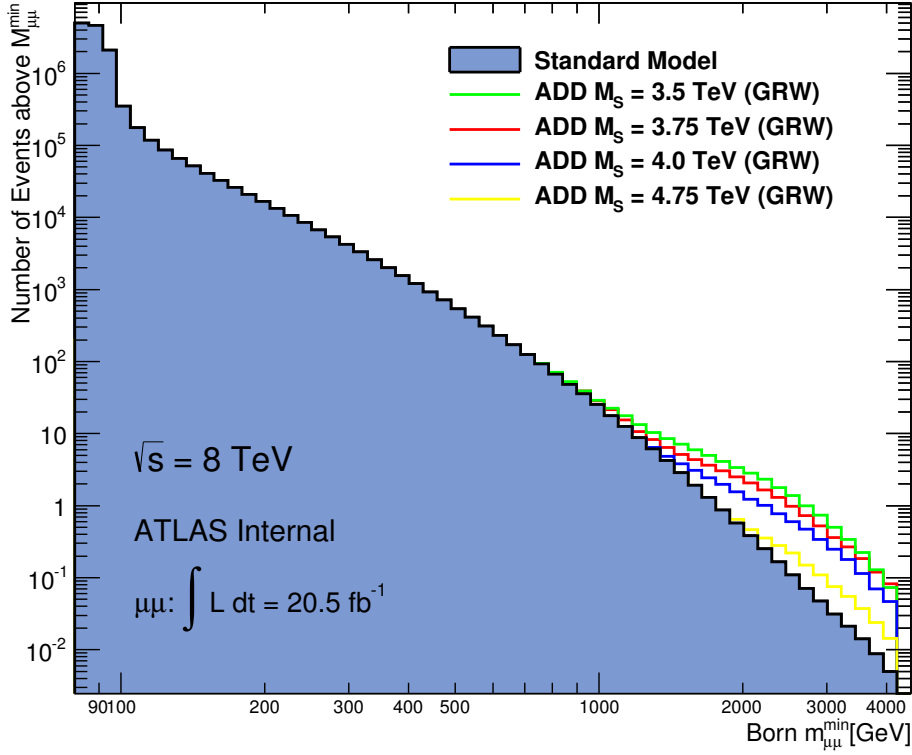


Figure 8.1: Integral of $m_{\mu\mu}^{\min}$ for generator level Drell-Yan and Drell-Yan+ADD signal processes. The event yields are normalised to 20.5 fb^{-1} .

Given the dependence of the theoretical cross section on M_S shown in equation 2.27, the number of expected events in a given mass bin used in the statistical analysis can be parametrized according to the equation [22]:

$$N^{exp}(M_S) = c_0 + \frac{c_1}{M_S^4} + \frac{c_2}{M_S^8} \quad (8.8)$$

where c_0 is the pure SM term, which can be obtained from the SM Monte Carlo background samples, and c_1 and c_2 represent interference with Drell-Yan and pure signal respectively and are determined by fitting. An example of such parametrizations can be found in figure 8.2, showing the number of expected signal+SM background events at generator level as a function of $1/M_S^4$ in the 1000-4500 GeV and 1900-4500 GeV regions in Born dimuon invariant mass. These regions are chosen based on the signal significance found in figure 8.3, showing an increase of the significance for $m_{\mu\mu} > 1000 \text{ GeV}$.

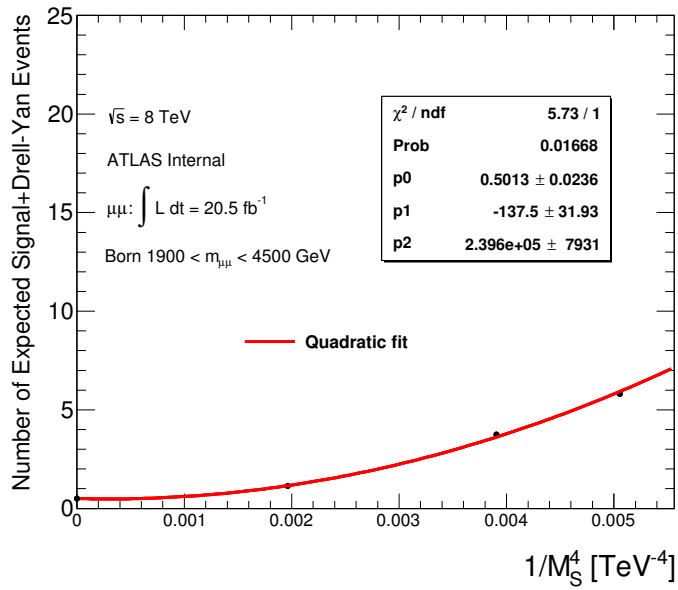
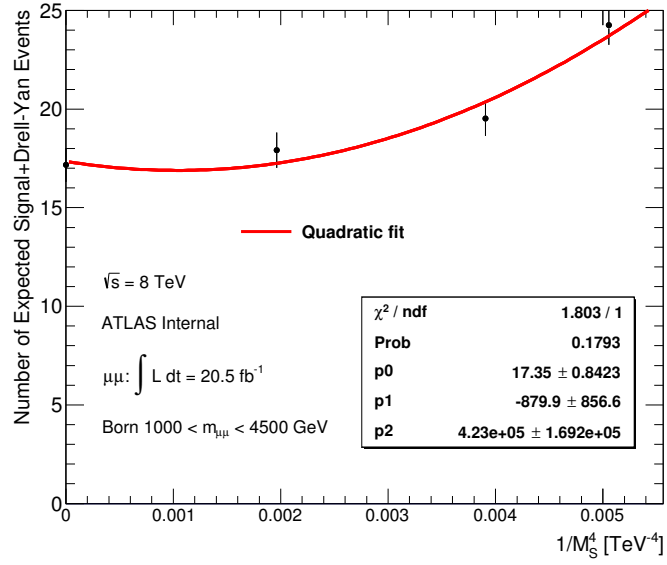


Figure 8.2: The number of expected signal+background events at generator level in the 1000-4500 GeV (top) and 1900-4500 GeV (bottom) region in Born dimuon invariant mass is shown against $1/M_S^4$. The quadratic fit from equation 8.8 is shown in red.

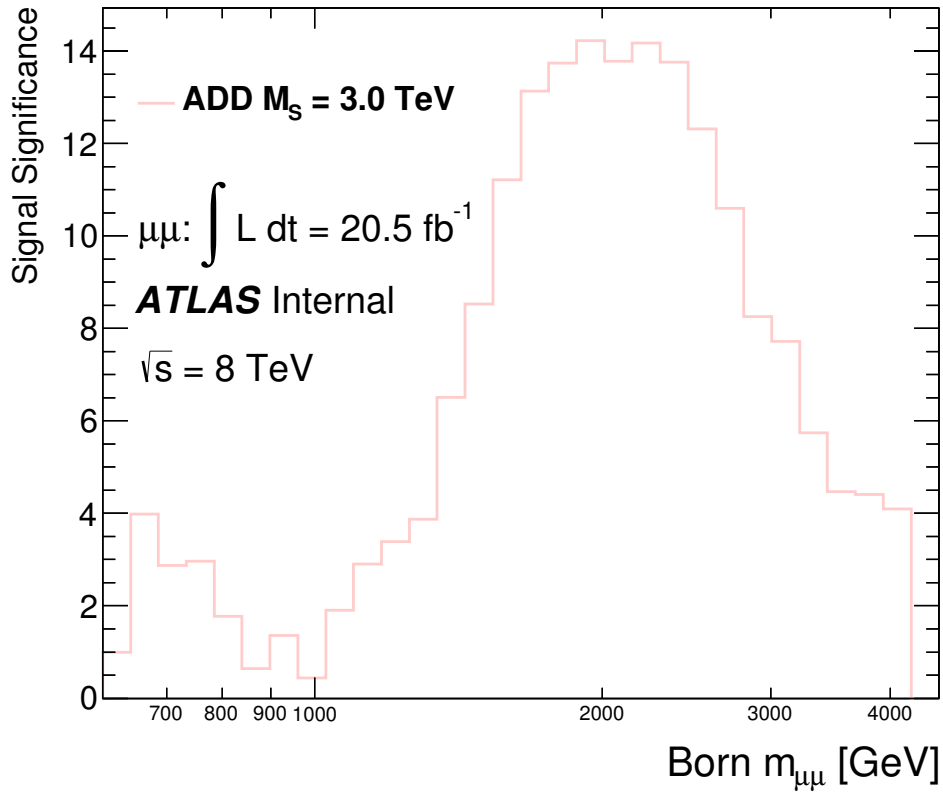


Figure 8.3: Signal significance against the Born dimuon invariant mass for an M_S value of 3.0 TeV.

Each of the points shown in figure 8.2 corresponds to the estimation made by the Monte Carlo ADD LED samples of a given value of M_S . While the parameter of interest of the search is M_S , the functional form of the cross section is dependent on $1/M_S^4$ and $1/M_S^8$ (equation 2.27). Exclusion limits are obtained using a uniform and positive prior in both $1/M_S^4$ or $1/M_S^8$ to account for the extreme cases where the interference and the pure signal term dominate. The motivation of using two different priors is to check how the 95% Bayesian upper limit extracted depends on the prior choice. Given the choice of prior, limits are extracted for either $1/M_S^4$ or $1/M_S^8$ using a constant positive prior probability in each of those two quantities. The

likelihood function then takes the following form:

$$\mathcal{L}(n_{obs}|1/M_S^4, \hat{\Omega}) = \frac{\mu^{n_{obs}} e^{-\mu}}{n_{obs}!} \prod_{i=1}^{N_{Sys}} G(\Omega_i, 0, 1) \quad (8.9)$$

$$\text{where } \mu = \sum_j \left(c_0 + \frac{c_1}{M_S^4} + \frac{c_2}{M_S^8} \right) (1 + \Omega_i \epsilon_{ij})$$

as mentioned already, MCMC is used to remove the dependence on the vector of nuisance parameters and equation 8.7 is used to obtain the 95% Bayesian upper limit on $1/M_S^4$ or $1/M_S^8$, which are then converted to a limit on M_S .

The use of parametrizations with the functional form shown in equation 8.8 allows an estimation of the expected event yields for values of M_S not available in the form of Monte Carlo samples, and is used to find the value of the parameter of interest which yields the 95% Bayesian upper limit. As observed in figure 8.2, the quality of the fit decreases as the value of the lower threshold in dilepton invariant mass increases. That is expected given that the lower threshold requirement in dilepton invariant mass also cuts into the signal event yields. The choice of an optimal region for exclusion limit extraction needs to take into consideration the quality of the fit. More details on how the exclusion limit depends on the choice of dilepton invariant mass region can be found in section 9.1.1.

8.3 QBH

The strategy followed to extract exclusion limits for the QBH search is a template shape method. This method follows the same approach as the counting experiment. However, the whole of the dilepton invariant mass spectrum is used (except the Z-peak region used for normalisation), separated into many dilepton invariant mass bins for the $m_{\ell\ell}$ range 128-4500 GeV. The lower threshold is chosen to avoid the Z-peak region, whereas the higher threshold is chosen as the highest point where current background estimations are reliable. The advantage of such an approach is that the dilepton invariant mass shape information can be used to better understand the nature of a possible signal, whereas this information is lost in a single bin counting experiment. Systematics are also evaluated on a bin-by-bin basis and are assumed to be correlated across all dilepton invariant mass bins. The likelihood function then becomes the product of the Poissonian probability over all mass bins considered:

$$\mathcal{L}(n_{obs}|N(\theta), \hat{\Omega}) = \prod_{k=1}^{N_{bin}} \frac{\mu_k^{n_{obsk}} e^{-\mu_k}}{n_{obsk}!} \prod_{i=1}^{N_{Sys}} G(\Omega_i, 0, 1) \quad (8.10)$$

$$\text{where } \mu_k = \sum_j N_j(\theta)(1 + \Omega_i \epsilon_{ijk})$$

where ϵ_{ijk} represents the effect of the systematic uncertainty i for process j in a mass bin k . Similarly as for the counting experiment method, the BAT is used to obtain the reduced likelihood and extract 95% Bayesian upper limits on the parameter of interest. It is however not possible to extract limits directly on the QBH model fundamental parameter (M_{th}). Given the functional form of the cross section (equation 2.34), the expected number of signal events in a given dilepton invariant mass bin cannot be parametrised in terms of M_{th} as is done for the ADD LED model. Instead, 95% Bayesian upper limits are extracted directly on the number of QBH signal events for a given value of M_{th} and are converted to cross section exclusion limits for the process $QBH \rightarrow \ell^+ \ell^-$. The number of QBH signal events, N_{QBH} , can be written as:

$$N_{QBH} = \sigma BR(QBH \rightarrow \ell^+ \ell^-) \cdot L \cdot A \epsilon_{QBH}(QBH \rightarrow \ell^+ \ell^-) \quad (8.11)$$

where L is the luminosity that the number of expected events is normalised to and $A \epsilon_{QBH}$ is the acceptance times efficiency of the selection applied for the QBH signal process for a given value of M_{th} . Since this analysis is normalised to the Z -peak region, the luminosity (L) can be rewritten in terms of the $Z \rightarrow l^+ l^-$ cross section in the region $80 < m_{\ell\ell} < 120$ GeV. The estimate on $\sigma BR(QBH \rightarrow \ell^+ \ell^-)$ can then be expressed in the following way:

$$\sigma BR(QBH \rightarrow \ell^+ \ell^-) = \frac{\sigma BR(Z \rightarrow \ell^+ \ell^-) \cdot A \epsilon_Z \cdot N_{QBH}}{N_Z \cdot A \epsilon_{QBH}} \quad (8.12)$$

where $A \epsilon_Z$ is the acceptance times efficiency for the Drell-Yan process in the normalisation region, calculated using Drell-Yan Monte Carlo simulation. To obtain a Bayesian upper limit on M_{th} , the theoretically predicted value of $\sigma BR(QBH \rightarrow \ell^+ \ell^-)$ can be compared to the upper limit on the cross section obtained as a function of M_{th} [87], as shown in chapter 9.2. The prior probability is chosen to be uniform and positive in σBR . This is motivated by the lack of knowledge of where BSM physics might lie and is expected to make the statistical analysis as general as possible. It should be noted that there is no evidence in literature that points to the choice of a different prior.

Figure 8.4 shows the signal $A \epsilon$ for all the values of M_{th} considered in the analysis. The third order polynomial fit shown in the figure is used as an input to the BAT. The signal $A \epsilon$ does

not exceed 50% due to the stringent Muon Station hits requirement, used to obtain the best possible muon momentum resolution. As M_{th} increases, the signal $A\epsilon$ is reduced due to muon charge misidentification and events reaching beyond the 4500 GeV higher mass threshold. As shown in table 7.4 the two effects have a similar magnitude for $M_{th} = 3.0$ TeV, each reducing the total $A\epsilon$ by 6-7%. At $M_{th} = 4.0$ TeV the effect of events reaching beyond the upper threshold in dimuon invariant mass becomes dominant, causing a loss of 17% in the total $A\epsilon$.

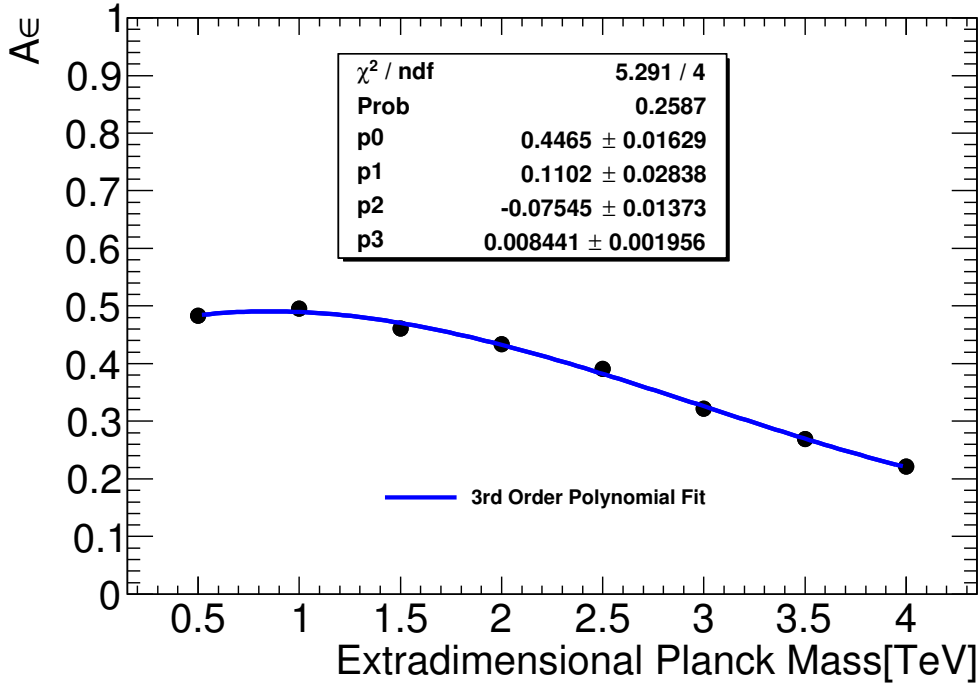


Figure 8.4: The signal $A\epsilon$ is shown for all of M_{th} values used for the search. A third order polynomial is fitted to the $A\epsilon$ and shown in blue.

8.4 Channel Combination

This thesis has so far focused on the search for BSM physics in the opposite sign dimuon channel to highlight the work of the author. The published ADD LED and QBH searches include independent searches on both the opposite sign dielectron and dimuon channel. Information from both independent searches can be combined in order to obtain stronger exclusion limits on the fundamental parameters of the models searched for. The work of the author includes using the BAT to compute the combined channel exclusion limits. The electron channel inputs required for the BAT were provided by electron channel specialists within

the ATLAS Exotics Working Group.

In order to combine the two channels an extended likelihood can be written as a product of the likelihood of each of the independent channels:

$$\mathcal{L}(n_{obs}|N(\theta), \hat{\Omega}) = \prod_{l=1}^{N_{channel}} \prod_{k=1}^{N_{bin}} \frac{\mu_{l,k}^{n_{obs_{l,k}}} e^{-\mu_{l,k}}}{n_{obs_{l,k}}!} \prod_{i=1}^{N_{Sys}} G(\Omega_i, 0, 1) \quad (8.13)$$

$$\text{where } \mu_{l,k} = \sum_j N_{lj}(\theta)(1 + \Omega_i \epsilon_{ijkl})$$

common systematic uncertainties, including PDF-related uncertainties, Beam Energy, Electroweak K -factor, Photon-Induced and Z cross section uncertainties are treated as correlated across channels.

8.5 Discovery statistics

The significance of deviations from SM expectations found in data is quantified by the p -value, the probability of obtaining a signal-like fluctuation as or more extreme than that observed in data given that the SM background only hypothesis is valid. The convention is that a p -value less than $1.35 \cdot 10^{-3}$ is evidence of BSM physics and less than $2.87 \cdot 10^{-7}$ is regarded as a discovery, which correspond to deviations of 3 and 5 standard deviations respectively.

To calculate the p -value, a test statistic based on the Neyman-Person lemma [126] is used. The lemma states that when trying to discriminate between two hypotheses, the log-likelihood ratio (LLR) can be used to reject one hypothesis over another. For the case of a BSM search, the aim is to understand whether the SM+signal hypothesis can be rejected in favour of the SM only hypothesis. As such, the LLR can be written as:

$$LLR = -2 \ln \frac{\mathcal{L}(n_{obs} | n_{signal} + n_{SM}, \hat{\Omega})}{\mathcal{L}(n_{obs} | n_{SM}, \hat{\Omega})} \quad (8.14)$$

the value of the parameter of interest can have a large effect on the likelihood of the Signal+SM background hypothesis. As such, a value of the parameter of interest is chosen such that the Signal+SM background likelihood is maximized. The BAT can then be used to obtain an expected LLR distribution and compared to the LLR found in data. The p -value (p) is

obtained by taking the ratio of the number of pseudo-experiments (N_{PE}) with an LLR more signal-like than the one observed in data to the total number of pseudo-experiments:

$$p = \frac{N_{PE}(LLR < LLR_{data})}{N_{PE}^{Tot}} \quad (8.15)$$

given that the LLR is defined to be negative, the more negative the observed value for the LLR the more signal-like it would be. In such a situation, most of the PEs would be less negative than the observed value and the result would be a small and therefore significant p -value. For the extreme opposite case, if the observed LLR value is zero, all of the PEs will have a more negative LLR than the observed value and that will lead to non-significant p -values close to 100%. The results for each of the searches are shown in the next chapter.

9 Results of the search

This chapter presents the results of the ADD LED and QBH searches using the methods described in the previous chapter. Model-dependent exclusion limits are extracted for both models and the probability of a signal-like excess is calculated. A study to show the potential exclusion limits that can be extracted for the QBH model using Run-2 data and the High-Luminosity LHC can be found in appendix E. As in previous chapters, plots that are not the work of the author are appropriately referenced. Throughout this chapter, the term exclusion limit will be used to refer to the 95% Bayesian upper limit.

Figure 9.1 shows the agreement between data and SM expectation for the tight and tight+loose muon selections. The significance of the deviations is defined as the number of standard deviations separating the observed and expected event yields in each of the mass bins used for the search (128-4500 GeV), as well as the Z-peak region used for normalization. No deviations larger than two standard deviations are found. Therefore, the data is consistent with SM expectations.

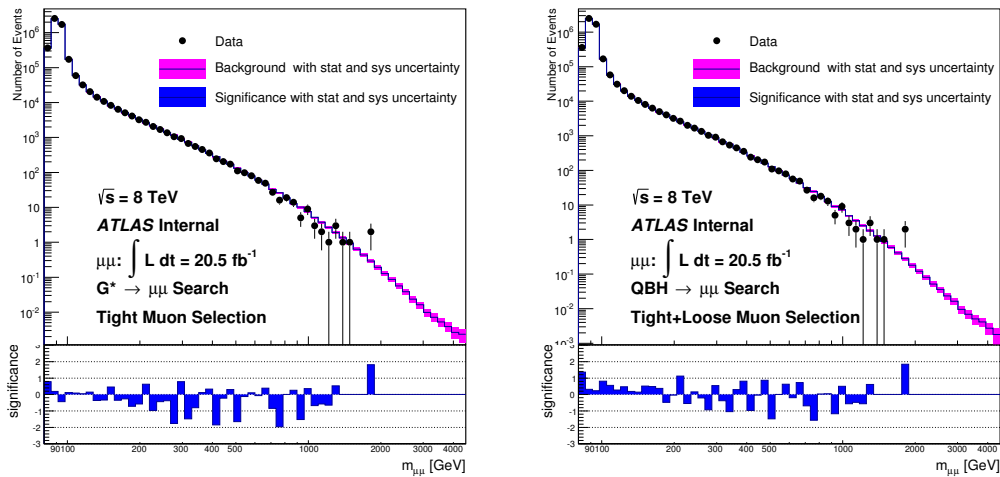


Figure 9.1: Local significance for the ADD LED search using the tight dimuon selection (left) and for the QBH search using the tight+loose muon selection (right).

9.1 Search for ADD Large Extra Dimensions

9.1.1 ADD Optimal Mass Cut

This section is based on the work presented in appendix B of [22]. The work and text presented here was written by the author in collaboration with Graham Savage. The plots shown for the muon and combined channel are the work of the author.

The ADD model predicts broad deviations from the SM DY spectrum. As explained in the previous chapter, a one bin search is performed where all muon and electron pairs passing the event selection are considered above an invariant mass threshold and below 4.5 TeV. The lower bound in invariant mass ($m_{\ell\ell}^{\min}$) of the search region was selected by computing the expected limit as a function of this lower bound. Only Monte Carlo simulation is used for this study. The lower edge of the single mass bin was varied from 1000 GeV to 2200 GeV in 100 GeV steps and the expected limits for each value of $m_{\ell\ell}^{\min}$ were determined. This was done independently for the electron and muon channels and then repeated for a combined lepton search. The threshold with the best expected limit was chosen to obtain results.

The expected number of ADD signal+background events after applying all the selection cuts in the single invariant mass bin is parametrized as a function of $1/M_S^4$ (or $1/M_S^8$) and used as input to the BAT. These parametrizations are shown in figure 9.2 for the muon channel as a function of $1/M_S^4$ for two possible values of $m_{\ell\ell}^{\min}$: 1300 and 1900 GeV. The point at $1/M_S^4 = 0$ represents the SM background-only expectation. While the quality of the fit decreases with an increasing $m_{\ell\ell}^{\min}$, as discussed in section 8.2, the fit still provides a reasonable description for the region $1900 < m_{\mu\mu} < 4500$ GeV in reconstructed dimuon invariant mass.

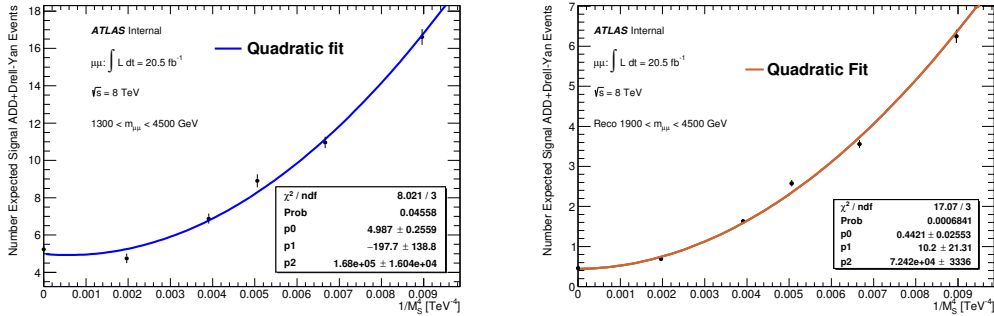


Figure 9.2: Number of expected events as a function of $1/M_S^4$ for minimum mass mass cuts of 1300 GeV (left) and 1900 GeV (right) in the muon channel.

The expected limits were computed by generating a 1000 pseudo-experiments using the BAT with the SM background-only hypothesis. Then the full Bayesian method calculation out-

lined in section 8.2 is carried out for each of the pseudo-experiments to extract 95% Bayesian upper limits. To determine the optimal value of $m_{\ell\ell}^{min}$, we use two definitions to extract the limit on M_S : the mean and the median of the PE expected limit distribution, as shown in figure 9.3. As can be observed in the figure, the PE distribution for $m_{\ell\ell}^{min} = 1900$ GeV collapses to a few results, whereas for $m_{\ell\ell}^{min} = 1300$ GeV a larger spread of possible results is obtained. That is because for the highest values of $m_{\ell\ell}^{min}$ considered the expected SM background event yields is very low (below one event), and the random walk algorithm used can only yield a few highly discretized exclusion limits. As a result, the median of the expected limit PE distribution can change from one value to another for small changes in the value of $m_{\ell\ell}^{min}$. To ensure that this does not affect our choice of minimum dilepton invariant mass threshold, an alternative definition of the expected limit is used: the mean of the expected limit PE distribution. Both definitions (mean and median) are compared in figure 9.3.

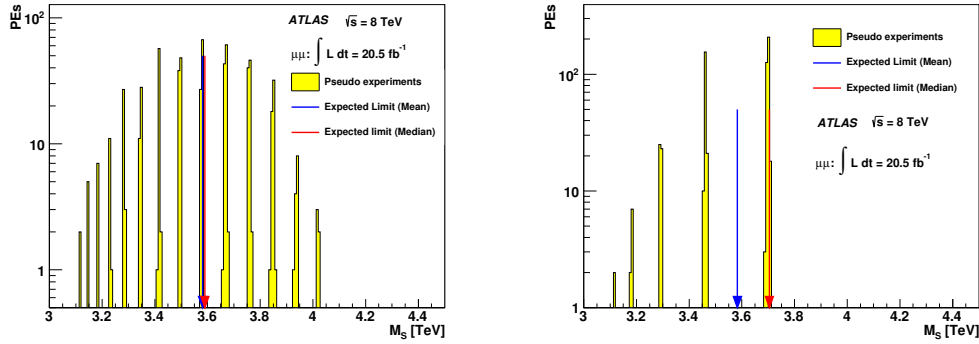


Figure 9.3: PE Distribution of expected limit values on M_S in the muon channel with a prior flat in $1/M_S^4$ for $m_{\mu\mu} > 1300$ GeV (left) $m_{\mu\mu} > 1900$ GeV (right). Both the mean and median of the distribution are highlighted.

As can be observed in figure 9.4 for the muon (combined) channel on the left (right) the mean limit definition has a smoother behaviour than the median limit. From the results obtained, the expected limit obtained is found to vary by $\sim 10\%$ for the highest and lowest exclusion limit using both definitions of the expected limit. The expected limit increases linearly with increasing $m_{\ell\ell}^{min}$ as the signal to background ratio increases (figure 8.3). However, when reaching $m_{\ell\ell}^{min} \sim 1.8$ -1.9 TeV, the invariant mass cut starts to significantly reduce the expected signal yields and the exclusion limit is slightly reduced ($\sim 5\%$). Considering the results obtained for the expected limit and the parametrizations, $m_{\ell\ell}^{min}$ was chosen to be 1900 GeV and used to extract the 95% upper Bayesian limits that are quoted in the published results in [79].

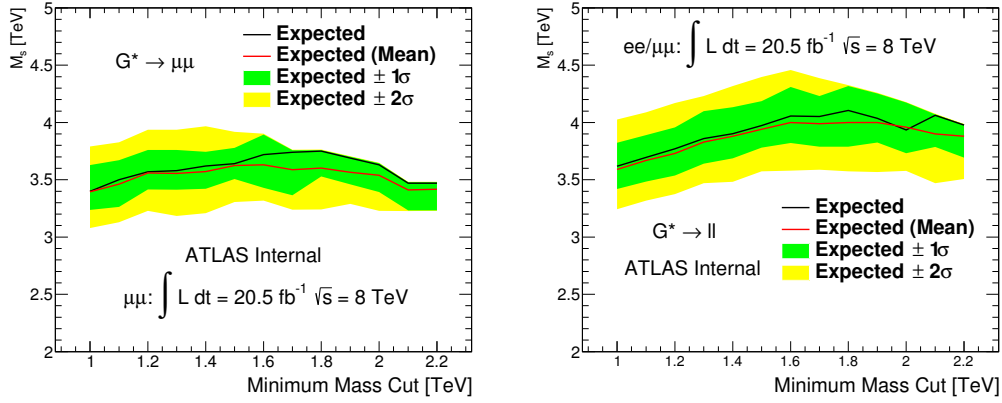


Figure 9.4: Expected (black) and mean (red) limit on M_S in the ADD GRW model determined as a function of minimum mass cut ($m_{\ell\ell}^{\min}$) used to define the search region using a $1/M_S^4$ prior on the left (right) for the dimuon (combined) channel.

9.1.2 Results

The strongest expected exclusion limit is obtained for a dilepton invariant mass bin covering the range 1900-4500 GeV. Figure 9.5 shows the number of expected ADD LED signal+SM background events in the region $m_{\ell\ell}$ 1900-4500 GeV after applying all the selection cuts for both $1/M_S^4$ and $1/M_S^8$. The parametrisation for $1/M_S^8$ is obtained by taking the parameters of the $1/M_S^4$ fit function and shifting the dependence in the x -axis from $1/M_S^4$ to $1/M_S^8$.

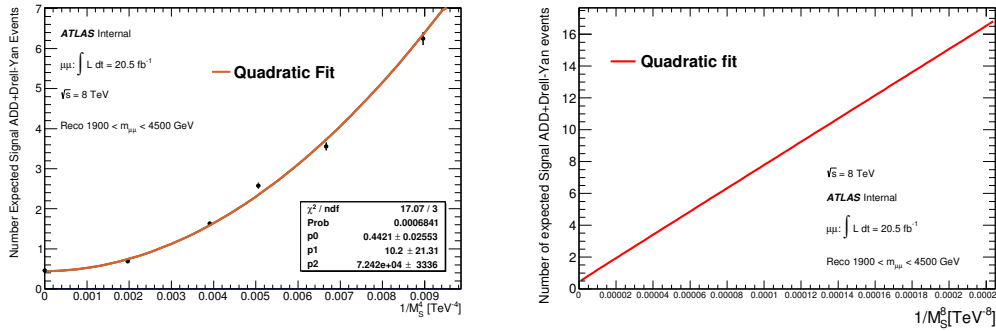


Figure 9.5: Number of expected events as a function of $1/M_S^4$ (left) and $1/M_S^8$ (right).

Tables 9.1 and 9.2 show the observed and expected event yields for the ADD LED search in the dielectron and dimuon channels respectively, in the range $1900 < m_{\ell\ell}^{\min} < 4500$ GeV. No events are found in data. That is consistent with SM expectations. Using the BAT, a 1000 PEs are run to obtain the expected exclusion limits on the parameter of interest ($1/M_S^4$ or $1/M_S^8$)

assuming that only SM physics is present. The LLR PE distributions for the ADD GRW muon channel for both prior choices are shown in figure 9.6. The p -values found are $> 6\%$ and $> 49\%$ for the $1/M_S^4$ and $1/M_S^8$ prior choices respectively. Therefore, no sign of ADD LED is found in data and exclusion limits are derived using the binned counting experiment described in section 8.2. The fact that the p -values are quoted as being larger than a given percentage is a consequence of a deficit in data being found when the search focuses on looking for an excess. A large portion of the PE are consistent with $LLR = 0$, the same LLR observed in data. It is therefore more appropriate to quote the p -value as being larger than a certain quantity [22]. It should be noted that such a choice of convention in quoting the p -value does not change the result of the search: no evidence for ADD LED is found. Figure 9.7 shows the expected limit PE distribution on the parameter of interest M_S for the ADD GRW $1/M_S^4$ (left) and $1/M_S^8$ (right) prior choices. The observed and expected limits are in good agreement. It can also be seen that the different prior definition affects the upper limits extracted, with the $1/M_S^8$ prior being a more conservative choice. As already mentioned, the $1/M_S^8$ prior describes the case where the pure signal term dominates the cross section, defined in equation 2.27, whereas the $1/M_S^4$ prior describes the case where the interference with Drell-Yan dominates. The observed posterior probability density function is shown in figure 9.8. Given that no sign of signal ADD LED is found the distribution peaks close to $\theta = 1/M_S^4 = 0$ and $\theta = 1/M_S^8 = 0$.

Table 9.1: Expected and Observed event yields in the ADD search region for SM processes and various benchmark values of M_S for the ADD GRW formalism in the muon channel.

Process	$1900 \leq m_{\mu\mu} \leq 4500$ GeV
Drell-Yan	0.44 ± 0.09
Top	$0.006 < 0.001$
Diboson	0.047 ± 0.005
Photon-Induced	0.05 ± 0.05
SM+ADD ($M_S = 3.00$ TeV)	11.7 ± 1.2
SM+ADD ($M_S = 3.25$ TeV)	6.4 ± 0.7
SM+ADD ($M_S = 3.50$ TeV)	3.9 ± 0.4
SM+ADD ($M_S = 3.75$ TeV)	2.4 ± 0.2
SM+ADD ($M_S = 4.00$ TeV)	1.7 ± 0.1
SM+ADD ($M_S = 4.75$ TeV)	0.8 ± 0.1
Total SM	0.544 ± 0.090
Data	0

As mentioned in section 8.4, a parallel electron channel search took place. Table 9.3 summarizes the expected and observed exclusion limits on M_S found for each independent channel and prior choice. The electron channel, as already observed in an earlier version of this

Table 9.2: Expected and Observed event yields in the ADD search region for SM processes and various benchmark values of M_S for the ADD GRW formalism in the electron channel [79].

Process	$1900 \leq m_{\mu\mu} \leq 4500$ GeV
Drell-Yan	0.43 ± 0.12
Top	$0.002 < 0.001$
Diboson	0.053 ± 0.005
Multijet	0.062 ± 0.012
Photon-Induced	0.06 ± 0.06
SM+ADD ($M_S = 3.00$ TeV)	17.5 ± 1.7
SM+ADD ($M_S = 3.25$ TeV)	9.5 ± 0.9
SM+ADD ($M_S = 3.50$ TeV)	5.8 ± 0.5
SM+ADD ($M_S = 3.75$ TeV)	3.7 ± 0.3
SM+ADD ($M_S = 4.00$ TeV)	2.56 ± 0.24
SM+ADD ($M_S = 4.75$ TeV)	1.1 ± 0.1
Total SM	0.61 ± 0.13
Data	0

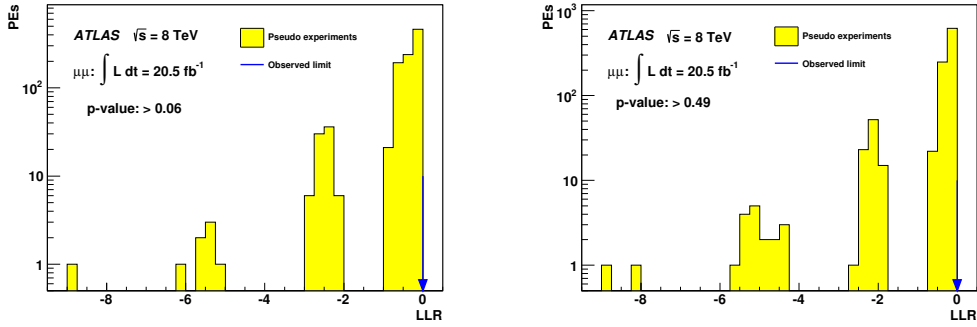


Figure 9.6: ADD GRW expected LLR PE distribution for a uniform positive prior in $1/M_S^4$ (left) and $1/M_S^8$ (right) choice for the muon channel. The observed LLR is shown by the blue arrow.

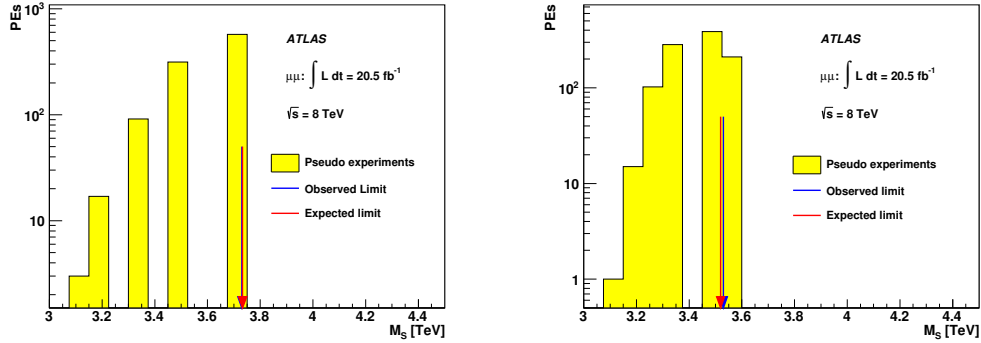


Figure 9.7: ADD GRW expected exclusion limits PE distribution for a uniform positive prior in $1/M_S^4$ (left) and $1/M_S^8$ (right) choice for M_S for the muon channel. The expected exclusion limit is the median of the distribution and is shown by the blue arrow, while the red arrow shows the observed exclusion limit.

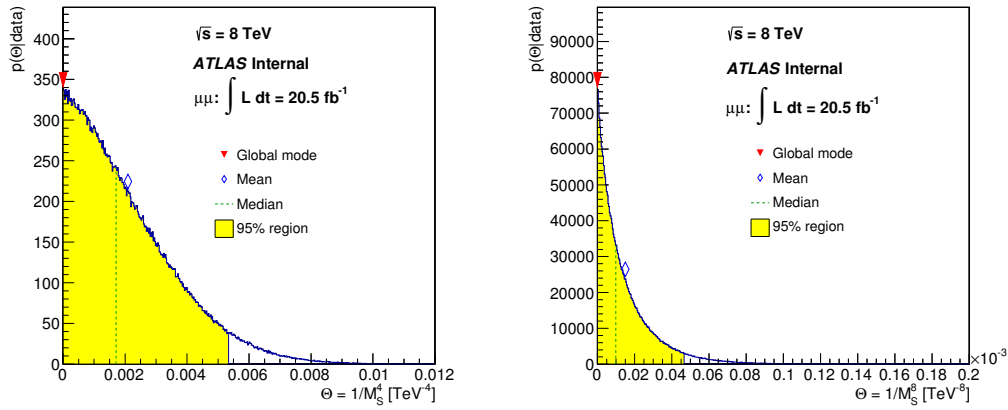


Figure 9.8: ADD GRW observed posterior probability density function for a uniform positive prior in $1/M_S^4$ (left) and $1/M_S^8$ (right) choice for $\theta = 1/M_S^4$ (left) and $1/M_S^8$ (right) for the muon channel. The 95% region is shown in yellow.

search [127], sets stronger exclusion limits. The reason behind that is the larger $A\epsilon$ of the electron channel event selection. The muon channel event selection includes stringent requirements in order to maintain good momentum resolution for TeV-order dimuon invariant masses, while electron momentum resolution is better throughout the invariant mass range considered for the search without the need of such stringent requirements.

Table 9.3: Expected and observed 95% CL lower exclusion limits on M_S for the GRW ADD search using a uniform positive prior in $1/M_S^4$ or $1/M_S^8$. Both electron and muon channel limits are shown, with all systematic uncertainties taken into account [22].

GRW ADD Limits [TeV]	$1/M_S^4$	$1/M_S^8$
Expected: ee	3.96	3.72
Observed: ee	3.96	3.72
Expected $\mu\mu$	3.72	3.52
Observed $\mu\mu$	3.73	3.52

The expected and observed combined exclusion limits were obtained using the BAT by forming a combined likelihood, as shown in equation 8.13. To obtain the reduced likelihood, the sources of systematic uncertainty that are treated as correlated across channels are: PDF, Electroweak K -factor, Photon-Induced, Beam Energy, and Z cross section [22], while other sources are treated as uncorrelated. No correlations between separate systematic uncertainties are considered.

The author, together with Graham Savage, was responsible for running the combined exclusion limits and hence the results published in [79] are reproduced here. Figure 9.9 shows the dilepton channel LLR distribution for each of the prior choices. The p -values obtained are consistent with those observed in the single dimuon channel search: no evidence for ADD LED is present in data. Figure 9.10 shows the distribution of the expected exclusion limits on M_S , with the observed limit also shown. In that case, given that no events are observed in data for either the electron or muon channels in the region 1900-4500 GeV, the deficit in data becomes apparent as stronger observed exclusion limits are obtained than the expected ones. Given the larger background expectation and set of systematic uncertainties, the expected limit PE distribution exhibits a smoother behaviour, as opposed to that observed for the standalone muon channel in figure 9.7, given the larger event yield expectation. Figure 9.11 shows the observed posterior probability density function, which exhibits the same trend observed in the muon channel, with $1/M_S^4$ and $1/M_S^8$ stacked against zero. The effect of the systematic uncertainties on the likelihood during MCMC integration is shown in figure 9.12. As expected, the largest shifts comes from the largest uncertainty: the PDF Variation. Other uncertainties such as the muon resolution or efficiency are shown to have a negligible effect. Given the deficit of data, the effect of the systematics is to decrease the background

expectation. Therefore, the pulls show a negative tendency.

Figure 9.13 is a summary of the limits for the uniform positive $1/M_S^8$ prior choice. Observed exclusion limits are within one standard deviations of the expected exclusion limit and are therefore in agreement. The exclusion limits obtained with the prior choices already presented were compared to those obtained using a uniform flat prior on the cross section. The results can be found in appendix B, and are found to be consistent with the prior flat in $1/M_S^8$.

The limits obtained for the GRW formalism are converted to other formalisms such as HLZ $n=3-7$ and Hewett using equation 2.28. The conversion however does not work for the case HLZ $n=2$, as it depends directly on M_S and $m_{\ell\ell}$. The observed posterior probability density function, the expected exclusion limit PE distribution and the LLR for the HLZ $n=2$ case can all be found in appendix D. Table 9.4 contains a summary of all the results obtained for each prior choice, formalism and channel. The strongest exclusion limit obtained is $M_S > 5.0$ TeV, obtained in the combined channel for the ADD HLZ $n=3$ model. The dimuon channel limits are comparable to those obtained by CMS in the search presented in [128], with an observed limit on M_S of 4.43 TeV in the dimuon channel for the HLZ $n=3$ formalism.

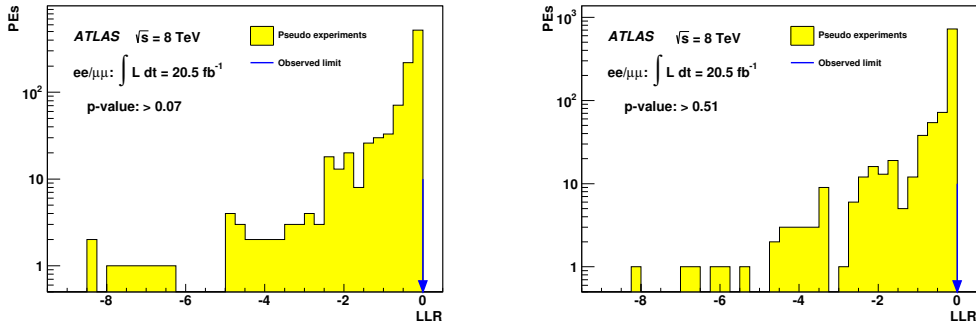


Figure 9.9: ADD GRW expected LLR PE distribution for a uniform positive prior in $1/M_S^4$ (left) and $1/M_S^8$ (right) choice for the dilepton channel. The observed LLR is shown by the blue arrow.

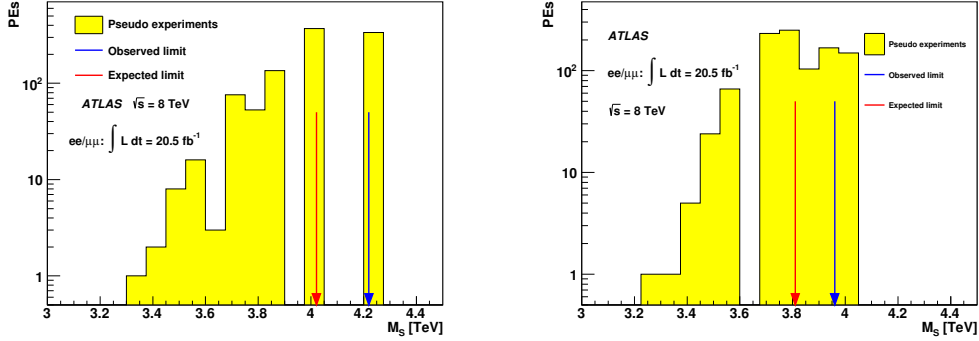


Figure 9.10: ADD GRW expected exclusion limits PE distribution for a uniform positive prior in $1/M_S^4$ (left) and $1/M_S^8$ (right) choice for M_S for the dilepton channel. The expected exclusion limit is the median of the distribution, while the blue arrow shows the observed exclusion limit.

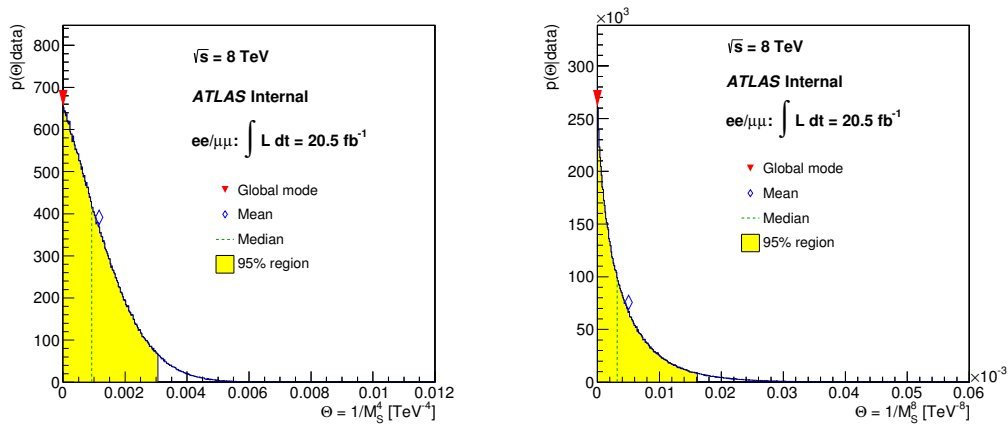


Figure 9.11: ADD GRW observed posterior probability density function for a uniform positive prior in $1/M_S^4$ (left) and $1/M_S^8$ (right) choice for $\theta = 1/M_S^4$ (left) and $1/M_S^8$ (right) for the dilepton channel. The 95% region is shown in yellow.

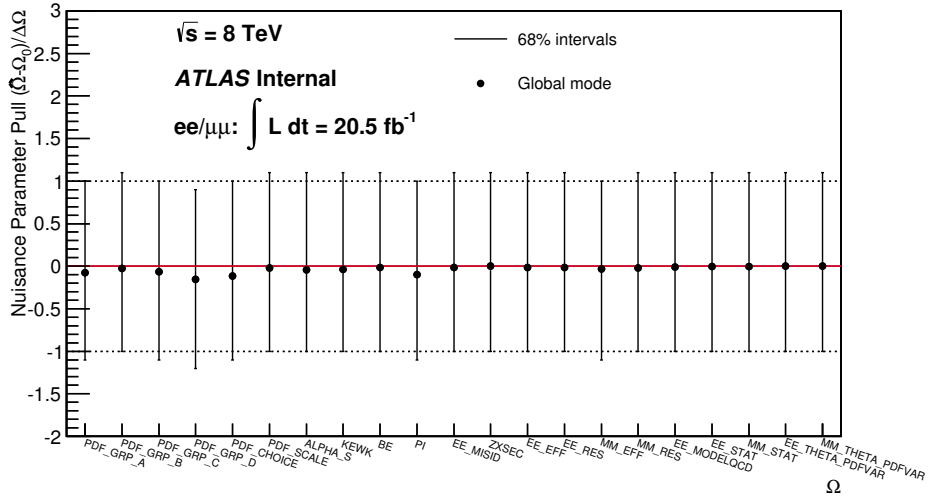


Figure 9.12: Observed pull distributions for each of the systematic uncertainties affecting the likelihood constructed in BAT to extract exclusion limits. This plot is for the dilepton channel and hence includes all the systematic uncertainties affecting both muon and electron channels.

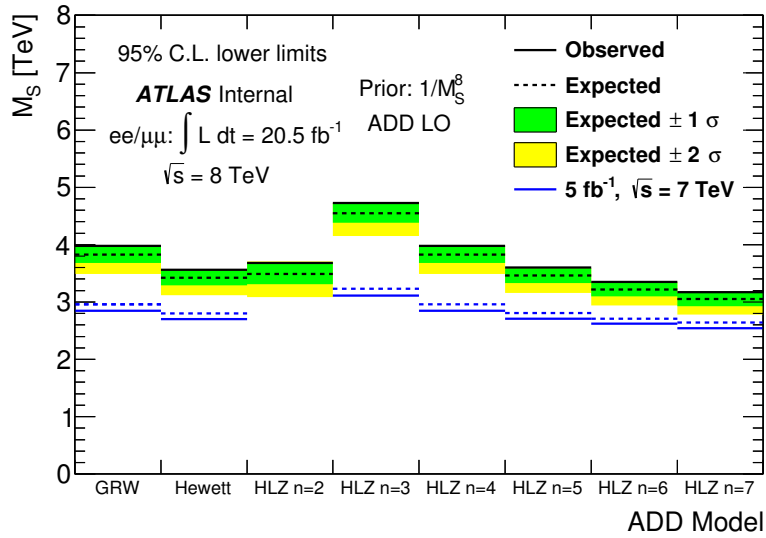


Figure 9.13: Summary of 95% CL lower exclusion limits on M_S for the combined dilepton ADD LED search using a uniform positive prior in $1/M_S^8$. Previous ATLAS search results [127] are also shown for comparison [79].

Table 9.4: Expected and observed 95% CL lower exclusion limits on M_S including systematic uncertainties, for ADD signal in the GRW, Hewett and HLZ formalisms [79].

Expected and Observed Limit on M_S ([TeV])									
Channel	Prior	GRW	Hewett	HLZ					
				n= 2	n=3	n=4	n=5	n=6	n=7
Expected: ee	$1/M_S^4$	4.0	3.6	3.6	4.8	4.0	3.6	3.4	3.2
Observed: ee		4.0	3.6	3.6	4.8	4.0	3.6	3.4	3.2
Expected: ee	$1/M_S^8$	3.7	3.3	3.1	4.4	3.7	3.3	3.1	2.9
Observed: ee		3.7	3.3	3.1	4.4	3.7	3.3	3.1	2.9
Expected: $\mu\mu$	$1/M_S^4$	3.7	3.3	3.4	4.4	3.7	3.3	3.1	2.9
Observed: $\mu\mu$		3.7	3.3	3.4	4.4	3.7	3.3	3.1	2.9
Expected: $\mu\mu$	$1/M_S^8$	3.5	3.1	3.1	4.2	3.5	3.2	2.9	2.8
Observed: $\mu\mu$		3.5	3.1	3.1	4.2	3.5	3.2	2.9	2.8
Expected: ll	$1/M_S^4$	4.0	3.6	3.9	4.8	4.0	3.6	3.4	3.2
Observed: ll		4.2	3.8	4.2	5.0	4.2	3.8	3.5	3.3
Expected: ll	$1/M_S^8$	3.8	3.4	3.5	4.5	3.8	3.4	3.2	3.0
Observed: ll		4.0	3.6	3.7	4.8	4.0	3.6	3.4	3.2

9.2 Search for Quantum Black Holes

The search for the QBH model is performed across the dimuon invariant mass range 128-4500 GeV. The likelihood then takes the form shown in equation 8.10. Expected and observed exclusion limits on $\sigma\text{BR}(QBH \rightarrow \ell^+\ell^-)$ are extracted for each M_{th} value considered for the ADD $n=6$ and RS $n=1$ models. The values of M_{th} considered range from 0.5 to 4.0 TeV in 0.5 TeV steps. The theoretical dependence of $\sigma\text{BR}(QBH \rightarrow \ell^+\ell^-)$ is then used to extract Bayesian upper limits on M_{th} . Expected limits are obtained by running 1000 pseudo-experiments with the BAT. The exclusion limits for the muon, electron and combined channels published in [78] are the work of the author. Electron channel inputs to the BAT such as the background and signal templates were provided by electron channel specialists. Systematic uncertainties in the BAT are treated in the same way as for the ADD LED search, but assuming that the uncertainties are correlated across all dilepton invariant mass bins probed.

Given that this search is performed across many mass bins, there is a danger of finding a fake signal due to the look elsewhere effect [129]. The look elsewhere effect relates to the increased probability of observing a signal-like statistical fluctuation in observations because of the size of the parameter space probed. To account for this effect a two-dimensional search is performed to find the most significant deviation in the observed dataset as a function of M_{Th} and the cross section of the BSM physics process (σ_{QBH}). Figure 9.14 shows the results of such a scan for the muon channel. Hot regions show the value of the larger excesses, with the white marker showing the most significant excess found in the observed dataset. The p-value of the most significant excess is 68%. Figure 9.15 shows the LLR distribution for the electron, muon and combined channels. The most significant p-value obtained found is 33.9% in the electron channel. Therefore, no evidence of an excess is found in the observed dataset.

Figures 9.16 and 9.17 show the 95% Bayesian upper limits obtained on $\sigma\text{BR}(QBH \rightarrow \ell^+\ell^-)$ against M_{th} for the electron, muon and combined channel respectively, together with the one and two standard deviation intervals. The limits on $\sigma\text{BR}(QBH \rightarrow \ell^+\ell^-)$ show a decreasing trend for $M_{th} > 2.0$ TeV. That is due to the signal $A\epsilon$ decreasing with increasing M_{th} , as shown previously in figure 8.4. Also, the standard deviation intervals become one-sided for the same region as the event yields cannot be lower than zero. The theoretical dependence of $\sigma\text{B}(QBH \rightarrow \ell^+\ell^-)$ on the value of M_{th} is overlaid in the plots and used to extract a 95% Bayesian upper limit on the threshold for QBH production. Tables 9.5 and 9.6 summarize the expected and observed exclusion limits obtained. The expected and observed exclusion limits are in good agreement.

The strongest exclusion limit on M_{th} obtained in this search is for the QBH ADD $n=6$ search at 3.65 TeV for the dilepton channel. This exclusion limit is however weaker than that found in other ATLAS searches published, such as [38] for the lepton+jet channel: 5.2 TeV. The

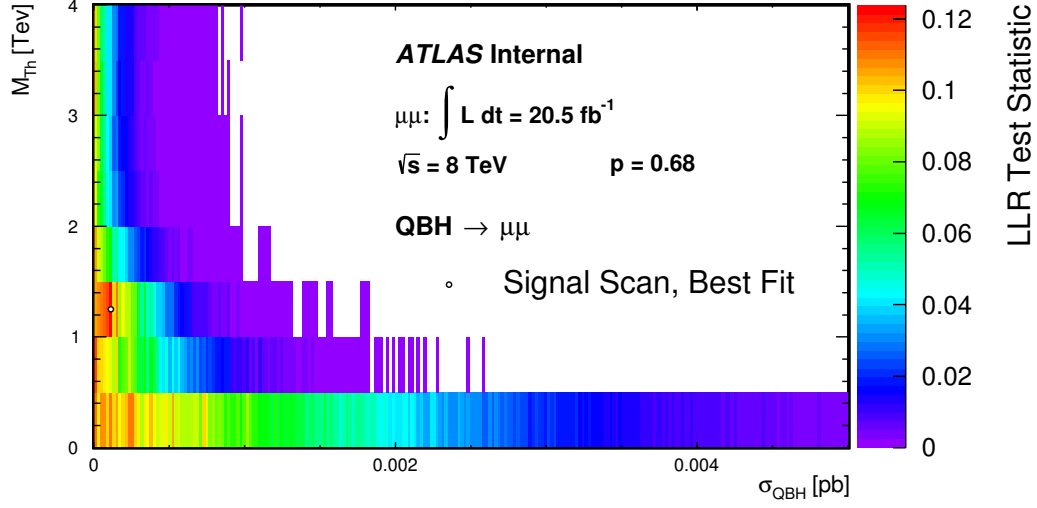


Figure 9.14: 2-D signal scan for the absolute value of the LLR test statistic as a function of M_{Th} and σ_{QBH} for the observed dataset. The white marker highlights the most significant deviation encountered

Table 9.5: 95% Bayesian upper limits on M_{th} for the QBH ADD $n=6$ model.

Process	QBH $\rightarrow e^+ e^-$	QBH $\rightarrow \mu^+ \mu^-$	QBH $\rightarrow \ell^+ \ell^-$
Observed limit M_{th} [TeV]	3.58	3.32	3.65
Expected limit M_{th} [TeV]	3.58	3.33	3.65

Table 9.6: 95% Bayesian upper limits on M_{th} for the QBH RS $n=1$ model.

Process	QBH $\rightarrow e^+ e^-$	QBH $\rightarrow \mu^+ \mu^-$	QBH $\rightarrow \ell^+ \ell^-$
Observed limit M_{th} [TeV]	2.17	1.95	2.24
Expected limit M_{th} [TeV]	2.15	1.94	2.22

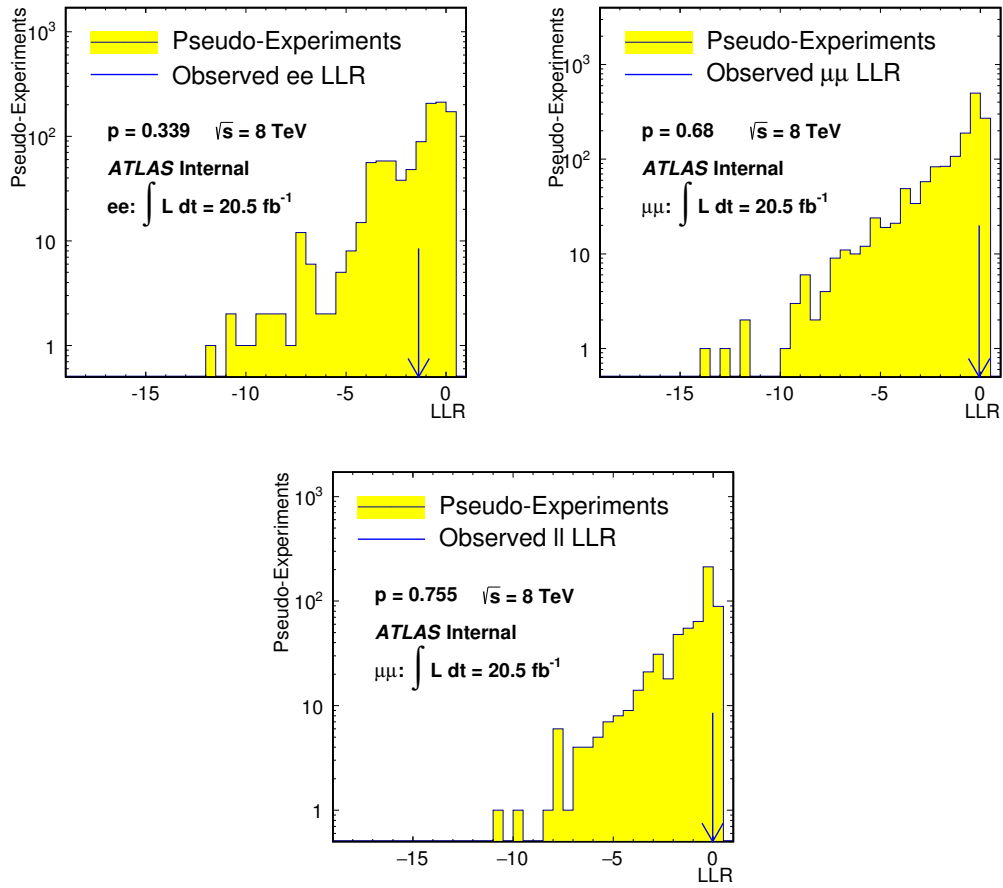


Figure 9.15: LLR distribution for the ADD $n=6$ QBH model for the electron (top left), the tight+loose muon selection (top right) and the combined dilepton (bottom) channel.

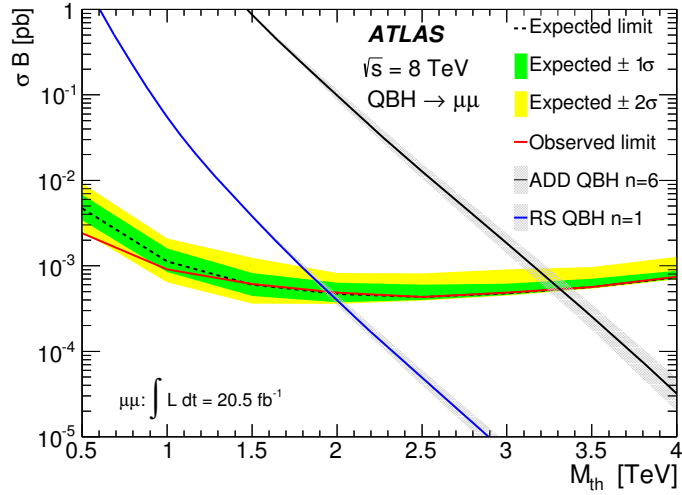
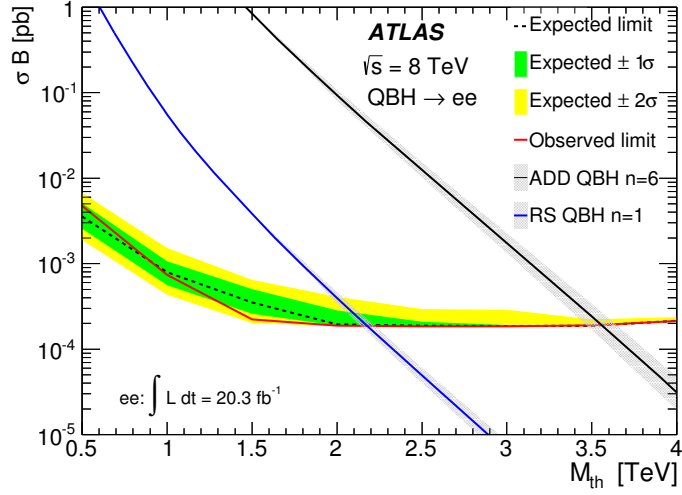


Figure 9.16: Expected and observed 95% Bayesian upper limits on σB for quantum black hole production in the ADD $n=6$ and RS $n=1$ models for the electron (top) and the tight+loose muon selection (bottom). The thickness of the ADD $n=6$ and RS $n=1$ theory lines represents the effect of the PDF uncertainty on the theoretical σB .

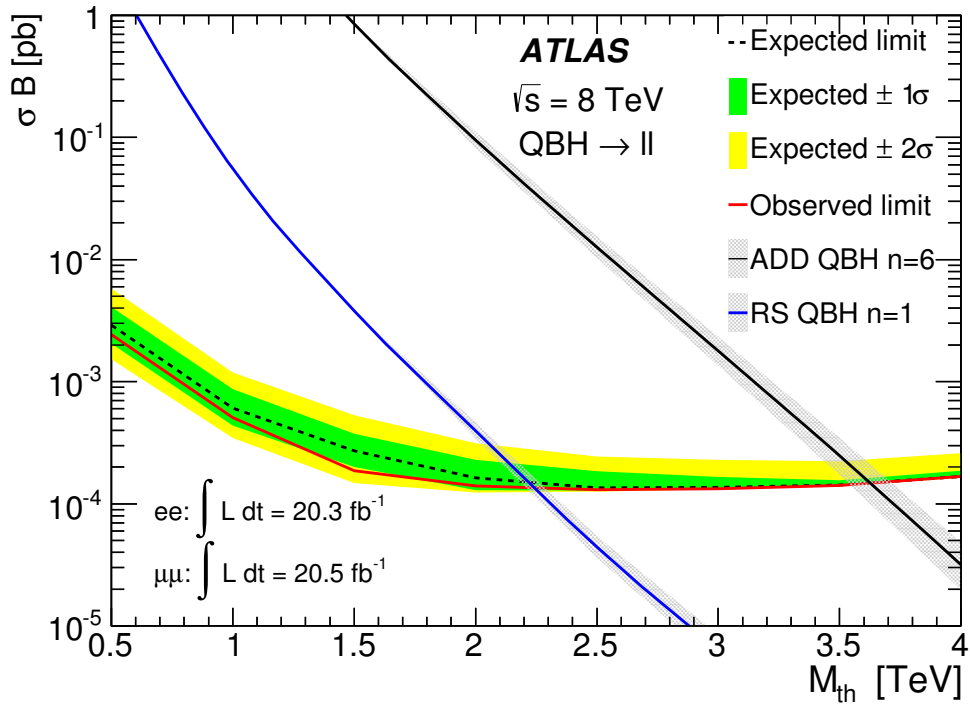
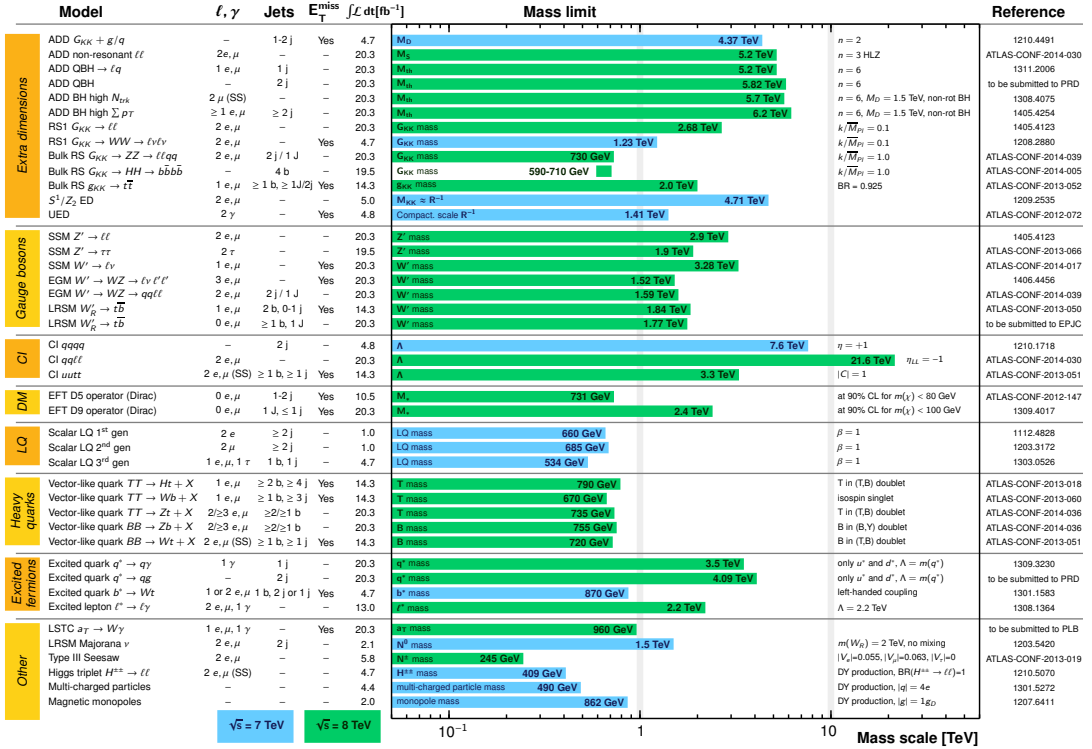


Figure 9.17: Expected and observed 95% Bayesian upper limits on σ_B for quantum black hole production in the ADD $n=6$ and RS $n=1$ models for the combination of dielectron and dimuon channels. The thickness of the ADD $n=6$ and RS $n=1$ theory lines represents the effect of the PDF uncertainty on the theoretical σ_B .



*Only a selection of the available mass limits on new states or phenomena is shown.

Figure 9.18: Summary of current limits from ATLAS searches for new phenomena [130].

caveat is that a lepton+jet final state assumes that Quantum Gravity violates lepton number conservation. The search presented in this thesis does not make such assumptions. The current strongest limits in ATLAS, as shown in figure 9.18, are found in the dijet channel [131] with a limit on M_{th} of 5.82 TeV. That is expected given that, as shown in Table 2.1, the dijet final has the highest branching ratio and hence the highest theoretical cross section.

10 Conclusion

The search for Quantum Gravity at the LHC during Run-1 has produced the strongest exclusion limits yet on the extradimensional Planck Scale and the threshold for forming quantum black holes. The increase in centre-of-mass energy and the larger expected luminosity in Run-2 means there is still potential to explore more regions of phase space and exclude further or, perhaps, find a potential signal. The limits obtained for the ADD LED model are competitive with those obtained in competing experiments. However, as outlined in chapter 9.2, the limits set on the dilepton channel for the QBH model are weaker than those obtained in other ATLAS searches in channels such as dijet or lepton+jet. A change of strategy to make a search involving dileptons more sensitive to New Physics should be considered. One of the interesting proposals would be to search for a QBH decaying to an electron and a muon. In [29], it is proposed that such a final state could arise if Quantum Gravity violates lepton number conservation. Such a search would have lower Standard Model backgrounds (although harder to estimate) than the analysis presented here and is expected to be more sensitive to a possible New Physics signal.

Appendix

A Dilepton p_T reweight

One of the known issues with the Monte Carlo Drell-Yan samples is the poor description provided for the dilepton p_T spectrum when compared to data. While the searches presented in this analysis focus on the dilepton invariant mass spectrum, a study is done to estimate the effect of this incorrect modelling. Each Monte Carlo generator uses a different model to estimate the dilepton p_T . The Powheg Drell-Yan dilepton p_T distribution is reweighted to a different model. This reweight is applied to the dilepton invariant mass spectrum to check if the incorrect modelling of the dilepton p_T has a large effect on the discriminant variable used for the statistical analysis. The tool used is named `BosonPtReweightingTool`, included in the `eGammaAnalysisUtils-00-04-54`. However, no reweighting exists at present time for the Powheg simulated Monte Carlo samples used in the searches presented here. As such, a reweighting to a different model is performed to estimate the effect a poor description of the dilepton p_T can have on the mass spectrum. The reweight applied is from Leading Order (LO) 2011 Pythia6 samples to the 2010 Pythia samples, where Monte Carlo simulation provided a good description of the data. While the samples used for this analysis are generated with Powheg at $\sqrt{s} = 8$ TeV, the reweighting is still expected to provide information on how much the expected dilepton invariant mass spectrum can change with different dilepton p_T models.

Figure A.1 shows the effect of the reweighting on the Powheg simulated Monte Carlo Drell-Yan dilepton p_T distribution. Figure A.2 shows the agreement of the nominal and reweighted dilepton p_T distributions to data. While the agreement to data does not improve, the effect of the reweighting on the mass spectrum, shown in figure A.3, is of about 1%. Therefore, a change of about 20% in the dilepton p_T is expected to produce a 1% shift in the dimuon invariant mass spectrum. It is hence expected to have a negligible impact on the limits extracted.

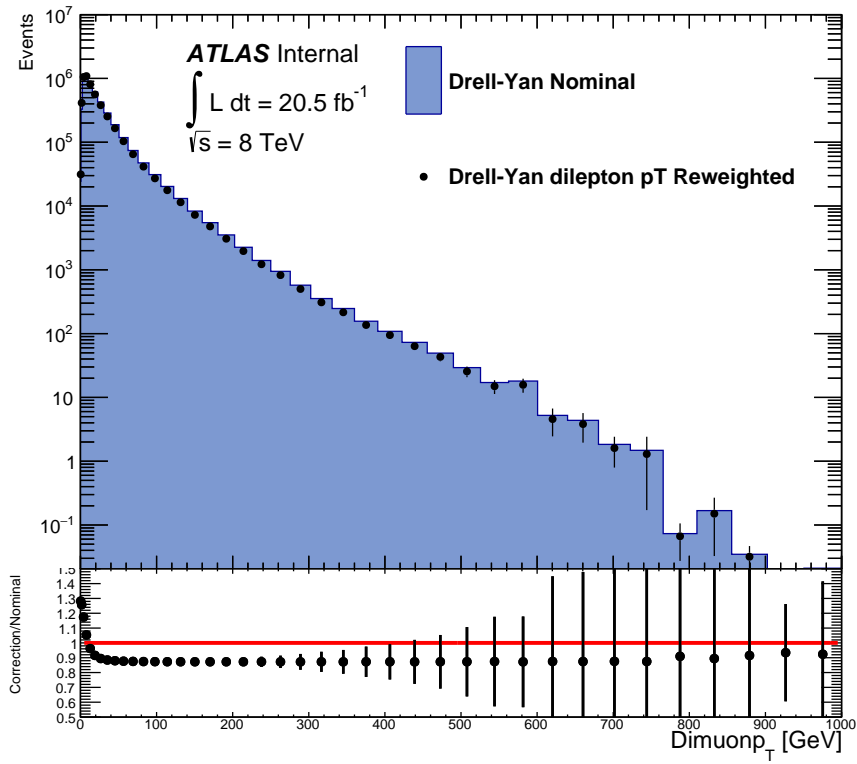


Figure A.1: Comparison of the Drell-Yan Dilepton p_T distribution before and after applying the boson p_T reweight.

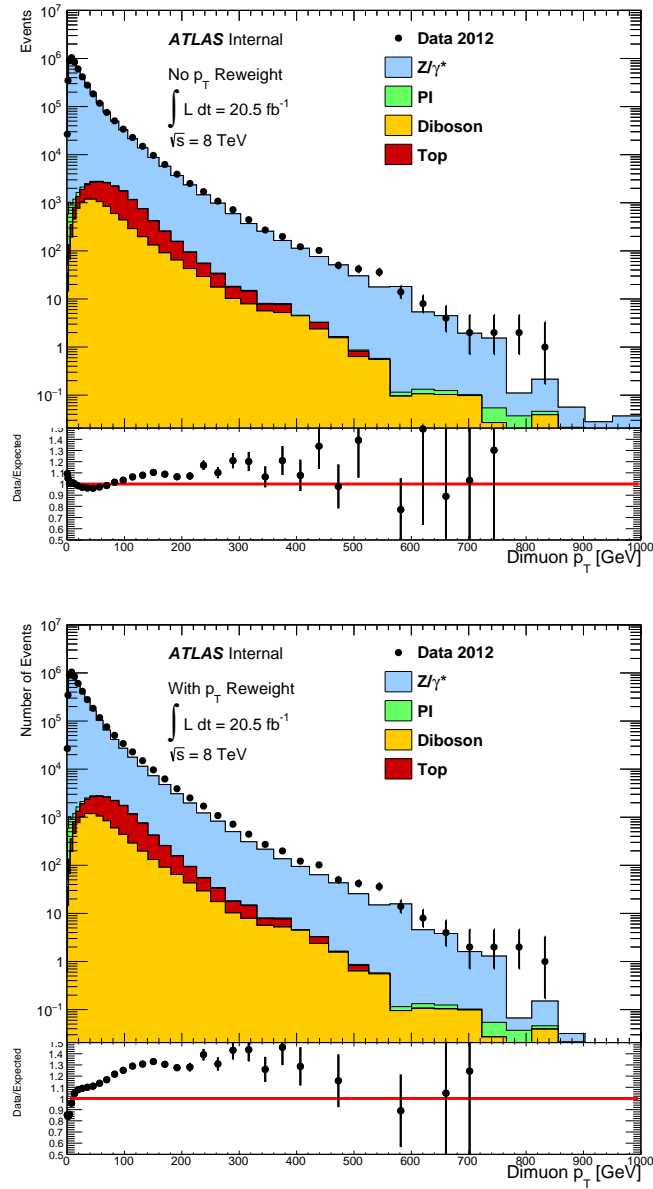


Figure A.2: Comparison of the agreement of the Monte Carlo simulated dilepton p_T distribution to that of the Data. The upper figure shows the agreement without applying dilepton p_T reweighting, while the lower one shows the effect of applying it.

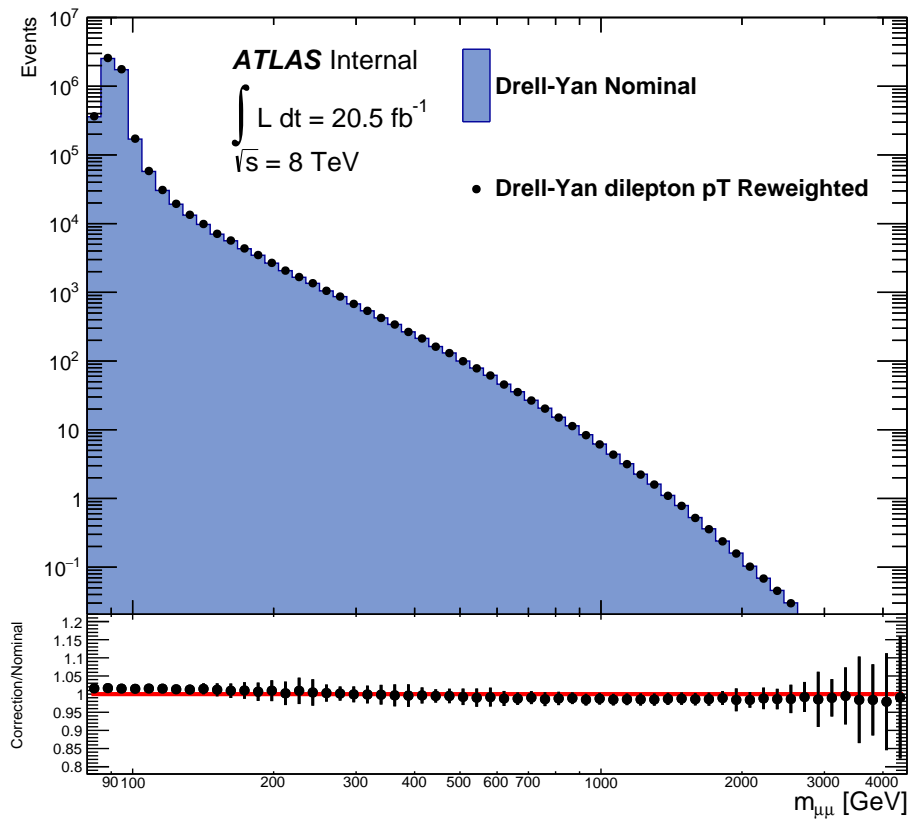


Figure A.3: Comparison of the Drell-Yan dimuon invariant mass spectrum before and after the dilepton p_T reweighting.

B ADD Large extra dimensions limits with a uniform prior on the cross section

The 95% Bayesian upper limits obtained for the ADD using a flat prior on $1/M_S^4$ and $1/M_S^8$ prior are summarized in table 9.4. To check the prior dependence of the results, these upper limits were compared against those obtained using a uniform prior on the Signal+Background cross section. As such, an upper exclusion limit is extracted directly on the number of Signal+Background events. The ADD LED parametrizations shown in figure 9.5 are then used to convert the upper limit on the number of signal events to a value of M_S . The expected limit PE distribution for both the electron and muon channels is shown in figure B.1, with the expected and observed limits highlighted. The expected exclusion limits in terms of the number of Signal+Background events are 3.10 and 3.08 for the electron and muon channels respectively, corresponding to a value of M_S of 3.75 and 3.52 TeV. The exclusion limits extracted on M_S are then consistent with those obtained using a flat prior in $1/M_S^8$.

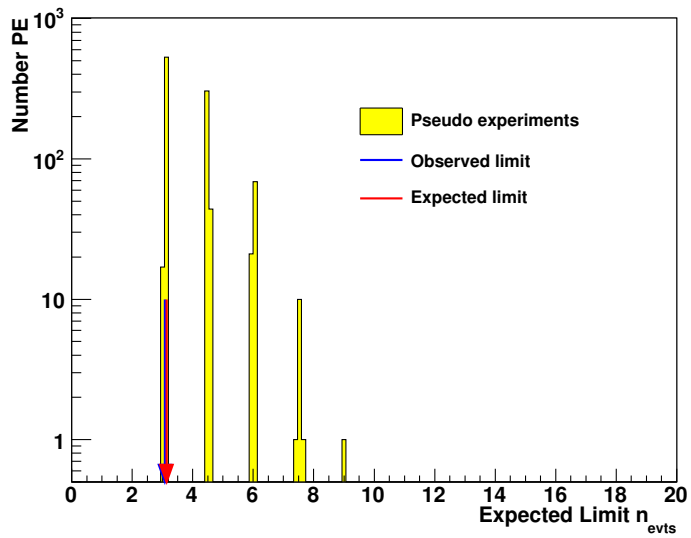
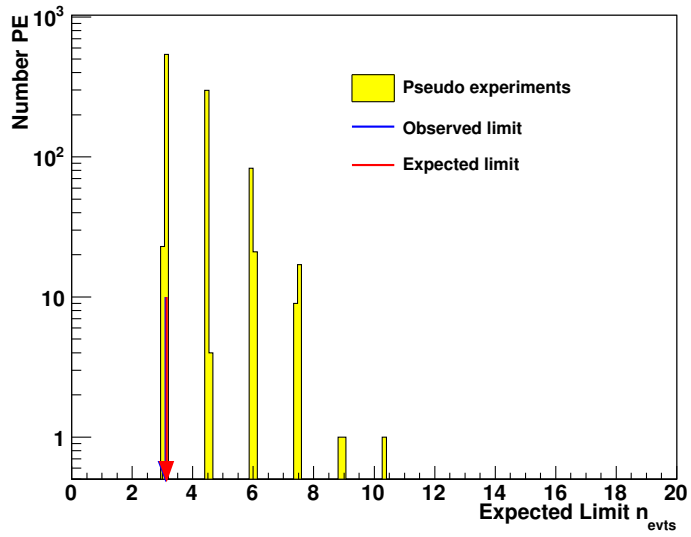


Figure B.1: Expected limit PE distribution for the electron (top) and muon (bottom) channels for a uniform prior on the cross section.

C QBH Limits with the Frequentist CL_S method

The results of the searches presented in this thesis are obtained in the context of the Bayesian interpretation of probability. There are two main schools of thought in this field: Bayesian and Frequentist. As a consequence, it is common that results from search experiments in particle physics are presented in the context of either of these two approaches. Chapter 8 summarizes the Bayesian approach, encapsulated in Bayes theorem (equation 8.1). The Frequentist interpretation defines probability as the relative frequency of an event occurring over a large number of trials:

$$P = \lim_{n_t \rightarrow \infty} \frac{n_s}{n_t} \quad (\text{C.1})$$

where n_s is the number of successes (an event occurring), n_t is the number of trials and P is the probability of a success. The Frequentist approach has the advantage of its results being independent of a prior probability. It is however expected that results using both interpretations converge when high statistics are available. This thesis does not aim to discuss which of the methods available is more adequate, but a cross-check of the benchmark Bayesian results is provided using a Frequentist approach. In the experimental Particle Physics field the current standard Frequentist method is the widely used CL_S method, presented in [132]. The CL_S technique is based on the use of the LLR test statistic (equation 8.14) to discriminate between the Background or the Signal+Background hypotheses on the observed data. The p -value of the the two hypotheses is calculated by generating a large number of pseudo-experiments using RooStats [133], a collection of statistical tools built and distributed with ROOT. The confidence intervals (CI)²⁴ are then defined in terms of the p -value:

$$1 - CI_B = p(LLR < LLR_{Data} | n_{Background}) \quad (\text{C.2})$$

$$CI_{S+B} = p(LLR > LLR_{Data} | n_{Signal+Background}) \quad (\text{C.3})$$

where $1 - CI_B$ is the probability of observing a signal-like fluctuation in the data assuming the background only hypothesis and CI_{S+B} is the probability of observing a downward fluctuation that looks background only-like, assuming the Signal+Background hypothesis. The confidence interval CI_{S+B} could be used at 95% CI to extract exclusion limits. However, in cases where the signal expectation is very small, a downward fluctuation in the signal yields can lead to excluding a signal of zero strength. As argued in [132], the CI on the Signal+Background hypothesis is normalised using the CI on the background-only hypothesis. The CI on signal is then defined as the ratio of these two probabilities:

$$CI_S = \frac{CI_{S+B}}{CI_B} \quad (\text{C.4})$$

²⁴The confidence intervals are commonly defined as CL. Given that in this thesis CL is already used for the Bayesian credibility intervals, CI is used to avoid confusion.

where the CI_S is the exclusion CI on the signal process searched for, and can be understood as the confidence interval in the signal hypothesis only. A limit on the parameter of interest of the signal process is found by increasing the signal cross section until $CI_S = 0.95$. Similarly to the Bayesian results already presented, the theoretical dependence of the parameter of interest on the signal cross section is used to extract limits directly on the model parameter. The likelihood for this Frequentist-based limit setting approach is defined as the product of Poissonian probabilities of observing n_{obs} events assuming the Signal+Background hypothesis, in order to be consistent with the benchmark Bayesian analysis. Similarly, the systematic uncertainties considered are the same as for the Bayesian analysis.

The results obtained are presented in figure C.1 and should be compared with the results shown in figure 9.16 (bottom). The upper limits obtained at 95% CI are summarized in table C.1 for the muon channel. The upper limits extracted at 95% CI are within 1%(2%) for the ADD n=6 (RS n=1) model than those extracted at 95% CL with a Bayesian approach. The Bayesian upper limits can be found in table C.2 for comparison.

Table C.1: 95% CI limits on M_{th} for the QBH ADD n=6 and RS n=1 models for the dimuon channel.

QBH $\rightarrow\mu^+\mu^-$	ADD n=6	RS n=1
Observed limit M_{th} [TeV]	3.32	1.99
Expected limit M_{th} [TeV]	3.30	2.00

Table C.2: 95% Bayesian upper limits on M_{th} for the QBH ADD n=6 and RS n=1 models for the dimuon channel.

QBH $\rightarrow\mu^+\mu^-$	ADD n=6	RS n=1
Observed limit M_{th} [TeV]	3.32	1.95
Expected limit M_{th} [TeV]	3.33	1.94

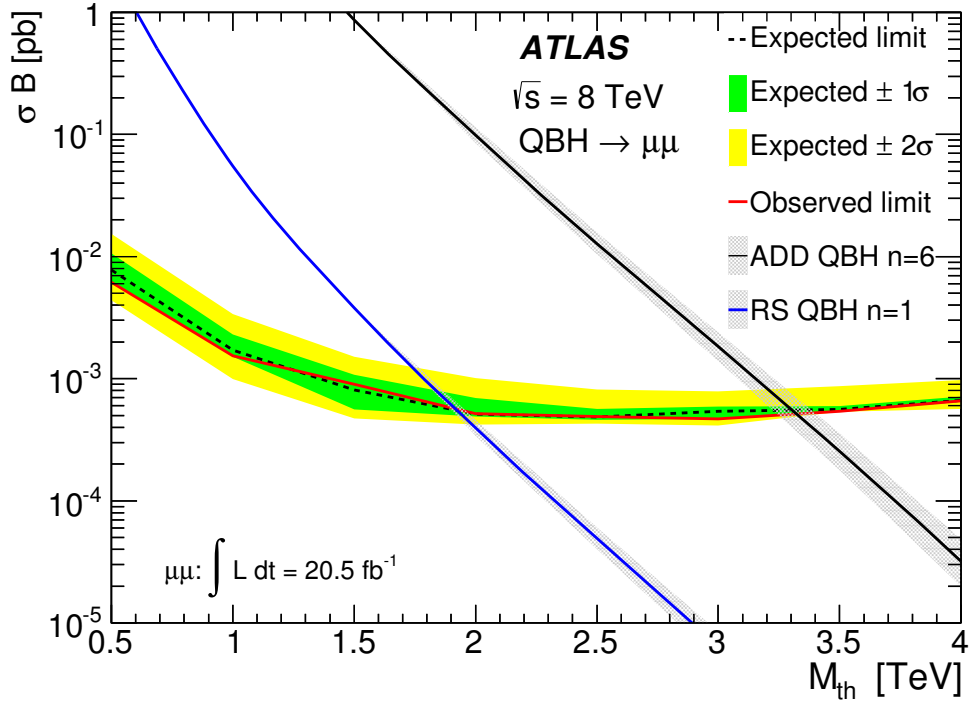


Figure C.1: Expected and observed 95% CI upper limits on σ_B for quantum black hole production in the ADD $n=6$ and RS $n=1$ models for the combination of dielectron and dimuon channels. The thickness of the ADD $n=6$ and RS $n=1$ theory lines represents the effect of the PDF uncertainty on the theoretical σ_B .

D Additional Plots

This section displays additional plots for the exclusion limit extraction the RS QBH and the ADD HLZ n=2 formalism as well as the dimuon mass spectrum with signal HLZ n=2 and RS QBH overlaid, both for the muon and combined dilepton channel.

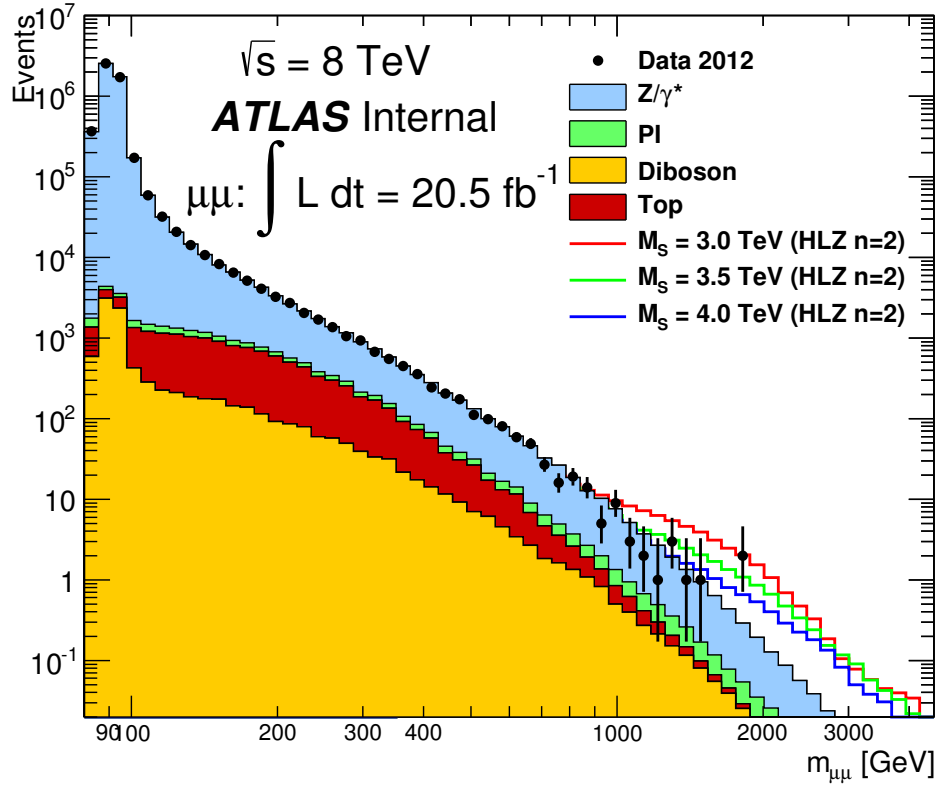


Figure D.1: Comparison of the invariant mass distribution for Data and Monte Carlo for the ADD LED search. Only 3-station muons are used for this search. The expected signal ADD LED+Drell-Yan invariant mass distribution for three benchmark M_S values for the HLZ n=2 formalism is overlaid.

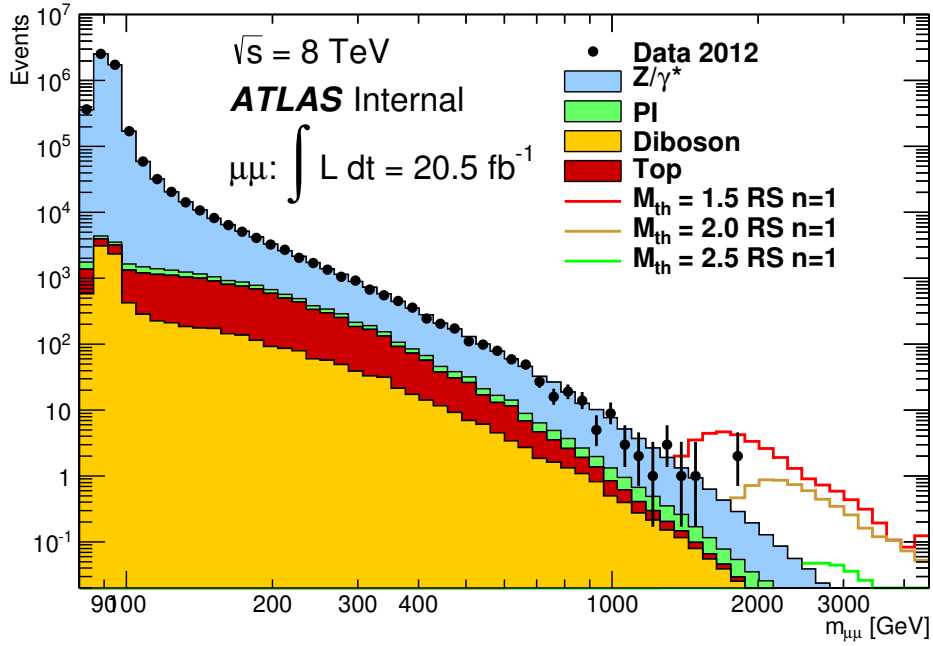


Figure D.2: Comparison of the invariant mass distribution for Data and Monte Carlo for the QBH search. The expected signal QBH invariant mass distribution for three benchmark M_{th} values for the RS model is overlaid.

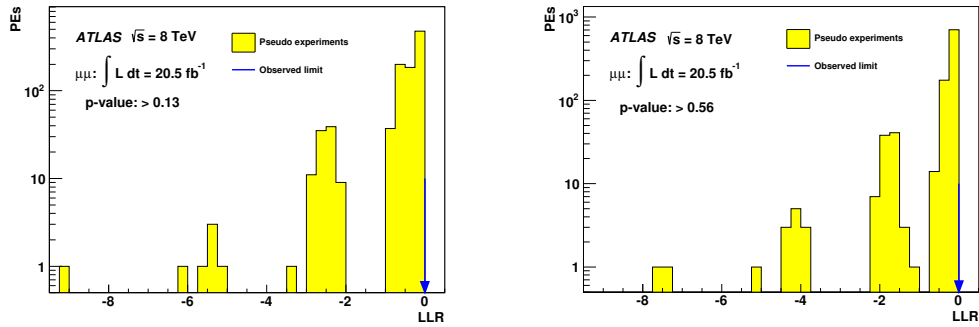


Figure D.3: ADD HLZ $n=2$ expected LLR PE distribution for a uniform positive prior in $1/M_S^4$ (left) and $1/M_S^8$ (right) choice for the dimuon channel. The observed LLR is shown by the blue arrow.

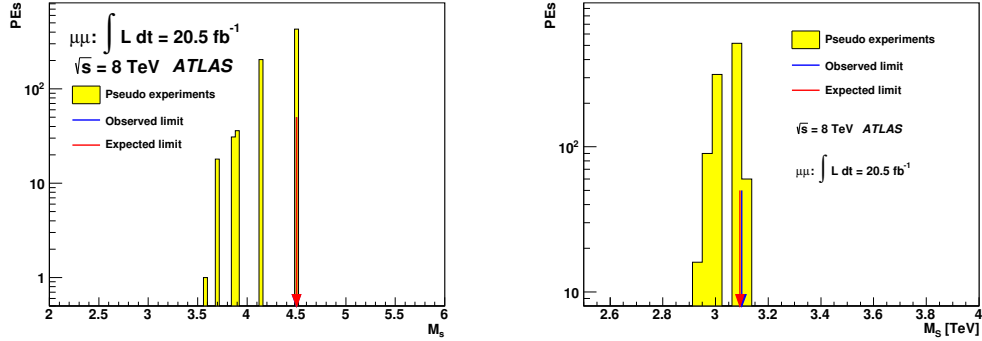


Figure D.4: ADD HLZ $n=2$ expected exclusion limits PE distribution for a uniform positive prior in $1/M_S^4$ (left) and $1/M_S^8$ (right) choice for M_S for the dimuon channel. The expected exclusion limit is the median of the distribution and is shown by the blue arrow, while the red arrow shows the observed exclusion limit.

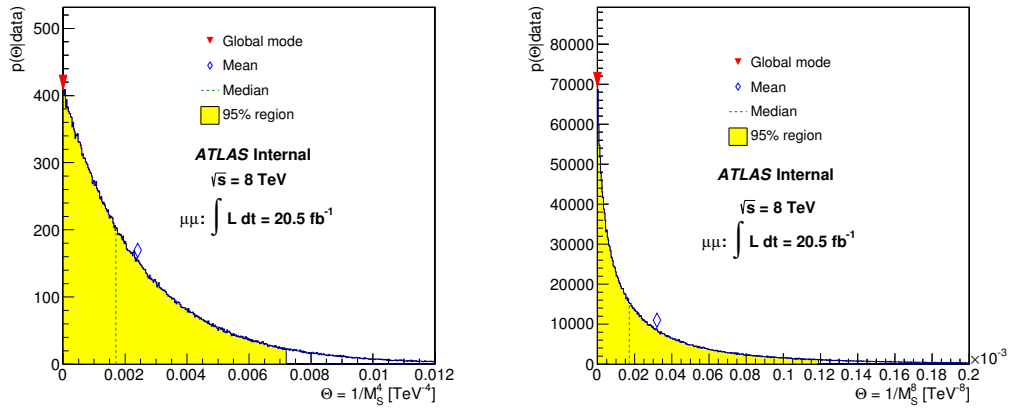


Figure D.5: ADD HLZ $n=2$ observed posterior probability density function for a uniform positive prior in $1/M_S^4$ (left) and $1/M_S^8$ (right) choice for $\theta = 1/M_S^4$ (left) and $1/M_S^8$ (right) for the dilepton channel. The 95% region is shown in yellow.

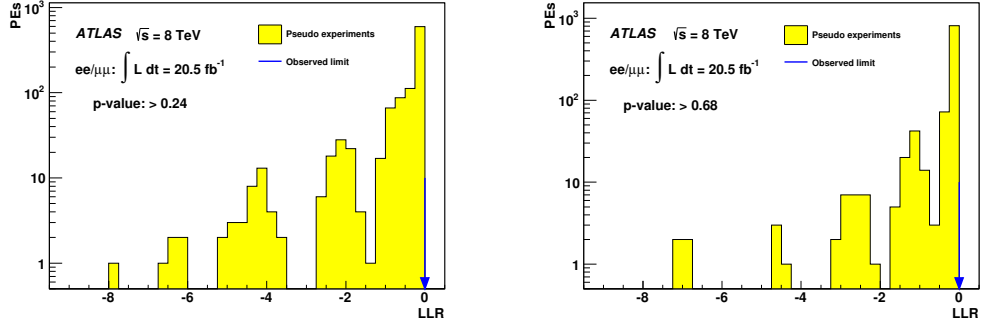


Figure D.6: ADD HLZ $n=2$ expected LLR PE distribution for a uniform positive prior in $1/M_S^4$ (left) and $1/M_S^8$ (right) choice for the dilepton channel. The observed LLR is shown by the blue arrow.

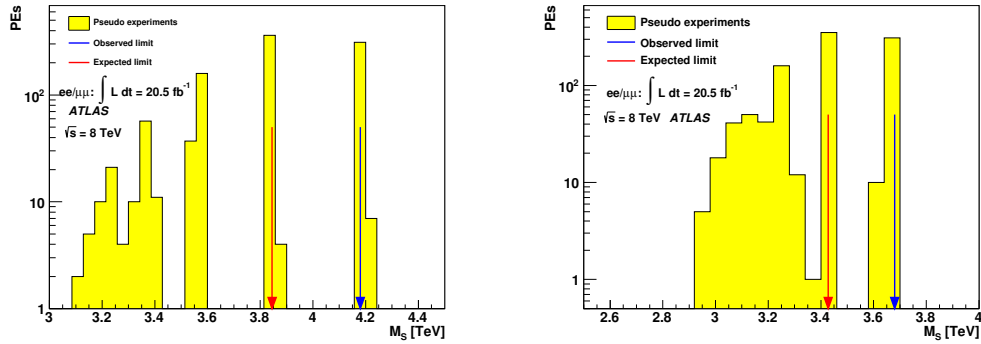


Figure D.7: ADD HLZ $n=2$ expected exclusion limits PE distribution for a uniform positive prior in $1/M_S^4$ (left) and $1/M_S^8$ (right) choice for M_S for the dilepton channel. The expected exclusion limit is the median of the distribution and is shown by the blue arrow, while the red arrow shows the observed exclusion limit.

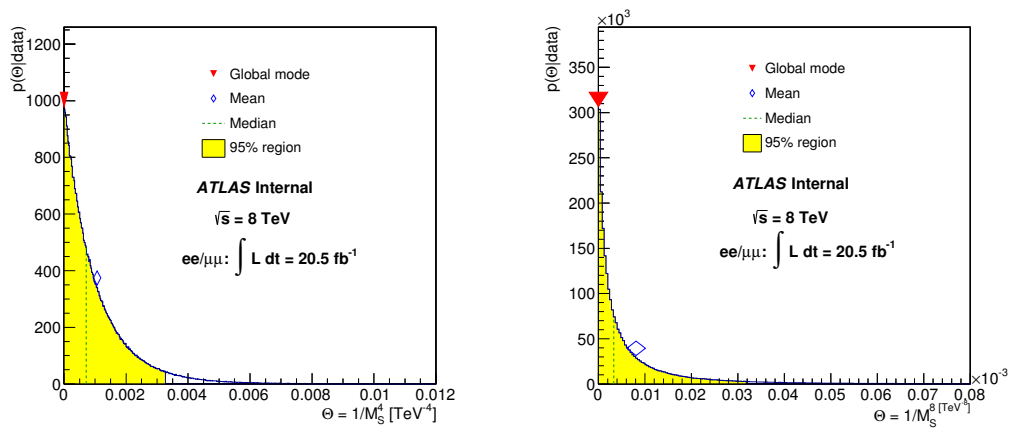


Figure D.8: ADD HLZ $n=2$ observed posterior probability density function for a uniform positive prior in $1/M_S^4$ (left) and $1/M_S^8$ (right) choice for $\theta = 1/M_S^4$ (left) and $1/M_S^8$ (right) for the dilepton channel. The 95% region is shown in yellow.

E QBH Sensitivity studies

At the time of writing the start of Run-2 is less than half a year away. While data is of course not yet available, Monte Carlo simulation using expected Run-2 conditions has already started. This section describes a study that aims to estimate, assuming the absence of signal, the exclusion limits that can be obtained for the QBH model using the 100 fb^{-1} of integrated luminosity that will be collected at a centre-of-mass energy of 13 TeV during Run-2. Going further, the case for the high-luminosity LHC is investigated by estimating the exclusion limits that can be reached using 3000 fb^{-1} .

This study does not aim to provide a conclusive result: all the necessary tools are still not in place for an extensive study. Instead, the aim is to provide an estimation of the exclusion limits that can be reached using LHC data at a centre-of-mass energy of 13 TeV for different amounts of integrated luminosity. As such, the systematics used are the same as was used in the 2012-2013 QBH search. At present time, from the considered SM backgrounds in Run-1, only Drell-Yan Monte Carlo simulated samples are available at $\sqrt{s} = 13 \text{ TeV}$. Given the status of the Drell-Yan process as the leading SM background of this search, Top and Diboson-related processes are neglected to simplify this study. Preliminary K -factors are used to estimate the Drell-Yan cross section up to NNLO. Monte Carlo simulation is also available to simulate a QBH decay to dilepton. Expected exclusion limits are defined as the 95% Bayesian CL, obtained using the already mentioned BAT.

Figure E.1 shows the dimuon invariant mass spectrum for the simulated signal and background processes considered after applying the tight muon selection outlined in section 7.2. Given the increased centre of mass energy it is expected that higher dimuon invariant masses will be accessible and, as such, the upper range shown in the plot is increased to 10 TeV, compared to the 4.5 TeV shown for the results obtained at $\sqrt{s} = 8 \text{ TeV}$. Figure E.2 shows the QCD+EW K -factor applied to the Drell-Yan process as a function of true dilepton mass.

The prospective limits obtained at $\sqrt{s} = 13 \text{ TeV}$ as a function of integrated luminosity are shown in figure E.3. It is expected that, assuming no signal is found, 1 fb^{-1} of collected integrated luminosity would already yield limits larger than those obtained using the Run-1 dataset. It should also be noted that the plot does not provide a strong case for the High Luminosity LHC, given that the prospective exclusion limits are expected to not improve by a large increase in luminosity. However, the study presented here assumes that the PDF uncertainties (the leading systematic in the Drell-Yan estimation) used in Run-1 will remain the same from Run-2 onwards. A better knowledge of the PDFs should improve the prospective limits presented here.

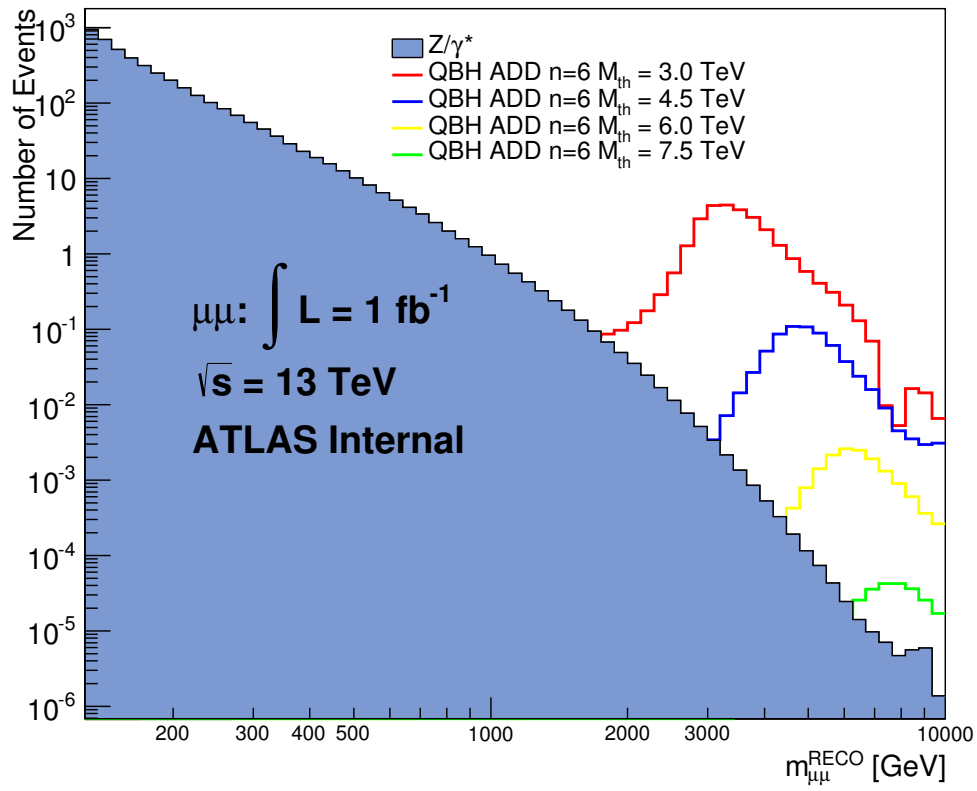


Figure E.1: Expected ADD QBH signal and background (Drell-Yan only) reconstructed dimuon invariant mass spectrum at a centre of mass energy of 13 TeV.

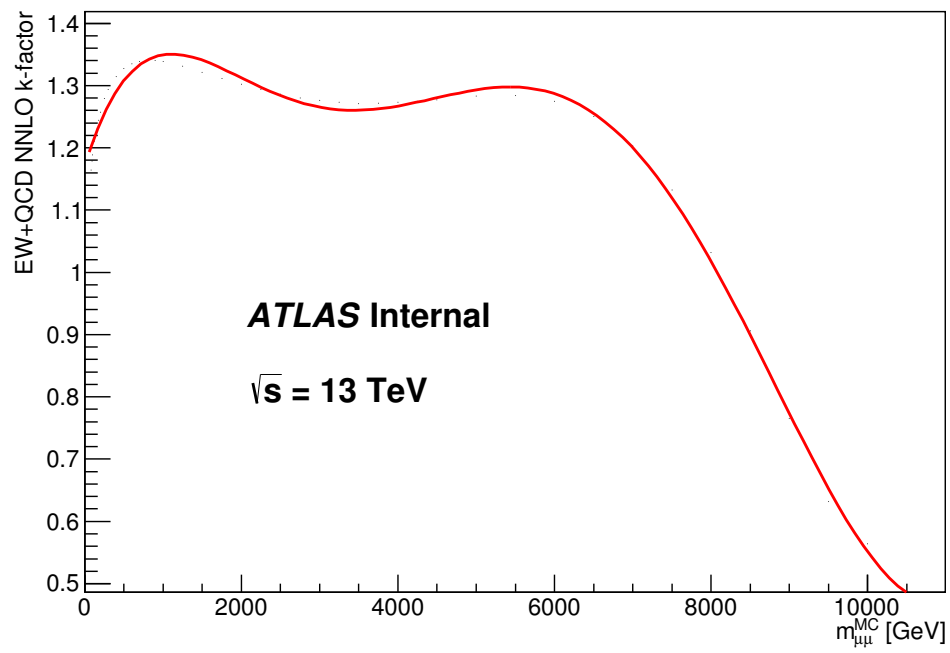


Figure E.2: QCD+EW K-factor applied to the Drell-Yan process as a function of the true dilepton mass.

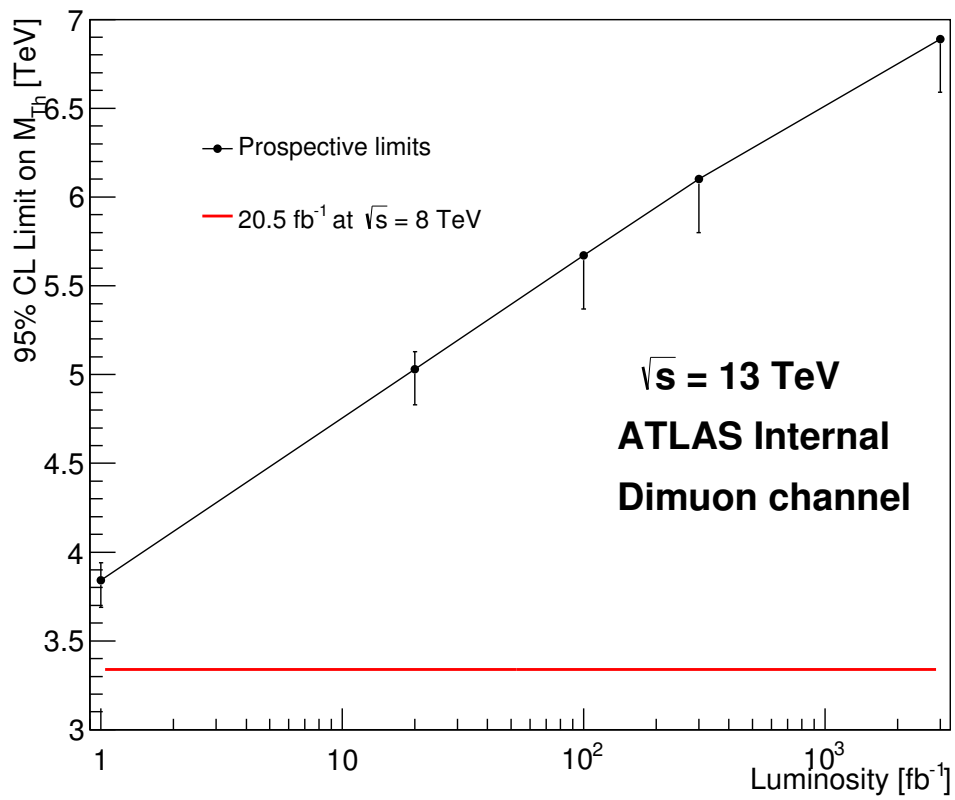


Figure E.3: Prospective limits with a centre of mass energy of 13 TeV against increasing integrated luminosity. The limit obtained using 20 fb^{-1} at $\sqrt{s} = 8 \text{ TeV}$ is shown by the red line.

Table E.1: Drell-Yan Monte Carlo samples used in the dimuon channel for the estimation of the prospective limits at $\sqrt{s} = 13$ TeV. The first column shows the internal ATLAS run number, then the generator level cross section times branching ratio and the mass range it corresponds to. In the last two columns, the number of events generated and the process it corresponds to are shown[87].

Dataset ID	$\sigma BR[\text{pb}]$ Powheg	$m_{\mu\mu}$ Range[GeV]	$N_{evt}[\text{k}]$	Signature
203519	$1.75 \cdot 10^1$	120-180	500	$\gamma^*/Z \rightarrow \mu\mu$
203520	2.92	180-250	250	$\gamma^*/Z \rightarrow \mu\mu$
203521	1.02	250-400	150	$\gamma^*/Z \rightarrow \mu\mu$
203522	$1.95 \cdot 10^{-1}$	400-600	100	$\gamma^*/Z \rightarrow \mu\mu$
203523	$3.74 \cdot 10^{-2}$	600-800	100	$\gamma^*/Z \rightarrow \mu\mu$
203524	$1.06 \cdot 10^{-2}$	800-1000	100	$\gamma^*/Z \rightarrow \mu\mu$
203525	$4.26 \cdot 10^{-3}$	1000-1250	100	$\gamma^*/Z \rightarrow \mu\mu$
203526	$1.42 \cdot 10^{-3}$	1250-1500	100	$\gamma^*/Z \rightarrow \mu\mu$
203527	$5.45 \cdot 10^{-4}$	1500-1750	100	$\gamma^*/Z \rightarrow \mu\mu$
203528	$2.30 \cdot 10^{-4}$	1750-2000	100	$\gamma^*/Z \rightarrow \mu\mu$
203529	$1.04 \cdot 10^{-4}$	2000-2250	100	$\gamma^*/Z \rightarrow \mu\mu$
203530	$4.94 \cdot 10^{-4}$	2250-2500	100	$\gamma^*/Z \rightarrow \mu\mu$
203531	$2.44 \cdot 10^{-5}$	2500-2750	100	$\gamma^*/Z \rightarrow \mu\mu$
203532	$1.25 \cdot 10^{-5}$	2750-3000	100	$\gamma^*/Z \rightarrow \mu\mu$
203533	$1.00 \cdot 10^{-5}$	3000-3500	100	$\gamma^*/Z \rightarrow \mu\mu$
203534	$2.93 \cdot 10^{-6}$	3500-4000	100	$\gamma^*/Z \rightarrow \mu\mu$
203535	$8.98 \cdot 10^{-7}$	4000-4500	100	$\gamma^*/Z \rightarrow \mu\mu$
203536	$2.81 \cdot 10^{-7}$	4500-5000	100	$\gamma^*/Z \rightarrow \mu\mu$
203537	$8.49 \cdot 10^{-6}$	> 5000	100	$\gamma^*/Z \rightarrow \mu\mu$

Table E.2: QBH samples for the ADD $n=6$ extra-dimension formalism used in the dimuon channel for the estimation of the prospective limits at $\sqrt{s} = 13$ TeV. The first column shows the value of M_{th} , while the second column lists the internal ATLAS run number and the QBH generator cross section times branching ratio. For each M_{th} value 10000 events were generated.

$M_{th}[\text{TeV}]$	Dataset ID	QBH $\sigma BR[\text{pb}]$	Signature
3.0	203437	$6.2 \cdot 10^{-2}$	QBH $\rightarrow \mu\mu$
4.5	203438	$1.6 \cdot 10^{-3}$	QBH $\rightarrow \mu\mu$
6.0	203439	$4.0 \cdot 10^{-5}$	QBH $\rightarrow \mu\mu$
7.5	203440	$7.5 \cdot 10^{-7}$	QBH $\rightarrow \mu\mu$

F BlackMax parameter choice

This section shows the file used in BlackMax to choose the parameters for black hole production and decay. The file is included in the BlackMax source code under the name “parameter.txt”. A full description of each of the parameters is provided in the BlackMax Manual [73].

```
Number_of_simulations
10000
incoming_particle (1: pp_2 : ppbar_3 : ee+)
1
Center_of_mass_energy_of_incoming_particle
14000
M_pl (GeV)
1000
definition_of_M_pl : (1: M_D_2 : M_p_3 : M_DL_4 : put_in_by_hand )
2
if_definition ==4
1.
Choose_a_case : (1: tensionless_nonrotating_2 : tension_nonrotating_
3: rotating_nonsplit_4 : Lisa_two_particles_final_states )
3
number_of_extra_dimensions
6
number_of_splitting_dimensions
0
size_of_brane (1/Mpl)
1.0
extradimension_size (1/Mpl)
10.
tension ( parameter_of_deficit_angle : 1_to_0 )
1.0
choose_a_pdf_file (200_to_240_cteq6 ) Or_>10000_for_LHAPDF
200
Chose_events_by_center_of_mass_energy_or_
by_initial_black_hole_mass (1: center_of_mass_2 : black_hole_mass )
1
Minimum_mass (GeV)
5000
Maxmum_mass (GeV)
14000
```

```

Include_string_ball:(1:no_2:yes)
1
String_scale(M_s)(GeV)
1000
string_coupling(g_s)
0.8
The_minimum_mass_of_a_string_ball_or_black_hole(in_unit_Mpl)
1.
fix_time_step(1:fix_2:no)
2
time_step(1/GeV)
1.e-5
other_definition_of_cross_section(0:no_1:yoshino_2:pi*r^2_3:4pi*r^2)
0
calculate_the_cross_section_according_to
(0:the_radius_of_initial_black_hole_1:centre_of_mass_energy)
1
calculate_angular_eigen_value(0:calculate_1:fitting_result)
0
Mass_loss_factor(0~1.0)
0.5
momentum_loss_factor(0~1.0)
0.5
Angular_momentum_loss_factor(0~1.0)
0.5
turn_on_graviton(0:off_1:on)
1
Seed
123589541
Write_LHA_Output_Record?_0=NO_1=Yes_2=More_Detailed_output
0
L_suppression(1:none_2:delta_area_3:anular_momentum_4:delta_angular_momentum)
1
angular_momentum_suppression_factor
1
charge_suppression(1:none_2:do)
1
charge_suppression_factor
1
color_suppression_factor
20

```



```

split_fermion_width (1/Mpl) _and_location (from -15 to 15) (up_to_9 extradimensions )
u_quark_Right (Note: do_not_insert_blank_spaces )
1.0
10.0,0.0,0.0,0.0,0.0,0.0,0.0,0.0,0.0
u_quark_Left (Note: do_not_insert_blank_spaces )
1.0
10.0,0.0,0.0,0.0,0.0,0.0,0.0,0.0,0.0
u_bar_quark_Right (Note: do_not_insert_blank_spaces )
1.0
10.0,0.0,0.0,0.0,0.0,0.0,0.0,0.0,0.0
u_bar_quark_Left (Note: do_not_insert_blank_spaces )
1.0
10.0,0.0,0.0,0.0,0.0,0.0,0.0,0.0,0.0
d_quark_Right (Note: do_not_insert_blank_spaces )
1.0
10.0,0.0,0.0,0.0,0.0,0.0,0.0,0.0,0.0
d_quark_Left (Note: do_not_insert_blank_spaces )
1.0
10.0,0.0,0.0,0.0,0.0,0.0,0.0,0.0,0.0
d_bar_quark_Right (Note: do_not_insert_blank_spaces )
1.0
10.0,0.0,0.0,0.0,0.0,0.0,0.0,0.0,0.0
d_bar_quark_Left (Note: do_not_insert_blank_spaces )
1.0
10.0,0.0,0.0,0.0,0.0,0.0,0.0,0.0,0.0
s_quark_Right (Note: do_not_insert_blank_spaces )
1.0
10.0,0.0,0.0,0.0,0.0,0.0,0.0,0.0,0.0
s_quark_Left (Note: do_not_insert_blank_spaces )
1.0
10.0,0.0,0.0,0.0,0.0,0.0,0.0,0.0,0.0
s_bar_quark_Right (Note: do_not_insert_blank_spaces )
1.0
10.0,0.0,0.0,0.0,0.0,0.0,0.0,0.0,0.0
s_bar_quark_Left (Note: do_not_insert_blank_spaces )
1.0
10.0,0.0,0.0,0.0,0.0,0.0,0.0,0.0,0.0
c_quark_Right (Note: do_not_insert_blank_spaces )
1.0
10.0,0.0,0.0,0.0,0.0,0.0,0.0,0.0,0.0
c_quark_Left (Note: do_not_insert_blank_spaces )

```

```

1.0
10.0,0.0,0.0,0.0,0.0,0.0,0.0,0.0,0.0
c_bar_quark_Right(Note: do_not_insert_blank_spaces)
1.0
10.0,0.0,0.0,0.0,0.0,0.0,0.0,0.0,0.0
c_bar_quark_Left(Note: do_not_insert_blank_spaces)
1.0
10.0,0.0,0.0,0.0,0.0,0.0,0.0,0.0,0.0
b_quark_Right(Note: do_not_insert_blank_spaces)
1.0
10.0,0.0,0.0,0.0,0.0,0.0,0.0,0.0,0.0
b_quark_Left(Note: do_not_insert_blank_spaces)
1.0
10.0,0.0,0.0,0.0,0.0,0.0,0.0,0.0,0.0
b_bar_quark_Right(Note: do_not_insert_blank_spaces)
1.0
10.0,0.0,0.0,0.0,0.0,0.0,0.0,0.0,0.0
b_bar_quark_Left(Note: do_not_insert_blank_spaces)
1.0
10.0,0.0,0.0,0.0,0.0,0.0,0.0,0.0,0.0
t_quark_Right(Note: do_not_insert_blank_spaces)
1.0
10.0,0.0,0.0,0.0,0.0,0.0,0.0,0.0,0.0
t_quark_Left(Note: do_not_insert_blank_spaces)
1.0
10.0,0.0,0.0,0.0,0.0,0.0,0.0,0.0,0.0
t_bar_quark_Right(Note: do_not_insert_blank_spaces)
1.0
10.0,0.0,0.0,0.0,0.0,0.0,0.0,0.0,0.0
t_bar_quark_Left(Note: do_not_insert_blank_spaces)
1.0
10.0,0.0,0.0,0.0,0.0,0.0,0.0,0.0,0.0
e_-_Left(Note: do_not_insert_blank_spaces)
1.0
-10.0,0.0,0.0,0.0,0.0,0.0,0.0,0.0,0.0
e_-_Right(Note: do_not_insert_blank_spaces)
1.0
-10.0,0.0,0.0,0.0,0.0,0.0,0.0,0.0,0.0
e+_Left(Note: do_not_insert_blank_spaces)
1.0
-10.0,0.0,0.0,0.0,0.0,0.0,0.0,0.0,0.0

```

```

e+_Right(Note: do_not_insert_blank_spaces)
1.0
-10.0,0.0,0.0,0.0,0.0,0.0,0.0,0.0,0.0
mu_-_Left(Note: do_not_insert_blank_spaces)
1.0
-10.0,0.0,0.0,0.0,0.0,0.0,0.0,0.0,0.0
mu_-_Right(Note: do_not_insert_blank_spaces)
1.0
-10.0,0.0,0.0,0.0,0.0,0.0,0.0,0.0,0.0
mu+_Left(Note: do_not_insert_blank_spaces)
1.0
-10.0,0.0,0.0,0.0,0.0,0.0,0.0,0.0,0.0
mu+_Right(Note: do_not_insert_blank_spaces)
1.0
-10.0,0.0,0.0,0.0,0.0,0.0,0.0,0.0,0.0
tau_-_Left(Note: do_not_insert_blank_spaces)
1.0
-10.0,0.0,0.0,0.0,0.0,0.0,0.0,0.0,0.0
tau_-_Right(Note: do_not_insert_blank_spaces)
1.0
-10.0,0.0,0.0,0.0,0.0,0.0,0.0,0.0,0.0
tau+_Left(Note: do_not_insert_blank_spaces)
1.0
-10.0,0.0,0.0,0.0,0.0,0.0,0.0,0.0,0.0
tau+_Right(Note: do_not_insert_blank_spaces)
1.0
-10.0,0.0,0.0,0.0,0.0,0.0,0.0,0.0,0.0
neutrino_e-(Note: do_not_insert_blank_spaces)
1.0
-10.0,0.0,0.0,0.0,0.0,0.0,0.0,0.0,0.0
neutrino_e+(Note: do_not_insert_blank_spaces)
1.0
-10.0,0.0,0.0,0.0,0.0,0.0,0.0,0.0,0.0
neutrino_mu-(Note: do_not_insert_blank_spaces)
1.0
-10.0,0.0,0.0,0.0,0.0,0.0,0.0,0.0,0.0
neutrino_mu+(Note: do_not_insert_blank_spaces)
1.0
-10.0,0.0,0.0,0.0,0.0,0.0,0.0,0.0,0.0
neutrino_tau-(Note: do_not_insert_blank_spaces)
1.0

```

```

-10.0,0.0,0.0,0.0,0.0,0.0,0.0,0.0,0.0,0.0
nu_tau+(Note:do_not_insert_blank_spaces)
1.0
-10.0,0.0,0.0,0.0,0.0,0.0,0.0,0.0,0.0,0.0
number_of_conservation
1
d,s,b,u,c,t,e,mu,tau,nu_e,nu_mu,nu_tau
1,1,1,1,1,1,0,0,0,0,0,0
1,1,1,1,1,1,-3,-3,-3,-3,-3,-3
0,0,0,0,0,0,1,1,1,1,1,1
0,0,0,0,0,0,0,0,0,0,0,0
0,0,0,0,0,0,0,0,0,0,0,0
0,0,0,0,0,0,0,0,0,0,0,0
0,0,0,0,0,0,0,0,0,0,0,0

```

G QBH samples parameter choice

A full list of the choice of parameters used to generate the samples follows for the ADD (Randall-Sundrum) model [134]:

- Beam 1 Energy = 4.0 TeV
- Beam 2 Energy = 4.0 TeV
- Extradimensional Planck Mass = minimum black hole mass, also known as M_{th}
- Maximum BH mass = 3-extra-dimensional Planck mass
- Extra dimension model: ADD (Randall-Sundrum)
- Total number of dimensions = 10 (5)
- PDF = MSTWLO 2008 LO
- Using PDG definition of the Planck Scale. As outlined in [29], for such a definition the function $k(n)$ mentioned in equation 2.34 takes the form:

$$k(n) = \left(2^n \sqrt{\pi}^{n+3} \frac{\Gamma(\frac{n+3}{2})}{n+2} \right) \quad (\text{G.1})$$

where $\Gamma(n) = \int_0^\infty x^{n-1} e^{-x} dx$

- Using black hole radius as the QCD scale for PDFs
- Yoshino-Rychkov factors for cross section enhancement [135] not used
- Two-particle decay probability not included. There exists the possibility of decays to more than two particles as explained in section 4 of [29], with the multiplicity probabilities shown in table 4. Therefore, by considering the two particle decays the cross section could be weighted by a factor accounting for the probability of a two particle decay.
- Include a Standard Model Higgs particle with a mass of 125 GeV
- Include graviton
- Assume neutrinos are only left-handed

References

- [1] <http://press.web.cern.ch/press-releases/2008/10/cern-releases-analysis-lhc-incident>
- [2] http://www.theregister.co.uk/2009/12/09/lhc_2_tev_collisions/
- [3] “Broken Symmetries and the Masses of Gauge Bosons”, Peter W. Higgs, *Phys. Rev. Lett.* 13, 508 (1964)
- [4] The ATLAS collaboration, “Observation of a new particle in the search for the Standard Model Higgs boson with the ATLAS detector at the LHC”, arXiv:1207.7214 [hep-ph] (2012)
- [5] The CMS collaboration, “Observation of a new boson at a mass of 125 GeV with the CMS experiment at the LHC”, arXiv:1207.7235 [hep-ph] (2012)
- [6] ”Relativistic Waves and Quantum Fields, by Andreas Brandhuber, ”<http://www.strings.ph.qmul.ac.uk/~andreas/RWQF/rwqf.html>
- [7] “Quantum Field Theory”, http://www.stfc.ac.uk/PPD/resources/pdf/Dasgupta_08_Intro_to_QFT.pdf
- [8] Introduction to Elementary Particles, 2nd edition, by David Griffiths, WILEY-VCH
- [9] <http://www.quantumdiaries.org/2010/03/07/more-feynman-diagrams-momentum-conservation/>
- [10] M. Kobayashi, T. Maskawa; Maskawa (1973). “CP-Violation in the Renormalizable Theory of Weak Interaction”. *Progress of Theoretical Physics* 49 (2): 652–657.
- [11] <http://schnapzer.com/?articleID=4875>
- [12] B. Pontecorvo (1957). ”Mesonium and anti-mesonium”. *Zh. Eksp. Teor. Fiz.* 33: 549–551. reproduced and translated in *Sov. Phys. JETP* 6: 429. 1957.
- [13] Particle Data Group, “Review of Particle Physics”, *Chin. Phys. C.* 38. 090001 (2014)
- [14] “The Standard Model”, http://www.stfc.ac.uk/PPD/resources/pdf/Teubner-_Standard_Model_2008.pdf
- [15] Alekhin, Djoaudi and Moch, “The top quark and Higgs boson masses and the stability of the electroweak vacuum”, arXiv:1207.0980 [hep-ph] (2012)
- [16] <http://www.stfc.ac.uk/2861.aspx>

- [17] Sabine Hossenfelder, “What Black Holes can teach us” arXiv:hep-ph/0412265v1 (2004)
- [18] Arkani-Hamed, Dimopolus and Dvali, “The Hierarchy Problem and New Dimensions at a millimeter” arXiv:hep-ph/9803315v1 (1998)
- [19] C. D. Hoyle et al, Sub-millimeter Tests of the Gravitational Inverse-square Law, Phys. Rev D 70 (2004)
- [20] Gleisberg et al, “Helicity Formalism for Spin-2 Particles”, arXiv:hep-ph/0306182 (2003)
- [21] T Han et al, “Kaluza-Klein States from Large Extra Dimensions”, arXiv:hep-ph/9811350 (1998)
- [22] The ATLAS Collaboration Exotics Lepton+X Working Group, “Search for contact interactions and large extra dimensions in the dilepton channel using pp collisions at $\sqrt{s} = 8$ TeV with the ATLAS detector”, Internal Support Note ATL-COM-PHYS-2013-1527
- [23] Jo Anne L. Hewett, “Indirect Collider Signals for Extra Dimensions”, arXiv: hep-ph/9811356v2 (1999)
- [24] Giudice, Ratazzi and Wells, “Quantum Gravity and Extra Dimensions at High-Energy Colliders”, arXiv: hep-ph/9811291v2 (2000)
- [25] Randall and Sundrum, “An Alternative to Compactification” arXiv:hep-ph/9906064v1 (1999)
- [26] Maxime Gabella, “The Randall-Sundrum model”, <http://www-thphys.physics.ox.ac.uk/people/MaximeGabella/rs.pdf> (2006)
- [27] Patrick Meade and Lisa Randall, “Black Holes and Quantum Gravity at the LHC”, arXiv:0708.3017v1 [hep-ph] (2007)
- [28] Dimopoulos and Landsberg, “Black Holes at the LHC”, arXiv:hep-ph/0106295 (2001)
- [29] Douglas Gingrich, “Quantum Black Holes with charge, colour and spin at the LHC”, arXiv:0912.0826v4 [hep-ph] (2010)
- [30] R. C. Myers and M. J. Perry Ann. Phys. 172, 304-347 (1986).
- [31] Giddings and Thomas, “High energy colliders as black hole factories: The end of short distance physics” PHYSICAL REVIEW D, VOLUME 65, 056010
- [32] Campbell, Huston and Stirling, “Hard Interactions of Quarks and Gluons: a Primer for LHC Physics”, arXiv:hep-ph/0611148v1 (2006)

- [33] E. Perez and E. Rizvi, The quark and gluon structure of the proton, IOP publishing Rep. Prog. Phys 76 (2013) 046201 (58pp)
- [34] “Particle creation by black holes” S. W. Hawking, Source: Comm. Math. Phys. Volume 43, Number 3 (1975), 199-220
- [35] The ATLAS collaboration, “Search for microscopic black holes and string balls in final states with leptons and jets with the ATLAS detector at $\sqrt{s} = 8$ TeV”, ATLAS-CONF-2014-016
- [36] Xavier Calmet, Wei Gong and Stephen D.H. Tsu, “Colorful quantum black holes at the LHC”, arXiv:0806.4605 [hep-ph] (2008)
- [37] “Modelling the evolution of black holes”, TeV scale gravity at the LHC meeting on 7th December 2011, talk given by Elisabeth Winstanley <https://indico.cern.ch/conferenceTimeTable.py?confId=162294#20111207>
- [38] ATLAS Collaboration, “Search for Quantum Black-Hole Production in High-Invariant-Mass Lepton+Jet Final States Using Proton-Proton Collisions at $\sqrt{s} = 8$ TeV and the ATLAS Detector”, arXiv:1311.2006 [hep-ph] (2014)
- [39] The ATLAS collaboration “The ATLAS experiment at the CERN Large Hadron Collider” JINST 3 (2008) S08003
- [40] <http://www.thenakedscientists.com/HTML/content/interviews/interview/980/>
- [41] <http://hypatia.iasa.gr/en/help.html>
- [42] <https://atlas.web.cern.ch/Atlas/GROUPS/PHYSICS/PAPERS/PERF-2011-01/>
- [43] <http://hedberg.web.cern.ch/hedberg/home/atlas/atlas.html>
- [44] <https://twiki.cern.ch/twiki/bin/view/AtlasProtected/StacoMuonCollection>
- [45] <https://twiki.cern.ch/twiki/bin/view/AtlasProtected/MuidMuonCollection>
- [46] <https://twiki.cern.ch/twiki/bin/view/AtlasProtected/MuonsCollection>
- [47] ATLAS Level-1 Calorimeter Trigger Technical Design Report, ATLAS TDR-12, August 1998. <http://cds.cern.ch/record/381429?ln=en>

- [48] <https://indico.cern.ch/event/048/session/3/contribution/76/material/paper/0.pdf>
- [49] The evolution and Performance of the ATLAS Calorimeter-Based Triggers in 2011 and 2012, Ivana Hristova ATL-DAQ-PROC-2012-051
- [50] https://twiki.cern.ch/twiki/bin/view/AtlasPublic/LuminosityPublicResults#Data_Taking_Efficiency_and_Pileu
- [51] ATLAS Collaboration, Performance of the ATLAS Detector using First Collision Data, JHEP 1009 (2010) 056, doi:10.1007/JHEP09(2010)056.
- [52] <https://twiki.cern.ch/twiki/bin/viewauth/AtlasProtected/EtMissD3PDContents>
- [53] R. Achenbach et al., The ATLAS Level-1 Calorimeter Trigger, 2008 JINST 3 P03001. (ATL-DAQ-PUB-2008-001) <http://www.iop.org/EJ/abstract/1748-0221/3/03/P03001>
- [54] The ATLAS Level-1 Calorimeter Trigger: PreProcessor implementation and performance, 2012 JINST 7 P12008
- [55] <https://indico.cern.ch/event/281326/session/0/contribution/4/1/material/slides/0.pdf>
- [56] <https://twiki.cern.ch/twiki/bin/view/AtlasPublic/L1CaloTriggerPublicResults>
- [57] Will Butinger, on behalf of the ATLAS Collaboration, “The ATLAS Level-1 Trigger”, Journal of Physics Conference Series 396 (2012) 012010
- [58] The ATLAS Collaboration, “Performance of the ATLAS Level-1 Trigger”, ATL-COM-DAQ-2012-033 (2012)
- [59] <https://svnweb.cern.ch/trac/atlasgroups/browser/Trigger/L1CaloUpgrade/TriggerTowerAnalysis>
- [60] <https://svnweb.cern.ch/trac/atlasoff/browser/PhysicsAnalysis/D3PDMaker/L1CaloD3PDMaker>
- [61] <https://twiki.cern.ch/twiki/bin/viewauth/AtlasProtected/WZElectroweakCommonTopics2012>
- [62] <https://twiki.cern.ch/twiki/bin/view/AtlasProtected/ElectronIdentification>

- [63] https://twiki.cern.ch/twiki/bin/viewauth/AtlasProtected/TechnicalitiesForMedium1#Tight_2011_and_2012
- [64] E/Gamma Working Group, ATL-PHYS-PUB-2011-006, “Expected Electron Performance in the ATLAS experiment” (2011)
- [65] <https://svnweb.cern.ch/trac/atlasoff/browser/PhysicsAnalysis/TopPhys/TopD3PDCorrections/tags/TopD3PDCorrections-12-01-20/Root/RecalcMETProc.cxx>
- [66] C.M. Harris, P. Richardson and B.R. Webber, “CHARYBDIS: A Black Hole Event Generator”, JHEP 0308:033, hep-ph/0307305 (2003)
- [67] M. Cavaglia, R. Godang, L. Cremaldi, D. Summers, “Catfish: A Monte Carlo simulator for black holes at the LHC” arXiv:hep-ph/0609001 (2006)
- [68] Dai, Starkman, Stojkovic, Issever, Rizvi and Tseng “BlackMax: A black-hole event generator with rotation, recoil, split branes and brane tension”, arXiv:0711.3012 [hep-ph], Physical Review D (Vol.77, No.7)
- [69] D. M. Gingrich, Monte Carlo event generator for black hole production and decay in proton-proton collisions, Comput.Phys.Commun. 181 (2010) 1917–1924, arXiv:0911.5370 [hep-ph].
- [70] T. Sjostrand, S. Mrenna, and P. Z. Skands, Comput. Phys. Commun. 178 (2008) 852, arXiv:0710.3820 [hep-ph].
- [71] G. Corcella, I. Knowles, G. Marchesini, S. Moretti, et al., JHEP 0101 (2001) 010, arXiv:0011363 [hep-ph].
- [72] <http://blackmax.hepforge.org/>
- [73] Rizvi, Issever, Dai, Starkman, Stojkovic, Tseng “The BlackMax Manual Version 2.00”, arXiv:0902.3577 [hep-ph] (2009)
- [74] Sean Carroll notes on General Relativity, <http://preposterousuniverse.com/grnotes/>
- [75] <http://www.optcorp.com/edu/articleDetailedEDU.aspx?aid=1706>
- [76] E. Boos et al, “Generic user interface for event generators”, arXiv:hep-ph/0109068v1 (2001)
- [77] QBH Project, <http://qbh.hepforge.org/>
- [78] ATLAS Collaboration, “Search for high-mass dilepton resonances in pp collisions at $\sqrt{s} = 8$ TeV with the ATLAS detector”, Phys. Rev. D. 90, 052005 (2014)

- [79] The ATLAS collaboration, “Search for contact interactions and large extra dimensions in the dilepton channel using proton–proton collisions at $\sqrt{s} = 8$ TeV with the ATLAS detector”, *Eur. Phys. J. C* (2014) 74:3134
- [80] The ATLAS Collaboration, “The ATLAS Simulation Infrastructure” *Eur. Phys. J. C* 70 (2010) 823
- [81] GEANT4 Collaboration, S. Agostinelli et al., *Nucl. Instrum. Meth. A* 506 (2003) 250
- [82] <https://twiki.cern.ch/twiki/bin/view/AtlasProtected/MuonPerformance>
- [83] <https://atlas-lumicalc.cern.ch/>
- [84] T. Gleisberg et al., *JHEP* 02, 007 (2009)
- [85] H.-L. Lai, M. Guzzi, J. Huston, Z. Li, et al., *Phys. Rev. D* 82 (2010) 074024, arXiv:1007.2241 [hep-ph].
- [86] A. Martin, W. Stirling, R. Thorne, and G. Watt, *Eur. Phys. J. C* 63 (2009) 189, arXiv:0901.0002 [hep-ph].
- [87] The ATLAS Collaboration Exotics Lepton+X Working Group, “Search for high-mass dilepton resonances in 21 fb^{-1} of pp collisions at $\sqrt{s} = 8$ TeV with the ATLAS detector”, Internal Support Note ATL-COM-PHYS-2013-1033
- [88] The ATLAS Collaboration, “Search for high mass dilepton resonances in pp collisions at $\sqrt{s} = 7$ TeV with the ATLAS experiment”, *Physics Letters B* 700 (2011) 163–180
- [89] The ATLAS Collaboration, “Search for high–mass dilepton resonances with 5 fb^{-1} of pp collisions at $\sqrt{s} = 7$ TeV with the ATLAS experiment”, ATL-COM-CONF-2012-007 (2012)
- [90] The ATLAS collaboration Exotics Lepton+X Working Group, “Search for high-mass dilepton resonances in 5 fb^{-1} of pp collisions at $\sqrt{s} = 7$ TeV”, Internal Support Note ATL-COM-PHYS-2012-111 (2012)
- [91] S. Alioli, P. Nason, C. Oleari, and E. Re, *JHEP* 1006 (2010) 043, arXiv:1002.2581 [hep-ph].
- [92] K. Melnikov and F. Petriello, *Phys. Rev. D* 74 (2006) 114017, arXiv:0609070 [hep-ph].
- [93] P. Golonka and Z. Was, PHOTOS Monte Carlo: a precision tool for QED corrections in Z and W decays, *Eur. Phys. J. C* 45 (2006) 97–107
- [94] J. Pumplin, D. Stump, J. Huston, H. Lai, P. M. Nadolsky, et al., *JHEP* 0207 (2002) 012, arXiv:0201195 [hep-ph].

- [95] The ATLAS Collaboration, J. M. Butterworth et al., Single and Diboson Production Cross Sections in pp collisions at $\sqrt{s} = 7$ TeV, ATL-COM-PHYS-2010-695 (2010)
- [96] S. Frixione and B. R. Webber, JHEP 0206 (2002) 029, arXiv:0204244 [hep-ph].
- [97] https://twiki.cern.ch/twiki/bin/view/LHCPhysics/TtbarNNLO#Top_quark_pair_cross_sections_at
- [98] M. Cacciari, M. Czakon, M. Mangano, A. Mitov, and P. Nason, Top-pair production at hadron colliders with next-to-next-to-leading logarithmic soft-gluon resummation, Phys. Lett. B710 (2012) 612622.
- [99] A.D. Martin, R.G. Roberts, W.J. Stirling, and R.S. Thorne, Parton distributions incorporating QED contributions, Eur. Phys. J. C39 (2005) 155-161.
- [100] <https://twiki.cern.ch/twiki/bin/viewauth/AtlasProtected/ExtendedPileupRewighting>
- [101] The ATLAS Collaboration, “Search for high mass resonances decaying to dilepton final states in pp collisions at a center-of-mass energy of 7 TeV with the ATLAS detector”, JHEP 1211 (2012) 138
- [102] ATLAS Collaboration, “Muon reconstruction efficiency and momentum resolution of the ATLAS experiment in proton-proton collisions at $\sqrt{s} = 7$ TeV in 2010” arXiv:1404.4562 [hep-ph] (2014).
- [103] <https://twiki.cern.ch/twiki/bin/viewauth/AtlasProtected/CutFlow2012Muons>
- [104] The ATLAS collaboration, “Vertexing Performance Data vs MC comparison for LPCC”, Internal Technical Note ATL-COM-PHYS-2011-1312 (2011)
- [105] <https://twiki.cern.ch/twiki/bin/view/AtlasProtected/MCPAnalysisGuidelinesData2012>
- [106] <https://twiki.cern.ch/twiki/bin/view/Atlas/TrigMuonEfficiency>
- [107] <https://svnweb.cern.ch/trac/atlasoff/browser/Trigger/TrigAnalysis/TrigMuonEfficiency/>
- [108] The ATLAS Collaboration, “Muon reconstruction efficiency in reprocessed 2010 LHC proton-proton collision data recorded with the ATLAS detector”, ATL-CONF-2011-063 (2011)
- [109] https://twiki.cern.ch/twiki/bin/view/AtlasProtected/MCPAnalysisGuidelinesData2012#Muon_Monte_Carlo_efficiency_scal

- [110] The ATLAS collaboration, “Measurement of the muon reconstruction performance of the ATLAS detector using 2011 and 2012 LHC proton-proton collision data”, arXiv:1407.3935 [hep-ph] (2014)
- [111] The ATLAS collaboration, “Preliminary Results on the muon reconstruction efficiency, momentum resolution and momentum scale in ATLAS 2012 pp collision data”, ATLAS-CONF-2013-088 (2013)
- [112] The ATLAS collaboration, “ATLAS Muon Momentum Resolution in the First Pass Reconstruction of the 2010 p-p Collision Data at $\sqrt{s} = 7$ TeV”, ATLAS-CONF-2011-046
- [113] <https://atlas.web.cern.ch/Atlas/GROUPS/PHYSICS/MUON/PublicPlots/2012/June/index.html>
- [114] C. Anastasiou, L. Dixon, K. Melnikov, and F. Petriello, High precision QCD at hadron colliders: Electroweak gauge boson rapidity distributions at NNLO, Phys. Rev. D 69 (2004) 094008.
- [115] R.D. Ball et al., Nucl.Phys. B867 (2013) 244, 1207.1303
- [116] S. Alekhin, J. Bluemlein, S.-O. Moch, “ABM11 PDFs and the cross section benchmarks in NNLO”, arXiv:1302.1516 [hep-ph] (2013)
- [117] A M Cooper-Sarkar, “PDF Fits at HERA”, arXiv:1112.2107 (2011)
- [118] D. Bardin et al., “SANC integrator in the progress: QCD and EW contributions”, JETP Lett. 96 (2012) 285–289
- [119] S. G. Bondarenko and A. A. Sapronov, “NLO EW and QCD proton-proton cross section calculations with mcsanc-v1.01”, arXiv:1301.3687 [hep-ph].
- [120] The ATLAS collaboration Exotics Lepton+X Working Group, “Search for high-mass dilepton resonances with 5 fb¹ of pp collisions at $\sqrt{s} = 7$ TeV with the ATLAS experiment (2011 update for the EPS conference)”, Internal Note ATL-COM-PHYS-2011-770 (2011)
- [121] J. Wenninger, Energy Calibration of the LHC Beams at 4 TeV, tech. rep., 2013. CERN-ATS-2013-040.
- [122] A Caldwell, D. Kollar, K. Kroninger, BAT - The Bayesian Analysis Toolkit, arXiv:0808.2552.v1 Aug 2008
- [123] Glen Cowan, Statistical Data Analysis, first edition Edition, Oxford University Press, Clarendon Press, Oxford, 1998.

- [124] The ATLAS Z' Working Group, ATLAS-COM-PHYS-2011-085, "Limit Setting and Signal Extraction Procedures in the Search for Narrow Resonances Decaying into Leptons at ATLAS"
- [125] W.R. Gilks, S. Richardson, D. Spiegelhalter (Editors), "Markov Chain Monte Carlo in practice", Chapman and Hall, 1996
- [126] Neyman and Pearson Phil. Trans. of the Royal Society of London A (1933)
- [127] The ATLAS Collaboration, "Search for contact interactions in dilepton events from pp collisions at $\sqrt{s} = 7$ TeV with the ATLAS detector" Phys. Lett. B 712 (2012) 40–58
- [128] The CMS Collaboration, "Search for physics beyond the standard model in dilepton mass spectra in proton-proton collisions at $\sqrt{s} = 8$ TeV", arXiv:1412.6302 [hep-ex] (2014)
- [129] Lyons, L. (2008). "Open statistical issues in Particle Physics". The Annals of Applied Statistics 2 (3): 887
- [130] <https://twiki.cern.ch/twiki/bin/view/AtlasPublic/CombinedSummaryPlots#ExoticsSummary>
- [131] The ATLAS collaboration, "Search for new phenomena in the dijet mass distribution using pp collision data at $\sqrt{s} = 8$ TeV with the ATLAS detector", arXiv:1407.1376
- [132] A L Read, "Presentation of search results: the CL_s technique", J. Phys. G: Nucl. Part. Phys. 28 (2002) 2693-2704
- [133] <https://twiki.cern.ch/twiki/bin/view/RooStats/WebHome>
- [134] <https://twiki.cern.ch/twiki/bin/view/AtlasSandbox/QuantumBlackHole>
- [135] H. Yoshino and V. S. Rychkov, "Improved analysis of black hole formation in high energy particle collisions," Phys. Rev. D71 (2005) 104028, arXiv:hep-th/0503171

List of Figures

2.1	Feynman diagrams for electron-positron annihilation (left) and electron scattering (right) [9].	8
2.2	Feynman diagrams for higher order QED processes [9].	9
2.3	Feynman diagrams for a three gluon vertex interaction (left), four gluon vertex (middle) and interaction with quarks (right) [9].	10
2.4	A neutron decays into a proton via the Weak interaction by the transformation of a Down quark into an Up quark [11].	11
2.5	Z^0 boson decaying to a quark-antiquark pair (left) and to lepton-antilepton pair (right).	12
2.6	W^\pm boson decaying to a quarks (left) and to a lepton-neutrino pair (right). . .	12
2.7	3-vertex (left) and 4-vertex (right) self-interaction for the Weak force mediators.	13
2.8	Graphical representation of the potential shown in equation 2.20.	14
2.9	2-D plane of the Top quark mass against the Higgs mass showing the different scenarios for the Electroweak vacuum state. The results obtained at the Tevatron and the LHC are shown at 95% confidence level, together with the expected results in the International Linear Collider [15].	15
2.10	The elementary particles of the Standard Model of Particle Physics, together with their mass, charge, spin and the forces each of the particles interact with [16].	17
2.11	Leading-order production mechanisms for virtual Graviton production at the LHC, and decay to the dielectron final state. Similar diagrams apply to the muon and photon decay channel [22].	20
2.12	Setup for the five dimensional Randall-Sundrum model [26].	21
2.13	Two particles with an impact parameter b smaller than the Schwarzschild radius (R_H) can form a black hole [17]	22
2.14	Stages of semi-classical black hole evaporation [37]	25

3.1	Schematic of the LHC ring with the location of each of the experiments: CMS, ATLAS, LHCb and ALICE. The Proton booster (Pb), Proton Synchrotron (PS) and Super Proton Synchrotron (SPS) accelerate the protons [40].	29
3.2	The ATLAS detector and its internal structure [39]	31
3.3	Schematic of the ATLAS coordinate system [41]	32
3.4	Sagitta (s) of a particle in a magnetic field, where r is the radius of curvature and L is the length traversed by the particle.	33
3.5	The ATLAS inner detector [39]	34
3.6	The ATLAS inner detector internal structure is shown together with the distance to the interaction point. The subsystems shown are the following ones: the pixel detector, the semi-conductor trackers and the transition radiation trackers [39]	35
3.7	Computer generated image of the ATLAS calorimeter system, showing each of the barrel and endcap components [39].	37
3.8	Schematic of a section of the LAr ECal showing the radiation lengths of each of the layers and the length in $\Delta\eta \times \Delta\phi$ of the trigger towers used for the Level-1 trigger of online event selection [39].	39
3.9	Computer generated image of the ATLAS muon system, showing each of the components of the muon spectrometer [39].	41
3.10	The resolution of the muon transverse momentum measurement is shown in the barrel region of the ID (left) and MS (right). The red line assumes a perfectly aligned ATLAS detector, while the solid blue line smears the simulated resolution to reproduce the one found in data. The shaded region shows the uncertainty on the extrapolation to high transverse momentum, coming from the uncertainties of the parameters used to smear the simulated resolution [42].	42
3.11	Layout of the muon tracking precision chambers in the barrel region in the transverse plane. The diameter of the outer circle is about 20 m [39].	43
3.12	Layout of the muon system seen from the y - z plane as defined in the ATLAS coordinate system. The dashed lines show the trajectories of infinite momentum muons. Muons are expected to traverse the three precision layers of precision tracking chambers [39].	44

3.13	Expected muon momentum resolution provided by the standalone muon spectrometer measurement for muons with $p_T = 100$ GeV as a function of the η - ϕ position [39].	45
3.14	Mechanical structure of an MDT chamber, showing the position of the read out (RO) electronics and the high voltage (HV) supplies [39].	46
3.15	Structure of a CSC chamber (left), and one of its strips (right) [43].	46
3.16	Expected magnetic field integral as a function of $ \eta $ for two particles with a azimuthal angle of 0 and $\pi/8$ [39].	47
3.17	Structure of the muon trigger in the barrel region. The first two layers of RPCs are mounted above and below the middle layer of MDTs respectively. The third layer of RPCs is mounted in the outer layer of MDTs [39].	48
3.18	Structure of the muon trigger chambers in the transverse plane [39].	49
3.19	Diagram of the L1 Trigger, composed of the Level-1 Calorimeter and the Muon trigger. The Central Trigger Processor, using input from the L1 systems, makes the decision on whether to accept an event and pass it to the next stage of trigger selection. [39].	51
3.20	Diagram of the ATLAS Trigger system [39].	52
3.21	Layers of the ATLAS computing model [48].	53
3.22	Peak instantaneous luminosity vs time [50].	53
3.23	Peak pile-up vs time [50].	54
3.24	Integrated luminosity delivered vs time [50].	54
3.25	Integrated luminosity delivered by the LHC compared to the one recorded by ATLAS and used in physics analysis [50].	55
4.1	<i>Architecture of the L1Calo trigger</i> [53].	59
4.2	The rate for different L1 triggers is shown against increasing instantaneous luminosity. The triggers EM18VH, MU15, TAU40, J75 and XE40 look for electrons, photons, muons, τ leptons, jets and E_T^{Miss} respectively. The number indicates the transverse energy threshold in GeV for the trigger to activate [55].	61

- 4.3 Figure showing the overall E_T^{Miss} rate at L1 for different noise cut settings. The 2011 configuration corresponds to a 1 GeV threshold for all trigger towers. The “Loose Forward” configuration increases the noise cuts in the forward calorimeter (FCAL) regions ($|\eta| > 3.5$): 6.5, 5.5 and 2.5 GeV in the first layer of the FCAL and 4.5 GeV in the second layer. The “Tight Forward” configuration further increases the noise cuts in the FCAL by 1 GeV and also increases the thresholds beyond $|\eta| = 2.5$ by 0.5 GeV. Finally, the “No FCAL” removes the forward calorimeter from the missing energy calculation. The data used to estimate the rate was taken in run 191426 during 2011 and corresponds to a pile-up of 15 and an instantaneous luminosity of $3.2 \cdot 10^{33} \text{ cm}^{-2} \text{ s}^{-1}$ [56]. 62
- 4.4 The L1_XE50 efficiency of selecting $W \rightarrow e\nu$ processes is evaluated as a function of the offline topological E_T^{Miss} . The trigger L1_XE50 selects events with an E_T^{Miss} larger than 50 GeV. Four different cases are simulated offline depending on the different settings for the trigger tower thresholds and the average number of interactions per crossing ($\langle\mu\rangle$ in the plot) [56]. 63
- 4.5 The plot shows the $\langle\mu\rangle$ -dependence of the rate of several L1Calo triggers through different runs with a 50 ns spacing between bunches, normalised to the instantaneous luminosity of each run. The left side corresponds to data taken during two runs in 2011 at $\sqrt{s} = 7$ TeV. The middle figure shows data from a 2012 run at $\sqrt{s} = 8$ TeV and 50 ns spacing. The right side shows the results for a special high luminosity run in 2011. L1_EM, L1_TAU and L1_J triggers look for electrons/photons, τ leptons and central jets ($|\eta| < 3.2$) respectively. L1_XE50 and L1_XE50_BGRP7 are E_T^{Miss} triggers. L1_XE50_BGRP7 has a veto on the first three bunches of a train. L1_4J10 activates when an event contains more than 4 jets each with $E_T > 10$ GeV and L1_FJ75 looks for forward jets ($|\eta| > 3.2$) with $E_T > 75$ GeV. The dashed lines correspond to fixed-rate lines [56]. 64
- 4.6 The shape of the liquid Argon pulse in ADC counts is shown against time [58]. 65
- 4.7 Trigger rates for three L1 objects per bunch crossing. The rates are relative to that of bunch crossing 141, in the middle of the bunch train. The E_T^{Miss} trigger is L1_XE25 [58]. 66
- 4.8 Number of events activating the E_T^{Miss} trigger L1_XE25 per bunch crossing for a whole bunch train. The figure proposes the separation of the bunch train in two parts: the “Start” and the “Bulk”. 67

4.9	Noise cuts optimized for the start of the bunch train for $\langle\mu\rangle=23$ for different values of occupancy vs $ \eta $ in 3 regions of the electromagnetic calorimeter. . .	69
4.10	Noise cuts optimized for the start of the bunch train for $\langle\mu\rangle=54$ for different values of occupancy vs $ \eta $ in 3 regions of the electromagnetic calorimeter. . .	69
4.11	Noise cuts optimized for the start of the bunch train for $\langle\mu\rangle=81$ for different values of occupancy vs $ \eta $ in 3 regions of the electromagnetic calorimeter. . .	70
4.12	Control plots for $W \rightarrow e\nu$ selection. The kinematic variables shown are the electron E_T (top left), transverse mass (top right), η (bottom left) and ϕ (bottom right). All plots are normalised to unity.	72
4.13	L1 E_T^{Miss} , MET_RefFinal_Et and E_T^{Topo} for the $W \rightarrow e\nu$ selection. All plots are normalised to unity.	72
4.14	Control plots for $t\bar{t}$ selection. The kinematic variables shown are the electron E_T (top left), transverse mass (top right), η (bottom left) and ϕ (bottom right). All plots are normalised to unity.	73
4.15	L1 E_T^{Miss} , MET_RefFinal_Et and E_T^{Topo} for the $t\bar{t}$ selection. All plots are normalised to unity.	74
4.16	L1 E_T^{Miss} distribution for Zero Bias data from the 2012 data-taking. The plot is normalised to unity.	75
4.17	Number of L1_XE25 counts against fractional occupancy usin Zero Bias data from the 2012 data-taking.	76
4.18	The efficiency of the L1 E_T^{Miss} trigger L1_XE25 efficiency for a $W \rightarrow e\nu$ selection is shown against the offline topological E_T^{Miss} . The average efficiency for $E_T^{\text{Miss}} > 40$ GeV is marked in black.	77
4.19	L1_XE25 efficiency for the lowest and highest values of occupancy used for the $W \rightarrow e\nu$ selection against the offline topological E_T^{Miss}	78
4.20	L1_XE25 efficiency for the lowest and highest values of occupancy used for the $t\bar{t}$ selection against the offline topological E_T^{Miss}	78
4.21	The E_T resolution of offline calibrated jets against the L1 jets is shown. The L1 jets consistently undershoot the E_T of the final calibrated jets.	79

4.22	The MET resolution is shown by subtracting the offline topological E_T^{Miss} from the L1 E_T^{Miss} for both the $W \rightarrow e\nu$ and $t\bar{t}$ selection.	79
4.23	The E_T^{Miss} resolution is shown for the $W \rightarrow e\nu$ selection for different jet multiplicities.	80
4.24	Relative efficiency of selecting $W \rightarrow e\nu$ vs Rate reduction factor with respect to the 2012 settings for the start of the bunch train. The occupancy values are next to each point.	81
4.25	Relative efficiency of selecting $t\bar{t}$ vs Rate reduction factor with respect to the 2012 settings for the start of the bunch train. The occupancy values are next to each point.	82
4.26	Relative efficiency of selecting $W \rightarrow e\nu$ vs Rate reduction factor with respect to the 2012 settings for the bulk of the bunch train. The occupancy values are next to each point.	82
4.27	Relative efficiency of selecting $t\bar{t}$ vs Rate reduction factor with respect to the 2012 settings for the bulk of the bunch train. The occupancy values are next to each point.	83
5.1	A rotating black hole and its ergosphere [75]	85
5.2	Comparison of the output of the BlackMax rotating black hole model and the two particle model for a number of variables: black hole mass (top left), total number of particles produced by the black hole decay (top right), particle transverse momentum (bottom left) and PDGID of the particles produced (bottom right). All histograms are normalised to unity.	86
6.1	Born Drell-Yan(DY)+ADD dimuon mass distribution for the ADD model in the GRW formalism normalised to 20.5 fb^{-1} . The cut-off at M_S is included since the model is no longer valid for dimuon invariant masses larger than the string scale.	91
6.2	*	92
6.3	The Drell-Yan Process.	94
6.4	Example of higher order corrections to the Drell-Yan Process with a gluon emission-absorption (left) and initial state radiation (right).	94
6.5	EW+QCD K -factor as a function of Born dilepton mass.	96

6.6	Diboson production at the LHC with leptons in the final state: WW production (top left), ZZ (top right) and WZ (bottom left and right).	97
6.7	Feynman diagram for $t\bar{t}$ (left) and single top (right) production. The top and bottom quark decays through the weak interaction can produce opposite sign dimuon final states.	98
6.8	Feynman diagram of a Photon-Induced process at the LHC with a dilepton final state.	99
6.9	PI correction to the Drell-Yan spectrum as a function of generator level dimuon mass for the analysis presented in [87] (“PI Correction”), with PI process estimated as K -factor, and [22] (“MC PI/DY + 1”), estimated directly from Monte Carlo samples.	101
6.10	LO parton-level cross section for photon-induced dilepton production as a function of dilepton invariant mass. Calculations are done using FEWZ and MRST2004qed PDF assuming either current quark or constituent quark mass [87].	102
6.11	The $\langle\mu\rangle$ distribution for data and Monte Carlo is shown on the left before and after applying the corrections from the PileUpRewightingTool to the simulated processes.	103
7.1	The reconstructed dilepton invariant mass is shown against the number of expected top quark background events and two fit functions are overlaid: dijet (blue) and Monomial (red). The “stitching” point of the top background at high mass is shown in black. The fit range is shown by the green lines. The black points show the the top quark background estimation from the Monte Carlo samples together with statistical errors.	106
7.2	The reconstructed dilepton invariant mass is shown against the number of expected top quark background events. The Monte Carlo estimation is shown in black and the dijet fit is shown in blue. The shaded brown region shows the systematic uncertainties associated with the estimation method. The fit range is shown by the green lines. The ratio between the dijet fit and the Monte Carlo estimate is shown in the bottom, with the shaded region showing the error associated with the ratio between the final estimation and Monte Carlo.	107
7.3	Total acceptance times efficiency for the tight dimuon selection (left) and the loose dimuon selection (right) as a function of the Z' pole mass. The blue line shows a 3rd order polynomial fit to the $A\epsilon$ [87].	111

7.4	The average fractional difference between the muon transverse momentum at generator and reconstructed level is shown as a function of generator level muon p_T . 3 station muons (left) and 2 station muons (right) are shown. The RMS from the mean value in each bin is shown.	112
7.5	The resolution for 3 and 2 station muons is shown for increasing generator level muon p_T . The error bars represent the error on the RMS from figure 7.4.	112
7.6	Reconstructed muon η (top left), ϕ (top right), and p_T (bottom) distributions for data and the SM background estimate using the Tight+Loose Muon selection for events with $m_{\mu\mu} < 400$ GeV.	115
7.7	Comparison of the Dilepton p_T distribution in Data and Monte Carlo for events with $m_{\mu\mu} < 400$ GeV.	116
7.8	Comparison of the Dilepton Rapidity distribution in Data and Monte Carlo for events with $m_{\mu\mu} < 400$ GeV.	117
7.9	Comparison of the dimuon invariant mass distribution in Data and Monte Carlo for events with $m_{\mu\mu} < 400$ GeV.	118
7.10	Average trigger scale factor as a function of the dimuon invariant mass. . . .	119
7.11	Average efficiency scale factor as a function of the dimuon invariant mass. . .	120
7.12	This plot shows the dimuon mass resolution for Combined muons coming from Z boson decays for data, simulated processes without corrections to the muon transverse momentum and simulated processes with the corrections applied. The resolution is the width of a Gaussian convoluted with the dimuon mass resolution at generator level [113].	121
7.13	This plot shows the effect of the corrections on the muon transverse momentum with the RMS on the y-axis.	122
7.14	The ratio of the smeared and scaled and nominal reconstructed dimuon invariant mass distributions is shown on the left. The plot on the right zooms in the Z peak region to show the effect of the <i>MuonMomentumCorrections</i> . .	122
7.15	Asymmetric uncertainty on the Drell-Yan cross section as a function of generator level $m_{\ell\ell}$ due to each PDF eigenvector taken separately. Here eigenvectors 1 to 10 are shown. The upwards and downwards PDF eigenvector variation are shown in red and blue respectively [87].	126

7.16	Asymmetric uncertainty on the Drell-Yan cross section as a function of generator level $m_{\ell\ell}$ due to each PDF eigenvector taken separately. Here eigenvectors 11 to 20 are shown. The upwards and downwards PDF eigenvector variation are shown in red and blue respectively [87].	127
7.17	The systematic uncertainty due to PDF variation on the Drell-Yan cross section is shown for each of the PDF variation groups used as a function of generator level dimuon mass. The black line shows the addition in quadrature of all the PDF variation systematic uncertainties.	128
7.18	The $A\epsilon$ for the ADD LED and its change due to PDF variation is shown for a few different benchmark values of M_S	129
7.19	A summary of the PDF systematic uncertainties on the Drell-Yan cross section as a function of generator level dimuon mass.	130
7.20	Systematic uncertainties due to different higher order EWK corrections calculations as a function of generator level dilepton mass. A quadratic fit to the points is shown in blue [87].	131
7.21	The charge selection efficiency (top) and the muon charge misidentification rate (bottom) is shown against the reconstructed invariant mass for the Monte Carlo simulated Drell-Yan process.	133
7.22	The plot shows the ratio between the Drell-Yan dimuon invariant mass spectrum obtained by increasing the rejection probability due to charge misidentification by 20% and the nominal Drell-Yan spectrum.	134
7.23	The total systematic uncertainty due the possibility of oversmearing and over-scaling for Combined muons is shown against the reconstructed dimuon invariant mass. A quadratic polynomial fit is overlaid.	135
7.24	The ratio between the beam uncertainty shifted cross section and the nominal cross section for vector boson production at 8 TeV is shown for increasing invariant mass [121].	136
7.25	Comparison of the invariant mass distribution for data and Monte Carlo for the QBH search combining the tight (3-station) and loose (2-station) muon selection. The expected QBH signal dimuon invariant mass distribution for two benchmark M_{th} values is shown. The ratio plot shows the ratio between data and the SM background. The grey band shows the range covered by all systematic uncertainties added in quadrature.	139

7.26	Comparison of the invariant mass distribution for Data and Monte Carlo for the ADD LED search. Only 3-station muons are used for this search. The expected signal ADD LED+Drell-Yan nvariant mass distribution for three benchmark M_S values is shown. The ratio plot shows the ratio between data and the SM background. The grey band shows the range covered by all systematic uncertainties added in quadrature.	140
7.27	Comparison of the Dilepton p_T distribution in Data and Monte Carlo for $m_{\mu\mu} > 400$ GeV.	141
7.28	Comparison of the Dilepton Rapidity distribution in Data and Monte Carlo for $m_{\mu\mu} > 400$ GeV.	142
7.29	Reconstructed muon η (top left), ϕ (top right), and p_T (bottom) distributions for data and the SM background estimate using the Tight+Loose Muon selection for $m_{\mu\mu} > 400$ GeV.	143
8.1	Integral of $m_{\mu\mu}^{min}$ for generator level Drell-Yan and Drell-Yan+ADD signal processes. The event yields are normalised to 20.5 fb^{-1}	147
8.2	The number of expected signal+background events at generator level in the 1000-4500 GeV (top) and 1900-4500 GeV (bottom) region in Born dimuon invariant mass is shown against $1/M_S^4$. The quadratic fit from equation 8.8 is shown in red.	148
8.3	Signal significance against the Born dimuon invariant mass for an M_S value of 3.0 TeV.	149
8.4	The signal $A\epsilon$ is shown for all of M_{th} values used for the search. A third order polynomial is fitted to the $A\epsilon$ and shown in blue.	152
9.1	Local significance for the ADD LED search using the tight dimuon selection (left) and for the QBH search using the tight+loose muon selection (right). . .	155
9.2	Number of expected events as a function of $1/M_S^4$ for minimum mass mass cuts of 1300 GeV (left) and 1900 GeV (right) in the muon channel.	156
9.3	PE Distribution of expected limit values on M_S in the muon channel with a prior flat in $1/M_S^4$ for $m_{\mu\mu} > 1300$ GeV (left) $m_{\mu\mu} > 1900$ GeV (right). Both the mean and median of the distribution are highlighted.	157

9.4	Expected (black) and mean (red) limit on M_S in the ADD GRW model determined as a function of minimum mass cut ($m_{\ell\ell}^{min}$) used to define the search region using a $1/M_S^4$ prior on the left (right) for the dimuon (combined) channel.	158
9.5	Number of expected events as a function of $1/M_S^4$ (left) and $1/M_S^8$ (right).	158
9.6	ADD GRW expected LLR PE distribution for a uniform positive prior in $1/M_S^4$ (left) and $1/M_S^8$ (right) choice for the muon channel. The observed LLR is shown by the blue arrow.	160
9.7	ADD GRW expected exclusion limits PE distribution for a uniform positive prior in $1/M_S^4$ (left) and $1/M_S^8$ (right) choice for M_S for the muon channel. The expected exclusion limit is the median of the distribution and is shown by the blue arrow, while the red arrow shows the observed exclusion limit.	161
9.8	ADD GRW observed posterior probability density function for a uniform positive prior in $1/M_S^4$ (left) and $1/M_S^8$ (right) choice for $\theta = 1/M_S^4$ (left) and $1/M_S^8$ (right) for the muon channel. The 95% region is shown in yellow.	161
9.9	ADD GRW expected LLR PE distribution for a uniform positive prior in $1/M_S^4$ (left) and $1/M_S^8$ (right) choice for the dilepton channel. The observed LLR is shown by the blue arrow.	163
9.10	ADD GRW expected exclusion limits PE distribution for a uniform positive prior in $1/M_S^4$ (left) and $1/M_S^8$ (right) choice for M_S for the dilepton channel. The expected exclusion limit is the median of the distribution, while the blue arrow shows the observed exclusion limit.	164
9.11	ADD GRW observed posterior probability density function for a uniform positive prior in $1/M_S^4$ (left) and $1/M_S^8$ (right) choice for $\theta = 1/M_S^4$ (left) and $1/M_S^8$ (right) for the dilepton channel. The 95% region is shown in yellow.	164
9.12	Observed pull distributions for each of the systematic uncertainties affecting the likelihood constructed in BAT to extract exclusion limits. This plot is for the dilepton channel and hence includes all the systematic uncertainties affecting both muon and electron channels.	165
9.13	Summary of 95% CL lower exclusion limits on M_S for the combined dilepton ADD LED search using a uniform positive prior in $1/M_S^8$. Previous ATLAS search results [127] are also shown for comparison [79].	165

9.14	2-D signal scan for the absolute value of the LLR test statistic as a function of M_{Th} and σ_{QBH} for the observed dataset. The white marker highlights the most significant deviation. encountered	168
9.15	LLR distribution for the ADD n=6 QBH model for the electron (top left), the tight+loose muon selection (top right) and the combined dilepton (bottom) channel.	169
9.16	Expected and observed 95% Bayesian upper limits on σ_B for quantum black hole production in the ADD n=6 and RS n=1 models for the electron (top) and the tight+loose muon selection (bottom). The thickness of the ADD n=6 and RS n=1 theory lines represents the effect of the PDF uncertainty on the theoretical σ_B	170
9.17	Expected and observed 95% Bayesian upper limits on σ_B for quantum black hole production in the ADD n=6 and RS n=1 models for the combination of dielectron and dimuon channels. The thickness of the ADD n=6 and RS n=1 theory lines represents the effect of the PDF uncertainty on the theoretical σ_B	171
9.18	Summary of current limits from ATLAS searches for new phenomena [130]. .	172
A.1	Comparison of the Drell-Yan Dilepton p_T distribution before and after applying the boson p_T reweight.	175
A.2	Comparison of the agreement of the Monte Carlo simulated dilepton p_T distribution to that of the Data. The upper figure shows the agreement without applying dilepton p_T reweighting, while the lower one shows the effect of applying it.	176
A.3	Comparison of the Drell-Yan dimuon invariant mass spectrum before and after the dilepton p_T reweighting.	177
B.1	Expected limit PE distribution for the electron (top) and muon (bottom) channels for a uniform prior on the cross section.	179
C.1	Expected and observed 95% CI upper limits on σ_B for quantum black hole production in the ADD n=6 and RS n=1 models for the combination of dielectron and dimuon channels. The thickness of the ADD n=6 and RS n=1 theory lines represents the effect of the PDF uncertainty on the theoretical σ_B	182

D.1	Comparison of the invariant mass distribution for Data and Monte Carlo for the ADD LED search. Only 3-station muons are used for this search. The expected signal ADD LED+Drell-Yan invariant mass distribution for three benchmark M_S values for the HLZ n=2 formalism is overlaid.	183
D.2	Comparison of the invariant mass distribution for Data and Monte Carlo for the QBH search. The expected signal QBH invariant mass distribution for three benchmark M_{th} values for the RS model is overlaid.	184
D.3	ADD HLZ n=2 expected LLR PE distribution for a uniform positive prior in $1/M_S^4$ (left) and $1/M_S^8$ (right) choice for the dimuon channel. The observed LLR is shown by the blue arrow.	184
D.4	ADD HLZ n=2 expected exclusion limits PE distribution for a uniform positive prior in $1/M_S^4$ (left) and $1/M_S^8$ (right) choice for M_S for the dimuon channel. The expected exclusion limit is the median of the distribution and is shown by the blue arrow, while the red arrow shows the observed exclusion limit.	185
D.5	ADD HLZ n=2 observed posterior probability density function for a uniform positive prior in $1/M_S^4$ (left) and $1/M_S^8$ (right) choice for $\theta = 1/M_S^4$ (left) and $1/M_S^8$ (right) for the dilepton channel. The 95% region is shown in yellow. . .	185
D.6	ADD HLZ n=2 expected LLR PE distribution for a uniform positive prior in $1/M_S^4$ (left) and $1/M_S^8$ (right) choice for the dilepton channel. The observed LLR is shown by the blue arrow.	186
D.7	ADD HLZ n=2 expected exclusion limits PE distribution for a uniform positive prior in $1/M_S^4$ (left) and $1/M_S^8$ (right) choice for M_S for the dilepton channel. The expected exclusion limit is the median of the distribution and is shown by the blue arrow, while the red arrow shows the observed exclusion limit.	186
D.8	ADD HLZ n=2 observed posterior probability density function for a uniform positive prior in $1/M_S^4$ (left) and $1/M_S^8$ (right) choice for $\theta = 1/M_S^4$ (left) and $1/M_S^8$ (right) for the dilepton channel. The 95% region is shown in yellow. . .	187
E.1	Expected ADD QBH signal and background (Drell-Yan only) reconstructed dimuon invariant mass spectrum at a centre of mass energy of 13 TeV.	189
E.2	QCD+EW K -factor applied to the Drell-Yan process as a function of the true dilepton mass.	190

E.3 Prospective limits with a centre of mass energy of 13 TeV against increasing integrated luminosity. The limit obtained using 20 fb^{-1} at $\sqrt{s} = 8 \text{ TeV}$ is shown by the red line. 191

List of Tables

2.1	Table extracted from [29] showing the branching ratios for the different allowed decays of a quantum black hole , depending on the electric charge (shown in the superindex in the column for State) and the initial state particles forming the QBH (shown in the lower index in the column for State). The branching ratios are calculated for both the case in which global symmetries are violated (V) and conserved (C).	26
4.1	Trigger tower granularity of L1Calo for different $ \eta $ regions.	58
6.1	Sherpa NLO cross-sections ($\sigma \cdot BR(G^* \rightarrow \mu\mu)$) for benchmark M_S values used in the ADD model search for the GRW formalism. Values are given for the true $m_{\mu\mu}$ range of each generated MC sample. For each mass range considered 10000 events were generated [22].	90
6.2	QBH samples for the ADD n=6 extra-dimension formalism used in the dimuon channel for the analysis presented in [78]. The first column shows the value of M_{th} , the second column the internal ATLAS run number and the third the QBH generator cross section times branching ratio to a dimuon final state. For each M_{th} value 10000 events were generated [87].	93
6.3	Drell-Yan Monte Carlo samples used in the dimuon channel for this analysis. The first column shows the internal ATLAS run number, then the generator level cross section times branching ratio and the mass range it corresponds to. In the last two columns, the number of events generated and the process it corresponds to are shown [87].	95
6.4	Summary of Diboson Monte Carlo samples used for this search. The Born level diboson invariant mass range of each sample is given in the second column. Both the generator level cross section used to generate the sample and the NLO cross section of each process are given in the third and fourth columns. The fifth columns shows the filter efficiency [87].	97
6.5	Top quark Monte Carlo samples used for this analysis. Both the MC@NLO cross section and the NNLO cross section are given in the second and third columns. The fourth columns shows the filter efficiency [87].	99

6.6	Summary of Photon-Induced Monte Carlo samples used for this search. The invariant mass range of each sample is given in the second column. The generator level cross section times branching ratio is shown in the third column [22].	100
7.1	The total number of top quark background events for $m_{\mu\mu} > 400$ GeV is shown for different “stitching” point choices. The error quoted comes from the uncertainty on the fit parameters.	105
7.2	Cutflow table presenting the relative and cumulative efficiencies for each important criterion for the tight (3 station muons) and tight+loose (3+2 station muons) muon selection. The efficiency values correspond to Monte Carlo samples for the dominant Drell-Yan background at dimuon masses in the range of 1.0-1.25 TeV and 2.0-2.25 TeV, each with 100000 generated events. Object quality includes the ID hits requirements together with the requirements on z_0 and d_0 [22].	113
7.3	Cutflow table presenting the relative and cumulative efficiencies for each important criterion for the tight (3 station muons) and tight+loose (3+2 station muons) muon selection. The efficiency values correspond to Monte Carlo samples for the signal QBH process for M_{th} values of 1.0 and 2.0 TeV, each with 10000 generated events. Object quality includes the ID hits requirements together with the requirements on z_0 and d_0	114
7.4	Cutflow table presenting the relative and cumulative efficiencies for each important criterion for the tight (3 station muons) and tight+loose (3+2 station muons) muon selection. The efficiency values correspond to Monte Carlo samples for the signal QBH process for M_{th} values of 3.0 and 4.0 TeV, each with 10000 generated events. Object quality includes the ID hits requirements together with the requirements on z_0 and d_0	114
7.5	Quantative summary of the systematic uncertainties taken into account for the expected number of events in the non-resonant dilepton analysis. Values are provided at three relevant benchmark dilepton masses of 1 TeV (2 TeV) [3 TeV]. N/A indicates that the uncertainty is not applicable.	138
7.6	The expected and observed number of events in the combined (tight + loose) dimuon channel for the QBH search. The region 80-120 GeV is used to normalize the total background to data. The errors quoted are the combination of statistical and systematic uncertainties, except for the total background expectation numbers where the statistical and systematic uncertainties are quoted separately and in that order [87].	138

7.7	Expected and observed event yields in the dimuon channel for the tight dimuon channel in the ADD LED search. The region 80-120 GeV is used to normalize the total background to data. The quoted errors consist of both the statistical and systematic uncertainties added in quadrature, except for the total background expectation numbers where the statistical and systematic uncertainties are quoted separately and in that order [22]	139
9.1	Expected and Observed event yields in the ADD search region for SM processes and various benchmark values of M_S for the ADD GRW formalism in the muon channel.	159
9.2	Expected and Observed event yields in the ADD search region for SM processes and various benchmark values of M_S for the ADD GRW formalism in the electron channel [79].	160
9.3	Expected and observed 95% CL lower exclusion limits on M_S for the GRW ADD search using a uniform positive prior in $1/M_S^4$ or $1/M_S^8$. Both electron and muon channel limits are shown, with all systematic uncertainties taken into account [22].	162
9.4	Expected and observed 95% CL lower exclusion limits on M_S including systematic uncertainties, for ADD signal in the GRW, Hewett and HLZ formalisms [79].	166
9.5	95% Bayesian upper limits on M_{th} for the QBH ADD n=6 model.	168
9.6	95% Bayesian upper limits on M_{th} for the QBH RS n=1 model.	168
C.1	95% CI limits on M_{th} for the QBH ADD n=6 and RS n=1 models for the dimuon channel.	181
C.2	95% Bayesian upper limits on M_{th} for the QBH ADD n=6 and RS n=1 models for the dimuon channel.	181
E.1	Drell-Yan Monte Carlo samples used in the dimuon channel for the estimation of the prospective limits at $\sqrt{s} = 13$ TeV. The first column shows the internal ATLAS run number, then the generator level cross section times branching ratio and the mass range it corresponds to. In the last two columns, the number of events generated and the process it corresponds to are shown[87].	

E.2 QBH samples for the ADD n=6 extra-dimension formalism used in the dimuon channel for the estimation of the prospective limits at $\sqrt{s} = 13$ TeV. The first column shows the value of M_{th} , while the second column lists the internal ATLAS run number and the QBH generator cross section times branching ratio. For each M_{th} value 10000 events were generated. 192